University of Naples Federico II

Ph.D. Program in

Ingegneria Strutturale, Geotecnica e Rischio Sismico

THESIS FOR THE DEGREE OF DOCTOR OF PHILOSOPHY

Fire modelling and structural thermo-mechanical assessment of Automated Rack Supported Warehouses

by

MARGHERITA AUTIERO

Advisor: Prof. Emidio Nigro

Co-Advisor: Dr. Donatella de Silva

2024

SCUOLA POLITECNICA E DELLE SCIENZE DI BASE

DIPARTIMENTO DI STRUTTURE PER L'INGEGNERIA E L'ARCHITETTURA

Fire modelling and structural thermo-mechanical assessment of Automated Rack Supported Warehouses

Ph.D. Thesis presented

for the fulfilment of the Degree of Doctor of Philosophy

in Ingegneria Strutturale, Geotecnica e Rischio Sismico

by

MARGHERITA AUTIERO

2024

Approved as to style and content by

_____

Prof. Emidio Nigro, Advisor

_____

Dr. Donatella de Silva, Co-advisor

University of Naples Federico II
Ph.D. Program in Structural and Geotechnical Engineering and Seismic Risk
XXXVI cycle - Chairman: Prof. Iunio Iervolino

www.dist.unina.it/dottorati-di-ricerca/dottorati

Candidate's declaration

I hereby declare that this thesis submitted to obtain the academic degree of Philosophiæ Doctor (Ph.D.) in Ingegneria Strutturale, Geotecnica e Rischio Sismico is my own unaided work, that I have not used other than the sources indicated, and that all direct and indirect sources are acknowledged as references.

Parts of this dissertation have been published in international journals and/or conference articles.

Naples, March 08, 2024

Margherita Autiero

"Non chi comincia ma quel che persevera" è il motto del Vespucci.
A tutti coloro che ostinatamente, caparbiamente,
nonostante tutto perseverano.

FRIO FRIOVSTO IMPERATOR ROMANORVM SEMPER AVGVSTVS

Abstract

The fire behaviour of the Automated Rack-Supported Warehouses (ARSWs) is a topic of great interest for both the scientific community and the manufacturers of industrial racks. ARSWs are a particular type of steel racks that combine the structural efficiency of steel construction with automated machines for handling stored products. This work has addressed the fire modelling and structural thermo-mechanical assessment of Automated Rack Supported Warehouses. The study is composed of two phases: the first one regards the investigation of the fire modelling which can be used in a multi-depth ARSW structure, by adopting localized fire models, zone models, and Computational Fluid Dynamics models. A fire model that allows vertical and horizontal propagation, starting from a localized fire, evaluated, and validated against experimental results available in the literature, is proposed. Also, a criterion to evaluate the vertical and horizontal propagation times is provided. The second part of the work focuses on the study of the structural collapse mechanism and on the methodologies of analysis that the designer should adopt to properly interpret it. Several thermo-mechanical analyses were carried out by using all the results of the proposed fire model and compared with different fire models available in the literature. To correctly analyse the progressive mechanism of collapse, an iterative procedure is proposed by using several subsequent implicit analyses carried out with SAFIR software, by comparing this one with an automatic procedure by using the software ABAQUS CAE which allows the implementation of implicit/explicit analyses.

Keywords: Automated Rack Supported Warehouses; cold-formed steel members; fire modelling; vertical fire propagation; thermo-mechanical analysis; numerical simulations.

Sintesi in lingua italiana

Il comportamento in condizioni di incendio dei Magazzini Autoportanti Verticali (MAV) è un argomento di grande interesse sia per la comunità scientifica che per i produttori di scaffalature industriali. I MAV sono un particolare tipo di scaffalature metalliche che combinano l'efficienza strutturale delle strutture in acciaio con macchine automatizzate per la movimentazione dei prodotti stoccati. Il presente lavoro di tesi ha affrontato la modellazione dell'incendio e l'analisi termo-meccanica strutturale dei MAV. Lo studio si compone di due fasi: la prima riguarda la definizione del modello di incendio che può essere utilizzato in un magazzino automatico del tipo multi-profondità, quali modelli di incendio localizzati, modelli a zone e modelli di fluido-dinamica computazionale. Viene proposto un modello di incendio che consente la propagazione verticale e orizzontale di un incendio localizzato, valutato e validato attraverso risultati sperimentali disponibili in letteratura. Viene quindi fornito anche un criterio per valutare i tempi di propagazione verticale e orizzontale. La seconda parte del lavoro si concentra sullo studio del meccanismo di collasso strutturale e sulle metodologie di analisi che il progettista deve adottare per interpretarlo correttamente. Diverse analisi termo-meccaniche sono state effettuate utilizzando tutti i risultati del modello di incendio proposto e confrontati con diversi modelli di incendio disponibili in letteratura. Per analizzare correttamente il meccanismo di collasso progressivo viene proposta una procedura iterativa che utilizza varie analisi implicite successive effettuate con il software di calcolo SAFIR; la procedura viene confrontata e validata con una procedura automatica condotta con il software ABAQUS CAE che permette l'implementazione di analisi implicite/esplicite.

Parole chiave: Magazzini Autoportanti Verticali; profili in acciaio sottili piegati a freddo; modellazione dell'incendio; propagazione dell'incendio verticale; analisi termo-meccaniche; simulazioni numeriche.

Aknowledgements

The Ph.D. journey was anything but easy; it tested my abilities and pushed me to the brink of insecurity. There were moments when I contemplated giving up, feeling inadequate to see it through. Yet, here I am, writing the acknowledgments, having completed it. I am deeply grateful to everyone who walked alongside me during this journey. Their support and influence made all the difference, shaping the experience into what it is today.

First of all, I have to thank my advisor, Prof. Emidio Nigro, for allowing me to do several interesting experiences during these Ph.D. years. The moments of discussion with Prof. Emidio Nigro about my research were always precious and illuminating for me.

I thank my Co-advisor, Dr. Donatella de Silva, for her never-ending support, as well as a big sister does. The quality of the results outlined in this thesis was greatly influenced by the daily discussions with Dr. Donatella de Silva.

I have to thank ROSSS Spa for hosting me for nine months and for allowing me to learn the most important aspects of the thesis topic. I extend sincere gratitude to Eng. Giovanni Lavacchini for generously sharing his expertise in automated rack-supported warehouses with constant professionality and kindness and for all the interesting discussions regarding the thesis topic.

I have to thank Dr. Alessandro Mei for our discussions about the topic that always illuminated and encouraged me.

I am also grateful to my colleague, Enrico Cardellino, this journey would not been the same without sharing its fatigue with a friend like him.

A particular mention goes to Giuseppe Lo Greco for supporting me in all the most important parts of this research with a never-ending kindness.

I also thank Dr. Naveed Alam, who hosted me for three months at Ulster University in Belfast (United Kingdom), where I experimented with an important part of the research presented in this dissertation. Dr. Naveed Alam with great humanity taught me a lot and in particular to believe in my research.

I would like to express my gratitude to the Reviewers of this thesis, Prof. Maurizio Orlando (University of Florence) and Prof. Ali Nadjai (Ulster University), for their valuable comments that helped me to improve the quality of my thesis.

My greatest acknowledgment goes to my greatest wealth, my parents. Thanks for giving me the freedom to choose, and above all the respect for all the sacrifices involved in this journey without ever stopping to believe in me. To my uncle Luigi and my big brother Lorenzo to give me their constant esteem. To my sister, "*Nur dei miei occhi*", for being more special than she thinks.

To all my girls Florencia, Filomena, Liliana, and Alessandra thanks for supporting me and for putting up with me at every moment.

Lastly to my biggest fan, Giuseppe, thanks for believing in me when I was not able to do it. All of this would not been possible without you.

Contents

Abstract ..... **i**

Sintesi in lingua italiana ..... **iii**

Aknowledgements ..... **v**

List of symbols ..... **xiii**

List of figures ..... **xv**

List of tables ..... **xxiii**

1. Introduction **1**

1.1. General overview 1

1.2. Objectives 3

1.3. Organization of the thesis 4

2. Steel structures in fire **7**

2.1. Fire resistance design 7

2.1.1. Actions in fire conditions 10

2.1.2. Thermal analysis 12

2.1.3. Mechanical analysis 15

2.1.4. Mechanical properties of carbon steel 20

2.1.5. Robustness of steel structures in case of fire 22

2.1.6. Fire induced progressive collapse 24

2.2. Automated rack supported warehouses (ARSW) 26

2.2.1. Design of ARSWs at ambient temperature 31

2.2.2. Design of ARSWs in fire conditions 36

2.2.3. Description of the typological ARSW structure 43

2.3. Fire models 46

2.3.1. Nominal fire curves 47

2.3.2. Input data for natural fire models 49
2.3.3. Localized fires 52
2.3.4. Zone models 57
2.3.5. Computational Fluid dynamics (CFD) models 60
2.3.6. Travelling fires 61
2.3.7. Open issues in fire models for rack structures 69
3. Fires Modelling of steel racks..... 71
3.1. Fire spread in large industrial premises and warehouse: study of a previous paper. 71
3.1.1. Test series 1 - Cone calorimeter tests 73
3.1.2. Test series 2 - Fire spread tests with one small rack 73
3.1.3. Test series 3 - Free burning tests (without ceiling) with four racks 76
3.1.4. Test series 4 - Study of the influence of the size of the enclosure 77
3.1.5. Test series 5 - Fire spread tests with four racks. 81
3.2. Simulation of the experimental tests 89
3.2.1. CFAST – Consolidated Fire and Smoke Transport 89
3.2.1.1. Input data required for the zone model. 90
3.2.1.2. The basic transport equation 90
3.2.1.3. Fire properties in CFAST 93
3.2.1.4. Ventilation in CFAST 93
3.2.2. Simulation of the test series 4 94
3.2.3. Simulation of the test series 1 and 2 99
3.2.4. Simulation of the test series 5 102
3.3. Proposed fire model for ARSW, CFAST 107

3.3.1. Previous model 111
3.3.2. Final model 114
3.4. Proposed fire model for ARSW, FDS 119
3.4.1. Results discussion 124
3.5. Benchmarks between fire models 131
4. Thermo-mechanical modelling of ARSWs 137
4.1. Steel structures collapse analysis 137
4.2. Modelling structures in fires with SAFIR: theoretical background and capabilities 139
4.2.1. Thermal analysis 141
4.2.1.1. Boundary conditions for thermal analysis 142
4.2.2. Mechanical analysis 144
4.3. Finite element model by using SAFIR software 148
4.3.1. Fire scenario with nominal fire curve ISO834 150
4.3.2. Fire scenario with zone model 156
4.3.3. Fire scenario with localized models 160
4.3.3.1. Heskestad/LOCAFI model 161
4.3.3.2. LOCAFI implementation in SAFIR 165
4.3.3.3. Results and discussion 167
4.3.4. Fire scenario with a combined fire model 173
4.3.5. Fire scenario with FDS 175
4.3.6. Benchmarks between thermo-mechanical analyses with different fire models 179
4.4. Study of a progressive collapse by using the SAFIR software 185
4.5. Modelling structures in fires with ABAQUS CAE: theoretical

background and capabilities 197
4.6. Finite element model by using Abaqus CAE software 198
4.6.1. Results and discussion 200
5. Conclusions and future work 209
Bibliography 214

List of acronyms

The following acronyms are used throughout the thesis.

PL	Performance level
SR	Steel rack
ARSWs	Automated Rack Supported Warehouses
DA	down-aisle direction
CA	cross-aisle direction
AMSWs	Automated Multi-Depth Shuttle Warehouses
CFS	cold-formed steel section
NIST	National Institute of Standards and Technology
CFD	Computational Fluid dynamics
RANS	Reynolds Average Navier Stokes
HERA	Heavy Engineering Research Association
LFM	Large Firecell Method
TFM	Travelling Fire Methodology
HRR	Heat release rate
DOF	Degree Of Freedom

List of symbols

The following symbols are used throughout the thesis.

$A_d\ (t)$	Indirect fire actions
A_{fi}	Maximum area of the fire
A_m/V	Section factor for unprotected steel member
A_m	Surface area of the member, per unit of length
A_{eff}	Effective cross-sectional area
c	Specific heat of steel
$D_{fire,eq}$	Equivalent diameter of the fire
E_θ	Young's modulus at elevated temperature
$f_{p,\theta}$	Proportional limit at elevated temperature
$G_{k,i}$	Characteristic value of the permanent actions
g_i	Mass of the i-th combustion material
H_i	Calorific value of the i-th combustion material
$\dot{h}_{net}$	Design value of the net heat flux per unit area
$\dot{h}_{net,c}$	Heat transfer by convection
$\dot{h}_{net,r}$	Heat transfer by radiation
k_{sh}	Correction factor for the shadow effect
k_θ	Reduction factor for a strength or deformation property at elevated temperature
$k_{0.2p,\theta}$	Reduction factor for the 0.2% proof strength at elevated temperatures
$P_k\ (t)$	Prestressing load
$Q_{k,i}$	Characteristic value of the variable actions
Q_c	Convective part of the HRR
q_{fd}	Design fire load
t_α	Time needed to reach a rate of heat release of 1 MW

V	Volume of the member, per unit of length
X_K	Characteristic value of a strength or deformation property for normal temperature
α_c	Coefficient of heat transfer by convection
θ_m	Surface temperature of the member
θ_r	Effective radiation temperature of the fire environment
Φ	Configuration factor
ε_m	Surface emissivity of the member
ε_f	Emissivity of the fire
σ	Stephan Boltzmann constant (= $5{,}67 \cdot 10^{-8}$ W/m^{2}k^4)
ρ	Unit mass of steel
λ	Thermal conductibility of the steel
v	Poisson ratio
$\Delta\theta_{a,t}$	The increase of steel temperature during a time interval from t to t+Δt
$\gamma_{M,fi}$	partial safety factor for the relevant material property for fire situation
χ_{fi}	Reduction factor for flexural buckling in the fire design situation
ρ_θ	The reduction factor for plate buckling
$\overline{\lambda_{p,\theta}}$	Non - dimensional slenderness at elevated temperatures

List of figures

Figure 2.1. Time (1), load (2), and temperature (3) domains for a nominal fire curve [11]. 17
Figure 2.2. Time, load, and temperature domains for a natural fire curve [11]. 18
Figure 2.3. Stress-strain relationship for carbon steel at elevated temperatures [11]. 21
Figure 2.4 Reduction factors for carbon steel for the design at elevated temperatures. 22
Figure 2.5. An ARSW during its construction. (Source: ROSSS s.p.a.) 27
Figure 2.6. Main directions of a Steel Rack (a) and nomenclature of all the structural elements (b). 28
Figure 2.7. Automated racking systems:(a) AS/RS, (b) shuttle system (source: www.mecalux.com) 29
Figure 2.8. shuttle system detail [38]. 29
Figure 2.9. Single-depth configuration (a) , double-depth configuration (b) [8]. 30
Figure 2.10. Pallet disposal in single-depth (a) and in double-depth (b) [8]. 30
Figure 2.11. An example of cold-formed steel member. Source: ROSSS s.p.a. 32
Figure 2.12. An example of a steel upright, beam and connector [52]..... 33
Figure 2.13. Plan view of the considered AMSW (dimensions in m). Source: ROSSS s.p.a. 44
Figure 2.14. Down-aisle direction of the considered AMSW (dimensions in m). Source: ROSSS s.p.a. 45
Figure 2.15. Cross-aisle direction of the considered AMSW (dimensions in m). Source: ROSSS s.p.a 45
Figure 2.16. Nominal fire curves. 48
Figure 2.17. Natural fire curve phases. 49
Figure 2.18. HRR curve phases. 51
Figure 2.19. Heskestad Model [1]. 53
Figure 2.20. Hasemi Model [1] 54

Figure 2.21. LOCAFI pool fire [108]. 55
Figure 2.22. Numerical heat flux and flame (top); heat flux with a conical flame (bottom right); heat flux with a cylinder shape (bottom right), [108]. 57
Figure 2.23. Schematic of control volumes in a two-layer zone model [112].58
Figure 2.24. Scheme of the near field and far field according to TFM [141] (a); Flapping angle and reduced near field temperature according to iTFM [142] (b). 63
Figure 2.25. ETFM heat fluxes combination: Hasemi (localized fire) and FIRM (zone model) [144]. 65
Figure 3.1. Results from the cone calorimeter test series 1 carried out by Lönnermark and Ingason [150]. 73
Figure 3.2. Side, front, and top views of the experimental set-up used in test series 2. × represent measurement position. Dimensions in mm [150]. 74
Figure 3.3. Comparison between test series 2 results: (a) in terms of temperature (position 2); (b) in terms of HRR (position 3) [150]. 75
Figure 3.4. Top view and side view of the experimental set-up used in test series 3. Dimensions are in mm [150]. 76
Figure 3.5. Comparison between test series 3 results in terms of HRR [1].... 77
Figure 3.6. Side and top views of the experimental set-up of the test series 4 [150]. 79
Figure 3.7. Comparison of heat release rates in test series 4 [150]. 80
Figure 3.8. Comparison of heat release rates in test series 4: 4.2 test (a), 4.3 test (b), 4.4 test (c), 4.5 test (d) [150]. 81
Figure 3.9. Side view of the experimental set-up of the test series 5 (a), plan view with thermocouples positions (b) [150]. 83
Figure 3.10. Time to flame reaching the ceiling and spread between racks (a), times depurated with times of the flame to reach the top of the commodities in rack 2 (b). 84
Figure 3.11. Comparison between gas temperature measurements in position 11 with different distances (y) between the top of the commodities and the ceiling [150]. 85
Figure 3.12. Comparison between temperatures in position 20 with different

slope of the ceiling and with and without beams, respectively [150]. 86
Figure 3.13. Comparison of times to activation of sprinkler without (left = blue) and with (right = red) beams, respectively [1]. 87
Figure 3.14. Comparison between temperatures recorded from, for each thermocouple and metal cylinders placed in position 20 at four different heights: 30 mm, 60 mm, 90 mm, from the ceiling [150], for the test 5.8 (a) and test 5.9 (b). 88
Figure 3.15. CFAST model in SMOKWIEV environment of test 4.2 (a), test 4.3 (b), test 4.4 (c) and test 4.5 (d)..... 95
Figure 3.16. Comparison between numerical and experimental results in terms of HRR curves for test 4.2 (a) and 4.3 (c) and temperatures for test 4.2 (b) and 4.3 (d)..... 97
Figure 3.17. Comparison between numerical and experimental results in terms of HRR curves for test 4.4 (a) and 4.5 (c) and temperatures for test 4.4 (b) and 4.5 (d)..... 98
Figure 3.18. CFAST model of the test 2.2. 101
Figure 3.19 CFAST results in terms of flame development for test 2.2. 101
Figure 3.20. Comparison between numerical and experimental results in terms of HRR curves (a) and temperatures (b). 102
Figure 3.21. Test 5.3 setup with fire propagation times. 103
Figure 3.22. HRR curves for the test 5.3: HRR curves of the 2nd rack (a) and of the lateral ones (b). 104
Figure 3.23. CFAST model of the test 5.3, dimensions are in meters. 105
Figure 3.24. Comparison between numerical and experimental results. 105
Figure 3.25. HRR curves: (a) calculated with scaling laws, (b) modified one. 109
Figure 3.26 Evaluation of the horizontal fire propagation time. 110
Figure 3.27. First CFAST model of the ARSW structure. 111
Figure 3.28. HRR curves for the central shoulder. 112
Figure 3.29. HRR curves for the adjacent shoulders. 113
Figure 3.30. Temperatures recorded in the CFAST model for the horizontal elements (a) and uprights one (b)..... 113

Figure 3.31. Final CFAST model of the ARSW structure. 115
Figure 3.32. Temperature distributions recorded by the thermocouples placed at the first 7 levels near the horizontal elements (a) and temperature of the hot zones (b) of the central shoulder. 116
Figure 3.33. Temperature distributions recorded by the thermocouples placed at the first 7 levels near the horizontal elements of the lateral shoulder. 117
Figure 3.34. Average of the temperatures recorded in the hot zone and in the cold zone at each level, for the central shoulder (a) and the lateral ones (b). .. 118
Figure 3.35. Temperature distribution within the structure for the proposed multi-cells zone model. 119
Figure 3.36. FDS model of the ARSW structure with AST devices positions. 120
Figure 3.37. FDS model with mesh definition. 123
Figure 3.38. Temperature distributions computed by FDS at the horizontal beams of the central shoulder. 124
Figure 3.39. (a) Smokeview image for the simulation at 5 minutes and (b) corresponding temperatures computed by FDS. 125
Figure 3.40. (a) Smokeview image for the simulation at 12 minutes and (b) corresponding temperatures computed by FDS. 125
Figure 3.41. (a) Smokeview image for the simulation at 20 minutes and (b) corresponding temperatures computed by FDS. 126
Figure 3.42. (a) Smokeview image for the simulation at 35 minutes and (b) corresponding temperatures computed by FDS. 126
Figure 3.43. Temperature distributions computed by FDS at the vertical beams of the truss. 127
Figure 3.44. Temperature distributions computed by FDS at the bottom chords of the truss. 127
Figure 3.45. Temperature distributions computed by FDS at the uprights of the central shoulder (III shoulder). 128
Figure 3.46. Temperature distributions computed by FDS at the upright on the left of the adjacent shoulders (II and IV shoulders). 129
Figure 3.47. Temperature distributions computed by FDS at the upright on

the right of the adjacent shoulders (II and IV shoulders). 129
Figure 3.48. Temperature distributions computed by FDS at the upright on the left of the adjacent shoulders (I and V shoulders). 130
Figure 3.49. Temperature distributions computed by FDS at the upright on the right of the adjacent shoulders (I and V shoulders)..... 130
Figure 3.50. Temperature distributions computed by FDS and CFAST at the horizontal beams of the central shoulder for the first three levels. 132
Figure 3.51. Temperature distributions computed by FDS and CFAST at uprights of the central shoulder for the first three levels. 134
Figure 4.1. Workflow of a thermo-mechanical analysis in SAFIR [185] 141
Figure 4.2. First step of the time integration procedure in SAFIR 145
Figure 4.3 The cross-aisle view of the FE model in the GID environment.. 148
Figure 4.4 Intensity of loads (in N) applied in the FE model..... 149
Figure 4.5. Effective law proposed by Franssen et al. [188] versus actual steel material law from the EC3 part 1-2. 150
Figure 4.6. ISO834 fire curve: deformed shape at 7.2 minutes in the Diamond environment. 151
Figure 4.7. ISO834 fire curve: temperature distribution within the cross section in the Diamond environment at 7.2 minutes (a), temperature distribution over time (b). 152
Figure 4.8. ISO834 fire curve: comparison between stress and resistance. . 155
Figure 4.9. Zone model, CFAST: deformed shape at 5.8 minutes in the Diamond environment. 157
Figure 4.10. Zone model, CFAST: temperature distribution within the cross section in the Diamond environment at 5.8 minutes (a), temperature distribution over time (b). 157
Figure 4.11. Zone model, CFAST: comparison between stress and resistance. 160
Figure 4.12. Cylindrical flame and conical shape for a flame not impacting the ceiling (a) and a flame impacting the ceiling (b) [108]. 163
Figure 4.13. H column modelling and modelling of a vertical member [108]. 163

Figure 4.14. Cylindrical flame and conical shape for a flame not impacting the ceiling (a) and a flame impacting the ceiling (b) [108]. 164
Figure 4.15. LOCAFI model [108]..... 166
Figure 4.16. (a) divisions of the flame (b) distance r between a facet of the fire and the section [108]..... 167
Figure 4.17. LOCAFI model: Temperature distributions of the horizontal elements at the first 6 levels 168
Figure 4.18. Temperature distributions along the 1st level of the upright, comparison between LOCAFI model and CFAST one. 169
Figure 4.19. LOCAFI model: deformed shape at 3.9 minutes in the Diamond environment. 170
Figure 4.20. LOCAFI model: Temperature distribution over time of the horizontal beam at 2nd level..... 170
Figure 4.21. LOCAFI models: comparison between stress and resistance. 172
Figure 4.22. Combined model CFAST-LOCAFI: deformed shape at 5.8 minutes in the Diamond environment..... 173
Figure 4.23. Combined model CFAST-LOCAFI: comparison between stress and resistance..... 174
Figure 4.24. CFD model, FDS: deformed shape at 6.2 minutes in the Diamond environment. 175
Figure 4.25. CFD model, FDS: temperature distribution within the cross section in the Diamond environment at 6.2 minutes (a), temperature distribution over time (b). 176
Figure 4.26. CFD model, FDS: comparison between stress and resistance. 178
Figure 4.27. Comparison between temperature distributions for the horizontal beams of the central shoulder for the first three levels obtained with CFAST, FDS and LOCAFI fire models. 180
Figure 4.28. Comparison between axial forces in the horizontal beams of the central shoulder for the first 3 levels obtained with CFAST, FDS and LOCAFI fire models..... 182
Figure 4.29. Comparison between bending moments in the horizontal beams

of the central shoulder for the first 3 levels obtained with CFAST, FDS and LOCAFI fire models. 183

Figure 4.30. Comparison between temperature distributions for the upright of the central shoulder for the first level obtained with CFAST, FDS and LOCAFI fire models. 184

Figure 4.31. Comparison between axial forces in the upright of the central shoulder for the first level obtained with CFAST, FDS and LOCAFI fire models. 185

Figure 4.32. Evolutions of the axial forces in the horizontal beams belonging to the first 5 levels of the central shoulder. 186

Figure 4.33. Evolutions of the horizontal displacements at the external point of the horizontal beams of the first 5 levels. 187

Figure 4.34. Deformed shape at 7.8 minutes in the Diamond environment of the structure without the beam at the 2nd load level. 188

Figure 4.35. Temperature distribution within the cross section over time (a), comparison between stress and resistance (b). 188

Figure 4.36. Evolutions of the axial forces in the horizontal beams belonging to the 3rd, 4th, and 5th levels of the central shoulder. 189

Figure 4.37. Evolutions of the horizontal displacements at the external point of the horizontal beams of the first 5th levels. 190

Figure 4.38. Deformed shape at 10.2 minutes in the Diamond environment of the structure without the beam at the 2nd and 3rd load level 191

Figure 4.39. Temperature distribution within the cross section over time (a), comparison between stress and resistance (b). 191

Figure 4.40. Evolutions of the axial forces in the horizontal beams belonging to the 4th and 5th levels of the central shoulder. 192

Figure 4.41. Evolutions of the horizontal displacements at the external point of the horizontal beams of the first 5 levels. 193

Figure 4.42. Deformed shape at 10.3 minutes in the Diamond environment of the structure without the beam at the 2nd, 3rd, and 4th load levels (a), comparison between stress and resistance of the truss' diagonal (b). 194

Figure 4.43. Deformed shape at 12.4 minutes in the Diamond environment of

the structure without the beam at the 2nd, 3rd, and 4th load levels and the truss' diagonal 195

Figure 4.44. Temperature distribution within the cross section over time, comparison between stress and resistance (b). 195

Figure 4.45. Evolutions of the horizontal displacements at the external point of the horizontal beams of the first 5 levels. 196

Figure 4.46 The cross-aisle view of the FE model in the ABAQUS CAE environment. 199

Figure 4.47 *Joint* and *Rotation* connectors [190] 199

Figure 4.48 Different stress-strain curves at various temperatures according to EC3 part l-2 for steel grade S355 200

Figure 4.49 Deformation sequence. Left: Von-Mises stresses; Right: Temperatures. 204

Figure 4.50 Comparison between stress and resistance at the last step of the implicit part. 205

Figure 4.51 Benchmark between ABAQUS and SAFIR displacements at the end of beam of the 2nd load level. 206

Figure 4.52 Comparison between ABAQUS (a) and SAFIR (b) collapse deformed shapes. 207

List of tables

Table 2.1 Performance levels according to the Italian fire prevention regulation [1]..... 8
Table 2.2 Cross-sections used for the considered AMSW..... 46
Table 3.1 Material properties for test series 4..... 94
Table 3.2 Fire parameters for HRR curve of test 2.2..... 100
Table 3.3 Fire parameters for HRR curve for a single level of the 2nd rack. 103
Table 3.4 Comparison between experimental and calculated propagation times..... 106
Table 3.5 Scaling factor for the model [21]..... 109
Table 3.6 Vertical propagation times calculated for ARSW structure..... 110
Table 3.7 Material properties for test series 4..... 121
Table 4.1 ISO834 fire curve: effective cross-sectional area for the coupled U section 80x40x2mm according to the capacity methods of the actual EC3. 152
Table 4.2 ISO834 fire curve: design buckling resistance at different exposure times for the coupled U section 80x40x2mm according to the capacity methods of the actual EC3..... 153
Table 4.3 ISO834 fire curve: effective cross-sectional area for the coupled U section 80x40x2mm according to the capacity methods of the new EC3. 153
Table 4.4 ISO834 fire curve: design buckling resistance at different exposure times for the coupled U section 80x40x2mm according to the capacity methods of the new EC3..... 154
Table 4.5 ISO834 fire curve: difference between design buckling resistance according to the two capacity methods..... 155
Table 4.6 Zone model, CFAST: effective cross-sectional area for the coupled C section 150x50x15x2mm according to the capacity methods of the actual EC3. 158
Table 4.7 Zone model, CFAST: design buckling resistance at different exposure times for the coupled C section 150x50x15x2mm according to the capacity methods of the actual EC3. 158
Table 4.8 Zone model, CFAST: effective cross-sectional area for the coupled C section 150x50x15x2mm according to the capacity methods of the new EC3.

..... 159
Table 4.9 Zone model, CFAST: design buckling resistance at different exposure times for the coupled C section 150x50x15x2mm according to the capacity methods of the new EC3. 159
Table 4.10 LOCAFI models: design buckling resistance at different exposure times for the coupled C section 150x50x15x2mm according to the capacity methods of the actual EC3. 171
Table 4.11 LOCAFI models: design buckling resistance at different exposure times for the coupled C section 150x50x15x2mm according to the capacity methods of the new EC3. 172
Table 4.12 CFD model, FDS: design buckling resistance at different exposure times for the coupled C 150x50x15x2mm according to the capacity methods of the actual EC3. 177
Table 4.13 CFD model, FDS: design buckling resistance at different exposure times for the coupled C 150x50x15x2mm according to the capacity methods of the new EC3. 177

Chapter 1

1. Introduction

1.1. General overview

The warehouses are typical buildings where many goods can be stored after their production and before their distribution to the consumers. Since the demand for storage space is growing, due to increasing mass production and consumption levels, highly optimized warehouses are needed. Automated Rack Supported Warehouses (ARSWs) are used in industrial facilities to optimize storage spaces because they combine the structural efficiency of steel construction with automated machines for handling stored products. ARSWs can be seen as the direct upgrade of traditional pallet steel racks (SR), since in ARSWs' case, the SRs are both the stored areas and the structure of the warehouse.

ARSWs are characterized, on one hand, by a peculiar structural configuration, that strongly influences their global behaviour and, on the other hand, by unique non-standard structural components. Indeed, these structures mainly consist of thin-walled sections obtained by cold-forming thin metal sheets (CFS) that, optimize the structural performance by reducing the steel weight, the costs, and the assembly time. But, at the same time, these types of sections are usually classified as class 4 cross-sections, according to EC3 part 1-1 [1], and so they can fail by a variety of buckling modes including global, local, and distortional buckling and their interactions. Moreover, in fire conditions, the thin thickness of these profiles, combined with the high thermal conductivity of the steel, induces a fast increase in the steel temperature with a significant loss in material stiffness and

strength. The research carried out on SRs, can be divided between those dealing with the analysis of global behaviour and those with single elements and connections. In the last decades, the structural behaviour of SRs has been investigated focusing on seismic aspects [2], while their structural behaviour under fire conditions is still poorly known.

Moreover, at present, fire design methods for CFS members are not as developed as for hot-rolled ones. Couto et al. 2014 [3] developed new expressions to determine the effective width of steel sections at high temperatures, which are proposed for the new drafts of the next generation of structural Eurocodes.

In the context of modern technical codes, as the new Italian technical fire prevention regulation [4], the fire resistance is defined as a passive fire protection measure to guarantee load bearing and compartmentation capabilities to the structures according to performance levels. Since the ARSWs are not involved in activities concerning the presence of people, except for the highly trained workers, the performance level (PL) I or II could be required for them, which means that the absence of external consequences due to structural collapse must be demonstrated. To comply with the PL, different design solutions can be chosen, based on prescriptive or performance-based approaches. In the ARSW structures considering the performance-based approach is essential, because the prescriptive one generally leads to the use of traditional passive fire protection systems, that in the case of CFS profiles, are difficult to apply, due to their high section factors (A_m/V) and very small critical collapse temperatures. This means that moving in the context of performance-based approach, the designer must prove analytically that the collapse mechanism is inward.

The first step of the performance-based approach is the selection of the design fire scenarios and the definition of the natural fire curves, according to the fire models. The fire that regards this type of structure starts like a localized fire and could develop in a traveling fire both in horizontal and vertical directions. At present, fire design methods for vertically traveling fires are not as developed as for horizontal ones [5]. Indeed, in the last decade, vertically traveling fires have been analysed like multi-floor fires in high-rise buildings [6], which represents a

different condition than the ARSWs one.
The study of the mechanism of collapse is related to the fire model adopted and the types of methodologies of analysis that the designer must adopt to properly interpret it. Moreover, for steel elements not protected with active or passive fire systems, fire can be a reason for failure and progressive collapse if the structure does not offer sufficient robustness. Assessing a steel structure's robustness in fire means evaluating its capability to resist a progressive collapse under elevated temperatures.

Extensive research has been carried out in the last 20 years about steel structures and their behaviour in case of fire by evaluating mechanism and load cases that lead to a progressive or disproportionate collapse [7]. At the same time a few works are present in literature that studies the structural behaviour of ARSW in case of fire [8].

1.2. Objectives

In this research scenario, this thesis proposes the study of a typological self-supporting automated warehouse, first defining the fire modelling and after studying the mechanism of collapse. One of the main objectives is to obtain a fire model that allows the vertical and horizontal propagation of localized fires to be considered in ARSW structures.

To achieve this goal some experimental results on steel racks available in the literature were considered to obtain a generalized model to calculate the vertical propagation times, to be used in a zones fire model for ARSW structures.

After defining the fire modelling the second goal of this thesis regards the evaluation of the mechanical response of ARSW and the analysis of their collapse mechanisms.

Therefore, this work focuses on the application of the different methodologies of analysis that the designer has to adopt to properly interpret the fire-induced collapse, by also giving a comparison between the methods for determining the fire capacity of the ARSW steel sections.

1.3. Organization of the thesis

The dissertation is organized into five chapters.

Chapter 1 contains the introduction to the thesis that was conducted through a general overview. In the previous section, there is a literature review, whereas this section further explains the organization of the document and shows the objectives of the thesis.

Chapter 2 provides all the theoretical background to understand the topic within all its aspects; for this reason, starting from the principles of the steel structures' design in fire conditions, the literature about fire-induced progressive collapse is described. In the second part of the chapter the Automated rack supported ware-houses structures are presented with their characteristics by briefly describing their design at ambient temperature and by discussing all the main critical aspects of their design in fire conditions. The third part of the chapter provides a review of the fire development aspects and fire modelling for their use in ARSW structures.

Chapter 3 describes the only experimental campaign on steel racks that was found in the literature, and their simulation carried out by using the CFAST software developed by NIST. Based on this validation a fire model that considers vertical and horizontal propagation for ARSW structure is proposed, both with a multi-cells zone model and computational fluid dynamics model.

Chapter 4 focuses on the study of the structural collapse mechanism and on the methodologies of analysis that the designer must adopt to properly interpret it. Several thermo-mechanical analyses were carried out by using all the results of the proposed fire model and compared with different fire models available in the literature. To correctly analyse the progressive mechanism of collapse an iterative procedure is proposed by using subsequent implicit analyses carried out with SAFIR, by comparing this one with an automatic procedure obtained with ABAQUS CAE which allows the implementation of implicit/explicit analyses.

Finally, Chapter 5, "Conclusions", summarizes the main points of all the previous Chapters of the thesis and contains some future development proposals.

Chapter 2

2.Steel structures in fire

In this Chapter the principles of the steel structures' design in fire conditions are illustrated. In §2.1 the key aspects of the fire resistance design are illustrated by analysing the steel's mechanical properties at elevated temperatures, which are the key to understanding why a fire-induced collapse can develop and by providing also the literature about fire-induced progressive collapse.

The Automated rack supported warehouses with their peculiarities are illustrated in §2.2, by briefly describing their design at ambient temperature in §2.2.1 and by discussing all the main critical aspects of their design in fire conditions in §2.2.2. In §2.3 are presented and discussed the fire models that will be used to represent the fire action in the ARSW, either be it in the form of gas temperatures in a compartment/or directly in the form of heat fluxes transmitted from the fire to the structural elements. Localised fires as well as travelling fires are considered.

2.1. Fire resistance design

In the context of modern technical codes, such as the new Italian technical fire prevention regulation [1], designing the fire safety of buildings means identifying the technical and management solutions aimed at achieving the *primary objectives of fire prevention*, which are:

1. safety of human life,
2. protection of people,
3. protection of property and the environment.

The *primary objectives of fire prevention* are achieved if the activities have been designed, implemented, and managed in such a way as to:

a. the load-bearing capacity of the construction has to be guaranteed for a specific time;
b. the generation and spread of both fire and smoke should be limited;
c. the spread of fire to neighbouring constructions should be limited;
d. occupants should be able to leave the building, where the fire originated;
e. the safety of rescue teams must be taken into consideration.

To achieve the listed safety objective, the first step of the fire safety design is the *fire risk assessment* where the result is a *fire prevention strategy* which means that the risk mitigation is carried out through preventive, protective and management measures that remove hazards, reduce risks, or protect against their consequences.

In this framework, fire resistance is defined as a passive fire protection measure to guarantee load bearing and compartmentation capabilities to the structures according to performance levels, selected by the designer to achieve the defined fire safety objectives. The Italian code, following the European ones, defines five performance levels (PL) depending on the importance of the building, which are listed in the following **Table 2.1**.

Table 2.1 Performance levels according to the Italian fire prevention regulation [1]

Performance level (PL)	Description
PL I	Absence of external consequences due to structural collapse
PL II	The structure has also to maintain its fire resistance capacity for a period sufficient for the evacuation of occupants to a safe area outside of the building
PL III	The structure has also to maintain its fire resistance capacity for a period equal (congruent) to the duration of the fire
PL IV	Limited damage of the structure after fire exposure
PL V	Complete serviceability of the structure after fire exposure

Different design solutions can be chosen to comply with the performance

level, based on prescriptive or performance-based approaches.

The analytical evaluation the bearing capacity, in case of fire, can be divided into six phases:

1. definition of fire scenarios;
2. evaluation of fire action;
3. evaluation of the thermal response (thermal analysis), which means the temperature field in the structure during the exposure time to a given thermal action;
4. evaluation of the mechanical action (load combinations), which means the design loads acting on the structure during the fire;
5. evaluation of the mechanical response (type of structural analysis and mechanical analysis), which means the exhibited behaviour of the structure as a function of the temperature-time curve of the fire;
6. verification of fire resistance, that is the level of safety expressed by the structure.

These steps are the same both for prescriptive and performance-based approach, with some simplification for the prescriptive one, the main difference between the prescriptive and the performance-based approaches is that the first one is based on standard fire resistance tests or empirical calculation methods, using nominal fire curves. On the other hand, the performance-based approach considers the complexity of structures and the inter-relationship between the various fire safety measures and systems, using specific natural fire curves, generally obtained by advanced thermo-fluid-dynamic analyses. Indeed, the first step of the performance-based approach design consists of the thermal input assessment through the selection of design fire scenarios, which represent qualitative description of the fire development, based on key aspects that characterise the real fire (e.g., compartment dimension, ventilation, fire loads...). The natural fire curves can be obtained through simplified or advanced models. The fire models will be further analysed in the following chapters.

2.1.1. Actions in fire conditions

The occurrence of a fire creates a situation that is different from those at ambient temperature and consequently specific and different load combinations must be considered for the fire limit state. These values are usually lower than the values considered for ambient temperature design, because the fire is a rare event, and a higher probability of failure is accepted in the fire situation than in normal conditions.

The fire situation is classified as an accidental situation in EN 1990 [9]. The design effect of actions for the fire situation, $E_{fi,d,t,}$ can be obtained using the combination of actions for accidental situation given by The Italian Building Code "Norme Tecniche per le Costruzioni" NTC2018 [1] must be considered:

$$G_{k1} + G_{k2} + P_k(t) + \sum_{i=1}^{n} \psi_{2i} Q_{ki} + A_d(t) \tag{2.1}$$

Where:

$G_{k,i}$ is the characteristic value of the permanent actions;

$P_k(t)$ is the prestressing load;

$Q_{k,i}$ are the characteristic value of the variable actions;

A_d (t) are the indirect fire actions;

γ_{GA} is the partial safety coefficient for permanent actions in exceptional situations equal to 1.0;

γ_P is the partial safety coefficient for the prestressing force in exceptional situations equal to 1.0;

$\psi_{2,\,i}$ is the combination coefficient for the quasi-permanent value of the i-th variable action.

In these equations, the symbol + means that the different loads must be combined and for this reason, they are not added in a mathematical sense, because they are of different nature, as explained below. Indeed, the term A_d represents the indirect fire actions, these are the variations of effects of actions induced in the elements by restrained thermal expansion. For this reason, they are loads of a different nature compared to the other actions.

Whereas G and Q represent "external" loads applied on the structure, A_d represents "internal" effects of actions, such as axial forces, shear forces, and bending moments, that appear in the elements because of the temperature increase. They have more to do with the structural analysis than with the applied loads.

These indirect actions are mentioned in different clauses of Eurocode 1 [10] and Eurocode 3 [1]. According to these, indirect fire actions must be considered except if one of the two following conditions occurs:

1) They may be recognized a priori to be either negligible or favourable. Indirect actions cannot develop in statically determinate structures. Still, no specific guidance is given in the Eurocodes on judging whether indirect fire actions are negligible or favourable in a statically indeterminate structure. Therefore, a designer will have to evaluate his case if he wants to use this clause to ignore indirect fire actions.
2) They are introduced by using safety-related models and conditions and/or are implicitly included in the calculation per effect of conservatively defined fire safety requirements.

Indirect actions from adjacent members need not be considered when fire safety requirements refer to members under standard fire conditions. Although it is not pointed out in the Eurocode, it seems as if a standard fire constitutes what is called in exception 2) conservatively defined fire safety requirements. It seems surprising that it is allowed to neglect a fire action that, in some cases, is not negligible or favourable. However, it must be considered that the mechanical analysis of an element under standard fire condition does not represent the true behaviour of the element in the real structure. The aim of such element analysis is simply to represent, in the mechanical model, what would occur if this isolated element was tested in a furnace under this fire curve. In such a test, indirect effects from adjacent members are not considered.

However, it is recommended consider that indirect actions in the performance-based design.

2.1.2. Thermal analysis

A thermal action in a structure determines a temperature increase of its structural elements. The determination of temperature distribution within a structural element generally requires the solution of a non-linear heat transfer problem. There is a transient internal conduction regime for radiative-convective conditions on the external surface of an element. The solution to the problem is obtained by solving the energy balance equation with its boundary conditions.

In particular, the temperature of any structural members is governed by the net thermal heat flux, $\dot{h}_{net}$ which is determined by considering heat transfer by convection $\dot{h}_{net,c}$and radiation $\dot{h}_{net,r}$ as [1]:

$$\dot{h}_{net} = \dot{h}_{net,c} + \dot{h}_{net,r} \tag{2.3}$$

The convective component per unit area is given by:

$$\dot{h}_{net,c} = \alpha_c \cdot (\theta_g - \theta_m) \tag{2.4}$$

The radiative component per unit area is given by:

$$\dot{h}_{net,r} = \Phi \cdot \varepsilon_m \cdot \varepsilon_f \cdot \sigma \cdot [(\theta_r + 273)^4 - (\theta_m + 273)^4] \tag{2.5}$$

where:

α_c is the coefficient of heat transfer by convection [W/m^2K^4];

θ_g is the gas temperature in the fire compartment, or near the member [°C];

θ_m is the surface temperature of the member [°C];

Φ is the configuration factor;

ε_m is the surface emissivity of the member;

ε_f is the emissivity of the fire;

σ is the Stephan Boltzmann constant (= $5{,}67 \cdot 10^{-8}$ W/m^2K^4);

θ_r is the effective radiation temperature of the fire environment [°C].

It is worth saying that in the following applications the effective radiation temperature of the fire environment, θ_r, in the **Eq. 2.5** is considered equal to the gas temperature near the member, θ_g, an assumption that is acceptable in the case of full fire-engulfed members [12]. According to EC3 part 1-2 [10] the emissivity

of flame ε_f is equal to 1, and the member surface one ε_m is equal to 0.7. The coefficient of heat transfer by convection (α_c) on the exposed side of the structural element depends on the type of time-temperature fire curve and it is provided by the EC3 part 1-2 [10].

Thus, the fire model provides the ambient gas temperature θ_g that is within the net heat flux, which defines the thermal input for the structural element. After defining the net heat flux $\dot{h}_{net}$ (W/m²) transmitted to the surface, the temperature distribution in the elements can be determined by solving the Fourier equation of heat transfer.

In particular, the evaluation of the temperature within the structural element under fire conditions is carried out by establishing the equality between the amount of thermal energy transmitted to the element by the combustion gases and the increase in the whole energy of the element.

In the hypothesis that the element is homogeneous, isotropic and Fourierian and that there are no terms of energy generation, the temperature field, in Cartesian coordinates, is identified by the following equations.

The governing equation for the two-dimensional non-linear, transient heat conduction within the cross section of a structural element, takes the following form:

$$\frac{\partial(\rho \cdot c \cdot \theta)}{\partial t} = -div(\lambda \cdot grad\theta) \tag{2.6}$$

Which means:

$$\frac{\partial(\rho \cdot c \cdot \theta)}{\partial t} + \frac{\partial}{\partial x}\left(\lambda \cdot \frac{\partial \theta}{\partial x}\right) + \frac{\partial}{\partial y}\left(\lambda \cdot \frac{\partial \theta}{\partial y}\right) + \frac{\partial}{\partial z}\left(\lambda \cdot \frac{\partial \theta}{\partial z}\right) = 0 \tag{2.7}$$

To integrate the Fourier equation of heat transfer **Eq. 2.6** it is necessary to consider the boundary conditions which define the transmission to be studied. These can be spatial, when they refer to the temperature field at t=0, or temporal when they assign the law of temperature variation on a region of the body.

The temperature field which satisfies **Eq. 2.6** within the structural element must satisfy the following boundary conditions:

- Geometric boundary conditions:

$$\theta(t = 0, x, y, z) = f(x, y, z) \tag{2.8}$$

- Temporal boundary conditions:

$$div(-\lambda \cdot grad\theta) = \dot{h}_{net} \tag{2.9}$$

Where:

$\theta = \theta(t, x, y, z)$ is the temperature at in x, y, z at the time t;
t is the time;
ρ is the unit mass of steel [kg/m^3];
c is the specific heat of steel [J/kgK];
λ is the thermal conducibilty of the steel [W/mK];

In the case of structures exposed to fire, the boundary conditions are of the mixed type, as the temperature field is assigned at the initial instant **Eq. 2.8** and the flow history acting on the element surface **Eq. 2.8**; in addition, the section may not be composed of homogeneous material.

It should be noted that both the governing **Eq. 2.6** and boundary conditions **Eq. 2.8** and **Eq. 2.9** are non-linear. The former is due to the thermal conductivity and specific heat that are temperature dependent (see Annex A), and the latter is due to the radiative boundary condition which involves a non-linear term of the temperature. Therefore, a closed-form solution to the governing **Eq. 2.6** and its boundary conditions is not possible, even for the cases with the simplest geometry and it is necessary to use *numerical methods* such as the finite element method on which many calculation codes for thermal analysis are based.

Alternatively, it is possible to apply *simplified formulations* that allow to define the thermal field in the element starting from the definition of the thermal flux on the element itself.

EC3 part 1-2 [10] provides a simple equation for calculating the thermal response of unprotected steel members. Assuming an equivalent uniform temperature distribution throughout the cross section, the increase of temperature $\Delta\theta_{a,t}$ in an unprotected steel member during a time interval Δt is given by:

$$\Delta\theta_{a,t} = K_{sh}\,\frac{A_m/V}{c_a\,\rho_a}\,\dot{h}_{net}\,\Delta t \tag{2.10}$$

Where:

$\Delta\theta_{a,t}$ is the increase of steel temperature during a time interval from t to t+Δt;

Is the correction factor for the shadow effect;

A_m/V is the *section factor for unprotected steel member* [m^{-1}];

A_m is the surface area of the member, per unit of length [m^2/m];

V_i is the volume of the member, per unit of length [m^3/m];

Δt is the time interval [s];

$\dot{h}_{net}$ is the design value of the net heat flux per unit area [W/m^2].

The **Eq. 2.10** shows that the temperature distribution within the cross section, strongly depends on the parameter A_m/V which is called "section factor" or "massivity factor" of the section. The parameter A_m/V is defined as the ratio of "the area of the surface through which heat is transferred to steel", that is, the exposed surface and the "volume of steel". Within this formula given the fire curve and given the properties of the material, the section factor is representative of the speed at which the section is heated. In practice, the higher the cross-section factor, the faster the steel section heats up.

2.1.3. Mechanical analysis

According to EC part 1-2 [10], the mechanical analysis shall be performed for the same duration as used in the temperature analysis and the verification of fire resistance should be made in one of the following three domains:

– *In the strength domain*:

$$E_{fi,d,t} \leq R_{fi,d,t} \tag{2.11}$$

Where $E_{\mathrm{fi,d,t}}$ is the design value of the relevant effects of actions in the fire situation at time t, which are related to direct and indirect actions is normally considered constant during the fire. $R_{\mathrm{fi,d,t}}$ is the design value of the resistance of

the member in the fire situation at time t.

Unlike the usual case at ambient temperature, where R_d is constant, in the case of fire both terms of the inequation may vary and R_d decreases due to damage induced by high temperatures and E_d varies because of thermal expansion contrasted by hyperstatic system.

– *In the temperature domain:*

$$\theta_d = \theta_{cr,d} \tag{2.12}$$

Where θ_d is the design value of steel temperature $\theta_{cr,d}$ is the design value of the critical temperature, i.e., the collapse temperature of the structural steel member.

– *In the time domain*:

$$t_{fi,d} \leq t_{fi,requ} \tag{2.13}$$

Where $t_{fi,d}$ is the design value of the fire resistance, i.e., the failure time and $t_{fi,requ}$ is the required fire resistance time.

In **Figure 2.1** these three possible domains are represented for the case of steel member subjected to a nominal fire curve. This figure shows the temperature of the structural steel element, θ_d, assuming a uniform temperature throughout the cross section, the design value of the effect of actions in the fire situation, $E_{fi,d,t,}$ which is considered as constant, the progressive loss of strength, $R_{fi,d,t,}$ and the critical temperature of the member $\theta_{cr,d}$.

According to technical code, for the standard fire exposure and so in the prescriptive approach members shall comply with the fire resistance criterion R (load bearing capacity). This criterion is defined in the national regulations for fire safety of buildings as a function of the type of building, the occupancy and its height and should be identified by the letter R followed by a number representing the required fire resistance period. For example, R60 means that this criterion is assumed to be satisfied where the load bearing function is maintained for 60 minutes of standard fire exposure ($t_{fi,d,}$ = 60 minutes in this case)

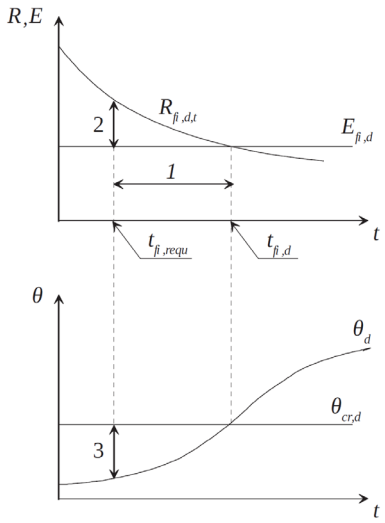

Figure 2.1. Time (1), load (2), and temperature (3) domains for a nominal fire curve [11].

For natural fires with a cooling phase, the load bearing function is ensured when collapse is prevented either during the complete duration of the fire, including the cooling phase (see **Figure 2.2**a) or during a specified period (see **Figure 2.2**b $t^1_{fi,requ}$)

From **Figure 2.2** it can be concluded that verification in either the temperature domain or in the strength domain, must be avoided for natural fire curves with a cooling phase [11]. This is because if the specified fire resistance time (see $t^2_{fi,requ}$ in **Figure 2.2**b) is greater than the time needed for the collapse, $t_{fi,d}$, the load bearing and the capacity is satisfied at $t = t^2_{fi,requ}$.This can lead to the wrong conclusion because failure has already occurred at time $t_{fi,d}$.

The design resistance R_{fi}, at time t, of a structure or a single element can be evaluated by three different assessment models. Each of these models is described below and increases in complexity:

- *Tabulated data* obtained from tests in standard furnaces, empirical methods, or numerical calculations. Tabulated data are widely used for concrete and concrete and composite steel structures in EC2 [13] and EC4 [14], respectively. However, no tabulated data are provided in EC3 [12], but at

the same time, the Annex A provides the "Nomogram" which is a simple operational tool, that the designer can use for the estimation of the fire resistance of unprotected steel members.

- *Simple calculation models* making use of simple analytical formulae for isolated members, by modifying the design resistance for normal temperature design to EN 1993-1-1[1], to consider the mechanical properties of steel at elevated temperatures and obtaining the temperature field through simplified formulations.
- *Advanced calculation models*, which are accurate, generally valid calculation models based on thermo-mechanical modelling of materials and structure.

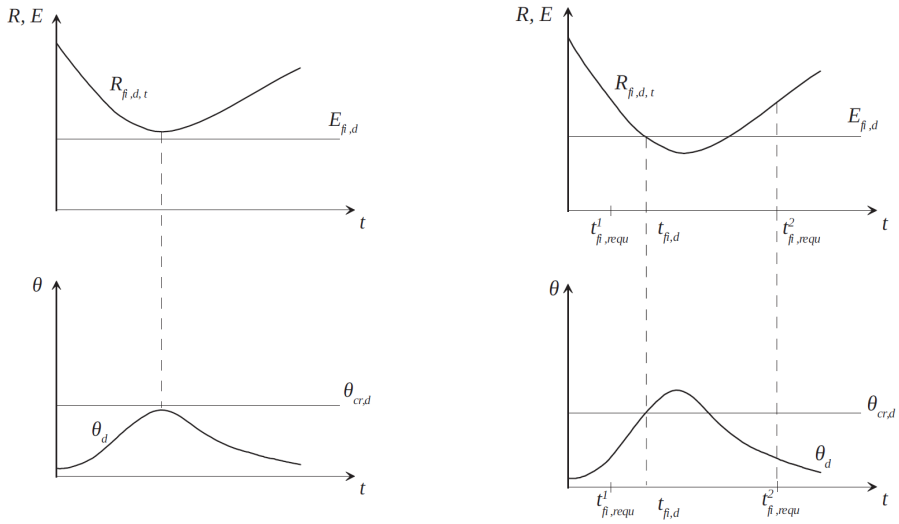

Figure 2.2. Time, load, and temperature domains for a natural fire curve [11].

In the contest of the strength domain, the design effect of actions for the fire design situation, $E_{fi,d}$ can be obtained either by using the accidental load combination as defined in **Eq. 2.1.**

Structural analysis under fire conditions can be carried out by studying all structures or by dividing them into substructures to be analysed separately, by considering each reciprocal interaction. This choice plays an important role, as

well as the structural aspects, of the fire model, whether they are defined within a prescriptive approach or a performance-based one.

Before carrying out the structural analysis it is therefore necessary to identify which parts of the structure should be analysed. In addition, structural analysis at high temperatures is made more complex by related to thermal dilations prevented and large displacements: these should be considered both in the calculation models and in the choice of substructures to be analysed.

In conclusion, the Eurocodes, and the National code [1], for fire resistance design, allow to carry out the use of one of the following types of analyses:

i. *Global structural analysis*. When a global structural analysis for the fire situation is carried out, the relevant failure mode, the temperature-dependent material properties and member stiffness, the effects of thermal expansions and deformations (indirect fire actions) shall be considered.
ii. *Analysis of part of the structure*, for example a portal frame or any other substructure. The boundary conditions at supports and the ends of members may be assumed to remain unchanged throughout the fire exposure.
iii. *Member analysis*, for example beams or columns, where only the effects of thermal deformations resulting from thermal gradients across the cross section need to be considered. The effects of axial or in-plane thermal expansions may be neglected. The boundary conditions at supports and the ends of members may be assumed to remain unchanged throughout the fire exposure.

It is worth saying that tabulated data can be applied only to member analysis. Moreover, the choice of the type of structural analysis also depends on the fire model that is being used. Member analysis can be applied to isolated structural elements (extracted from the whole structure, element by element) and can be performed either by using simple calculation models or advanced calculation models. This type of analysis is largely used under nominal fire conditions like the standard fire defined in ISO 834.

When analysing part of the structure or carrying out a global analysis, a certain number of structural members should be considered to act together so that the interaction effect between them is directly considered (load redistribution from weak heated parts to cold parts outside the fire compartment). Advanced calculation methods, normally based on the Finite Element Method together with a global analysis provide more realistic models of mechanical response of structures in fire than simple models.

2.1.4. Mechanical properties of carbon steel

When exposed to fire, all commonly used structural materials reduce their mechanical strength and stiffness. One of the mostly penalized materials is the steel, because of its elevated thermal conductivity and the small dimensions of the structural member sections.

At elevated temperatures, as showed in **Figure 2.3** the shape of the stress-strain diagram is modified compared to the shape at room temperature, instead of a linear perfectly plastic behaviour as for normal temperature, the model recommended by EC3 part 1-2 [12] at elevated temperature is an elastic-elliptic perfectly plastic model, followed by a linear descending branch introduced at large strains when the steel is used as material in advanced calculation models to avoid numerical problems.

In an accidental limit state such as fire, higher strains are acceptable. For this reason, EC3 part 1-2 [12] recommends a yield strength corresponding to 2% total strain rather than the conventional 0.2% proof strain (see **Figure 2.3**). However, for members with Class 4 cross sections, EC3 part 1-2 [12] recommends, in its Annex E, a design yield strength based on the 0.2% proof strain.

The stress-strain relationship at elevated temperature shown in **Figure 2.3** is characterised by the following three parameters:

- The limit of proportionality, $f_{p,\theta}$,
- The effective yield strength, $f_{y,\theta}$,
- The Young's modulus, $E_{a,\theta}$,

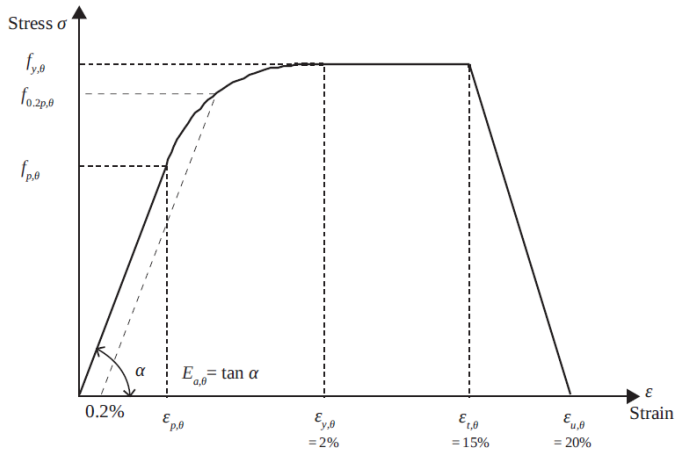

Figure 2.3. Stress-strain relationship for carbon steel at elevated temperatures [11].

The design values for the mechanical (strength and deformation) material properties in the fire situation $X_{d,fi}$ are defined in Eurocode 3, as follows:

$$X_{fi,d} = K_\theta \cdot X_K / \gamma_{M,fi} \tag{2.14}$$

Where:

X_K is the characteristic value of a strength or deformation property (generally f_k or E_k) for normal temperature design to EC3 part 1-1 [1];

K_θ is the reduction factor for a strength or deformation property ($X_{k,\theta}/X_k$), dependent on the material temperature;

$\gamma_{M,fi}$ is the partial safety factor for the relevant material property, for the fire situation, taken as equal to 1.

Following **Eq. 2.15** the yield strength at temperature θ is given by:

$$f_{y,\theta} = k_{y,\theta} f_y \tag{2.15}$$

The Young's modulus at temperature θ, is given by:

$$E_{a,\theta} = k_{E,\theta} E_a \tag{2.16}$$

In the same way the proportional limit at elevated temperature is given by:

$$f_{p,\theta} = k_{p,\theta} f_y \tag{2.17}$$

According to Annex E of EC3 part 1-2 [12] for members with Class 4 cross section under fire conditions, the design yield strength of steel should be taken as the 0.2% proof strain and thus for this class of cross section the yield strength

at temperature θ, is given by:

$$f_{y,\theta} = f_{0.2,p,\theta} = k_{0.2,p,\theta} f_y \tag{2.18}$$

Figure 2.4 shows a graphical representation of reduction factors for the stress-strain relationship of carbon steel at elevated temperatures, where the reduction factor (relative to f_y) for the design strength of hot rolled and welded thin-walled sections (Class 4), given in Annex E of EC3 part 1-2 [12], is also presented.

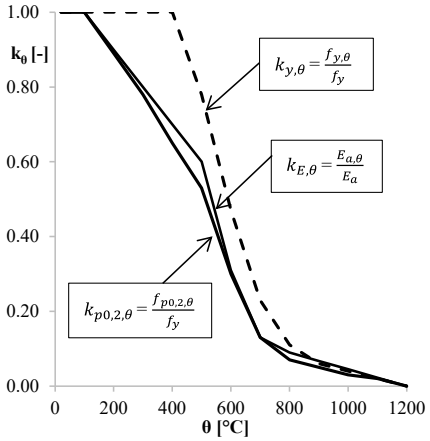

Figure 2.4 Reduction factors for carbon steel for the design at elevated temperatures.

This figure shows that the stiffness of steel decreases with increasing temperature. In particular, the structural steel can withstand approximately 400°C before it begins to soften. At about 600°C, the steel will lose about half of its strength with a $k_{y,\theta}$=0.47. While its stiffness starts reducing at about 100°C, till losing the 20% at 300°C and the 60% at 500°C.

2.1.5. Robustness of steel structures in case of fire

As seen before steel shows a remarkable decrease in strength and stiffness as the temperature increases, therefore, deflections, local buckling, and twisting of the steel member can occur, and if the bare steel structures do not reach the required level of fire resistance it is necessary to use fire protection. Moreover, for steel elements not protected with active or passive fire systems, fire can be a reason for failure and progressive collapse if the structure does not offer sufficient

robustness. Robustness can be defined as the ability of a structure to resist failure due to environmental or operational damage. It can be seen as a measure of how well a structure can handle stresses and strains from exceptional load conditions.

World Trade Centre fires in New York City in 2001 have pointed out the issue of designing structures to resist progressive collapse such as the need for proposed analysis and design methods. Adam et al [15] have pointed out that not a uniform accepted definition of progressive or disproportionate collapse exists. It can be defined as an event where the failure of a single element results in the collapse of the entire structure or a large part of it.

In Europe, EC1 part 1-7 [16] defines accidental actions, while in the United States of America, ASCE 59-11 [17] is used with a blast orientation, other than some military publications [18] .However, none of these refers directly to the possibility that a fire can trigger a progressive collapse. Some codes, such as EC1 part 1.7 defines a few strategies that the designer can use. Ellingwood et al. [19] analysed three increasingly complex methods which are: indirect design methods, specific local resistance, and alternate load path (ALP) approach. It is worth saying that the last two ones are called *direct methods,* since compared to the *indirect* ones, the robustness is checked and not presumed [9]. Moreover, a fourth approach can be identified: the risk-based methods [15].

The methods can be summarised as follows:

1. Indirect design methods, also known as tying-force prescriptive rules;
2. Direct design methods,
   a. Alternative load path (ALP) approach;
   b. Specific local resistance, known as key element design;
3. Risk-based methods.

All common codes (in the EC1 part 1- 7, for example) recommend tying farce prescriptive rules for structures with a low risk of progressive collapse. They aim to provide minimum levels of tying, continuity, and ductility. However, the latter is not checked explicitly, and tying is provided through horizontal and vertical ties achieved by prescribing a minimum tying farce requirement.

ALP approaches based on the notional *member removal concept* are deterministic

rather than prescriptive. These approaches aim to demonstrate robustness explicitly (*direct design method*) through the analysis of the structure under codified damage conditions, assessing the ability of the structure to redistribute the additional loads from the areas subjected to local damage. While the fundamentals of this approach are clear, in practice, the ALP analysis requires several assumptions and simplifications, resulting in a considerable number of potential assumption combinations that can lead to design/assessment solutions with different levels of robustness [8].
The key-element design approach, also known as the enhanced (or specific) local resistance approach in the US, is a method used when the ALP method cannot demonstrate sufficient load redistribution ability of the structure. In this approach, key elements (i.e., structural members, the failure of which activates a progressive collapse) are identified and designed to resist accidental loads, so the focus is on avoiding each key element's local failure.
The last general design approaches investigated are risk-based approaches. Most codes consider risk implicitly in design by the building classification and design methods recommended for each class or risk category. Risk considerations are also included in some codes to define the overall design strategy. For example, when the accidental action is identified, EC1 part 1-7 [16] recommends considering measures to mitigate the risk of the accidental action by (a) preventing or reducing the action, (b) protecting the structure so that it resists the action, and (e) providing minimum robustness by designing the struc-ture for the action. In addition, codes generally provide some tolerance levels for the risk of collapse (e.g., based on relative area of collapse, structural damage limits, acceptable levels of likelihood, or levels of protection).

A more in-depth description of these methods can be found in [19], [20], and [15].

2.1.6. Fire induced progressive collapse

Assessing a steel structure's robustness in fire means evaluating its capability to resist a progressive collapse under elevated temperatures.

Extensive research has been carried out in the last 20 years about steel structures and their behaviour in case of fire by evaluating mechanism and load cases that lead to a progressive or disproportionate collapse.

Starossek in his book [21] examined the progressive collapse of structures, outlining the current procedure as outlined in codes and illustrating design methods with examples. Fu and Isobe [22],[23] presented numerical examples and modelling techniques to explore progressive collapse under different accidental actions, beyond those induced solely by fire.

Ali et al. [24] explored the performance of 2D portal frames by examining lateral displacements and collapse modes to find the clearance distance required between the frame and the firewall to allow the frame to expand laterally without contacting and damaging the wall. Chen et al. [7] and Liew [25] have used a mixed-element approach to perform steel frame explosion and fire analysis. The authors combined shell and beam elements, using shells for critical members and beams for the rest of the structure. Dong et al. [26] built three two-story, two-bay composite steel frames and exposed them to both dead load and thermal load from furnace heating. They concluded that the fire-resistance design of structures cannot be based on the performance of single. Instead, interactions among members in the entire structure must be considered. This observation aligns with findings from the Cardington fire test [27].

To prevent the side-sway of a building, P.J. Moss et al. [28] examined the behaviour of a 3D portal frame, varying the base supports and the fire severity and considering (or not) the effects of the concrete encasement on the columns. The study concludes that the only way to reach the goal is to protect columns against fire or design them to remain standing. Sun et al. [29] introduced a static/dynamic explicit procedure to avoid numerical instabilities and follow the collapse of a structure. Moreover, in subsequent work [30] they applied the procedure to study the collapse behaviour of braced steel frames exposed to fire, highlighting the beneficial effect of hat-truss and vertical bracings on progressive collapse.

Fang et al. [31] examined the key factors involved in the robustness assess-

ment of steel-composite structures under localized fire. They introduced an approach for robustness assessment that provides a practical framework for addressing these concerns. Moreover, Fang et al. presented in another work [32] a simplified energy-based robustness assessment based on a Temperature-Independent Approach (TIA), in the sense that the maximum temperature is assumed to be unknown, thus adopting a similar basis to specific robustness provisions where event-independent local damage scenarios are employed. Agarwal and Varma [33] analysed the role of interior gravity columns in steel buildings with composite floor systems concluding that gravity columns govern the overall stability of building structures under fire conditions. Jiang et al [34] employing explicit dynamic analysis, explored planar steel frames' possible progressive collapse mechanisms when one column failed under elevated temperature. The authors find three progressive collapse mechanisms: cantilever beam, pull-in farce in-duced, and high load ratio member failure.

Porcari et al. [35], through an extensive literature review focusing on the mechanisms involved in fire-induced progressive collapse of steel building structures, concluded that the durability of fireproofing significantly influences robustness when subjected to blast or other sources of stress. Chen et al [36] introduced a probabilistic assessment method for a steel-framed building in scenarios involving the sudden removal of a column due to catastrophic events. Additionally, they developed a deterministic method and proposed a robustness index (RI) to evaluate structural robustness performance based on acceptable probabilities of global failure and structural collapse.

2.2. Automated rack supported warehouses (ARSW)

The warehouses are typical buildings where many goods can be stored after their production and before their distribution to the consumers. The demand for storage space is growing, due to increasing production and increasing consumption levels, therefore highly optimized and reliable warehouses are needed. Automated Rack Supported Warehouses (ARSWs) are used in industrial facilities to optimize storage spaces; these structures combine the structural efficiency of

steel construction with automated machines for handling stored products.

A fundamental difference exists between traditional Steel Racks (SRs) ARSWs. SRs are designed to carry on the structural self-weight and the weight of the stored goods. ARSW are self-bearing rack structures committed to support, besides self-weight and weight of products, also environmental loads (i.e., wind, snow, and seismic action) and all the other non-structural elements such as clads, equipment, etc. A typical structure during its construction is shown in the following **Figure 2.5**.

Figure 2.5. An ARSW during its construction. (Source: ROSSS s.p.a.)

SRs have two principal directions, as shown in **Figure 2.6**a; the cross-aisle (CA) direction and the down-aisle (DA) direction. The traditional structural steel racking system consists of a regular sequence of frames, made of two uprights (= the vertical members), connected in the DA direction, by pallet beams devoted to bringing the goods. While, in the CA direction, the two uprights are linked together by horizontal beams and by a bracing system to provide lateral stability of the structure in this direction. The nomenclature of all the structural elements is listed in **Figure 2.6**b.

In the CA direction, all the frames are connected by an upper truss (**Figure**

2.5). Since in the DA direction pallets must be placed easily, no bracing systems can be placed but the main lateral force-resisting system is provided by tower bracing, placed at both ends of the down-aisle section (see **Figure 2.14**).

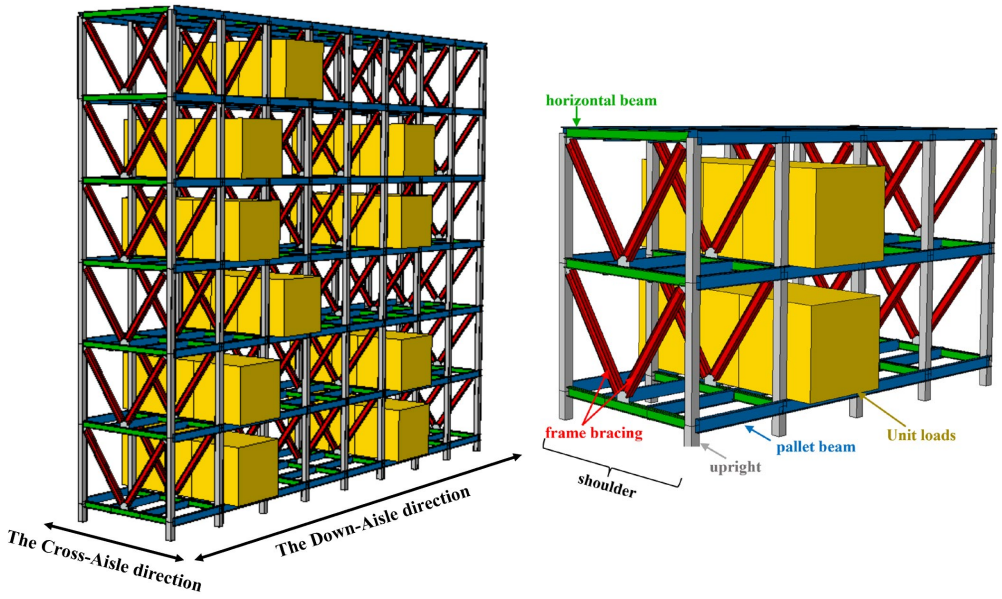

Figure 2.6. Main directions of a Steel Rack (a) and nomenclature of all the structural elements (b).

Within the AMSWs all the goods are stored in unit loads, therefore the pallets represent the support for these ones (see **Figure 2.8**). In the ARSW the handling of the pallets can be done by using two typical systems, AS/RS, and shuttle systems, which are shown in **Figure 2.7**.

In the case of AS/RS, a stacker crane moves on a rail back and forth along the DA direction and has direct access to the pallets. When it has reached the load bay, where it must pick up the load unit, the stacker crane can move up and down to reach the level and pick up the goods with its fork, like a forklift. This means that in ARSW there must be as many aisles as stacker cranes (see **Figure 2.7**a).

On the other hand, a shuttle system does not have direct access to all the unit

loads, and it is composed of two parts: a shuttle carrier and a shuttle (see **Figure 2.8**).

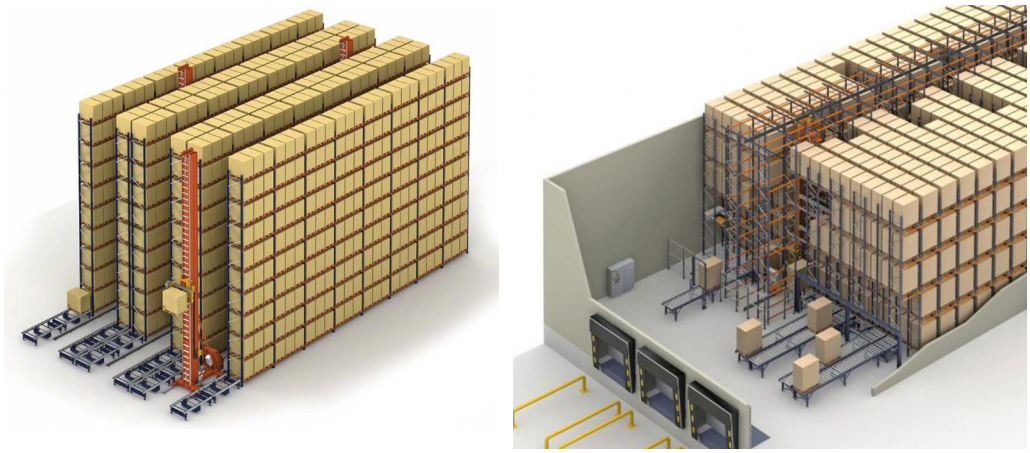

(a) (b)

Figure 2.7. Automated racking systems:(a) AS/RS, (b) shuttle system (source: www.mecalux.com)

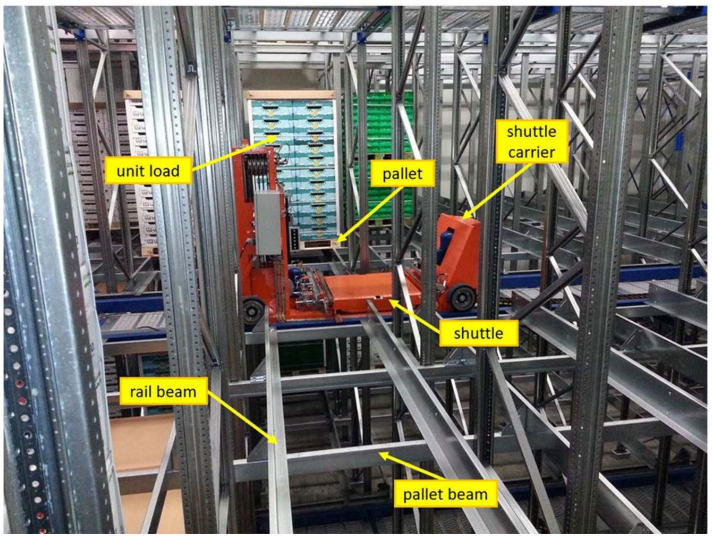

Figure 2.8. shuttle system detail [38].

The shuttle carrier moves back and forth on the aisle along the DA direction,

and when it has reached the target unit load, the shuttle starts moving on rail beams underneath pallets to reach the first pallet of the line and take it back to the carrier. In this case, an aisle can be sufficient, but usually, there are as many shuttles as load levels. It is worth mentioning that the rail and pallet beams form a horizontal grid of beams, enhancing the stiffness of the structure.

Besides the handlings but still connected to them, three building types of auto-mated warehouses can be defined depending on the pallet disposal: single-depth, double-depth, and multi-depth. In the single-depth configuration, there is one unit load line per frame (see **Figure 2.9**a) and two pallet beams connecting the frames (see **Figure 2.10**a); in the double-depth configuration, there are two unit loads per frame in the CA direction (see **Figure 2.9**b) and four pallet beams connecting the frames (see **Figure 2.10**b).

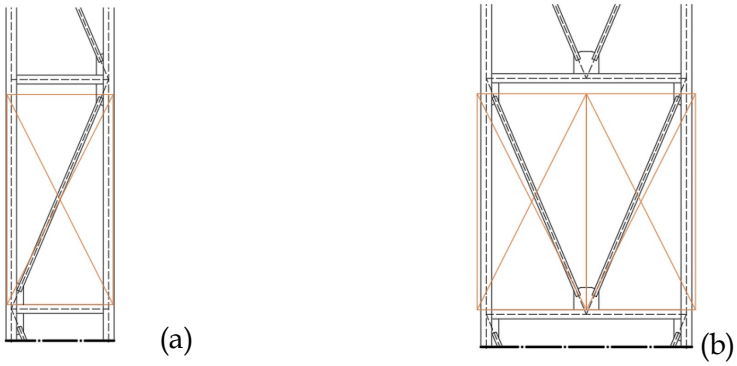

Figure 2.9. Single-depth configuration (a) , double-depth configuration (b) [8].

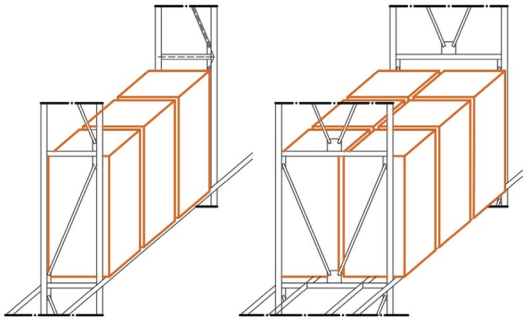

Figure 2.10. Pallet disposal in single-depth (a) and in double-depth (b) [8].

In this dissertation, the focus is given to Automated Multi-Depth Shuttle Warehouses (AMSWs), as a specific ARSW type. AMSWs are compact systems providing large surface occupation and maximum storage density. In AMSWs, the handling of unit loads is realized by a system of shuttles that move goods along rails in the warehouse DA and CA directions (see **Figure 2.8**).

2.2.1. Design of ARSWs at ambient temperature

ARSWs can be seen as the direct upgrade of traditional pallet SR, where in the case of ARSWs, the steel racks are both the stored areas and the structure of the warehouse.

To design ARSW, designers must refer to EN1993-1-1 [1] and EN1993-1-3 [39] for steel structures and EN1998-1-1 for seismic action [40]. Moreover, they usually refer also to specialist regulations such as EN15512 [41] which provides principles for the structural design of pallet racking systems, and EN16681 [42] which indicates principles for the seismic design of pallet racking systems. The Italian Building Code "Norme Tecniche per le Costruzioni" NTC2018 must be considered [37].

Hence, while well-established principles and rules supported by experimental evidence and theoretical research are available and presented in [43] for the usual SR. For the ARSWs, which are systems larger, taller, and more complex than usual SR, manufacturers and designers have questioned the suitability of the available regulations for these ARSWs, for years. In Italy new guidelines are available from June 2023 [44], these ones provide a framework in terms of regulations and procedures, for the design, improvement, and adaptation of industrial metal racks in the earthquake zone. The guidelines identify the references and regulatory limits for the design of new racks and provide the first elements for assessing the seismic vulnerability of existing racks. As mentioned above, ARSWs are characterized, on one hand, by a peculiar structural configuration, that strongly influences global behaviour and, on the other hand, by unique non-standard structural components and connections. Indeed, these structures

mainly consist of thin-walled sections obtained by cold-forming thin metal sheets that, on one hand, optimize the structural performance by reducing the steel weight, the costs, and the assembly time. On the other hand, these types of sections are usually classified as class 4 cross-section, according to EN1993-1-1 [1] and it has much lower strength and stiffness than hot-rolled steel members, these members can fail by a variety of buckling modes including global, local and distortional buckling and their interactions. For this reason, in general, racks are made with channel sections and stiffened with additional folds (called "lip") to reduce local and distortional buckling phenomena caused by the small thickness of the sections (typically from 1.5 mm to 3.0 mm), (see **Figure 2.11**).

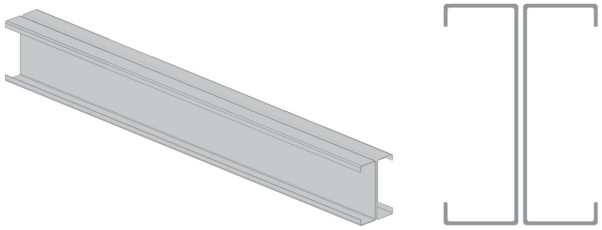

Figure 2.11. An example of cold-formed steel member. Source: ROSSS s.p.a.

However, an ARSW can be characterized even by hollow square sections depending on the dimensions and the requested payload.

Following this observation, the numerous research carried out on SRs, being them traditional ARSWs', or innovative ones can be divided between those dealing with the analysis of global behaviour and those with single elements and connections (as uprights, diagonal-to-upright connections, pallet beam-to-upright connections, and upright base connections).

In the last decades, the global structural behaviour of traditional racks along both CA and DA directions, has been investigated focusing especially on a seismic point of view. In this framework the guidelines for ordinary racks EN15512 [41] and EN16681 [42] could lead the designer to structural choices and technical solutions that are not always adequate and on the safe side [45], for this reason one possibility is the application of Eurocodes 3 [39] and 8 [40] requirements for

steel constructions. Different studies have investigated the efficiency of Eurocodes' design and analysis rules for ARSW, in terms of feasibility, structural performance and costs demonstrating how the capacity design requirements for ARSW are challenging to satisfy especially in terms of the maximum difference of the over-strength factor between load levels, requested in the case of X-braces steel-structures [2], indeed it is enough to think to the number of stories with reduced inter-story height and to the high number of stories.

These uncertainties and difficulties regarding code prescriptions have led designers to consider ARSW as "non-dissipative" structures.

Only in recent years capacity design approaches specifically made for ARSWs have been proposed in the literature ([46], [47]), defining rules and hierarchies that consider the characteristics of these structural systems.

Many authors have analysed the components' behaviour, stressing their peculiarities' strong influence on global behaviour. As an instance, the typical uprights adopted in SRs are often characterized by open mono-symmetric and lipped cross-section, with continuous perforation along their height, that allows to fit the tabs of the beams and bolt the bracing system in the cross-aisle direction (see **Figure 2.12**). Since the effects of the holes must be considered in the design, these characteristics make the behaviour of this element different not only from hot rolled sections but also from common structural cold-formed profiles used in light-weight constructions.

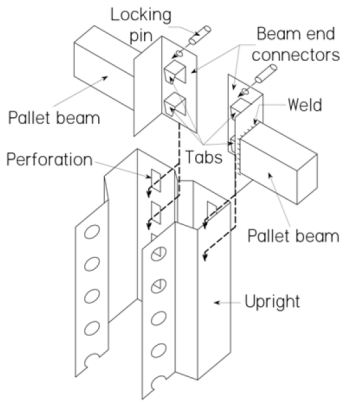

Figure 2.12. An example of a steel upright, beam and connector [52].

Each buckling mode exhibits a different post-buckling behaviour. This aspect must be considered in the design of cold-formed structures and, nowadays, almost every steel specification proposes refined design approaches to consider local, distortional, and overall buckling phenomena as well as their mutual interactions. However, due to large number of cross-section shapes and perforation patterns available in the market, many codes recommend executing laboratory tests to assist the design [41], [48], [49].

At ambient temperatures, EN1993-1-5 [50] gives two methods to consider the effects of local buckling in the design, i.e., the "effective width method" and the "reduced stress method". On the other hand, the Eurocode [50] considers the distortional buckling strength by using a reduced thickness in the edge stiffener and/or deformed part of the compression flange.

The behaviour of thin-walled steel members in centric and eccentric compression and particularly of stub uprights of pallet-rack systems have been widely investigated by many researchers through experimental tests. Tests on stub columns have been performed to determine the effective area and to investigate local buckling [51],[52], while tests on slender upright specimens have been executed to investigate distortional and global buckling modes, together with mixed buckling modes [53]-[55]. In this same way also the behaviour of thin-walled steel members in centric and eccentric compression and particularly of cold formed steel members (CFS) have been widely investigated by many researchers through experimental tests. Test on fixed-ended cold-formed steel rack-section columns were carried out to investigate the local–distortional interaction [56]. While experimental test and numerical analysis on stainless steel I-columns were carried out to study the interaction of local and global flexural buckling showing that the design specifications of the current Australian/New Zealand standards for stainless steel [57] and of the Eurocode 3 [50] failed to predict this interaction effect in stainless steel I-columns [58],[59].

Appendix A of EN 15512 [41] standard describes a test procedure to derive the effective area of a cold formed steel section. A stub upright with both ends fixed (or welded) in a thick steel plate is loaded axially. The maximum load bearable by the upright is measured and it is named characteristic failure load, P_k.

Thus, the effective area of the cross-section is $A_{eff} = P_k/f_{ym}$, where f_{ym} is the mean of the yield stresses obtained from tensile tests of metal sheet coupons.

Methods to evaluate the buckling behaviour of cold-formed sections (CFS) are various and still topic of debate.

The latest trend is to move from simplified design models to design procedures based on "whole section" analysis, avoiding the use of the effective width method. One example is the Direct Strength Method (DSM) [61]-[63], this method is already included in the Australian/New Zealand [57], North American [64] and Brazilian [65] cold-formed specifications for the design of cold-formed steel columns and beams.

Another approach is the Erosion of Critical Bifurcation Load (ECBL), which uses the rigid-plastic theory to introduce the local failure mode of thin-walled sections into the global behaviour of the member characterized by an Ayrton-Perry equation [66]-[67] .

Recently, a method that obtained a large popularity is the finite element method, which provides solutions of the governing differential equations, and it is the only tool to design and study profiles with holes. To reduce computational efforts, the finite strip method was developed: it falls into the category of numerical methods that are specifically designed for prismatic members and for this reason it can't be used for profiles with holes, while a finite strip elastic buckling solutions for thin-walled metal columns with different perforation patterns was developed by using finite element method (FEM) [68] .

Several researchers [69],[70] have prepared user-friendly computer software for this calculation, which is available to practical designers.

Finally, Generalized Beam Theory (GBT) is an extension to conventional engineering beam theory that allows cross-section distortion to be considered [71]-[74]. A comparison among the three European alternatives: EC 3 part 1-1 [1], EC 3 part 1-3 [39] and EN 15512 [41] was carried out to evaluate the upright load carrying capacity with numerical buckling analyses and highlighted that in few cases they lead to design from the unsafe side [75]. Different researchers proposed an experimental and numerical forms of the failure domain for these types

of uprights [77]-[78].

The nonlinear behaviour of the beam-to-column joints is also noteworthy. This joint is usually made with a boltless connector welded to the pallet beam, and the connector has a variable number of tabs that hook inside the spaced holes in the upright. Evaluating the mechanical behaviour of a steel rack joint is theoretically difficult because of the large number of upright-to-beam joints and profiles used as uprights or beams. Monotonie and cyclic tests have been carried out in the last two decades over steel rack joints (for example, [79]-[80]) high-lighting the pinching behaviour of this kind of connection [81]-[83]. Moreover, full-load rack structures have a very high live-to-dead load ratio, making them sensitive to second-order effects, in these cases in literature pushover analysis seems a reliable method to study and design racks in seismic areas [84]-[86].

Nevertheless, some of the abovementioned peculiarities are reduced if the structure is made with hollow square sections. In these cases, the uprights-to-beam joints are generally blind-bolted with one or multiple bolts passing through the hollow square uprights. The behaviour of this joint has not been studied deeply in the literature and requires further analysis to be thoroughly characterized.

2.2.2. Design of ARSWs in fire conditions

As explained previously, these structures mainly consist of cold-formed steel members (CFS), that optimize the structural performance by reducing the steel weight, the costs, and the assembly time. However, under fire conditions, the thin thickness of these profiles, combined with the high thermal conductivity of the steel, induces a fast increase in the steel temperature with a significant loss in material stiffness and strength.

At present, fire design methods for CFS members are not as developed as for hot-rolled ones and the available ones are generally based on past research on hot-rolled steel members and they could be inadequate for this type of members.

At elevated temperatures, to account for local buckling the actual EC3 part 1-2 [12] suggests for Class 4 cross-sections a default critical temperature of 350 °C,

if no fire design is conducted, which means that even for a requirement of 15 min of fire resistance, passive fire protection should normally be used for current profiles. Alternatively, the informative Annex E of the EC3 part 1-2 [12] suggests (*i*) using an effective cross-section (A_{eff}) calculated with the effective width method, according to EC3 part 1-5 [50], by considering the steel properties at ambient temperature, which means that the effective properties of a steel plate should be kept unchanged as the one as at ambient temperature, (*ii*) taking the 0.2% proof strength ($f_{0.2p,\theta}$) for the design yield strength of steel (see **Figure 2.3**) instead of the stress at 2% total strain (f_y), as normally used in the fire design of other cross-sectional classes.

This means that the design buckling resistance of a compressed member for the actual Eurocode can by evaluated as follow:

$$N_{b,fi,t,Rd} = \chi_{fi} A_{eff} k_{0.2p,\theta} \frac{f_y}{\gamma_{M,fi}} \tag{2.19}$$

Where:

χ_{fi} the reduction factor for flexural buckling in the fire design situation provided in EC3 part 1-2 [12];

A_{eff} effective cross-sectional area;

$\gamma_{M,fi}$ is the partial safety factor for the relevant material property, for the fire situation, taken as equal to 1.

$k_{0.2p,\theta}$ is the reduction factors for the 0.2% proof strength at elevated temperatures.

These recommendations are based essentially on the work of Ranby (1998) [88] who has demonstrated that this methodology leads to accurate results for determining the ultimate load of thin plates susceptible to local buckling at elevated temperatures. Indeed, at elevated temperatures the reduction factor for plate buckling would be, $\rho_\theta = \rho_\theta(\overline{\lambda_{p,\theta}})$ with the corresponding non - dimensional slenderness at elevated temperatures, given by the following equation:

$$\overline{\lambda_{p,\theta}} = \sqrt{\frac{f_{y,\theta}}{\sigma_{cr,\theta}}} = \sqrt{\frac{k_{0.2p,\theta}}{k_{E,\theta}}} \sqrt{\frac{f_y}{\sigma_{cr}}} \cong 1.0 \sqrt{\frac{f_y}{\sigma_{cr}}} = \overline{\lambda_p} \tag{2.20}$$

The ratio $\sqrt{k_{0.2p,\theta}/k_{E,\theta}}$ is almost equal to 1 and since that $\overline{\lambda_{p,\theta}} \cong \overline{\lambda_p}$ this means that it is possible to consider, $\rho_\theta = \rho$. This methodology, however, could lead to under-estimating the cross-sectional resistance if only some of the plates of the cross-section are susceptible to local buckling [3], in this case, using the 0.2% proof strength for the whole cross-section is, thus, very limiting.

On the other hand, there is an inconsistency pointed out by Renaud et. Al (2006) [89] regarding the reduction factors for the 0.2% proof strength at elevated temperatures, $k_{0.2p}$, given in Table E.1 of EC3 part 1-2 [12]. Indeed, these values do not correspond to the ones calculated according to the stress–strain relationship of steel at elevated temperatures given in the same norm, and it is unknown to the scientific community, where these values given in EC3Part 1-2 [12] come from.

Due to all these mentioned limitations, new expressions to determine the effective width of steel sections at high temperatures were developed [3].

This design curve has been calibrated as close as possible to the existing design curve by introducing the factors α_θ and β_θ on the expressions of EC3 part 1-5 [50], hence the influence of the imperfections is taken into account as in the original formulas developed by Winter [90] and additionally the non-linear steel constitutive law at elevated temperatures is also accounted for, furthermore by using the factor ε_θ steel grade is also taken into account in this new proposal. Moreover, by using these expressions, the strength at a total strain of 2% ($f_{y,\theta}$) can be used to calculate the resulting effective cross-sectional resistance, instead of using the 0.2% proof strength ($f_{0.2p,\theta}$). According to this proposal, for internal compression elements the following expression is proposed [3]:

$$\rho_\theta = \frac{\left(\overline{\lambda_p} + \alpha_\theta\right)^{\beta_\theta} - 0.055(3+\psi)}{\left(\overline{\lambda_p} + \alpha_\theta\right)^{2\beta_\theta}} \leq 1 \tag{2.21}$$

Where the coefficients α_θ e β_θ are equal to:

$$\alpha_\theta = 0.9 - 0.315\frac{k_{0,2p.\theta}}{\varepsilon_\theta k_{y.\theta}}$$
$$\beta_\theta = 2.3 - 1.1\frac{k_{0,2p.\theta}}{k_{y.\theta}} \tag{2.22}$$

$$\varepsilon_\theta = 0.85\varepsilon = 0.85\sqrt{\frac{235}{f_y}}$$

According to this proposal, for outstand compression elements the following expression is proposed [3]:

$$\rho_\theta = \frac{\left(\overline{\lambda_p} + \alpha_\theta\right)^{\beta_\theta} - 0.188}{\left(\overline{\lambda_p} + \alpha_\theta\right)^{2\beta_\theta}} \leq 1 \tag{2.23}$$

Where the coefficients α_θ e β_θ are equal to:

$$\alpha_\theta = 1.1 - 0.630\frac{k_{0.2p.\theta}}{\varepsilon_\theta k_{y.\theta}}$$
$$\beta_\theta = 2 - 1.1\frac{k_{0.2p.\theta}}{k_{y.\theta}} \tag{2.24}$$

The new expressions are temperature-dependent leading to a variation in the effective cross-section properties under fire situations. For this reason, a simplified proposal, not temperature dependent, was investigated in [91], based on the assumption that the influence of the temperature on the range of the critical temperatures usually expected for steel members (from 350 °C to 750 °C) are negligible leading to a simpler yet accurate design. According to this proposal, for internal compression elements the following expression is proposed [91]:

$$\rho = \frac{\left(\overline{\lambda_p} + 0.9 - \frac{0.26}{\varepsilon}\right)^{1,5} - 0.055(3+\psi)}{\left(\overline{\lambda_p} + 0.9 - \frac{0.26}{\varepsilon}\right)^{3}} \leq 1 \tag{2.25}$$

According to this proposal, for outstand compression elements the following expression is proposed [91]:

$$\rho = \frac{\left(\overline{\lambda_p} + 1.1 - \frac{0.52}{\varepsilon}\right)^{1,2} - 0.188}{\left(\overline{\lambda_p} + 1.1 - \frac{0.52}{\varepsilon}\right)^{2,4}} \leq 1 \tag{2.26}$$

It is worth saying that these expressions are proposed for the new drafts of the next generation of structural Eurocodes.

This means that the design buckling resistance of a compressed member for the new Eurocode can by evaluated as follow:

$$N_{b,fi,t,Rd} = \chi_{fi} A_{eff} k_{y,\theta} \frac{f_y}{\gamma_{M,fi}} \quad (2.27)$$

Where in this case the effective cross-sectional area determined according to the new equations explained before.

Kankanamge et al. carried out an intensive parametric study on the behaviour of cold-formed steel lipped channel beams subject to lateral–torsional buckling at elevated temperatures, by providing a comparison among the three European alternatives: EC 3 part 1-2 [12], EC 3 part 1-3 [39] and the design method developed by Kankanamge et al. [92] based on AS/NZS 4600 [57] for ambient temperature design was investigated for fire situation. The EC3 part 1-2 [12] suggests that the buckling curve should be the same as that for hot-rolled steel members, the authors found that in this way the predictions were over-conservative for high temperatures except for beams with very high slenderness.

The EC3 part 1-3 [39] suggest a design by using a unique buckling curve, like the design method developed by Kankanamge et al.

The authors showed that using a single buckling curve is inadequate to obtain the ultimate moment capacities of cold-formed steel beams at varying elevated temperatures. Hence these design methods are unsafe or over conservative for some temperatures and slenderness ratios. Therefore, other buckling curves in EC3 part 1-1 [1] were proposed for different temperature ranges for the fire design of CFS members.

For all these reason, Kankanamge et.al [93] have proposed a new fire design methodology for CFS lipped channel beams subjected to lateral-torsional buckling at elevated temperature, based on modified AS/NZS 4600 design rules [57]. The proposed formula is a variation of the ambient temperature DSM by replacing the mechanical properties at ambient temperature with the reduction factors depending on the temperature ($E = k_{E,\theta} \cdot E_{20}$, $f_y = k_{y,\theta} \cdot f_{y,20}$) and using the $f_{p,\theta}/f_{y,\theta}$ factor for considering the non-linearity in the stress-strain curve of steel. However, this design method did not provide accurate load- bearing capacity predictions for the full range of temperatures and slenderness ratios.

Other new simplified fire design rules were proposed [94] but they were specifically developed for CFS floor systems.

Laíma et.al. [95] developed a simplified fire design methodology for single and built-up cold-formed steel beams based on the European guidelines.

The proposed formula is a variation of the ambient temperature design method proposed in EC 3 part 1-2 [12], by modifying the dimensional slenderness at elevated temperatures ($\lambda_{LT\theta}$) considering the smooth relationship between the parameters $k_{y,\theta}$ and $k_{E,\theta}$. As well as that the coefficient values of 0.5 and α were modified to β and α′ to consider higher geometric imperfections in members under higher initial load levels.

In these ARSWs structures to consider the performance-based approach, instead of the prescriptive one, is essential because this one generally requires a minimum fire resistance performance for structural elements that lead to the use of traditional passive fire protection systems, that in the case of these metal profiles are difficult to apply, because of their high section factors (A_m/V) and very small critical collapse temperatures. Indeed, considering the intumescent paints, in order to ensure the bearing capacity against fire, a very high thickness of more than 1,000μ should be applied to the element [96]. Moreover, this paint should be applied when the rack is already built, therefore the practical application would be very difficult due to the features of these profiles. All these aspects would lead to high costs.

To minimize risks, warehouses must be equipped with fire prevention, detection, and extinguishing systems. Since their fire vulnerability, these structures are typically protected by active fire protection measures to limit any structural damage. At the same time, the fire protection of a warehouse can be a big challenge because one hand they have generally a high fire load, due to the materials of the stored goods that facilitate fire propagation: plastic, cardboard, or wood, flammable liquids, etc. On the second hand in the ARSW can be stored a lot of different types of goods, for this reason also the choice of active fire protection could be different, such as sprinkler system with water or lather. Moreover, installing a significant number of sprinklers with related pipes inside a rack could be problematic because often there is not enough space [97].

In recent years the usage of oxygen reduction systems (ORS) [98] has

emerged. This system injects nitrogen into the warehouse, decreasing the concentration of oxygen and thus preventing the development of a fire. This family of systems can be installed inside ARSWs because there is no constant presence of workers, and the ones admitted to accessing the warehouse are highly trained.

However, the use of active fire protection can lead to losing the stocked goods and in any case, they could fail their job, therefore the study of the fire scenario without these systems should be deeply analysed. Recent studies [99] have shown that in many cases these systems may not work and therefore, to consider the fire scenario without an active system, as one of the most critical for mechanical analyses, is necessary.

Referring to the performance levels defined by Italian technical fire prevention regulation [1] and showed in **Table 2.1**, the PLI could be required for ARSWs, indeed, among the criteria required to fall into the PL I, there is the request that the building is not involved in activities concerning the presence of people, except for the occasional and short-term activity of highly trained workers. The latter is generally the condition of every ARSW.

For these reasons, moving in the context of alternative solutions, or rather in the performance-based approach, the absence of external consequences due to structural collapse must be demonstrated, which means that the designer must prove analytically that the collapse mechanism is inward, and implosive. The code suggests the following technical measures to guide the collapse, such as:

- adoption of criteria of the hierarchy of the fire resistance (e.g., assignment of an over fire resistance to the perimeter structures elements compared to the internal ones;
- spatial distribution of the fire loads towards inner areas;
- adoption of convenient structural forms (e.g., with inclination towards the interior, ...);
- use of fire control systems with higher availability.
- pyramidal stacking of the fuel materials;
- adoption of constraints that facilitate implosive collapse.

The study of the mechanism of collapse is related to the fire model adopted and the types of methodologies of analysis that the designer must adopt to properly

interpret it.
Zaharia and Franssen [100],[101] studied the case of a two-dimensional ARSW built in Belgium. This study aimed to illustrate a fire resistance requirement, R15, within the context of a prescriptive approach, and to prevent the progressive collapse in the event of the sprinklers malfunction. The ISO fire curve was considered as a fire model as a uniformly heated temperature history. The resulting fire resistance time was a mere 2 minutes, but the authors suggested potential layout changes that could extend this time to 6 minutes. Moreover, the authors affirmed that a natural fire scenario might be more realistic, but under this fire curve, the progressive collapse of the structure cannot be avoided, in fact, the local collapse of rack uprights, initiates the global collapse.
Other authors [102],[103] and [104] used a similar approach to study the collapse dynamic of an ARSW, by considering natural fire curves obtained thanks to Computational Fluid Dynamics simulation. Battistini et al. [102]proposed a loading scheme to control collapse since automated rack warehouses are usually never full. Madeddu et al. [103] analysed the last step of the static implicit analysis to draw conclusions on the final collapse of the structure. Di Felice et al. [104] proposed a hierarchy to control the collapse based on the selective cooling of some columns employing water-spraying. Mei et al. [8] provide a robustness evaluation and highlights some possible aspects to be considered in the structural design to avoid a progressive collapse in the event of a fire. The analyses were performed by using the LOCAFI method for localized fires and nonlinear dynamic finite element simulations.

2.2.3. Description of the typological ARSW structure

Starting from these considerations, one typological self-supporting automated warehouse was studied, the structure object of this dissertation represents a very common Automated Multi-Depth Shuttle Warehouses (AMSWs), consisting of a steel-supporting structure and equipped with infill panels and roofing with sandwich panels. This AMSW has a rectangular plan with a total length of

52 m and a width of 35m, it consists of a central block, used for the storage of the reels, and two side lanes served by stacker cranes for handling the reels (see **Figure 2.13**).

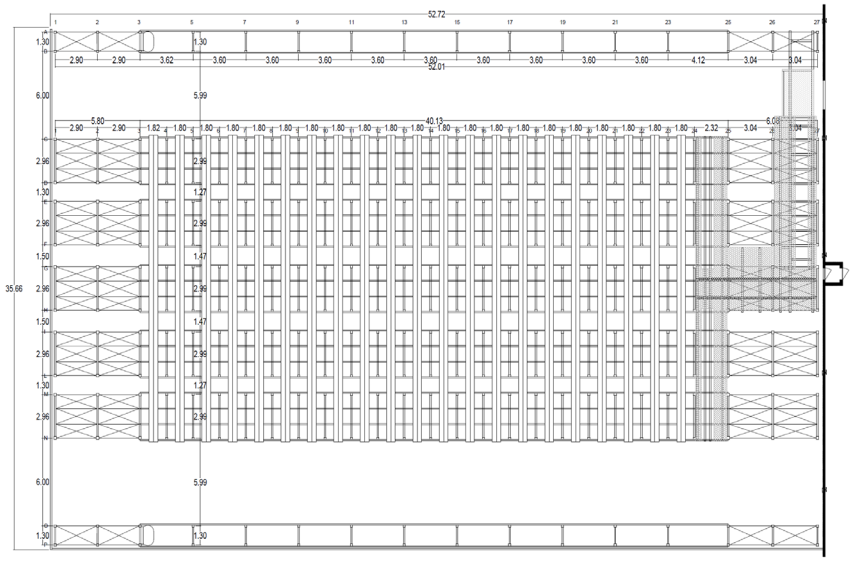

Figure 2.13. Plan view of the considered AMSW (dimensions in m). Source: ROSSS s.p.a.

In the down-aisle direction, **Figure 2.14**, the central block consists of a succession of frames, while at either end of the warehouse, the first two spans of the structure host the bracing towers. In this direction, the frames are joined with pallet beams with open section cold formed profiles.

For each span, a unit load (a paper reel) is stored; the UDCs are supported by particularly designed channels resting on the principal beams. The handling of unit load (UDC) is realized by a system of shuttles and satellites that move goods along rails in the warehouse cross and down aisle directions.

In the cross-aisle direction each frame is composed of five shoulders with V-shaped braces (see **Figure 2.15**) and it is characterized by 13 load levels placed at 2 m, with a total height of 29.8 m. The nomenclature adopted in the following analyses and consideration is also reported in the following **Figure 2.15**.

The warehouse structural system consists of hot-rolled tubular columns with

hollow square (HSS) cross section and cold formed horizontal and diagonal elements with C cross-sections. All the cross-sections are reported in **Table 2.2**.

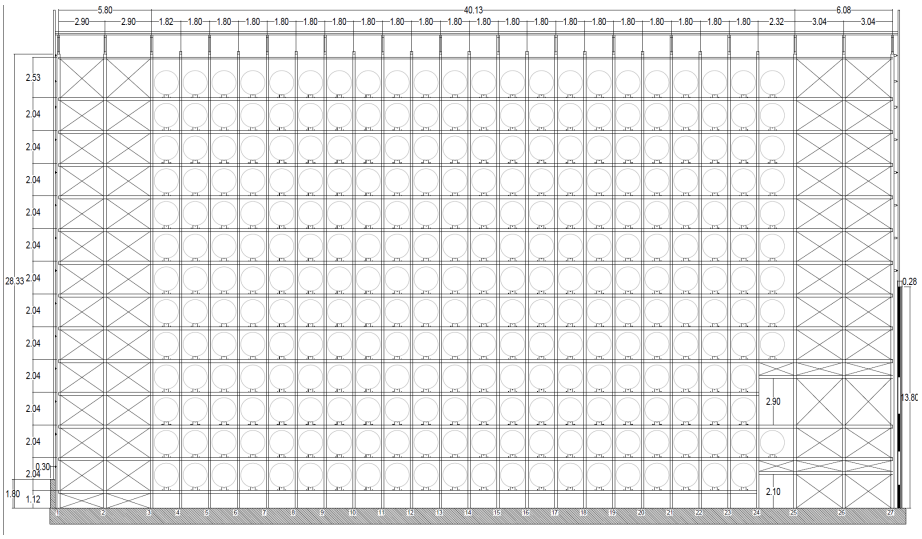

Figure 2.14. Down-aisle direction of the considered AMSW (dimensions in m).
Source: ROSSS s.p.a.

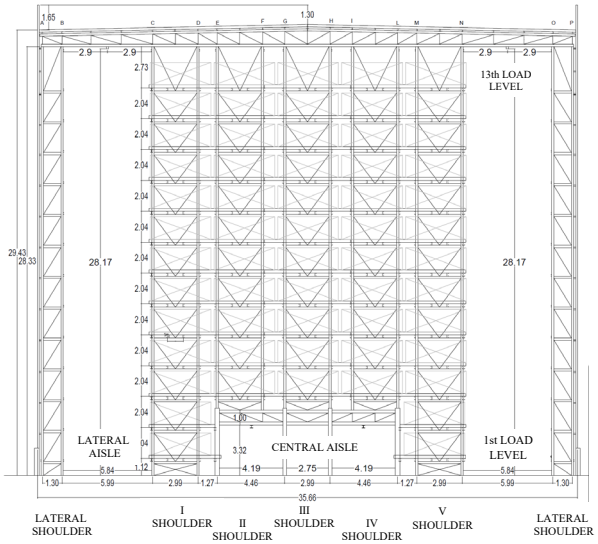

Figure 2.15. Cross-aisle direction of the considered AMSW (dimensions in m).
Source: ROSSS s.p.a

Table 2.2 Cross-sections used for the considered AMSW.

Structural Element	Cross- section	A_m/V [m^{-1}]	Steel grade	Notes
upright (1st section)	HSS 150x150x10	100	S355	from 0 to 8 m
upright (2nd section)	HSS 150x150x5	200	S355	from 8 to 16 m
upright (3rd section)	HSS 150x150x3	333	S275	from 16m to top
frame bracing of the central shoulder, (1st section)	2xC 150x60x15x2	755	S250	-
frame bracing of the central shoulder, (2nd section)	2xC 120x60x20x2	793	S250	13th load level
horizontal beam of the central shoulder	2xC 150x50x15x2	737	S250	-
frame bracing of the lateral shoulder, (1st section)	2xC 110x50x20x2	788	S350	from 0th to 4th and 12th levels
frame bracing of the lateral shoulder, (2nd section)	2xC 110x50x20x1.5	995	S250	from 5th to 11th levels
horizontal beam of the lateral shoulder, (1st section)	2xU 80x40x2	760	S250	from 1st to 5th and from 12th to 13th levels
horizontal beam of the lateral shoulder, (2nd section)	2xU 80x40x1.5	1013	S250	from 6th to 11th levels
frame bracing of the lateral shoulder	2xC 110x70x20x2	818	S350	13th load level
column of the portal	HEB 240	131	S355	-
bottom chord of the portal	HSS 200x150x10	106	S355	-
upper chord of the portal	HSS 300x150x10	105	S355	-
diagonal and vertical beams of the portal	HSS 120x120x10	109	S355	-
bottom/upper chords of the truss	HSS 150x150x3	333	S275	-
diagonal beam of the truss	2xC 150x50x15x2	737	S250	-
vertical beam of the truss	2xC 120x60x20x2	793	S250	-

2.3. Fire models

The thermal action represents the action of the fire on the structure and EC1

part 1-2 [10] gives different possibilities to consider this thermal action. One possibility consists of time-temperature relationships, these are relationships that give the evolution as a function of time of a temperature within the environment, that represents the surrounding structure. This temperature, together with the appropriate boundary conditions, can be used to determine the heat flux transmitted from the environment to the structure (see **Eq.2.3 - 2.5**).

Another possibility consists of relationships that directly give the heat flux affecting the structure, which is then combined with the flux reemitted by the structure to determine the evolution of the temperatures in the structure.

In the context of EC1 part 1-2 [10] and the new Italian technical fire prevention regulation [1], the distinction is made between nominal temperature-time curves, on one hand, and natural fire models on the other hand.

As explained in §2.1 the nominal fire curves are used in the contest of the prescriptive approach where the thermal action to be used is normally a legal requirement defined by the country or region where the building is located and depending on its size, use and occupancy. The Italian code gives prescriptive requirements that define both the time-temperature curve and the time (called *the fire resistance*) the structure must survive when exposed to this curve.

On the other hand, by using the preformed based approach, it is the responsibility of the designer to use an appropriate representation of the fire, although the Eurocode gives some guidance in the form of limits of application to some of the proposed natural fire models.

2.3.1. Nominal fire curves

The code provides three types of nominal fire curves (standard ISO834, hydrocarbon, and external curve), selected according to the nature of the combustible materials in the compartment. They are called nominal because they are not supposed to represent a real fire.

For fire that develop indoors with the prevailing combustion of cellulosic material, the design fire corresponds to that one defined by the standard nominal

fire curve, ISO834, which describes the average temperature of the flue gases, which grows over time in a logarithmic manner according to the following equation:

$$\theta_g = 20 + 345log10(8t + 1) \tag{2.28}$$

For fire that develop indoors with the prevailing combustion of hydrocarbons, such as gasoline, the design fire corresponds to that one defined by hydrocarbon fire curve given by the following equation:

$$\theta_g = 20 + 1080 \cdot (1 - 0.325 \cdot e^{-0.167 \cdot t} - 0.675 \cdot e^{-2.5 \cdot t}) \tag{2.29}$$

For fire that occurs externally from the building, the design fire corresponds to that one defined by external fire curve given by the following equation:

$$\theta_g = 20 + 660 \cdot (1 - 0{,}687 \cdot e^{-0.32 \cdot t} - 0{,}313 \cdot e^{-3{,}8 \cdot t}) \tag{2.30}$$

All these curves are displayed in the following **Figure 2.16** where it possible to observe how all the nominal fires are characterized, unlike the natural fire curves, by a trend of temperatures always tending to increase over time, and with an important initial speed, since they are referred to the post-flashover phase.

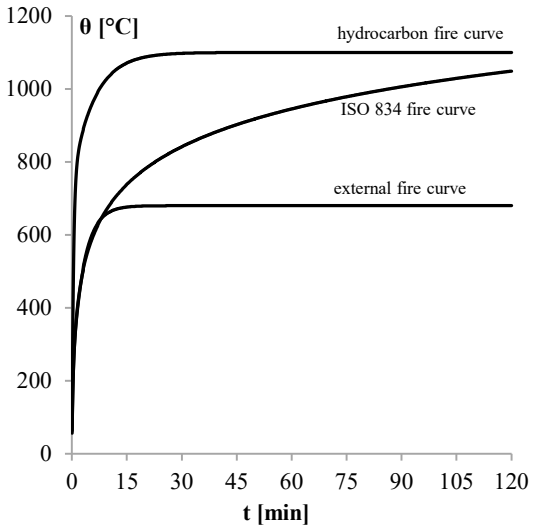

Figure 2.16. Nominal fire curves.

2.3.2. Input data for natural fire models

The natural fire curves follow all the four phases of the fire development: the *ignition* and *fire growth process*, the *fully developed stage*, and the *decay stage*, which are schematized in the following **Figure 2.17**.

When one or more combustible materials are heated from a heat source, ignition occurs, in the growth phase the fire spreads slowly by involving other combustible materials in combustion; while the latter are burning, the gas temperature inside the room increases rapidly, and there is a radiant flux from flames to other items. If there is enough oxygen and combustion materials within the compartment, a *flashover* can occur, this one represents a transition phase in which the flames, from a localized fire, quickly propagate to the entire compartment volume, becoming a fully developed fire. After the flashover, a constant combustion phase begins. Until reaching a decay phase as the fuel burns out.

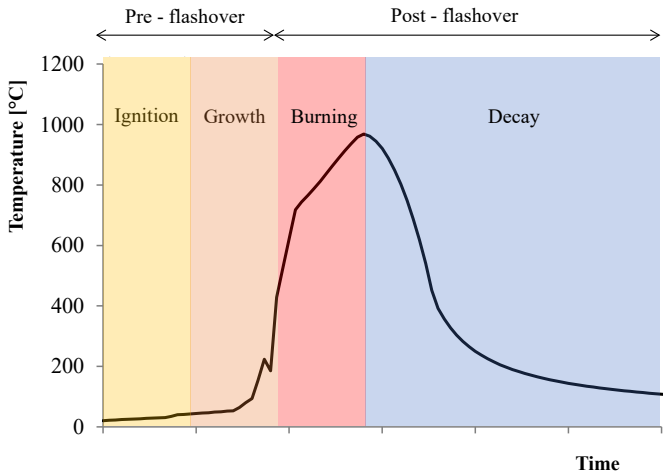

Figure 2.17. Natural fire curve phases.

One of the first input data that is necessary to carry out the fire resistance design is the *fire load density*, which can be determined for a specific project by performing a fire load survey. In this case, the content as well as the combustible parts of the construction should be considered. Net calorific values of the combustible materials must be considered and modified by the effect of moisture if

relevant. The characteristic fuel loads q_{fk} [MJ/m^2] can be calculated as follows:

$$q_{fk} = \frac{\sum_{i=1}^{n} g_i \, H_i \;\; m_i \;\; \psi_i}{A} \tag{2.31}$$

Where:

g_i [kg] is the mass of the i-th combustion material;

H_i [MJ/kg] is the calorific value of the i-th combustion material;

m_i [-] is a combustion factor, the value of which is between 0 and 1;

ψi [-] is the limiting factor of participation in combustion;

A [m^2] is the floor area of the compartment.

Most often, the characteristic fire load density is determined from a classification of occupancy of the compartment. Such classification is proposed on national level [1]. Moreover, Informative annex E of EC1 part 1-2 [10] gives a table that lists characteristic fire load densities for a selection of occupancies. The 80% percentile from this table is taken as the characteristic value of the fire load density for the content. Fire loads from the construction material of the building should be added to these values if relevant.

A design value of the fire load q_{fd} is then calculated based on the characteristic value q_{fk} using the following equation:

$$q_{fd} = \delta_{q1}\delta_{q2}\delta_n q_{fk} \tag{2.32}$$

Where, the factor δ_{q1} considers the risk of fire activation, i.e., the risk that a severe fire occurs. The risk of a fire occurring is higher in compartments with larger area. The factor δ_{q2} considers the risk of fire activation due to the type of occupancy. The factor δ_n considers the effect of active firefighting measures.

In addition to the fire load density, to apply natural fire models, another important parameter is the Rate of Heat Release (HRR) density.

HRR can be the results of experimental test or defined by codes and standards. The EC1 part 1-2 [10] and the Italian Fire Code [1] provide the same procedure to calculate the HRR, the curve is divided into three parts, reflecting the fire stages of **Figure 2.17**.

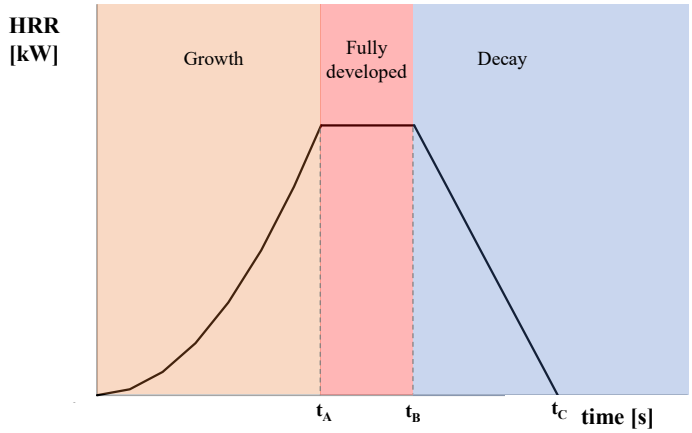

Figure 2.18. HRR curve phases.

The power released by the fire Q, often called the rate of heat release HHR [kW], can be calculated as a function of time according to the following equation:

$$Q = 10^3 \left(\frac{t}{t_\alpha}\right)^2 \leq A_{fi} HRR_f \tag{2.33}$$

Where:

t_α is the time needed to reach a rate of heat release of 1 MW, in [s];

HRR_f is the maximum rate of heat release produced by 1 m² of fire in case of fuel-controlled conditions, [kW/m²];

A_{fi} is the maximum area of the fire, which is the fire compartment in case of uniformly distributed fire load, but which may be smaller in case of a localised fire, in [m²].

The parameter t_α and the maximum rate of heat release HRR_f, for different occupancies, are given in the national and European codes.

Each phase has a fixed duration that is reported in the following equations, which provide the three steps of the grow phase end and the plateau start **Eq.2.36**, plateau end and decay start **Eq.2.35**, and decay end **Eq. 2.36**:

$$t_A = \sqrt{HRR_{max} \frac{t_\alpha^2}{1000}} \tag{2.34}$$

$$t_B = t_A + \frac{70\%\ q_f\ A_f - \frac{1000}{3\ t_\alpha^2} t_A^3}{HRR_{max}} \tag{2.35}$$

$$t_C = t_B + \frac{2 \cdot 30\%\ q_f\ A_f}{HRR_{max}} \tag{2.36}$$

2.3.3. Localized fires

The compartment fire scenario assumes that the gas temperature rises uniformly. For compartments that are reasonably small and where the fire load is uniformly distributed, this is usually reasonably realistic. However, as the size of the compartment increases or if the fire load is in a relatively small area, this assumption tends to become increasingly conservative, because the fire may not reach the flashover conditions during its evolution and consequently it could remain within an area of the compartment. These are called "localized fires" and unlike the post-flashover fire, where the temperature of the gas can be considered uniform in the compartment, the temperatures of the surrounding flame and gases are not uniform and need to be determined at each point of the compartment.

In the Annex C of the EN1991-1-2 [1] provides simplified formulations for the determination of thermal actions in the case of localized fires. These calculations are different according to whether the flame impacts the ceiling or not and they were derived from two different research.

The first researcher that analysed the problem was Heskestad [105],[106], who developed a method for calculating the height of a flame and its temperature along the vertical axis in case the flame does not impact the ceiling (**Figure 2.19**).

The independent variables used are the diameter of flame, D, and the heat release ratio (HRR), Q. The empirical correlation, based on experiments proposed by Heskestad to calculate the temperature along the plume, is reported in following **Eq. 2.37**:

$$\theta(z) = 20 + 0.25\ {Q_c}^{2/3} (z - z_0)^{-5/3} \leq 900 \tag{2.37}$$

Where:

Q_c, is the convective part of the HRR in [W] (fixed as 0.8Q);

z is the height along the flame axis in [m];

z_0 is the virtual origin of the axis, given by the following formula:

$$z_0 = 1.02D + 0.00524\,Q^{2/5} \tag{2.38}$$

It is worth saying all the proposed formulations are applicable for flame diameter (D) less than or equal to 10 m and HRR less than or equal to 50 MW.

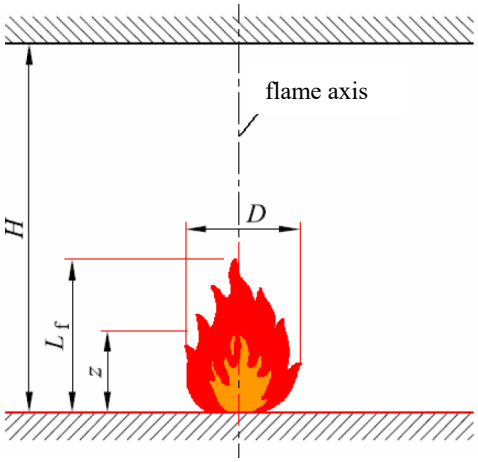

Figure 2.19. Heskestad Model [1].

Since the Heskestad model does not consider the case in which the flame impacts the ceiling (**Figure 2.20**) this limitation was superseded by Hasemi, et al. [107]. The Hasemi method uses Heskestad **Eq. 2.37** to calculate temperature along the plume and propose empirical correlation to evaluate heat fluxes received by elements situated at the ceiling level.

The heat flux ($\dot{h}$) in [W/m²] received by the fire exposed unit surface area at the level of the ceiling is given by:

$$\begin{aligned} \dot{h} &= 100\,000 && for\ y \le 0.3 \\ \dot{h} &= 136\,300\ to\ 120\,000\ y && for\ 0.3 < y < 1.0 \\ \dot{h} &= 15000\ y^{-3.7} && for\ y \ge 1.0 \end{aligned} \tag{2.39}$$

Where:

y is a parameter [-] given by:

$$y = \frac{r + H + z'}{L_h + H + z'} \tag{2.40}$$

r is the horizontal distance [m] between the vertical axis of the fire and the point along the ceiling where the thermal flux is calculated, see (**Figure 2.20**.);
H is the distance [m] between the fire source and the ceiling, see (**Figure 2.20**);
L_h is the horizontal flame length and z′ is the is the vertical position of the virtual heat source [m] and evaluated by using the HRR.

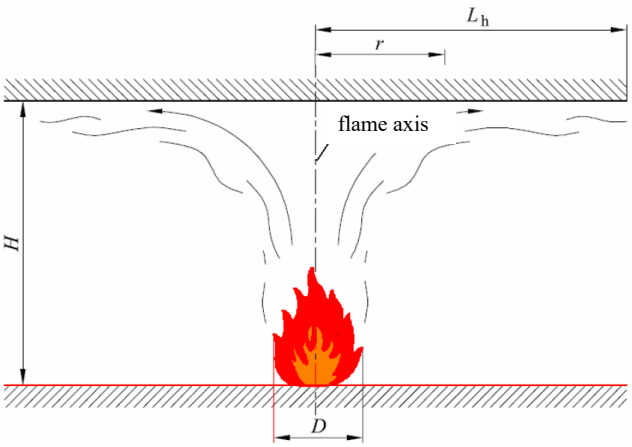

Figure 2.20. Hasemi Model [1].

EN 1991-1-2 Annex C [1] does not give a method for assessing the temperature or the heat flux received by a vertical member at a given distance from the fire source i.e., that is not engulfed in the fire.

Additionally, the EN 1991-1-2 Annex C method conservatively sets the emissivity of the flame (ε_f) as equal to 1.0, which tends to produce conservative results when compared to tests.

Under the European Union's Research Fund for Coal and Steel (RFCS) project LOCAFI [108], work was carried out to improve the Annex C methodology for localized fires. Through a series of tests, and subsequent numerical and analysis work, refinements to the methodology were proposed, addressing these limitations. The experimental campaign allowed to evaluate the influence of several parameters:

- Fuel type.

- Pool diameter.
- The presence or not of a column engulfed in the pool.
- Type of columns.
- Position, diameter, and number of pools
- Configuration with or without ceiling.

A total of 82 tests were performed to define the flame length and temperature, the influence of the column on the flame, and evaluate the heat flux on the column.

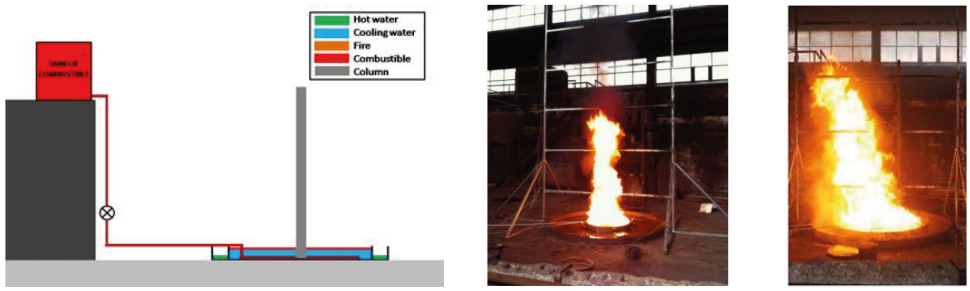

Figure 2.21. LOCAFI pool fire [108].

The experimental campaign concluded that the heat flux equations in the Eurocode 1 needs to be adjusted because the comparisons between the experimental results and the analytical ones confirms that Eurocode recommendations overestimate the thermal exposure and thereby the steel temperatures by several hundred degrees.

Numerical analyses followed the experimental campaign, to simulate the experimental tests numerically, to carry out a parametric study and finally to validate a simplified analytical model capable of predicting the thermal action received by a structural member in a compartment where a localized fire occurs.

The analytical model has been development with two levels of refinement:

A model based on numerical integration for implementation into advanced models like SAFIR and Ansys (named "geometric model"); and a model based on analytical formulae for handmade use or implementation into basic engineering tools like Excel spreadsheets (that will be called "simplified model" in the

present report).

In both geometric and simplified models, the configurations where the thermal exchanges are drawn by convective fluxes (members engulfed in the fire or situated inside the smoke layer) are treated by application of the existing equation available in EC1 part 1-2. The major heat exchanges, by radiation, will be calculated by representing the fire as a virtual solid flame that radiates in all directions. The first step of this calculation is again common to the geometric and simplified models and consists of defining the geometry of the virtual solid flame representing the localized fire and the distribution of temperature as a function of time.

The shape of the virtual solid flame representing the thermal action of the localized fire may be cylindrical or conical. The cylindrical shape flame is simpler to deal with but usually represents less accurately the thermal attack induced by the fire and leads to overestimated radiative heat fluxes.

In case the flame length is higher than the ceiling level, the cylinder or the cone must be truncated and a radiant ring, representing the spreading of the flame under the ceiling, should be considered outside the truncated cylinder or cone.

The difference between the geometric and simplified models is the calculation method used for the assessment of the radiative heat fluxes exchanged between the virtual solid flame and the elements:

In the geometric model, the virtual solid flame and the exposed element are respectively meshed into finite radiating bands and finite faces. Then, the total radiative heat flux received by a face is the sum of the radiative fluxes coming from all the radiating bands. It should be noted that for exposed elements with I-shape or any other concave section, an equivalent rectangular shape must be considered.

The simplified model was defined based on configuration factors, to propose a calculation method without surface integral (that generally requires the implementation into a solver). For simple shapes like cylinders or rings, direct formulae are available under several conditions. By means of slight adaptations of the virtual solid flame these conditions are satisfied and the calculation of radiative

heat fluxes can be calculated using the concept of configuration factor.

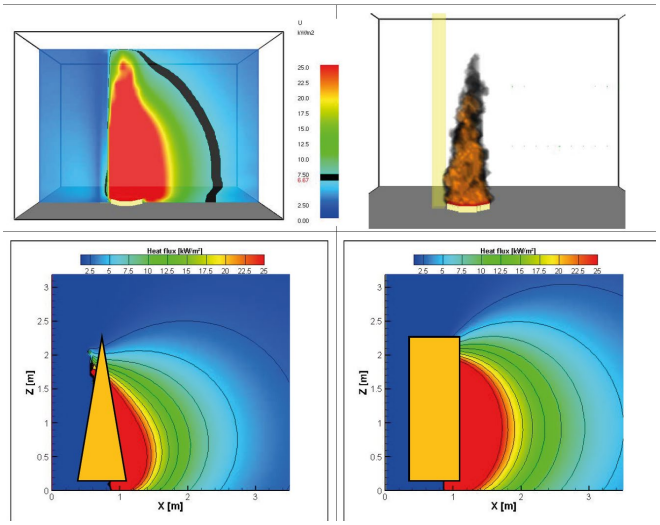

Figure 2.22. Numerical heat flux and flame (top); heat flux with a conical flame (bottom right); heat flux with a cylinder shape (bottom right), [108].

The validation work has consisted of comparing the results obtained from the calibrated FE models and from the new analytical models (geometric and simplified, cylindrical or conical flame shape). As a result of this validation work, it may be stated that:

- Cylindrical flame shape leads to significant overestimations of the radiative heat fluxes where conical flame shape gives good correlations or slight and acceptable safe-sided discrepancies.
- The differences between the results obtained from geometric and simplified models are limited.

The LOCAFI model will be further analysed in the following chapters.

2.3.4. Zone models

Zone models are fire models that can be used to compute the development of the temperature in a fire compartment based on differential equations expressing

mass balance and energy balance equilibrium. Zone models assume that a compartment can be vertically subdivided into zones, see **Figure 2.23**, with homogeneous properties in terms of temperature and composition: a hot layer with combustion products, located near the ceiling, and a cold layer with fresh clean air at the bottom, separated by a moving interface. The properties and the layer height can vary over time and are identified when solving global conservation equations [109].

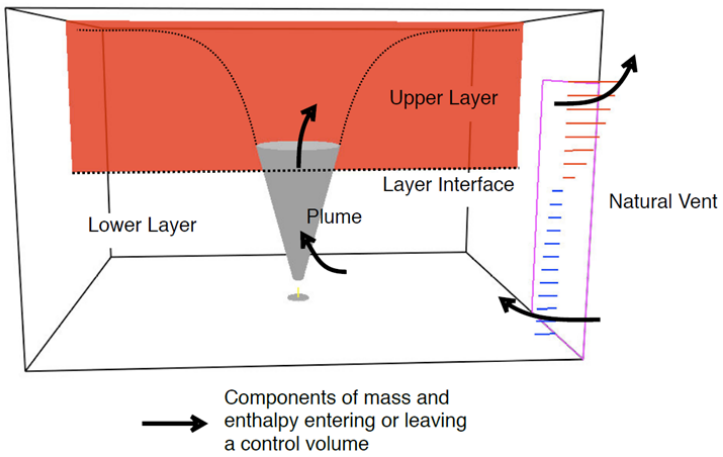

Figure 2.23. Schematic of control volumes in a two-layer zone model [112].

When a given criteria is met, the zone model switches from a two-zone model to a one-zone model, representative of a fully developed fire, where uniform temperature is considered in the whole compartment. One zone model represents a post-flash-over situation whereas two zone models represent a pre-flash-over situation.

Eurocode 1 [10] gives very few recommendations on zone models except that gas properties, mass exchanges and energy exchanges should be considered and that an iterative procedure is involved. This means that the differential equations must be integrated with time to obtain the time-temperature curve [110]-[111] . This is the reason why zone models require computer software. For this reason, the National Institute of Standards and Technology (NIST) developed the CFAST

software [112] applying a two-zone fire model capable of predicting the environment in a multi-compartment structure subjected to a fire. While Cadorin [113] developed a zone model that allows switching from a two-zone models to a one zone model and so it is valid in pre and post flashover fire phase, which was validated against full scale fire tests and implemented in the OZone software [114],[115].

The CFAST software will be further analysed in the following chapters.

In a thesis by Bong [116] guidance on how to determine which numerical model to use for different enclosure sizes, is provided. The two-zone model, BRANZFIRE, was seen to give very good predictions of the hot gas layer temperature and layer height, compared to data from FDS, in enclosures up to 600 m^2 and relatively good predictions up to 1200 m^2. However, for larger enclosures, the FDS simulations demonstrated a non-uniform temperature distribution in both the horizontal and vertical direction, which was not captured with the two-zone model. Moreover also, in a room fire experiment, while a stratified layer situation can be observed, the layer interface is not always clear, and the temperature varies rather gradually with height. For these reasons, a new zone modelling approach called multi-layer zone model was developed by Suzuki [117] and modified by Xiaoju [118], to predict vertical distributions of temperature in a fire compartment. In this model, the space volume in a compartment was divided into an arbitrary number of horizontal layers as the control volumes, and the physical properties, such as temperature and species concentrations, in each layer were assumed to be uniform. The boundary walls were also divided into segments following the layer division and the radiation heat transfer between the layers and between the layers and the wall segments were calculated, as well as the convective heat transfer between the layers and the wall segments. The principal equations for each laminated horizontal layer are derived from the conservation equations of mass and energy. One of the assumptions of this model is that the fire plume flow does not mix with the upper layer as soon as it penetrates the layer interface but continues to rise until it hits the ceiling, and all the heat released by the fire rises into the top layer.

The multi-zone concept is not as established as two-zone models since only a few models have been presented. Therefore, multi-zone models' accuracy and possible benefits need to be investigated further. Johansson [119] indicates that the multi-zone model gives reasonable estimates of gas temperatures in well-ventilated large spaces, and also concluded that there is a potential for the multi-zone concept to be a complement to more advanced numerical modelling methods like Computational Fluid Dynamics that requires an extensive computational time.

2.3.5. Computational Fluid dynamics (CFD) models

The assumptions required for zone fire modelling become unnecessary when using computational fluid dynamics (CFD) modelling. Indeed, the full, partial differential equation set, expressing the principles of local conservation of mass, momentum, energy, and species, the field equations, are solved using numerical methods subject only to the boundary conditions of the problem [120]. These equations are solved numerically to yield time-varying predictions of temperature, gas velocity, gas species concentrations, and so forth, on a three-dimensional mesh of control volumes that spans the geometry being modelled.

Therefore, in the CFD models, there is a grid-based division of the computation domain, and results are obtained for each cell of the mesh. The physics behind fire are complex and occur at different scales in time and space (combustion, radiation, smoke generation and movement, pyrolysis, etc.). Therefore, some simplifications are still needed and introduced.

Unlike two zone models, CFD models enforce the conservation laws in each of the thousands or millions of relatively small control volumes. However, the exact solution of the governing equations, resolving fully the length and time scales that occur in the turbulent flows associated with fire, is still beyond the capabilities of even the largest computers currently available. To capture the details of the chemical processes of a fire would require spatial resolution of less than 1 millimetre. Therefore, it is necessary to modify the governing equations

to model the unresolvable turbulence. Two main approaches are currently employed in CFD simulations of fire: Large Eddy Simulation (LES) and Reynolds averaged Navier-Stokes (RANS) equations. With RANS model, a widely used technique, the equations of motion for fluid flow are time-averaged then solved discretely. With LES (Large Eddy Simulation), the turbulent flow is characterized by solving large-scale motions while the small-scale motions are removed through a filtering operation, and their effect modelled using sub-grid scale models. It implies that the large-scale phenomena are well resolved while the small eddies are not well resolved.

To handle turbulent viscosity in LES, different models can be used: Deardoff, Constant Smagorinsky, Dynamic Smagorinsky, Vreman, etc.).

Several studies have been carried out to compare CFD results with experimental data [122]-[124], allowing to demonstrate the CFD capacities to model compartment fires.

2.3.6. Travelling fires

The traditional fire models assume uniform burning and homogeneous temperature conditions throughout a compartment, regardless of its size.
In the last years, multiple accidental fires occurred that have led to structural failures such as: the Interstate bank fire in Los Angeles in 1988, the One Meridian Plaza fire in Philadelphia in 1991, World Trade Centre fires in New York City in 2001 [125], Windsor tower fire in Madrid in 2005 [126], Faculty of Architecture fire at TU Delft in 2008 [127], Grenfell Tower in London in 2017 and Moro Tower in Milan in 2021, all these events pointed out the issue of the fire spread modelling in large spaces and its implications on the response of structures. Indeed, during these events the fires had been observed to move along the floor plates and vertically across different floors, hence, these fire scenarios are classified as "travelling fires" at the University of Edinburgh in 2007, due to Rein et al. [128]. These types of fires are likely to occur in large compartments (floor area above 100 m^2) and can create a heterogeneous temperature field which can be very

damaging to the structure [129]. This non-homogeneous nature of fire has also been observed during several experiments in the past [130]-[134]and has also been demonstrated recently in the Malveira fire tests [135]. All the experimental tests allow understanding the fire dynamics, evaluating temperature evolution, and observing the structural response of a travelling fire.

he first researcher who attempted a detailed analysis of fire spread in compartments was Clifton in 1996 [136] in a report for the Heavy Engineering Research Association (HERA) of New Zealand, he proposed that in large compartments (firecells) without any partitions, fires could move across the floor. Clifton proposed a model, called Large Firecell Method (LFM) where each Firecell at a defined time, was divided into four design areas, where each of these could be in the following states – fire, pre-heat, smoke logged and burned-out. Each of these design areas is then subjected to time-temperature curves (parametric fire curves [1]) individually and sequentially.

This pioneering model for localised fire moving throughout the enclosure and generating non-uniform heating in the compartment was not widely used, due to insufficient experimental validation [137], Clifton stated that this methodology should mostly function as a research tool and should only be used for single element checks in design [141].

Stern-Gottfried and Rein [5] and [141] developed a Travelling Fire Methodology (TFM), to provide a spatial and temporal evolution of the temperature field within a compartment. This model considers that the fire-induced thermal field is divided in two regions: the near field and the far field, as illustrated in **Figure 2.24**a. These regions are relative to the fire, which travels within the compartment following a one-dimensional path. The “near field” is the burning region of the fire and where structural elements are exposed directly to flames (and experience the most intense heating). The “far field" is the region remote from the flames where structural elements are exposed to hot combustion gases (the smoke layer), but experience less intense heating than from the flames. The near field region is analogous to the design area of the LFM [136].

The methodology is independent of the fire model selected and can utilise simple analytical expressions or sophisticated numerical simulations. Indeed,

the first version of this methodology used the CFD code Fire Dynamics Simulator (FDS) as the fire. Later work was developed using an analytical correlation [139]. A uniform temperature equal to 1200°C was assumed for the "near field", while Alpert's ceiling jet correlation was adopted to calculate far field smoke temperature, given by:

$$T - T_\infty = \frac{5.38}{H}\left(\frac{\dot{Q}}{r}\right)^2 \tag{2.41}$$

Where:

T [°C] is the peak ceiling jet temperature;

T_∞ [°C] is the ambient temperature;

$\dot{Q}$ [kW] is the heat release rate of the fire plume;

H [m] is the height of the compartment ceiling;

r [m] is the distance from the centre of the fire plume.

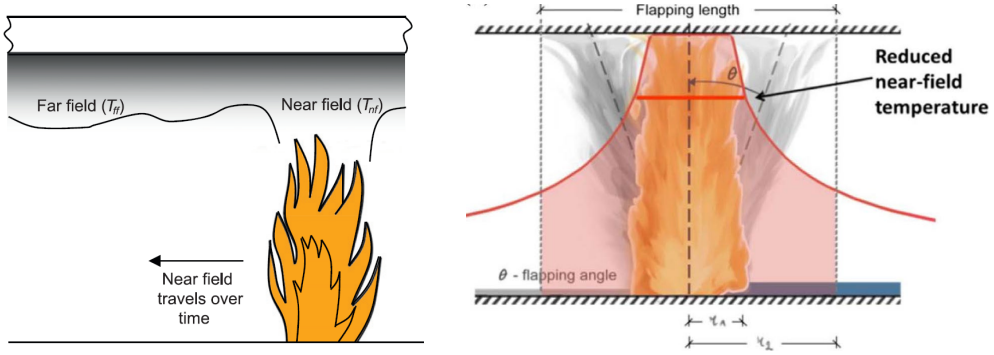

(a) (b)

Figure 2.24. Scheme of the near field and far field according to TFM [141] (a); Flapping angle and reduced near field temperature according to iTFM [142] (b).

The fire spread S (m/s) is not an input, it is given by:

$$S = L_f(q_f/RHR_f) \tag{2.42}$$

Where:

L_f is the length of the flame in m;

HRR_f is the maximum heat release rate per unit area in [MW/m²];

q_f is the fire load density in [MJ/m²];

Heat release rate (HRR) of the fire is calculated from the heat release rate per

unit area and local burning time is obtained from the HRR and fire load density, indicating a semi-steady state fire spread [129].

The TFM does not assume a single, fixed fire scenario but rather accounts for a whole family of possible fires, allowing identification of the most challenging heating scenarios for the structure to be used as input to the subsequent structural analysis. Temperature–time curves for a family of fires, fires is generated by covering the full range of all possible fire sizes, it is assumed in the model that each time the fire would burn a certain surface area A_b (m^2), which is a percentage of the total floor area A_t (m^2) ranging from 1% to 100% [143]. In this way, the methodology overcomes the fact that the exact size of an accidental fire cannot be determined a priori.

However, both TFM and LFM models neglect some aspects of the fir dynamics. For instance, the accumulation of a hot smoke layer is ignored in both models. Moreover, the fire path of the near field is not specified in the TFM model, as there are too many uncertainties, such as the ignition point, ventilation conditions, and fuel load distributions, which combine to preclude determination of the actual fire path in a real building.

Some of the uncertainties associated with the original model were later improved and reported as the improved travelling fire methodology (iTFM) [142], by excluding unrealistic fire sizes and behaviour, by accounting for the localised fire dynamics, specifically, reducing the range of possible fire sizes which should be implemented by realistically considering fire spread rates. Furthermore, the concept of flapping angle was introduced (see **Figure 2.24** b), to account for the near field temperature range from 800 °C to 1200 °C, rather than the conservative 1200 °C used in the previous version. This may lower the ceiling temperatures for some fir sizes but remains a significant approximation [143].

In 2016, a new travelling fire framework was proposed by Dai et al. [143]-[144] the ETFM (Extended Travelling Fire Method) framework. It is based on a "mobile" version of Hasemi's localized fire model, which quantifies the local effect of fire on adjacent structural members combined with a simple smoke layer calculation for the areas of the compartment away from the fire. This combined fire model enables the analysis to capture both spatial and temporal changes of the

thermal field thus addressing more fire dynamics than Clifton's model and Rein's model.

Such methodology also considers that the fire-induced thermal field is divided into two regions: the near field, for which a mobilized version of Hasemi model, i.e., a localised fire model, is considered, and the far field, for which a calculation of a smoke layer based on FIRM zone model, see **Figure 2.25**.

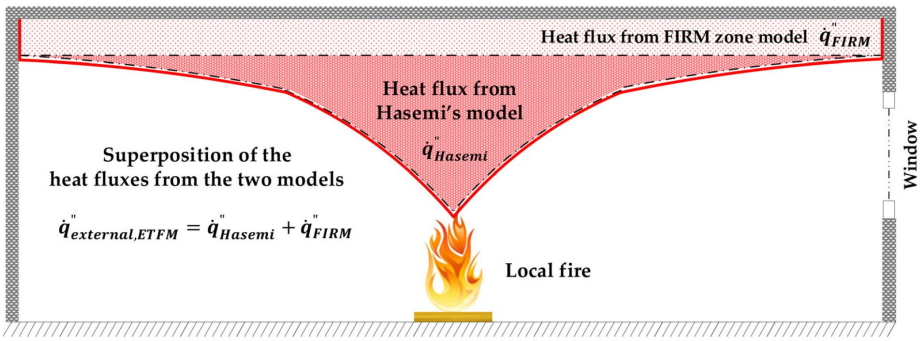

Figure 2.25. ETFM heat fluxes combination: Hasemi (localized fire) and FIRM (zone model) [144].

Implementing Hasemi's localized fire model into the ETFM framework, three key parameters should be decided at each time step: fire origin, fire diameter D (m), and HRR (W), which together the travelling fire speed are the two most important parameters in this travelling fire framework.

The fire origin is defined as the midpoint of the distance between the front edge and the back of the travelling fire while the fire diameter D (m) is evaluated as the diameter of a circular source with equivalent burning area. Heat release rate Q,(W), is defined under the assumption that fire is at the steady state, given by:

$$Q = 1000 \cdot RHR_f \cdot A_{fi} \tag{2.43}$$

Where: HRR_f [W/m²] is the maximum heat release rate per unit area in fuel-controlled conditions and A_{fi} (m²) is the burning area.

The ETFM framework also accounts for the accumulation of a hot smoke layer, variable fuel load distribution along the fire path, both of which are ignored in previous models.

However, the current framework still employs a predetermined localized fire path. Indeed, the localised fire crosses the compartment following a one-dimensional path, with a speed decomposed into two variables: the constant fire spread rate, which determines the front edge of the fire, and the burn-out time, which determines the back-edge of the fire.

The ETFM model allows consideration of non-uniform burning rates, fuel load densities, and heat release rates. The application of the zone model to evaluate the hot smoke layer temperature allows accounting for energy conservation, mass conservation, ventilation with vertical openings, and heat losses through compartment boundaries. It is noted that the two previously described methodologies force a traveling fire representation by specifying that the temperature field from other existing models will move through the compartment and have not attempted to explicitly account for the mass and energy balance in the compartment; thus, the ETFM framework in principle addresses more of the fire dynamics. Although the used zone model presents some limitations (for example, the heat loss through boundaries is a constant fraction of the total energy) by comparison to other existing zone models such as (OZone [114] CFAST [112]). A potential limitation of the ETFM framework is the limited applicability of Hasemi's localised fire model, indeed, this model provides heat fluxes at the ceiling level when the fire impacts the ceiling. Consequently, columns and beams when the fire does not impact the ceiling fall out of this situation.

Furthermore, this methodology sums the results (thermal impact) obtained with the localised fire and of the zone model, while the Annex D of the EC1 part 1-2 [1] states that in the case of a localised fire, a combination of results obtained with a two-zone model and a localised fire approach may be considered. In particular, the temperature field in the member may be obtained by considering the maximum effect at each location given by the two fire models.

Nevertheless, the ETFM is described as a framework, implying users may modify the localised fire and zone models depending on their specific design fire conditions [144]. Hence Dai et al. provide a method for extending every localized fire model to become a travelling fire.

Another limitation of the ETFM framework is from the simplicity of the representation of ventilation, as in reality this may play a very important role, e.g., changing the fire travelling trajectory, heat release rate, etc [143].

Nowadays, great effort is produced to evaluate travelling fires experimentally and to represent the effect of such travelling by using the Computational Fluid Dynamics (CFD) code Fire Dynamics Simulator (FDS) [145].

At present, fire design methods for vertically travelling fires are not as developed as for horizontally ones. In the last decade, the vertically travelling fires have been analysed like multifloor floor fires in high-rise buildings. There are three possible mechanisms that enable fire to travel from one floor to an adjacent floor (SFPE 2016, [120]).

1) internal burning, the fire can travel upwards by compromising the perimeter fire barrier materials between the floor slab and curtains walls, or by igniting the interior vertical ductwork through floors.
2) external burning, which is associated with most fully developed compartment fires, could ignite combustibles in the upper floors by radiation heat transfer through glazing or by direct flame impingement through other openings.
3) external flaming could also ignite external insulation material which could then involve many floors on fire even more rapidly.

Modelling the process of vertical fire spread can be complicated by several factors, such as the geometry of the façade, the shape of the opening [146], the fire resistance of the glazing, the ambient atmosphere, and the type of occupancy. In 2009 Usmani et al. [6],analysed the problem and faced it up for structural fire analysis by recognizing that post-flashover fires can develop at different time intervals for different floors. Therefore, a simple yet important parameter, time delay ($\Delta_{t,\,delay}$) has been introduced to study the structural performances in vertical travelling fires. The authors found that local or global collapse is possible in multi-floor fires, they distinguished two different typological collapses: weak and strong floor mechanisms.

Roben et al. [147] examined the impact of vertically travelling fires on a multi-

storey structure. The building they examined was characterized by a concrete core and a steel–concrete composite floor system. The study assumed three floors were on fire. Although the authors noted that horizontally travelling fires would give a more realistic representation of the fire spread through a compartment, the authors assumed horizontally uniform fires for their study. The heating curve used was a generalised exponential curve given by Flint [148] which was applied to each floor but with a time delay between floors, however, no theoretical background or physical justification of the method is given.

Three fire scenarios were used: uniform heating on all three floors, a time delay of 500 s between each floor, and a time delay of 1500 seconds between each floor. The authors noted that many factors influence the vertical spread rate. The values used in the study were to capture the range of eyewitness accounts of vertical flame spread of between 6 and 30 min in the Windsor Tower fire. The results, primarily examined in terms of horizontal displacements of columns and total axial forces of floors, showed that the vertically travelling fire with a short time delay induced a similar structural response to that of the uniform heating case. However, the primary difference observed was a "cyclic pattern induced in columns" for the travelling fire. This pattern was also observed for the long delay travelling fire, but with longer time intervals. The authors note that this cyclic deflection pattern has not been examined before and has a significant impact on the structure and, therefore, should be considered in design. Moreover, the author assumed that a global collapse will not occur, and all the members would cool down to ambient temperature.

Kotsovinos et al. [149] studied the key structural effects of vertically travelling fires on a concrete core and a steel–concrete composite floor system. The authors assumed that the fire travels upward progressively, from one floor to the other. The post-flashover fires for each floor are represented by parametric fires as given in EC1 part 1-2 [1], and a simple time delay is used to simulate the beginning of heating on each successive floor, the Δt_{delay} was varied from 600 to 2500 seconds. The results showed that simultaneous multiple floor fires have been found to be more conservative than vertically travelling fires in terms of global structural behaviour, a suitable number of floors simultaneously burning at the

same time can be used as a conservative upper bound for global behaviour by designers, travelling fires are seen to produce higher tensile axial forces in the floors and thus the potential of connection failure is increased. Finally, the authors stated that values for travelling times cannot be de fined as these depend on multiple parameters specific to a building or structure, and thus cannot be generally applicable.

2.3.7. Open issues in fire models for rack structures

Moving in the context of alternative solutions, or rather in PBA, the first step is the selection of the design fire scenarios and the definition of the natural fire curves, according to the fire models. The design fire scenario is a qualitative description of the fire development during the time, identifying key events that characterise the fire and differentiate it from other possible fires. A fire scenario is largely influenced by different conditions as internal ventilation; external environmental conditions; active protection system effectiveness; type, position, and dimension of fire ignition; type and distribution of fire load; fire load density; and windows and door state (close or open). The number of possible fire scenarios is usually too large and the analysis of each one is not practicable. Therefore, the design fire scenarios should be chosen, to analyse the most severe cases for the structure.

It is worth noting that, as analysed in [8] fire scenarios for ARSW will consider primarily the chance of an electrical malfunction that causes the burning of the stacker crane. Moreover, the malfunction is considered at the lower building level; this choice is made because rack uprights are more stressed at the lower level, so the fire possibility is considered riskier.

Since they are large and high structures a fully developed fire seems unrealistic and for this reason the fire model that better fits in this case could be the localized fire model.

All these considerations lead to affirm that for the ARSW single or double

depth the fire scenario at the base within the aisles for stacker cranes can be modelled by considering the localized fire (LOCAFI model). On the other hand, in the case of multi-depth ARSW because of their configuration and the presence of the shuttle systems, the fire could start like a localized fire also within the load levels and could develop into a traveling fire both in horizontal and vertical directions. As seen before at present, fire design methods for vertically traveling fires are not developed as for horizontal ones. Indeed, in the last decade, vertically traveling fires have been analysed like multi-floor fires in high-rise buildings, which represents a different condition than the ARSWs one. For these reasons, to study the fire behaviour of the ARSW showed in §2.2.3, in the context of this dissertation it was necessary to obtain a fire model that allowed the vertical and horizontal propagation of localized fires to be considered.

Chapter 3

3. Fires Modelling of steel racks

This Chapter provides a fire model that considers vertical and horizontal propagation, properly validated against experimental results in steel racks available in the literature. In §3.1 the experimental campaign on steel racks available in the literature is described in detail. These experimental results were simulated by using the CFAST software developed by NIST considering multi-cells approach as shown in §3.2. Based on this validation a fire model that considers vertical and horizontal propagation for ARSW structure is proposed in §3.3. The same fire scenario was modelled also by using FDS software which allows the analysis of the ventilation effect on the fire propagation, as shown in §3.4. Finally, in §3.5 benchmarks between the two fire models are illustrated.

3.1. Fire spread in large industrial premises and warehouse: study of a previous paper.

In order to obtain a fire model considering the vertical propagation of localized fires, some experimental results were looked for in the scientific literature. Since, at the time of writing this dissertation, no one has carried out an experimental campaign on automated clad-rack warehouses, it was necessary to consider works regarding usual steel racks.

In particular, the work used as principal references for validating the fire model was the one carried out by Lönnermark and Ingason [150], which performed several fire scale tests (1:5), to investigate the fire spread in rack storages. The focus of this experimental campaign was on the fire spread from an initial

fire in rack storage to adjacent racks without any suppression system. Indeed the authors affirm that most of the large-scale tests with rack storage carried out worldwide include tests with sprinkler systems [151] - [156] ,but no large-scale tests have been performed where the fire is allowed to spread from the initial rack to adjacent racks without the interference of a sprinkler system. Such tests would be too difficult to perform due to the risk of damaging the test facilities and of course due to their high costs.

For these reasons, Ingason has performed several tests [157] - [161], both large scale and model scale, where the effects of the geometry and type of fuel on the fire growth in rack storages, have been investigated. The results have shown that there is a good correlation between the large-scale tests and the model scale tests in a scale 1:3. Therefore, the authors decided to perform the tests in a model scale. In particular, the most appropriate scale was found to be 1:5, for practical reasons related to the dimensions of the fire hall used.

When carrying out tests on the model scale, the measured values of the various parameters must be scaled up to a large scale using various physical scaling laws [162]. The technique means that it is possible to investigate fire behaviour in larger stores - i.e., with more and higher racks relatively cheaply.

In most of the tests carried from the authors [150], to simulate the conditions that would be encountered in a large warehouse the walls around the model racks were eliminated. However, walls were used in some of the tests, to investigate the effect of fire gas ventilation on the fire development.

The test program presented in the report, consisted of six different test series:

1) Test series 1: Cone calorimeter tests of the cardboard boxes used in the rack storage tests;
2) Test series 2: Fire spread tests with one small rack;
3) Test series 3: Free burning tests (without ceiling) with four racks;
4) Test series 4: Study of the influence of the size of the enclosure;
5) Test series 5: Fire spread tests with four racks.

In the following paragraph, a description of the test setup and its results will

be presented. It is worth saying that more attention will be paid to the tests used as a validation of the fire model explained in the following chapters.

3.1.1. Test series 1 - Cone calorimeter tests

During these test series the cardboard material of the boxes was tested in a cone calorimeter according to ISO5660 [163] - [164], to obtain information about the flammability and thermal response properties of the material.

Specimens with dimensions equal to 100×100 mm and with a thickness of one layer equal to 6 mm, were tested horizontally and by exposing them to radiation of 50 kW/m^2.

Test Series 1 included 4 tests in total, by varying the thickness of the box and by using more than one layer of the cardboard. Test series 1 allowed evaluation: the time to ignition, time to extinction, heat release rate (HRR), developed energy, smoke production, mass loss rate, total mass loss, and heat of combustion. At the end of these tests, the authors decided that reference in the following tests would be made to the double-thick cardboard box. The results from the tests series 1 are presented in **Figure 3.1**.

Parameter	Test 1.1	Test 1.2	Test 1.3	Test 1.4
Time to ignition (min:s)	0:05	0:07	0:06	0:07
Extinction (min:s)	1:08	1:51	3:39	3:56
Total test time (min:s)	3:08	3:51	5:39	5:56
Max. heat release rate (kW/m^2)	206	247	242	186
Average HRR, 3 min (kW/m^2)	72	125	148	133
Total developed energy (MJ/m^2)	13.0	23.9	34.4	35.6
Max. smoke production rate (m^2/(m^{2}s))	1.1	0.7	1.6	0.9
Average mass loss rate (g/(m^{2}s))	4	6.8	6.7	6.7
Total mass loss (g)	6.4	13.4	19.8	20.4
Effective heat of combustion (MJ/kg)	17.7	15.7	15.3	15.4
Specific smoke production (m^2/kg)	21	17	12	6

Figure 3.1. Results from the cone calorimeter test series 1 carried out by Lönnermark and Ingason [150].

3.1.2. Test series 2 - Fire spread tests with one small rack

The test series 2 consisted of the analysis of the vertical propagation of the fire

within one rack, filled with 4 boxes in an 2x2 configuration, while the flue width (w), the height of the rack (number of levels), and the wall thickness of the boxes (single, double, or triple boxes) were varied.

Six tests were carried out, in total:

- 2.1 test: one rack, 2 × 2 × 4 boxes, single boxes, 50 mm flue width;
- 2.2 test: one rack, 2 × 2 × 4 boxes, double boxes, 50 mm flue width;
- 2.3 test: one rack, 2 × 2 × 4 boxes, triple boxes, 50 mm flue width
- 2.4 test: one rack, 2 × 2 × 4 boxes, double boxes, 75 mm flue width (interrupted)
- 2.5 test: one rack, 2 × 2 × 4 boxes, double boxes, 75 mm flue width
- 2.6 test: one rack, 2 × 2 × 5 boxes, double boxes, 50 mm flue width

The experimental set-up of test series 2 is shown in **Figure 3.2**. In tests 2.1 - 2.3 and 2.5 four levels of boxes were used, and gas temperatures were measured by using thermocouples of type K (0.25mm) in two positions: x2 and x3 (see **Figure 3.2**).

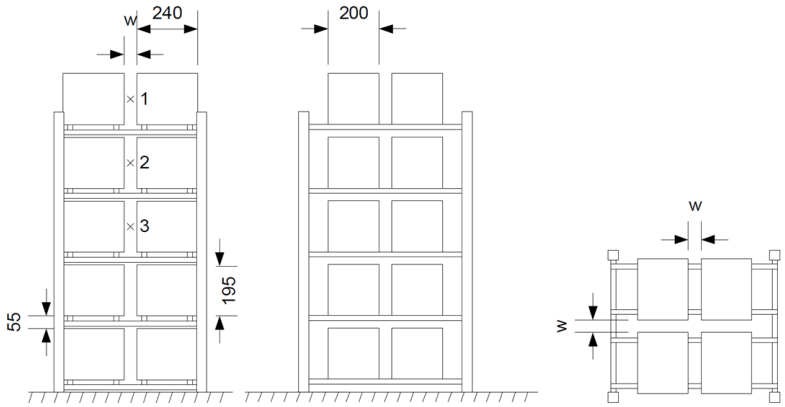

Figure 3.2. Side, front, and top views of the experimental set-up used in test series 2. × represent measurement position. Dimensions in mm [150].

In tests 2.6 five levels of boxes were used and gas temperatures were measured in positions: x 1 and x 2 (see **Figure 3.2**). In addition, in each test the heat release rate (HRR) was measured by oxygen calorimetry (ISO 9705) [165]. The fire gases were collected by a hood and guided through a pipe where the gas

temperature and gas flow were measured and the concentrations of oxygen, carbon dioxide and carbon monoxide were analysed.

The test series 2 results are showed in **Figure 3.3**

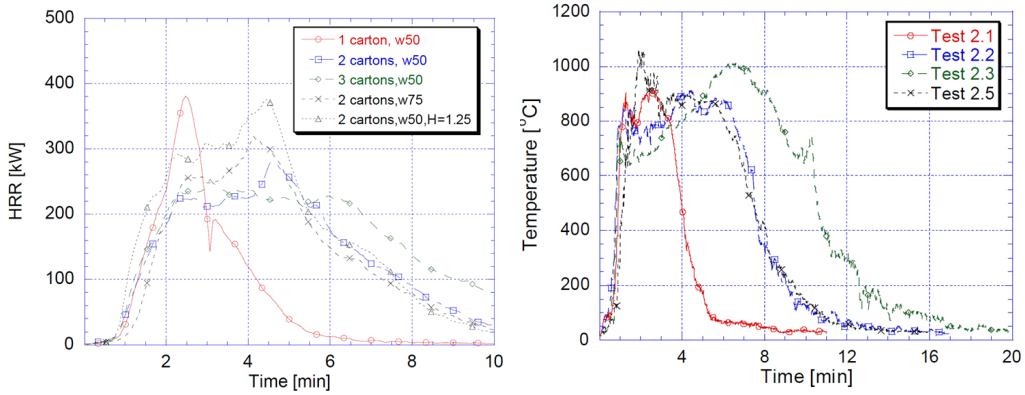

(a) (b)

Figure 3.3. Comparison between test series 2 results: (a) in terms of temperature (position 2); (b) in terms of HRR (position 3) [150].

By analysing the test results, it is possible to see how the variation in the wall thickness affected the results significantly. In particular, the test with single boxes (Test 2.1) had a fast increase in HRR and a higher HRR maximum. The reason for this behaviour is that the flames, burned through the box wall, more easily leading to an increased exposed surface area. The low amount of fuel made the material burn out relatively quickly.

The test with double and triple boxes (Test 2.2 and 2.3, respectively) burned similarly at the beginning of each test. The increase in flue width (w) from 50 mm to 75 mm slowed the increase in HRR, indeed test 2.5, with the flue width 75 mm, had the slowest increase in HRR of all the tests in series 2. The maximum HRR was, however, somewhat higher than the corresponding test with a flue width of 50 mm (Test 2.2). The fire behaviour of the case with five levels of double boxes and a flue width (w) of 50 mm best suited the purposes of the tests with large racks and therefore it was decided to use dimensions corresponding to this case in all the other test series.

3.1.3. Test series 3 - Free burning tests (without ceiling) with four racks

The aim of test series 3, was to study the fire spread within and between the racks storage without a ceiling, for this reason four rack storage systems were placed next to each other with a distance, between the racks, equal to 480 mm corresponding to 2.4 m in real scale, (see **Figure 3.4**).

However, the main aim of these test series 3 was to measure the HRR from the experimental set-up with four racks beneath the industry calorimeter, since with the ceiling that will be added for the test series 5 (explained in the following §3.15) the HRR could no longer be measured accurately.

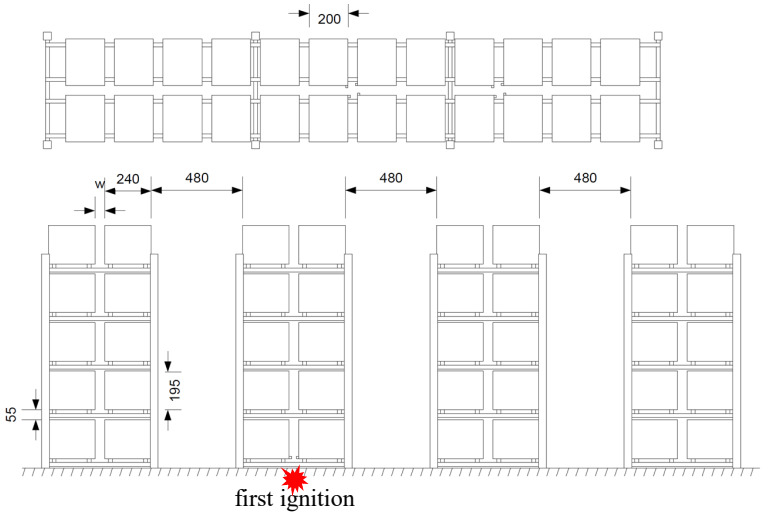

Figure 3.4. Top view and side view of the experimental set-up used in test series 3. Dimensions are in mm [150].

The HRR was measured according to the same principles as in test series 2, however, in this case the test set-up was placed under the SP Industry calorimeter [166]-[167]. In addition to the HRR, the heat flux towards the commodity surface in rack 1 was measured by a heat flux meter, to register the total heat flux before, and at the time of, the fire spread. The heat flux meter (Medtherm prod no 1211864) was placed in the centre flue of the fifth level of cartons in Rack 1.

Two different tests were carried out for this test series (3.1 and 3.2), by varying the position for ignition. For both tests, the ignition took place at the bottom of rack 2 (see **Figure 3.4**), but in test 3.1 the ignition sources were placed in the canter of the rack, while in test 3.2 the ignition sources were placed in the third flue from the right. The ignition sources consisted of pieces of fibre board (10 mm × 10 mm × 12 mm) soaked with 1 mL heptane and wrapped in a piece of polyethylene. Each rack was characterized by five levels, for each level there were 24 boxes arranged in 12 rows and two columns, at 50 mm from each other. Rack 2, where the ignition took placed, contained double boxes while racks 1,3, and 4, contained single boxes.

The test series 3 results showed that the position of ignition affects the development of the fire and the HRR curve (see **Figure 3.5**). Indeed, the initial fire spread is similar in the two tests, but a higher maximum HRR was reached when the ignition was in the centre of the rack (test 3.1). On the other hand, test 3.2 (with the ignition sources placed in the third flue from the right) has a larger HRR curve which led to a higher total release of energy.

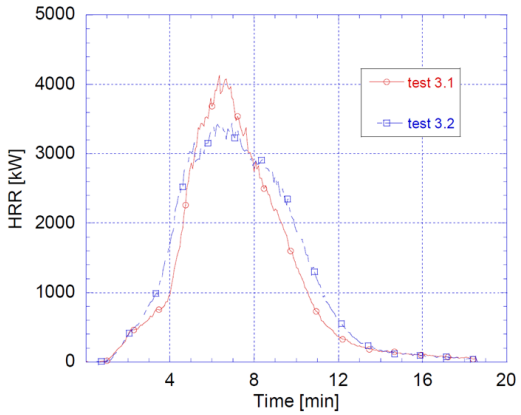

Figure 3.5. Comparison between test series 3 results in terms of HRR [1].

3.1.4. Test series 4 - Study of the influence of the size of the enclosure

The aim of test series 4, was to study the effect of the enclosure and of the

openings on the fire development. These test series 4 were different compared to the other ones because they consisted of a fire test with pine wood cribs used as fuel. Each of these wood cribs was built of 50 pieces with dimensions 21 mm × 21 mm × 300 mm, with 5 pieces in each of 10 layers. This means that the final box has dimensions 300x300mm with a total height equal to 210 mm.

The influence of the enclosure on the fire development was studied by varying the length of an enclosure while the width was 1 m, and the height was 0.925 m in each test. Three different lengths of the enclosure were used: 1 m, 1.7 m, and 2.4 m, respectively. In most of the tests the opening (0.3 m × 0.3 m) was placed on one of the long sides, but in one case with the largest volume the opening was placed on one of the short sides to study the influence of the distance from the fire to the opening.

Within test series 4, five different tests were performed:

- 4.1 test: Wood crib, free burning on a scale;
- 4.2 test: Wood crib burning inside enclosure, 1 m × 1 m × 0.925 m;
- 4.3 test: Wood crib burning inside enclosure, 1 m × 1.7 m × 0.925 m;
- 4.4 test: Wood crib burning inside enclosure, 1 m × 2.4 m × 0.925 m;
- 4.5 test: Wood crib burning inside enclosure, 1 m × 2.4 m × 0.925 m; door opening on the short side.

The scale of these tests was not defined, but the authors gave a reasonable idea of the scale, by assuming that the ceiling height of most industrial and warehouse buildings is in the range of 10 m to 30 m, they estimated that the scale was in the order of 1:10 to 1:30. This means that the size of the opening in large scale would be 3 m by 3 m up to 9 m by 9 m. This would correspond to an opening area of 9 m^2 up to 81 m^2. The floor area (volume) of the building would vary from 100 m^2 (925 m^3) up to 240 m^2 (2220 m^3) in scale 1:10 and from 900 m^2 (24775 m^3) up to 2160 m^2 (59940 m^3) in scale 1:30.

The HRR was measured in the same way as in test series 2, such as by oxygen calorimetry (ISO 9705) [165]. The main measurements were made by using five thermocouples, one was placed in the opening and four in a thermocouple tree. The thermocouple in the opening was placed 5 cm below the soffit of the opening, on the vertical centreline. The thermocouples in the tree were positioned 5

cm, 10 cm, 20 cm, and 50 cm, below the ceiling, while the entire thermocouple tree was placed 10 cm from each wall in one of the front corners in the enclosure case with the dimensions 1 m × 1 m × 0.925 m, and it was left in the same position when the short walls were moved outwards.

Figure 3.6 shows the setup of these test series 4, where the dashed lines indicate different positions of the short walls (dimensions in mm). The mark (×) indicates position of thermocouple; the mark over a line represents a thermocouple in the opening (different positions of the opening were used).

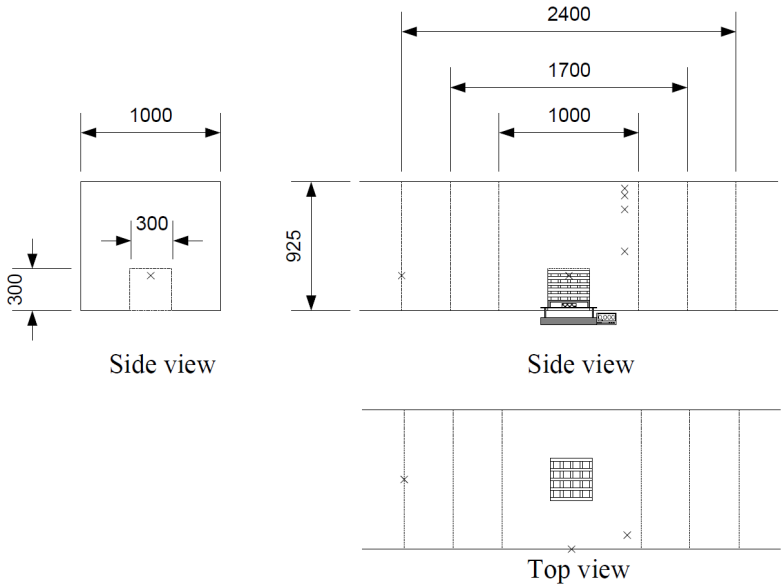

Figure 3.6. Side and top views of the experimental set-up of the test series 4 [150].

Figure 3.7 shows the comparison of heat release rates in test series 4. The results showed that the HRR is affected by the enclosure, indeed there was a large difference between the free burning wood crib tests (4.1 test) and the tests with wood cribs in an enclosure (4.2 - 4.5 tests). The size of the enclosure affected the HRR, but the differences decreased when the enclosure size increased.

In particular, the HRR in the free burning case (test 4.1) is much higher than the HRRs for the cases where the wood crib was place inside an enclosure. The

size of the enclosure also affected the results. The case with the smallest enclosure (1 m × 1 m × 0.925 m), i.e., 4.2 test, reached the lowest maximum HRR max. For the other cases with larger enclosures the difference in maximum HRR was rather small.

There is also a difference in burning rate. The case with the smallest volume corresponds to the slowest burning rate, but there was almost no difference between the cases with a length of the enclosure of 1.7 m (4.3 test) and 2.4 m (4.4 test), respectively. The case with the largest volume had the slowest fire development. The position of the door opening had only a small influence on the results in this set-up. This difference is probably due to the difference in fill-up time for the smoke in the enclosure and therefore a difference in time before the smoke exits the enclosure and reaches the measurement station for HRR.

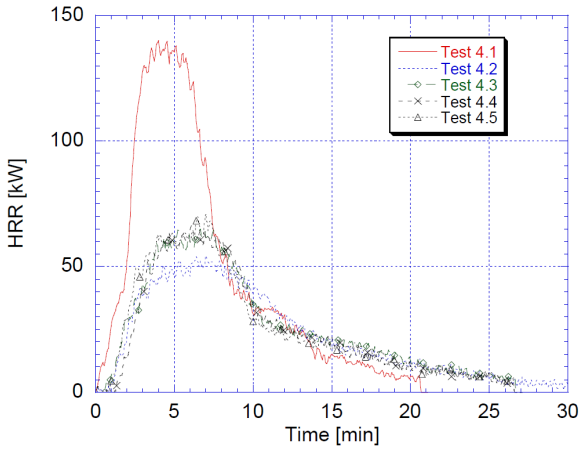

Figure 3.7. Comparison of heat release rates in test series 4 [150].

Figure 3.8 shows the results for test series 4 in terms of temperatures measured from each thermocouple. The same considerations can be made, that was a large difference between the free burning wood crib tests and the tests with wood cribs in an enclosure. The size of the enclosure affected the HRR, but the differences decreased when the enclosure size increased.

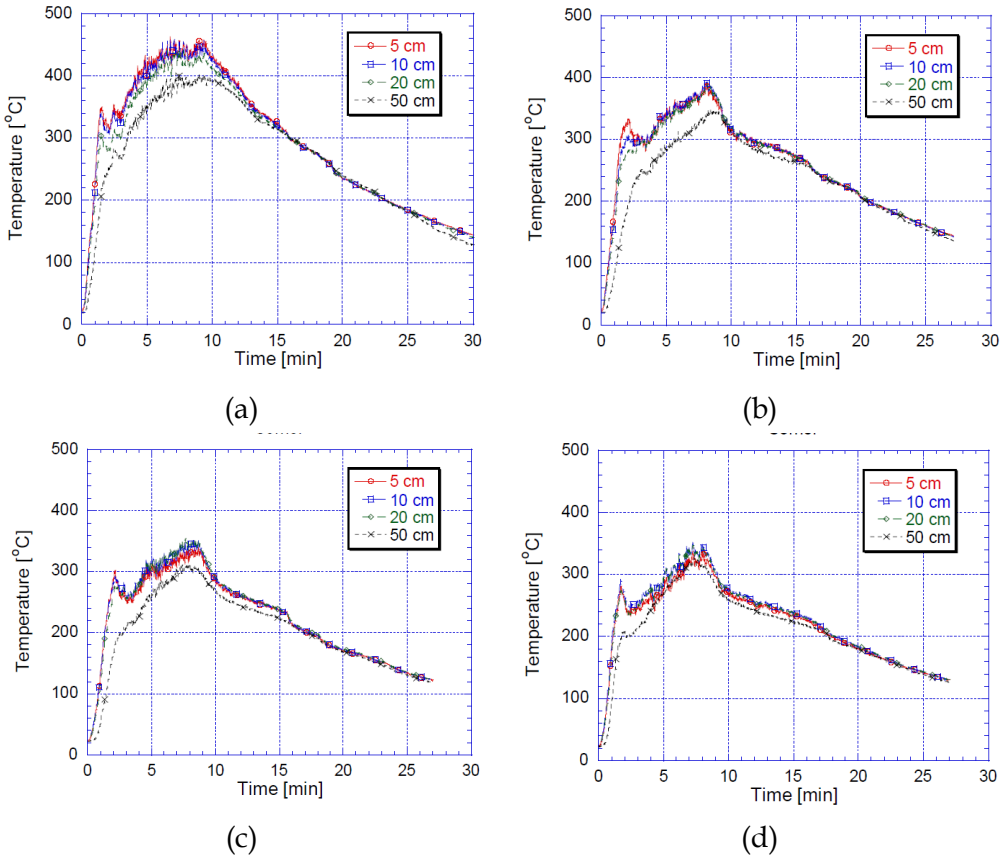

Figure 3.8. Comparison of heat release rates in test series 4: 4.2 test (a), 4.3 test (b), 4.4 test (c), 4.5 test (d) [150].

3.1.5. Test series 5 - Fire spread tests with four racks.

In test series 5, the same set-up of the test series 3, with four racks, was placed under a ceiling to study the effect of the distance between the commodities and the ceiling, the slope of the ceiling, and the presence of beams under the ceiling on the results. In particular, the height, y, between the top of the commodities and the ceiling, and the slope of the ceiling were varied. In some of the tests 180 mm deep beams were installed beneath the ceiling. The beams were placed with 1.2 m between them (see **Figure 3.9**a). In two of the tests, walls were raised to construct a room with a door opening (0.6 m × 0.6 m) at the centre of the front

wall. In one of the two room tests four ventilation openings (0.24 m × 0.48 m) were opened near the corners of the ceiling.

In this test series, two main results were investigated, such as the time for fire spread from one rack to the next and the gas temperature and flow rate near the ceiling. For this reason, temperatures were the main measurement with thermocouples placed in 24 different positions beneath the ceiling (see **Figure 3.9**b) while a circular plate thermometer with a diameter equal to 113 mm, was placed level with the ceiling, in position 25.

For the test series 5, each of the four racks, were filled with 2 × 12 × 5 boxes with flue width (w) of 50 mm, with single wall thickness of the boxes in rack 1,3 and 4, double wall thickness of the boxes in rack 2.

In each test the ignition took place at the bottom of the centre flue in rack 2.

Within test series 5, nine different tests were performed. In particular:

- 5.1 test: 1.2 m distance between ceiling and top of boxes;
- 5.2 test: 0.2 m distance between ceiling and top of boxes;
- 5.3 test: 0.6 m distance between ceiling and top of boxes;
- 5.4 test: 0.6 m distance between ceiling and top of boxes, four beams added beneath the ceiling;
- 5.5 test: 0.6 m distance between ceiling and top of boxes. Four beams added beneath the ceiling. The ceiling was sloped.
- 5.6 test: it was a retesting of test 5.3; because the rack storages were in test 5.3 not positioned exactly the same way as in the rest of the tests;
- 5.7 test: 0.6 m distance between ceiling and top of boxes. Sloped ceiling. No beams;
- 5.8 test: 0.6 m distance between ceiling and top of boxes. Walls with one opening 0.6 m × 0.6 m.
- 5.9 test: 0.6 m distance between ceiling and top of boxes. Walls with one opening 0.6 m × 0.6 m and four fire ventilation openings in the ceiling (each 0.24 m × 0.48 m).

As said before, during this test series 5, two main results were investigated, such as the time for fire spread from one rack to the next and the gas temperature and flow rate near the ceiling.

During each test, the process of fire spread was the same, i.e., the fire started in rack 2, and after it spread first to racks 1 and 3 and later to rack 4.

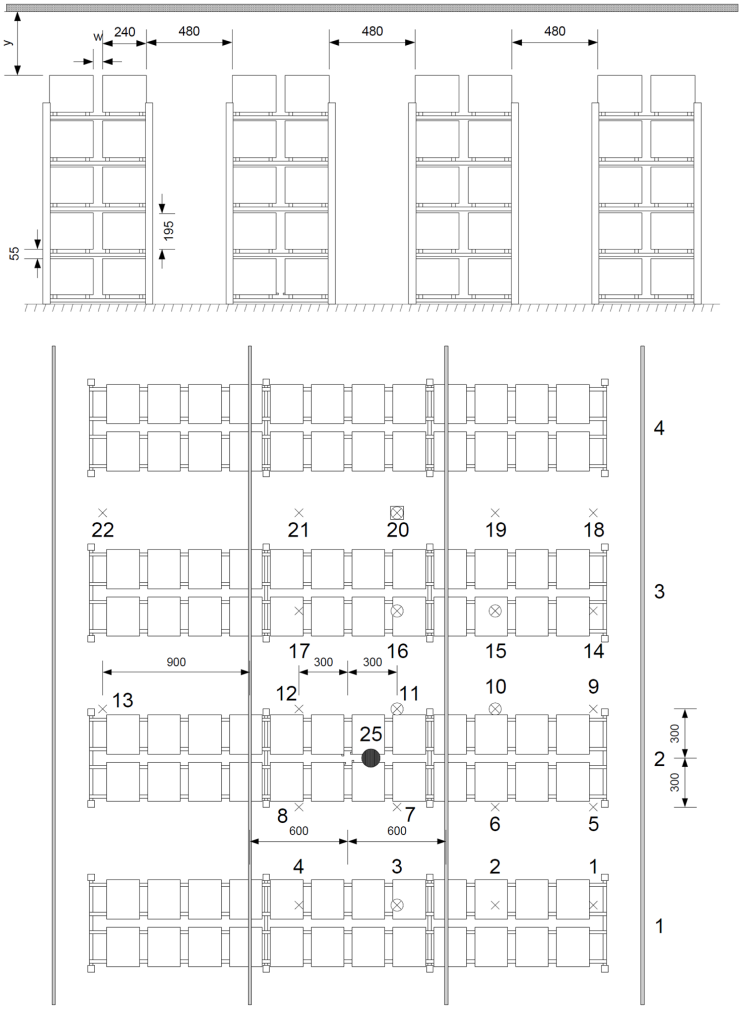

Figure 3.9. Side view of the experimental set-up of the test series 5 (a), plan view with thermocouples positions (b) [150].

The times when the fire spread to the different racks were registered and listed in **Figure 3.10**a together with the time for the flame to reach the ceiling. There was a difference in flame spread within rack 2 (the rack where ignition

took place), which means that the time for the flames to reach the ceiling varied between the tests.

Figure 3.10b shows the time for the flame to reach the ceiling and flame spread between racks, but in this case, the time when the flames reach the top of the commodities in rack 2 is subtracted from the times to fire spread, hence these spread times are starting from the time the flame reaches the top of commodities in rack 2.

Test id	Flames reach ceiling [min:s]	Fire spread to rack 1 [min:s]	Fire spread to rack 3 [min:s]	Fire spread to rack 4 [min:s]
5.1	1:15	3:39	3:37	4:50
5.2	0:57	2:40	2:38	2:58
5.3	0:49	2:15	2:17	2:50
5.4	1:03	2:22	2:17	2:57
5.5	1:12	2:31	2:24	2:56
5.6	1:11	2:24	2:24	2:54
5.7	1:09	2:34	2:32	3:04
5.8	1:30	3:15	3:03	3:38
5.9	1:03	2:26	2:24	2:50

(a)

Test id	Flames reach ceiling [min:s]	Fire spread to rack 1 [min:s]	Fire spread to rack 3 [min:s]	Fire spread to rack 4 [min:s]
5.1	0:15	2:39	2:37	3:50
5.2	0:02	1:45	1:43	2:03
5.3	0:09	1:35	1:37	2:10
5.4	0:08	1:27	1:22	2:02
5.5	0:07	1:25	1:19	1:51
5.6	0:09	1:22	1:22	1:52
5.7	0:05	1:30	1:28	2:00
5.8	0:07	1:52	1:40	2:15
5.9	0:08	1:31	1:29	1:55

(b)

Figure 3.10. Time to flame reaching the ceiling and spread between racks (a), times depurated with times of the flame to reach the top of the commodities in rack 2 (b).

Figure 3.11 shows the gas temperature in position 11 (3 cm below the ceiling) for three different distances between the commodities and the ceiling, test 5.1, 5.2 and 5.3 replaced by 5.6. The results show that the ceiling distance affects the fire development. The fastest development is obtained for the case with a distance equal to 0.2 m, i.e., the shortest distance tested. However, after a while the increase is stopped, and a period of relatively constant temperature follows. During this period the temperatures for the case with a distance of 0.6 m are higher, while at the end of the test the temperatures in the 0.2 m case are the highest

again. Temperatures in 1.2 m case are slower than the other two cases but reach approximately the same maximum temperatures as the 0.2 m case. At the end of the tests the temperatures for the 0.6 m case and the 1.2 m case are approximately the same.

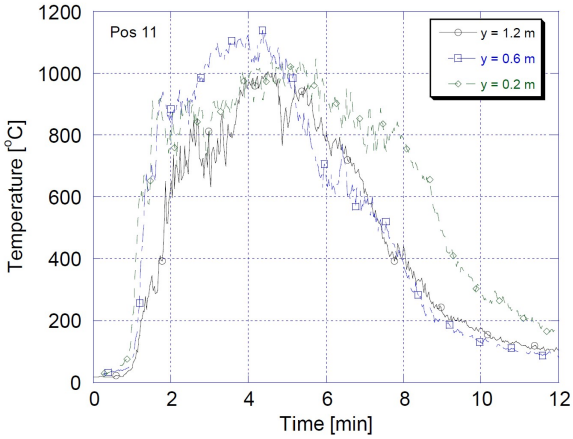

Figure 3.11. Comparison between gas temperature measurements in position 11 with different distances (y) between the top of the commodities and the ceiling [150].

The differences in fire spread between tests with different distance to the ceiling can also be seen in **Figure 3.10**b where the time to fire spread to the other racks is much longer in the 1.2 m case (Test 5.1). The 0.6 m case (Test 5.6) obtains the fastest fire spread. The fire spread in the 0.2 m case (Test 5.2) is approximately 20 s slower than in the 0.6 m case.

Figure 3.12 shows the gas temperature in position 20, i.e., 3 cm below the ceiling, for four different cases: sloping and non-sloping ceiling, and with or without beams.

The beams collect the hot smoke and increase the temperature, at least in the beginning and in the later part of the tests. The effect of the slope is not as large but could still be seen, increasing the temperature in position 20.

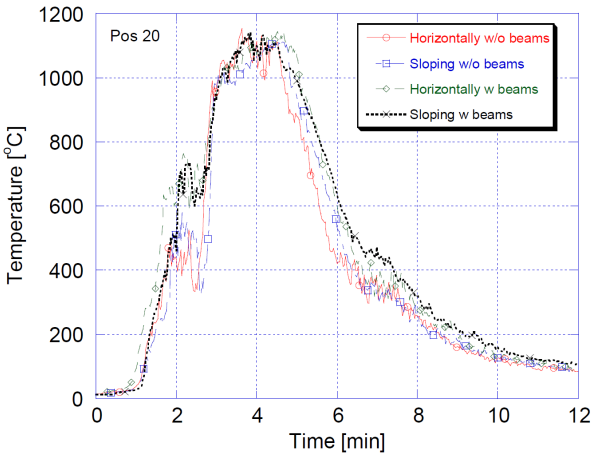

Figure 3.12. Comparison between temperatures in position 20 with different slope of the ceiling and with and without beams, respectively [150].

One aim of the tests was to study how the estimated time to activation of a sprinkler would be affected by variation of different conditions, e.g., the height of the ceiling, the slope of the ceiling, and, most importantly, whether beams are present at the ceiling or not. To simulate sprinkler bulbs, special metal cylinders with thermocouples in the centre were designed. The cylinders were 14 mm long and 4 mm in diameter. At one of the ends of the cylinder a hole (1.3 mm in diameter) was drilled to mount a thermocouple inside the cylinder. At the beginning of the test series the material in the cylinders was brass, but because of the high temperature on the cylinders a majority of the cylinders were replaced by steel cylinders after test 5.2.

In **Figure 3.13** the times to activation of sprinklers at different positions are presented. For each position two numbers are given. These correspond to the cases without (left) and with (right) beams, respectively. It is worth saying that the sprinkler bulbs were only simulated, but no real sprinkler was activated, i.e., no water was applied.

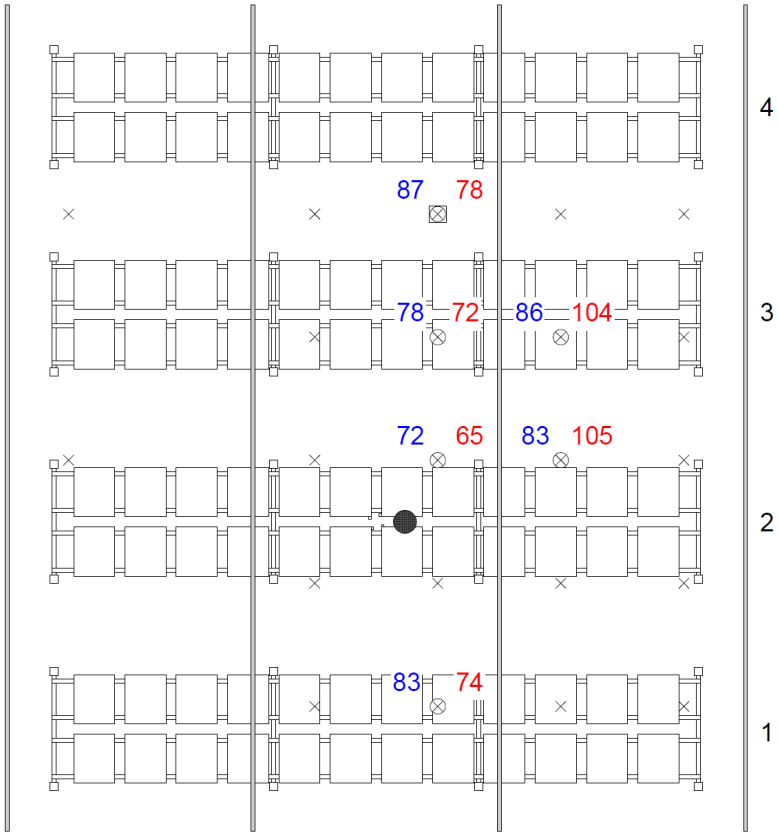

Figure 3.13. Comparison of times to activation of sprinkler without (left = blue) and with (right = red) beams, respectively [1].

For the results it is possible to see how beams affect the time to activation of sprinklers. The slope of the ceiling has some effects but was not seen to be significant.

The effect of the enclosure was also seen in Test 5.8 results. **Figure 3.14**a shows the gas temperature recorded from each thermocouple and metal cylinders placed in position 20 at four different heights: 30 mm, 60 mm, 90 mm, from the ceiling. The results show that in this case the fire development and spread were significantly slower than in the corresponding case without walls. The gas temperature near the ceiling was approximately 400 °C during a large part of the test. It is in the beginning of the test and later, approximately 29 minutes after ignition

(when the fire spreads to rack 4), that the temperatures are higher.

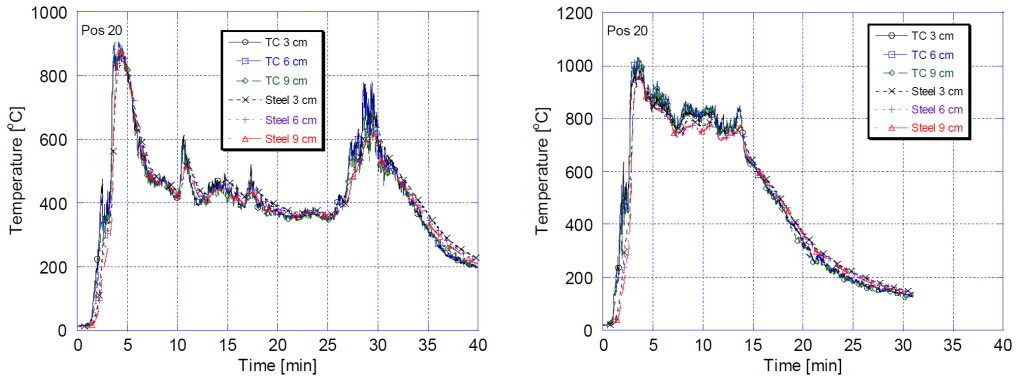

Figure 3.14. Comparison between temperatures recorded from, for each thermocouple and metal cylinders placed in position 20 at four different heights: 30 mm, 60 mm, 90 mm, from the ceiling [150], for the test 5.8 (a) and test 5.9 (b).

In Test 5.9, fire ventilation was opened when the thermocouples inside the metal cylinders at the fire ventilation had reached 94 °C. This made a significant difference for the fire development.

Figure 3.14b shows the gas temperature recorded from each thermocouple and metal cylinders placed in position 20 at four different heights: 30 mm, 60 mm, 90 mm, from the ceiling. The gas temperatures near the ceiling were higher and the fire developed and spread in a similar way as the corresponding tests without walls (and without fire ventilation).

In conclusion from the results of test series 5 it is possible to affirm that the ceiling height had a significant influence on the fire spread. The case with the longest distance to the ceiling i.e., 1.2 m case (Test 5.1) had the slowest fire spread. This can be explained by the lower radiation from the flames and gases near the ceiling towards the other racks, which is an important process for the fire spread. For the same reason the case with the lowest height i.e., 0.2 m case (Test 5.2) should have had the fastest fire spread, but the results shows that this was the case of 0.6 m (Test 5.6). The explanation for thus is that, in the case with the short distance between the commodities and the ceiling, the fresh air does not easily reach the combustion zone. Instead, the flames are embedded in smoke, which

means that the combustion conditions are poorer.

There seems to be an optimum height between the stored goods and the ceiling (1 metres to 6 metres). If the height is higher the radiation towards the commodities is decreased. If the height is lower the combustion conditions change and decreases the combustion efficiency.

3.2. Simulation of the experimental tests

The tests carried out by Lönnermark and Ingason [150] and described in the previous paragraphs have been simulated numerically by using the software CFAST [112] developed by NIST. In this way, it was possible to compare the experimental data with the numerical program, verify the correspondence, define the differences and the reasons that justify them, and finally to model, based on the collected information a model that allows studying the vertical propagation of localized fires in a multi-depth ARSW.

3.2.1. CFAST – Consolidated Fire and Smoke Transport

CFAST is a two-zone fire model that predicts the thermal environment caused by a fire within a compartmented structure, and that allows the modelling of different compartments that can communicate with each other. Each compartment is divided into an upper and lower gas layer, indeed the term zone in the fire model refers to the layers being modelled. The fire drives combustion products from the lower to the upper layer via the plume (see **Figure 2.23)**. The temperature within each layer is uniform, and its evolution in time is described by a set of ordinary differential equations derived from the fundamental laws of mass and energy conservation. Because the governing equations are relatively simple, CFAST simulations typically require a few tens of seconds of CPU time on typical personal computers.

3.2.1.1. Input data required for the zone model.

All the data required to run the CFAST model reside in a single input file that the user generates.

The file consists of the following information:

- material properties (e.g., thermal conductivity, specific heat, density, thickness, heat of combustion)
- compartment dimensions (height, width, length)
- construction materials of the compartment (e.g., concrete, gypsum)
- dimensions and positions of horizontal and vertical flow opening such as doors, windows, and vents.
- mechanical ventilation specification
- fire properties (e.g., heat release rate, lower oxygen limit, and species production rates as a function of time)
- sprinkler and detector specification
- positions, sizes, and characteristics of targets
- specifications for visual output from the model

3.2.1.2.The basic transport equation

The equations used to model pressure, layer height and temperatures in CFAST take the form of an initial value problem for a system of ordinary differential equations. These equations are derived from the principles of conservation of mass and energy using the ideal gas law as an equation of state to relate temperature and density. They predict the evolution in time of the compartment pressure (at the floor), upper layer volume, and layer temperatures due to the net gain or loss of mass and energy in these layers.

The primary assumption of a zone model is that properties such as temperature can be approximated throughout a control volume by a representative average value. Many formulations based upon these assumptions can be derived [110]. Though equivalent mathematically, these formulations differ in their numerical solution.

The exchange of mass and energy or heat between zones is due to physical phenomena such as fire plumes, natural and forced ventilation, convective and radiative heat transfer, and so on. For example, a vent exchanges mass and heat between zones in connected rooms, a fire plume typically adds heat to the upper layer and transfers entrained mass and heat from the lower to the upper layer, and convection transfers heat from the gas layers to the surrounding walls.

The momentum within any one zone is assumed to be zero. Momentum exchange between zones in adjacent compartments is accounted for in terms of horizontal or vent flow equations (Bernoulli's law).

As said before each compartment is divided into two control volumes or zones, a relatively hot upper layer, and a relatively cool lower layer, as illustrated in **Figure 2.23**. The gas temperature and density are assumed constant in each layer. The compartment is assumed to have a single value of pressure, P and all thermodynamic parameters are assumed to be constant.

The mass conservation equation simply asserts that the rate of change of the mass of layer i is equal to the sum of mass source terms, $\dot{m}_i$:

$$\frac{dm_i}{dt} = \dot{m}_i \tag{3.1}$$

Mass source terms include plume mass entrainment and supply/exhaust ventilation. Next, the firs law of thermodynamics states that the rate of change in the layer's internal energy, $c_v m_i T_i$ is equal to the sum of heat source terms $\dot{q}_\iota$, minus the work associated with expansion or contraction of the layer $P\frac{dV_i}{dt}$:

$$\frac{\mathrm{d}(\mathrm{c_v m_i T_i})}{\mathrm{dt}} = \dot{\mathrm{q}}_\iota - \mathrm{P}\frac{\mathrm{dV_i}}{\mathrm{dt}} \tag{3.2}$$

Included in $\dot{q}_\iota$ are the fire's heat release rate, convective losses to walls, and radiation exchange.

The layer's temperature, mass and volume are related to the compartment pressure by the ideal gas law:

$$PV_i = m_i R T_i \tag{3.3}$$

A system of ordinary differential equations for the compartment pressure, upper layer volume, and upper- and lower-layer temperature can be derived using **Eqs. 3.1–3.2**, for details see [112]:

$$\frac{dP}{dt} = \frac{\gamma - 1}{V}(\dot{q_1} + \dot{q_u}) \tag{3.4}$$

$$\frac{dV_u}{dt} = \frac{1}{P\gamma}\left((\gamma - 1)\dot{q_u} - V_u \frac{dP}{dt}\right) \tag{3.5}$$

$$\frac{dT_u}{dt} = \frac{1}{c_p m_u}\left(\dot{q_u} - c_p \dot{m}_u T_u + V_u \frac{dP}{dt}\right) \tag{3.6}$$

$$\frac{dT_1}{dt} = \frac{1}{c_p m_1}\left(\dot{q_1} - c_p \dot{m}_1 T_1 + V_1 \frac{dP}{dt}\right) \tag{3.7}$$

An algebraic equation for each wall surface temperature (ceiling, upper wall, lower wall, and floor) is also solved:

$$\dot{q}'' + k\frac{\partial \boldsymbol{T}_w(0,t)}{\partial x} = 0 \tag{3.8}$$

Where:

$\frac{\partial T_w(0,t)}{\partial x}$ is the temperature gradient at the wall surface.

$\dot{q}''$ is the net radiative and convective heat flux from the adjacent gas layer.

for brevity the temperature wall profiles are referred to collectively as $T_w(x,t)$. The (x; t) spatial coordinate x refers to the depth inside the wall; x=0 is the wall surface.

The temperature gradient in **Eq. 3.8** is evaluated by advancing a known temperature profile from t_{old} to t using the heat conduction equation:

$$\frac{\partial \boldsymbol{T}_w}{\partial t} = \frac{k}{c\rho}\frac{\partial^2 \boldsymbol{T}_w}{\partial x^2} \tag{3.9}$$

with a constant temperature boundary condition:

$$\boldsymbol{T}_w(0,t) = T_w \tag{3.10}$$

Where ρ, c and *k* are the density, specific heat, and thermal conductivity of the wall material.

In order to solve the zone fire modelling equations CFAST uses the differential/algebraic solver DASSL [19, 20] to solve the differential equations **Eqs. 3.4** through **Eq. 3.7** and the algebraic equation (once it is discretized) **Eq. 3.8** for P, T_u, V_u, T_l and T_w.

3.2.1.3. *Fire properties in CFAST*

Fires in CFAST are specified by the user in terms of a time-dependent heat release rate (HRR), an effective fuel molecule, and the yields of the products of incomplete combustion like soot and CO.

Fires can be specified in multiple compartments and are treated as totally separate entities, with no interaction of the plumes. These fires are generally referred to as "objects" and can be ignited at a prescribed time, temperature, or heat flux.

CFAST does not include a pyrolysis model to predict, as opposed to specify, the growth and spread of the fire. Rather, the transient pyrolysis rates for each fire are prescribed by the user.

The HRR of the fire is specified by the user, but it may be constrained by the availability of oxygen in the compartment. The combustion of a hydrocarbon fuel is described by the following single step reaction:

$$C_{nc}H_{nH}O_{nO}N_{nN}Cl_{n_{Cl}} + v_{o_2}O_2 \rightarrow v_{co_2}CO_2 + v_{H_2O}CO_2 + v_{CO}CO + \\ + v_s Soot + v_{HCl}HCl + v_{HCN}HCN + v_{N_2}N_2 \quad (3.11)$$

The user must specify the composition of the fuel molecule and the yields of soot and CO, y_S and y_{CO}, which are the mass of CO or soot emitted per unit mass of fuel burned and which are related to their stoichiometric coefficients as follows:

$$v_s = \frac{M_F}{M_S} y_s \quad (3.12)$$

$$v_{CO} = \frac{M_F}{M_{CO}} y_{CO} \quad (3.13)$$

$$v_{HCN} = \min\left(n_N, \frac{M_F}{M_{HCN}} y_{HCN}\right) \quad (3.14)$$

As fuel and oxygen are consumed, heat is released, and various products of combustion are formed. The heat is released as radiation and convective heat.

3.2.1.4. *Ventilation in CFAST*

CFAST models three types of vent flow: natural flow through vertical vents (such

as doors or windows), natural flow through horizontal vents (such as ceiling holes or hatches) and forced flow via mechanical ventilation. Forced flow can occur through either vertical or horizontal vents.

3.2.2. Simulation of the test series 4

The first test series that was modelled in CFAST was test series 4, for several reasons; firstly among all the experimental tests carried out by the authors [150] it is the only series in which the dimensions of the compartments are defined, (except for the 4.1 test which was not modelled), but also for the higher availability of input data and of results, such as temperature curves recorded by thermocouples and provided by the final annexes of the paper.

Within test series 4, five different tests were performed, all the datils are listed in §3.1.4. In order to create the input file for the CFAST models of each test, first the properties of the materials were defined, as equal for all four tests. Three materials were defined, and listed in **Table 3.1**:

Table 3.1 Material properties for test series 4

	thermal conductivity [kW/m°C]	**specific heat** [kJ/kg°C]	**density** [kg/m^3]	**thickness** [m]	**emissivity** [-]
steel	0.005	0.65	7800	0.004	0.7
plasterboard	0.0025	1	810	0.1	0.8
concrete	0.00125	1	2400	0.3	0.8

The compartment dimensions for each test were provided by authors in [150]. Regarding the construction materials of the compartment, the ceiling and the floor were considered made of concrete, while the walls were considered made of plasterboard. The ventilation condition was defined like the test setup i.e., by a square wall vent with dimensions equal to (0.30 m x 0.3 m) placed in the middle of one of the long sides, while for test 4.5, with the largest volume, the opening was moved on one of the short sides, on the one that, is placed at 1.20 m from the fire.

In CFAST models, objects referred to as "targets," may be added to any compartment to represent measurement devices. Targets absorb thermal radiation from the fire, walls, and hot gas layer, but targets do not affect the fire simulation. In each test a series of steel targets were placed along the same vertical, at different distances from the ceiling, near the corner of the first compartment. It is worth saying that despite the dimensions of the compartment having been changed by passing from test 4.2 to test 4.3 to test 4.4 and 4.5, the position of the thermocouples has never changed, leaving, in this way, their mutual position unchanged.

The compartments so defined are shown in the following **Figure 3.15**.

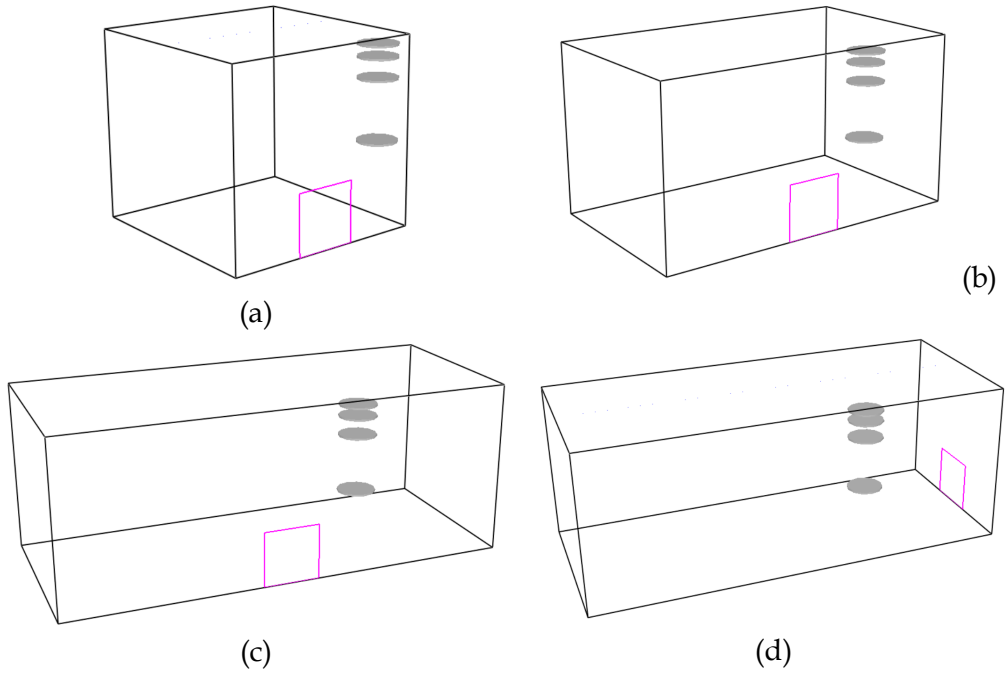

Figure 3.15. CFAST model in SMOKWIEV environment of test 4.2 (a), test 4.3 (b), test 4.4 (c) and test 4.5 (d).

To define the input fire in CFAST the first step is the definition of the Heat Release Rate (HRR) curve, this one was evaluated for points starting from the HRR output curve provided by the authors in [150], in this way it was possible to obtain the HRR input curve for the CFAST's models, which are shown in the

following **Figure 3.16**a, c, and **Figure 3.17**a,c.

Regarding the determination of some materials properties and fire properties required by the program, the *SFPE Handbook of Fire Protection Engineering* [120] was consulted indeed this one in chapter 1-5 provide the thermochemistry of the most common materials, and as a consequence it was possible to find that the heat of combustion of pine wood can be considered equal to 19.4 kJ/g.

In chapter 3-4, instead, the values of CO Yield and Soot Yield are provided. In particular, the Soot Yield (y_S), in lack of specific value for pine wood, was considered equal to 0.015 g/g which is the common value for both wood (red oak) and wood (Hemlock) conifer wood. While the CO Yield (y_{CO}) was equal to 0.005 g/g for pine wood.

No information related to the parameters of HCN Yield and TS Yield has been found in the literature and therefore they have been fixed zero in every analysis carried out. Regarding the stoichiometry of the material, the chemical structure of wood was considered equal to C6H10O6 as indicated in *SFPE Handbook of Fire Protection Engineering* [120].

Finally, to complete the table related to the definition of the fire in CFAST, it was necessary to calculate the fire area $A_{fi}(t)$, because the heat release rate is linked to the fire area. The fire area is the burning area of fuel, in real fires, it is usually varying with time, in some cases (ex. pool fire tests), the fire area can be constant.

The fire area Afi(t) can be defined function of time:

$$A_{fi}(t) = A_{fi,max} \frac{RHR(t)}{RHR_{max}} \tag{3.15}$$

Where, the maximum fire area $A_{fi,max}$ in a compartment is the floor area on which combustible is present. In most case the maximum fire area is equal to the floor area. The hypothesis is made that the maximum value of the fire area arrives when the rate of heat release is maximum [114].

Once the models of the four tests were defined, by running the analyses CFAST provided the temperature curves recorded by the four thermocouples.

For each test, it was noted that the temperature of the thermocouple closest to the ceiling was significantly higher than the temperatures recorded by the other

thermocouples that were in the cold zone, they recorded temperatures equal instant by instant. To compare the numerical results with the experimental ones the curve representing the average of the four thermocouples was considered.

The following figures represent, for each test: the comparison between the experimental HRR curve and its reconstruction, the comparison between the experimental temperatures and the numerical ones calculated with CFAST that are the ones recorded by the thermocouples at different heights, and their mean value.

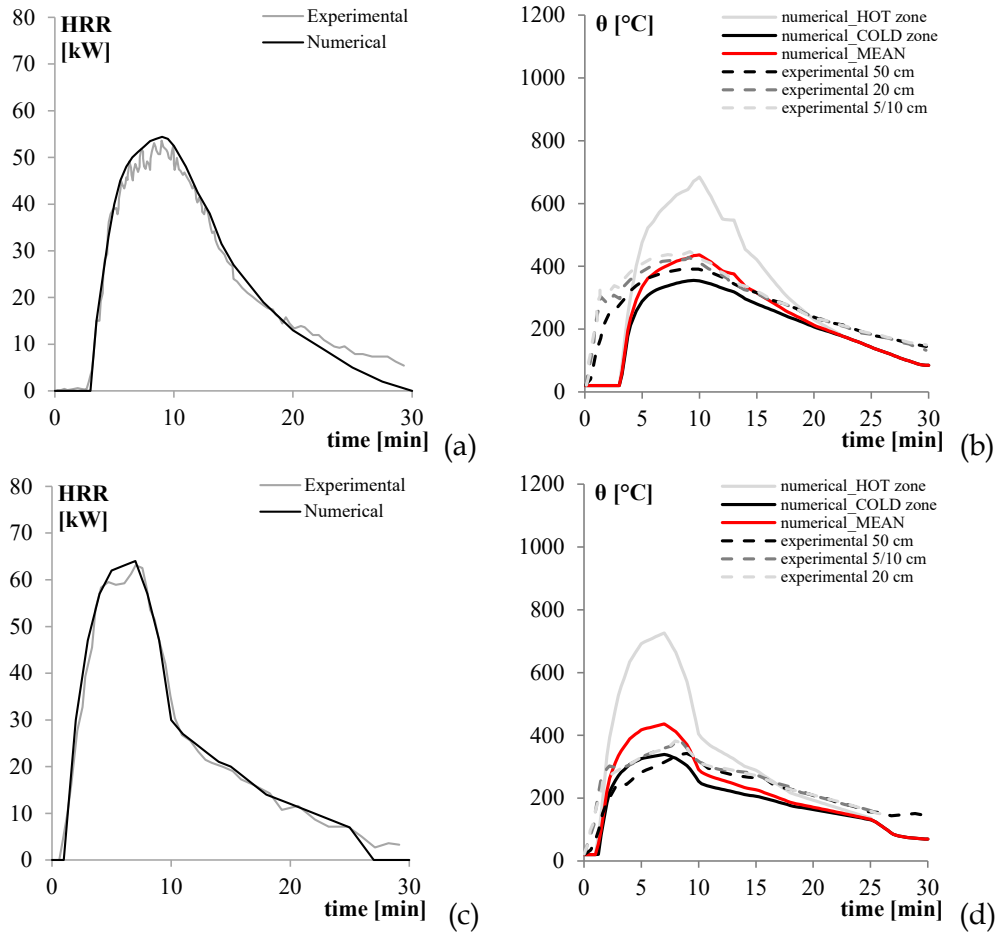

Figure 3.16. Comparison between numerical and experimental results in terms of HRR curves for test 4.2 (a) and 4.3 (c) and temperatures for test 4.2 (b) and 4.3 (d).

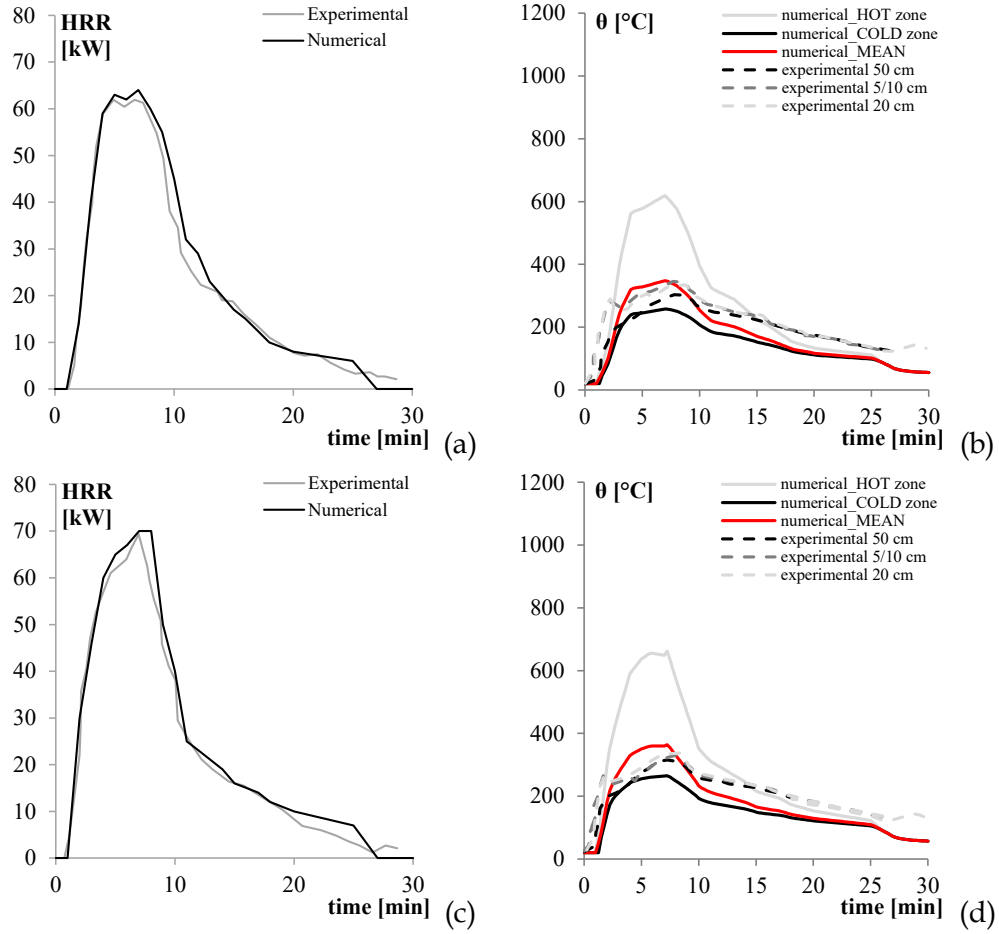

Figure 3.17. Comparison between numerical and experimental results in terms of HRR curves for test 4.4 (a) and 4.5 (c) and temperatures for test 4.4 (b) and 4.5 (d).

By analysing the comparisons between the experimental and the calculated temperatures, some general considerations can be made:

- The initial part of each numerical temperature curve is characterized by a time delay due to the same delay of the experimental HRR curve and then in the reconstructed HRR curve. Referring to test 4.2 where the time delay is maximum, this leads to numerical temperatures lower than the lower the experimental ones for the first minutes. During the heating this difference is recovered, indeed, the two peaks are almost coincident both in terms of time

and in terms of temperature. For the other three tests, although it is not explicitly stated by the authors, probably they have provided the HRR curves without the time delay, indeed the numerical and experimental results are in very good agreement.

- Regarding the maximum temperature, except for test 4.3, the numerical temperature curves, obtained like the mean values between the hot and cold zone ones, have very similar peak values: slightly lower but at the same time for test 4.2, very similar but earlier for test 4.4 and slightly higher and earlier for test 4.5.

Finally, by considering that the numerical temperature curves are based, first of all, on HRR curves evaluated for points starting from the HRR output curve provided by the authors derived from the combustion product measurements and then by an empirical method also subject to errors, and, secondly, since some aspects of the chemistry of the fire were not explicitly stated, but they have been evaluated from the literature, it is possible to affirm that the results of this comparison can be considered satisfactory for its purpose.

Therefore, the CFAST program can be used to model numerically all the fire tests carried out by the authors.

3.2.3. Simulation of the test series 1 and 2

In order to model the vertical propagation of a localized fire, the main aim was to simulate the Test series 5, that, as seen in 3.1.5, consists of the study of the vertical and horizontal fire propagation for a group of four racks.

However, to validate all the CFAST models also the Test series 1 and 2, which provide the necessary input data, were modelled.

First, the Heat Release Rate (HRR) curves that characterize the fire scenarios were defined. Test series 2.2 was modelled first, since this one refers to boxes with a double thickness, the HRR curve was set starting from results of the test series 1.2 (see **Figure 3.1**) and by doing some considerations:

- The Maximum Heat Release Rate (HRR_{max}) was considered equal to 247 kW/m^2, like the test results.

- The total developed energy (q_f) for a single box was equal to 23.9 MJ/m^2, but to consider 4 boxes per level, this value was amplificated obtaining a value of q_f equal to 95.6 MJ/m^2.
- The value of t_α was considered equal to 250 s, which is the value between the ones that the Eurocode provides for bookshops (150 s) and offices (300 s), therefore similar uses of paper and paperboard.
- The fire area A_f was calculated as the floor area of the shelves containing the boxes multiplied by 4 to represent the 4 levels of boxes. The dimensions of the shelves are: 0.24+0.05+0.24m equal to 0.53 m in one direction, 0.20+0.05+0.20 equal to 0.45 m in the other one. As a result, it was possible to obtain the fire area A_f equal to 0.53x0.45x4 equal to 0.954 m^2.

The parameters calculated are summarized in the following **Table 3.2**:

Table 3.2 Fire parameters for HRR curve of test 2.2

HRR_f	A_f	q_f	t_α	HRR_{max}	t_a	t_b	t_c
[kW/m^2]	[m^2]	[kJ/m^2]	[s]	[kW]	[min]	[min]	[min]
247	0.954	95600	250	236	2.0	5.9	9.7

By knowing these parameters it was possible to evaluate the HRR curve, which was compared with the experimental one, see **Figure 3.20.** From this comparison, it is possible to realize that the calculated HRR curve and the experimental one are very similar to each other in terms of pattern and duration, and therefore the HRR curve calculated can be considered representative of fire test 2.2 and can be used like the HRR input curve for the CFAST model.

To model Test2.2 setup a single compartment with the rack dimensions of 0.64x0.56 m in plan and 1.60 m in height, was modelled in CFAST. Since this compartment represents the single rack, each surface was characterized by the thermal properties of the steel, see **Table 3.1**. Along the walls 4 openings per side (always considered open), were defined to simulate the rack openings.

The compartment modelled is shown in **Figure 3.18** while the flame development is shown in **Figure 3.19**.

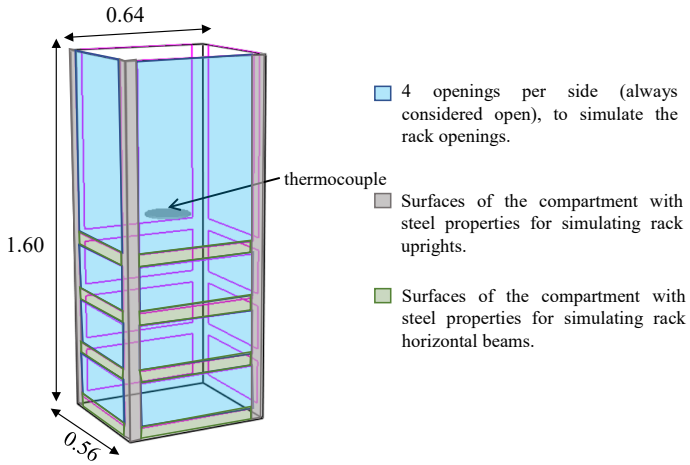

Figure 3.18. CFAST model of the test 2.2.

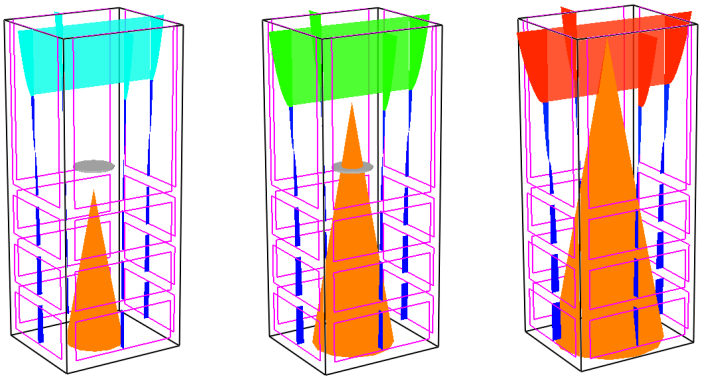

Figure 3.19 CFAST results in terms of flame development for test 2.2.

A single type of fire has been defined, characterized by the previously calculated HRR curve and by all the parameters like the heat of combustion and CO yield, soot yield, and stichometry, as explained in test 4. The fire defined in this way was placed in the middle of the compartment at the height of the bottom shelf. A steel target in the middle of the rack was modelled, such as the thermocouple 2 in test 2.2.

Figure 3.20b shows the comparison between the experimental temperatures and

the numerical ones. The temperature calculated in CFAST, regards the fire durations and the temperatures range can be considered coherent with the one recorded experimentally. Differences between the two curves can be justified by several reasons:

- the error already affecting the HHR curve is also reported in terms of temperature.
- since in the model, a single fire in the centre of the shelf was placed and not 4 fires in the centre of the 4 boxes, the CFAST thermocouple was along the fire axis, leading to higher temperatures than the experimental ones.
- the results could be affected by errors because the modelled compartment is slightly larger than the minimum size allowed in CFAST program.

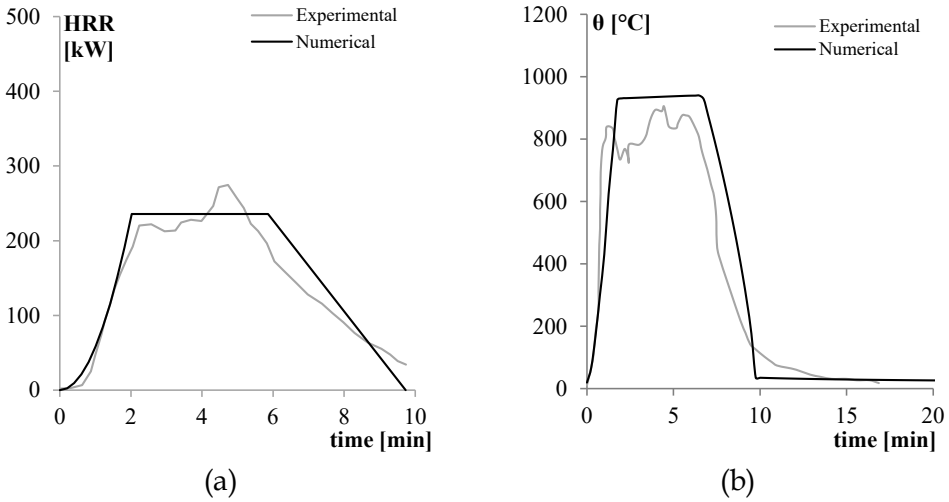

Figure 3.20. Comparison between numerical and experimental results in terms of HRR curves (a) and temperatures (b).

In conclusion, modelling the test 2.2 it was possible to validate the CFAST model for a single rack.

3.2.4. Simulation of the test series 5

Finally, the main test, for our purpose, such as the fire test 5 was simulated, this test was selected also because it is the only one that provided the vertical fire

spread between levels of the racks, the ignition took place at the bottom of 2nd rack (first ignition to I level), with vertical propagation up to the other V levels and horizontal propagation to the other three racks (see **Figure 3.21**). This propagation was considered in the CFAST model by assigning time delays to the HRR curves, starting from the HRR curve of a single level.

The Heat Release Rate (HRR) curve of the single levels of the 2nd rack was evaluated by using the same procedure used to evaluate the HRR curve of the entire rack for the test 2.2, i.e., starting from the test series results 1.2 and by considering that the 2nd rack of test 5.3 was characterized by 24 double thickness boxes for each level. The parameters calculated are summarized in the following **Table 3.3**.

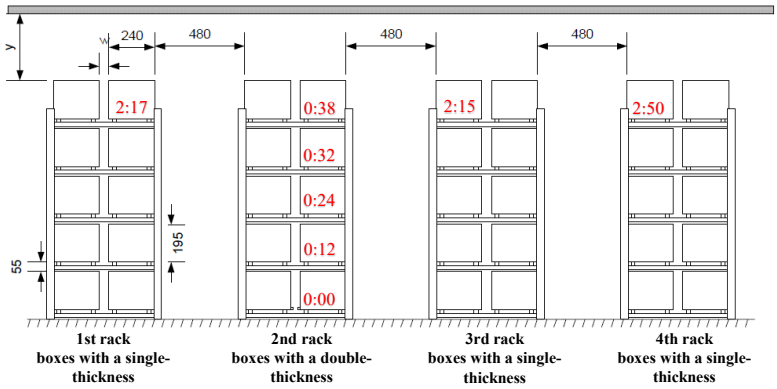

Figure 3.21. Test 5.3 setup with fire propagation times.

Table 3.3 Fire parameters for HRR curve for a single level of the 2nd rack

HRR_f	A_f	q_f	t_α	HRR_{max}	t_a	t_b	t_c
[kW/m^2]	[m^2]	[kJ/m^2]	[s]	[kW]	[min]	[min]	[min]
247	1.96	95600	250	484	2.5	6.3	10.2

Therefore, starting from HRR curves of a single level, these ones were then summed moment by moment, referring to the exact time delays provided in [1], and obtaining the HRR curve of the whole 2nd rack, shown by the red curve in **Figure 3.22**a.

For the other three racks the test results didn't provide the vertical time delays, in this case, the HRR curve of the whole rack was directly evaluated. Starting from the results of the test 1.1 (see **Figure 3.1**), since this one refers to boxes with a single thickness, it was possible to obtain the HRR curve of a single level of the rack for test 2.1 which refers to 4 boxes. Since the single level of the 1st, 3rd, and 4th rack of test 5.3 consists of 24 boxes and the entire rack has 5 levels, the HRR curve of the single level corresponds to 6 times the HRR of 4 racks, while the HRR curve of the whole racks corresponds to 30 times the HRR of 4 racks. The HRR curve obtained is shown in **Figure 3.22**b.

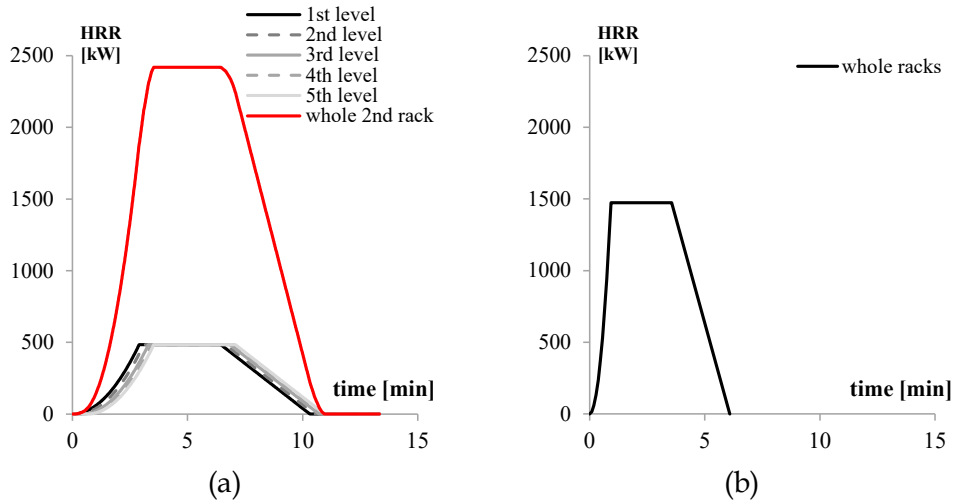

Figure 3.22. HRR curves for the test 5.3: HRR curves of the 2nd rack (a) and of the lateral ones (b).

These HRR curves provided the input of the CFAST program. To model the test 5 setup a large compartment of 16x15 m in plan and 1.85 m in height, was modelled, its dimensions were not provided by authors [150], and for this reason, they were defined to guarantee proper ventilation to reach the decay phase of the fire test. Within this one, 4 compartments representing the 4 racks of 0.64x3.06 m and in 1.85 m in height, were modelled (see **Figure 3.23**).

The surfaces of the large compartment were plasterboard to simulate the walls of the test setup, while the 4 compartments representing the racks were characterized by the thermal properties of the steel (see all properties listed in **Table**

3.1). Along the walls, 5 openings per side (always considered totally open), were defined to simulate the rack openings. For each rack, the corresponding fire was placed at the base, in the middle of the compartment.

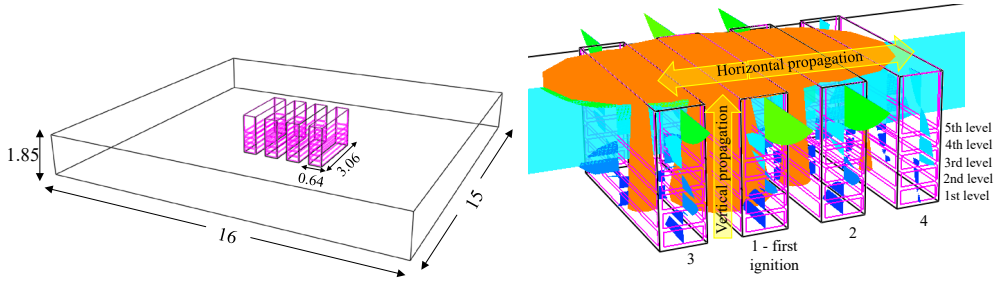

Figure 3.23. CFAST model of the test 5.3, dimensions are in meters.

In particular, the fire of the 2nd rack was modelled by the red HRR curve as shown in **Figure 3.22**a. As regards the lateral racks, the fire of the 1st, 3rd, and 4th racks was modelled using the HRR curve shown in **Figure 3.22**b applied at 129seconds, 130seconds and 150 seconds respectively as defined by authors [150] and showed in **Figure 3.21**a.

The following **Figure 3.24** shows the comparison between the experimental results and the numerical ones, in terms of temperature.

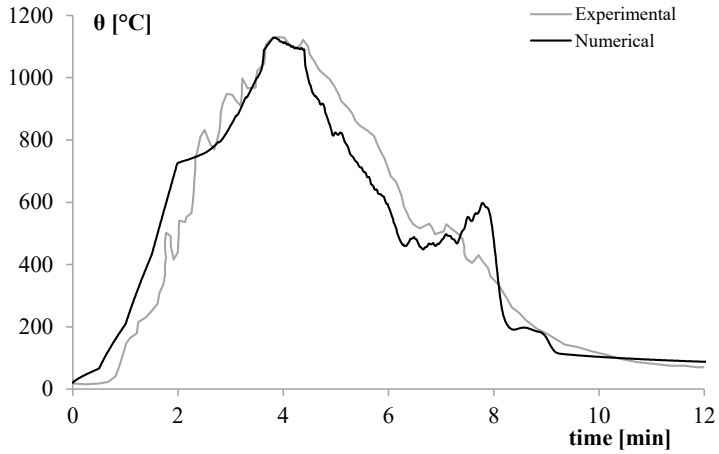

Figure 3.24. Comparison between numerical and experimental results.

The temperature calculated in CFAST regarding the maximum temperature, is coherent with the one recorded experimentally. The heating phase is not too

different, indeed only a time delay is observed in the numerical temperature. The same is true for the first part of the cooling phase, while, after 8 minutes, the temperatures are very similar.

To define a generalized model for the vertical propagation, it was necessary first to validate the propagation times of Test 5.3. It was found that these are equal to the times for the flame to reach the upper level of the racks calculated by using the flame lengths L_f for a localized fire proposed in the Annex C of the EN1991-1-2 [1] and given by:

$$L_f = -1.02\, D_{fire,eq} + 0.0148\, HRR\ (t)^{0.4} \tag{3.16}$$

Where:

HRR(t) is the heat release rate of the fire in [W];

$D_{fire,eq}$ is the equivalent diameter in [m]; which can be evaluated by using the expression, given in [108], indeed if the main combustible involved in the localized fire is not circular, then it is modelled as a circle assuming that the area on the ground is equal. The equivalent diameter is calculated with:

$$D_{fire\ eq} = \sqrt{\frac{4A_{fi}(t)}{\pi}} \tag{3.17}$$

Where:

$A_{fi}(t)$ is the area of localized fire in [m²] which was calculated by using the **Eq. 3.15.**

Table 3.4 Comparison between experimental and calculated propagation times.

Load Level	Experimental time [s]	Calculated time [s]
1st	0	0
2nd	12	13
3rd	24	25
4th	32	38
5th	38	50

These values were obtained by considering Eq. 3.16 in the following way: once the load level height was obtained from the equation, the HRR curve of the upper level was added, and so on.

From the results obtained end shown in **Table 3.4** it is possible to observe that

the calculated times are in good agreement with the time provided by the experimental test and for this reason it is possible to affirm that the vertical propagation of the fire can be modelled like the time for the flame to reaches the following load level along its vertical. In particular, it is worth saying that the values are all the more consistent at the first levels compared to the following ones, this is because the formula was calibrated to consider only one fire and not the overlapping of more fires, moreover the exponential leads to an asymptote at a certain time, which doesn't allow to reach a higher fire length.

3.3. Proposed fire model for ARSW, CFAST

Thanks to the simulation and validation of the fire tests carried out by Lönnermark and Ingason [150] by using the software CFAST [112] it was possible to obtain the parameters which define the design fire, that together with the method to calculate the times for the vertical propagation, can be applied to obtain a fire model for the ARSW structure.to proceed it is worth remembering that the fire tests carried out by [150] were small-scale fire tests. Thus, the first step to obtaining a real fire model is to scale up these fire parameters in a way that they can be representative of a full-scale fire configuration by using various physical scaling laws. Physical scaling has been widely used in the fire safety science community, allowing a better understanding of fire dynamics. Indeed, Heskestad [168] reviewed scaling techniques, mainly pressure modelling and Froude modelling. Quintiere [169] also reviewed the scaling applications in fire research with a focus on ceiling jets, burning rate, flame spread and enclosure fires. Perricone et al. [170] investigated the thermal response of a steel tube covered by insulating materials using scaling principles.

Li and Ingason provided a general scaling method for pallet fires presented in [162] modelled ad hoc on cellulosic material fires that develop in steel racks structures. This method is based on the Froude scaling technique in particular, these coefficients can be used for scaling the parameters that define a fire in terms of HRR value, volumetric flow, propagation speed, time, energy released, mass

and temperature, in relation to the geometric ratio between the full-scale dimensions L_f (in real scale) and the model scale dimensions L_m (in reduced scale).

Heat Release Rate (HRR) [kW]
$$HRR_{full\ scale} = \left(L_f / L_m\right)^{5/2} HRR_{model\ scale} \quad (3.18)$$

Volume flow [m^3/s]
$$V_{full\ scale} = \left(L_f / L_m\right)^{5/2} V_{model\ scale} \quad (3.19)$$

Velocity [m/s]
$$u_{full\ scale} = \left(L_f / L_m\right)^{1/2} u_{model\ scale} \quad (3.20)$$

Time [s]
$$t_{full\ scale} = \left(L_f / L_m\right)^{1/2} t_{model\ scale} \quad (3.21)$$

Energy [kJ]
$$E_{full\ scale} = \left(L_f / L_m\right)^{3} E_{model\ scale} \quad (3.22)$$

Mass [kg]
$$m_{full\ scale} = \left(L_f / L_m\right)^{3} m_{model\ scale} \quad (3.23)$$

Temperature [K]
$$T_{full\ scale} = T_{model\ scale} \quad (3.24)$$

Considering the ARSW structure shown in the previous chapter, and the fire test 5.3 that was validated in the previous paragraph, it was necessary to scale the behaviour of the double-thickness cardboard box with dimensions of 0.24 m x 0.2 m x 0.195 m against a box to be included in the generic storage module of the ARSW structure, which has a length equal to 4.00 m, the width equal to 1.66 m and the height equal to 1.50 m. Since these three dimensions are different, by scaling you go from a box cubic box to a very elongated transverse-direction box. For this reason, it was calculated a geometrical ratio equal to 11.76, by using the following expression which is a proportion between areas:

$$\frac{L_f}{L_m} = \sqrt{\frac{A_f}{A_m}} \quad (3.25)$$

This geometrical ratio equal to 11.76, led to different scale factors used for the time and the HRR values, respectively 3.4 and 474.

Regarding the value of t_α, firstly the same value of the fire test equal to 250s was considered. The HRR curve obtained for a box with table thickness in real

scale is shown in **Figure 3.25**a. On the other hand, by carrying out a critical analysis of the HRR obtained, it is possible to observe that the parabolic section of the curve is characterized by a slope that makes the first phase too fast. This HRR for paper material is not consistent with the value according to Italian regulation [171] that for paper material proposes a t_α equal to 150s.

For this reason, it was decided to modify the HRR curve showed in **Figure 3.25**a by applying only to the parabolic section the suggestion of the code, leaving unchanged the peak, the duration, and the descending phase of the HRR curve. The HRR curve modified in this way is shown in **Figure 3.25**b.

Table 3.5 Scaling factor for the model [21].

	Small scale box	Full scale box	L_f/L_m
length	0.240	4.00	16.7
width	0.200	1.66	8.3
height	0.195	1.5	7.7
	Proportion of the equivalent area.		11.76

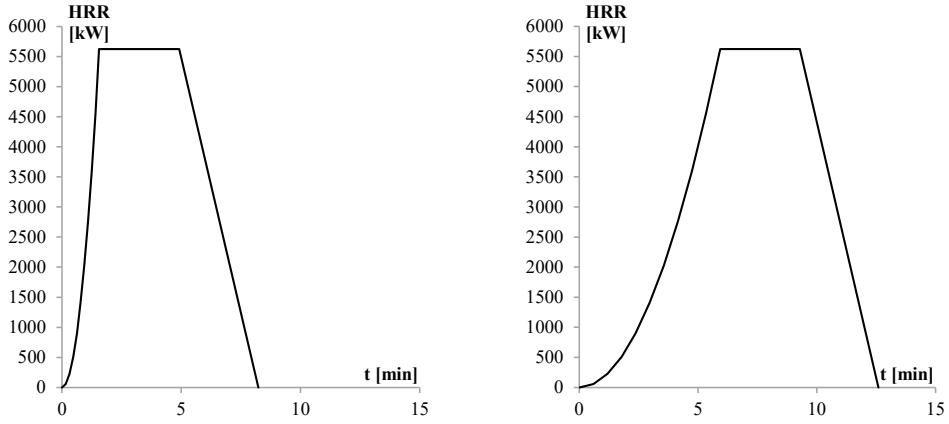

(a) (b)

Figure 3.25. HRR curves: (a) calculated with scaling laws, (b) modified one.

According to the method validated before to calculate the vertical fire propagation, these ones were calculated for the ARSW structure. Placing the first ignition at the base of the central shoulder (see **Figure 3.27**) and considering that the

height of the load cell is equal to 2.04 meters, the ignition time was the time at which the flame length reaches this height, and its multiples. In this way it was possible to obtain the vertical propagation times shown in the following **Table 3.6**.

Table 3.6 Vertical propagation times calculated for ARSW structure.

Time [s]	Reached height [m]	Description
0	0.00	Fist ignition at the base
107	2.04	The flame reaches the 2nd level
244	4.09	The flame reaches the 3rd level
368	6.12	The flame reaches the 4th level
515	8.15	The flame reaches the 5th level
691	10.20	The flame reaches the 6th level
800	11.59	The flame reaches the 7th level

It is worth saying that since the flame length fails to reach the height of the 7th level equal to 12.24 m it was supposed that there was no ignition of the 7th load level, and therefore the proposed fire model will consider a vertical fire propagation within the first six load levels.

Regarding the study of the horizontal fire propagation, a time delay between the ignition of the first shoulder and the ignition of the adjacent ones was evaluated.

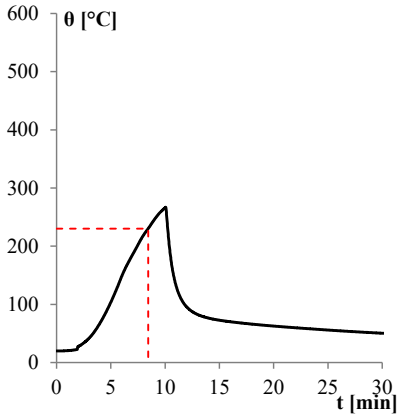

Figure 3.26 Evaluation of the horizontal fire propagation time.

In particular, the time required for the combustible material stored in the adjacent load cells to reach a temperature of 230 °C that is the paper auto-ignition temperature [120] was considered, obtaining a time equal to 506 seconds e.g., 8.4 minutes (see **Figure 3.26**).

Once the HRR curve for a box in real scale and fire propagation times were obtained, all the input data for the CFAST model were evaluated.

3.3.1. Previous model

In CFAST, a first large compartment that represents one transversal cross section was modelled. Within this one, 5 compartments representing the 5 racks shoulder and 1 steel compartment representing the bottom steel frame, were modelled. In this way, 7 compartments were modelled, in total (see **Figure 3.27**). The lateral shoulders were not modelled as a compartment because they were considered cold.

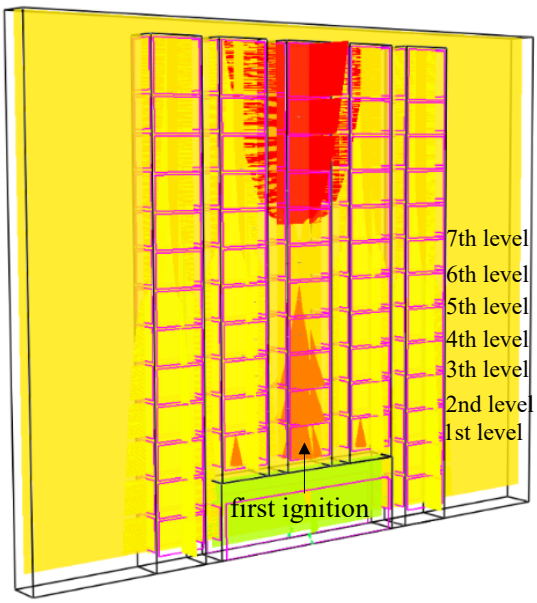

Figure 3.27. First CFAST model of the ARSW structure.

Each compartment representing the shoulders was characterized by the thermal properties of the steel. Along the walls, different openings per side (always considered totally open), were defined to simulate the rack openings at each load level.

It is worth saying that once the compartment is characterized by openings and the fire can travel from one compartment to another one, the meaning of the compartment is lost, so in the following descriptions, the term "cell" will be used to refer to this type of zones modelling. Thanks to the time delays calculated previously (see **Table 3.6**), it is possible to affirm that for this fire model, the ignition took place at the bottom of the central shoulder (first ignition to 1st level), with vertical propagation up to the other six levels and horizontal propagation to the other two shoulders.

For this reason, in the CFAST model, for each shoulder, 6 HRR curves were assigned at the middle height of each load level with the corresponding time delays, defined previously.

In this way, 18 HRR curves were assigned, in total, these HRR curves are showed in the following **Figure 3.28** for the central shoulder and in **Figure 3.29** for the adjacent ones.

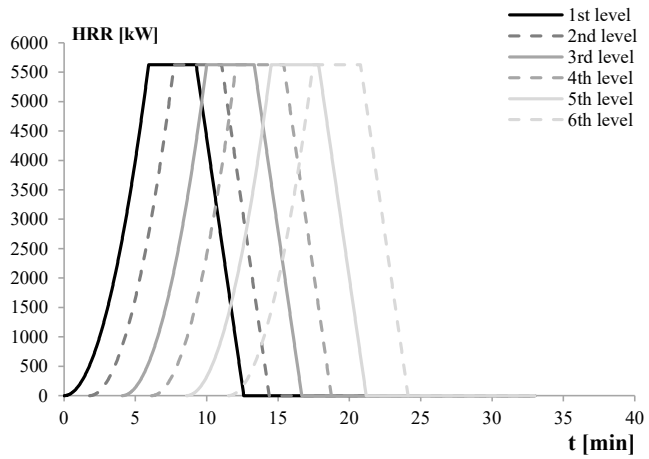

Figure 3.28. HRR curves for the central shoulder.

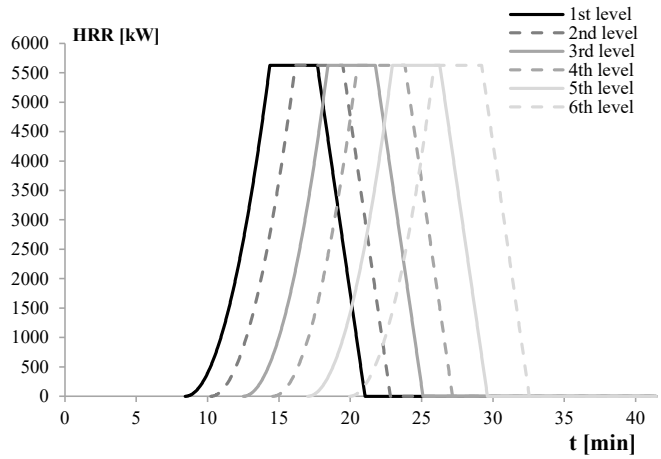

Figure 3.29. HRR curves for the adjacent shoulders.

For the analysed fire scenario, **Figure 3.30** shows the temperature distributions recorded by the CFAST thermocouples placed at the first four levels near the horizontal elements and uprights ones.

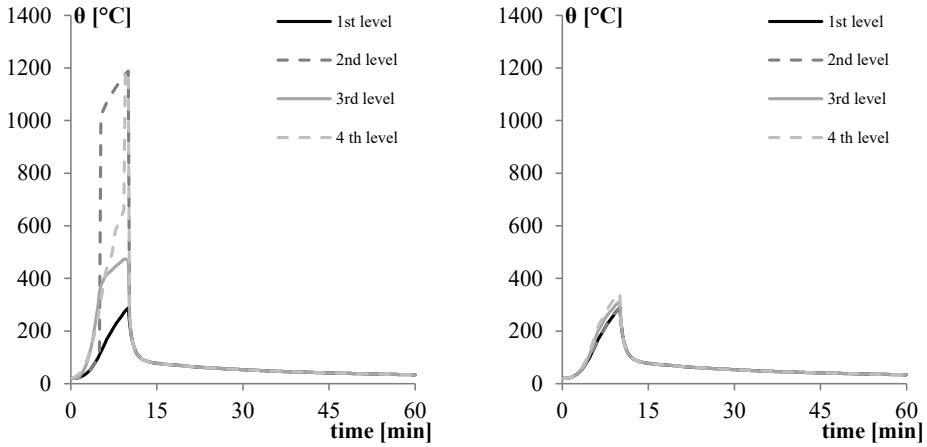

Figure 3.30. Temperatures recorded in the CFAST model for the horizontal elements (a) and uprights one (b).

By analysing the results, these ones seem to be not consistent because of the heating phase which is characterized by a strong discontinuity, and the different

temperatures reached for the 3rd level compared to the other ones. Moreover, since in this type of model, there is only one hot zone at the upper level of each compartment (i.e., shoulder), it was not possible to compare the temperature of the hot zone with the temperature recorded by the thermocouple, to see if the thermocouples work properly.

In conclusion, this type of model didn't work properly and for this reason, different modifications were made.

3.3.2. Final model

Starting from the previous considerations, the first modification that was made in the CFAST model to better represent the fire scenario, concerned the different modelling of each shoulder. Every single unit of the load was modelled as a single cell but communicating between them thanks to horizontal openings (ceiling/floor vent). In this way a model with different compartments/cells allowed comparing the temperatures recorded by the thermo-couple with the temperatures of the hot zone and cold zone. Indeed, such a model allowed dividing each load level into two zones instead of the entire shoulder.

The second modification that was made in the CFAST model concerned the ventilation condition, the first large compartment that represented one transversal cross section was modified by referring to the dimension of the entire volume of the ARSW representing the entire ARSW, but since it was noted that even this condition underestimated the oxygen supply, and also considering some studies in the scientific literature regarding the loss of the sandwich panels after their damage due the fire [121], a bigger volume was considered to provide more oxygen to the fire.

The result was, a fluid dynamics model too complex for processing by using CFAST, with different errors during the analysis. Therefore, it was decided to achieve a good compromise between the complexity of the model, the potential of the software, the processing time and the amount of data generated.

The fluid dynamic model that met these requirements consists of an extremely large external compartment (Compartment 1) capable of providing the amount

of oxygen necessary for the full development of all the HRR curves. Within this one, 5 compartments representing the 5 shoulders and 1 steel compartment representing the bottom steel frame, were modelled (see **Figure 3.31**).

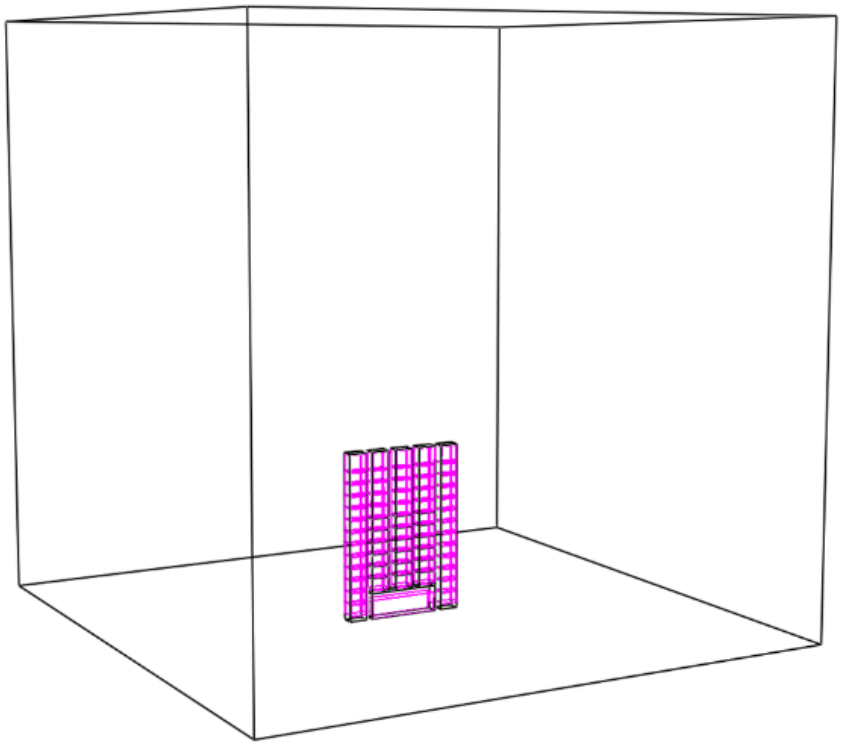

Figure 3.31. Final CFAST model of the ARSW structure.

As said before, for the central three shoulders, the first six load levels which were directly affected by the presence of a fire, were modelled as a single compartment but communicated among them. The result was a model with seven compartments for each shoulder in particular: six single compartments related to the first six levels where, with several delays, the fire develops and the seventh compartment grouping the remaining load levels where no fire was defined.

Figure 3.32a shows the temperature distributions recorded by the CFAST thermocouples placed at the first seven levels near the horizontal elements, while **Figure 3.32**b shows the temperature of the hot zone.

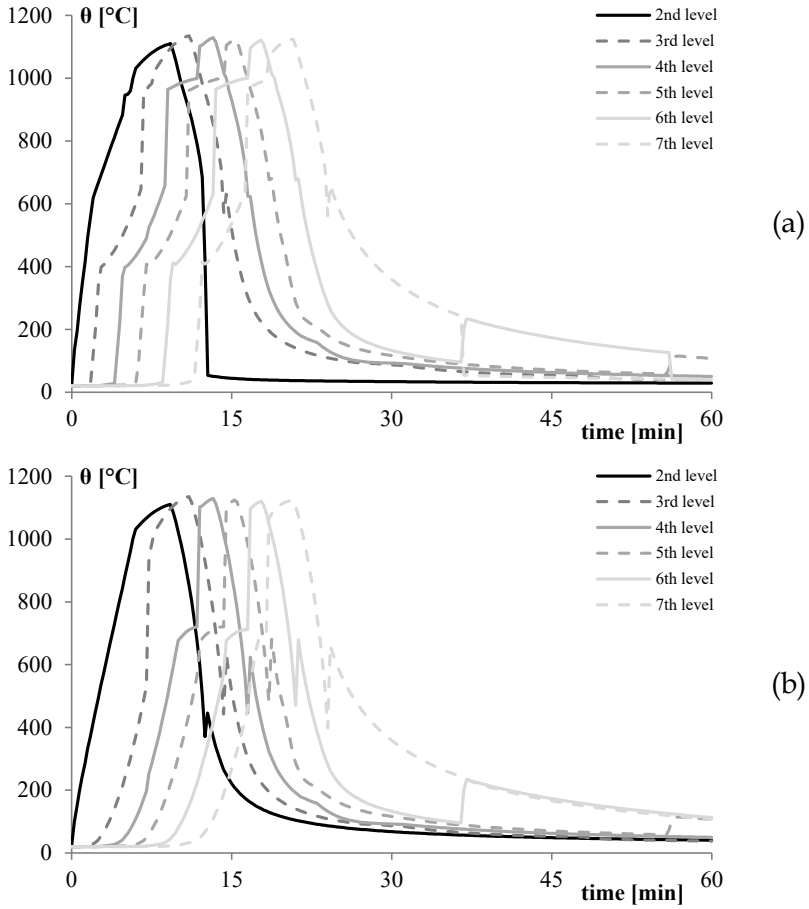

Figure 3.32. Temperature distributions recorded by the thermocouples placed at the first 7 levels near the horizontal elements (a) and temperature of the hot zones (b) of the central shoulder.

By analysing temperature results, it is possible to appreciate, how the time delay imposed for the HRR curves was found also in the natural fire curves. All the curves reach a maximum temperature equal to about 1120 °C. The results confirm that the measurements of the thermocouples near the transverse elements are in good agreement with the temperatures recorded in the hot zone of each compartment where a fire is present. Moreover, the new modelling allows also overcoming the problem of the strong discontinuity that characterized the heating phase in the previous modelling, because, in the previous modelling, the

thermocouple was engulfed in the flame and passed from 20° to 1200° very quickly.

In the new modelling, the thermocouple near the generic transverse is always in the hot zone, during all the thermal transients. Thus, it heats up in the same way as the gases that are concentrated there, with slower heating but reaching the same peak of temperature.

Figure 3.33 shows the temperature distributions recorded by the CFAST thermocouples placed at the first seven levels near the horizontal elements of the adjacent shoulders, where also in this case it is possible to appreciate, how the time delay imposed for the HRR curves was found also in the natural fire curves.

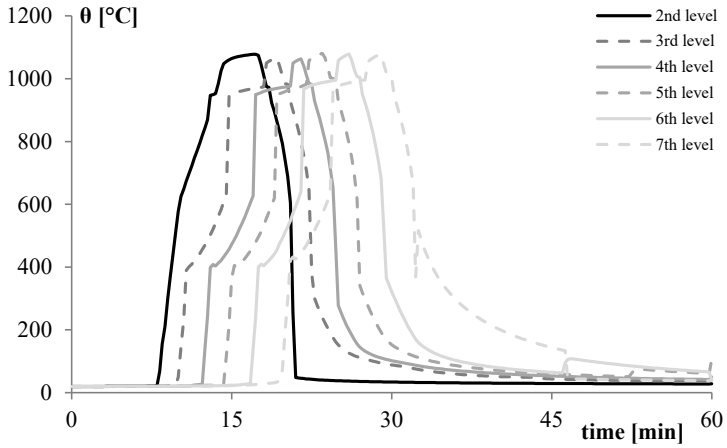

Figure 3.33. Temperature distributions recorded by the thermocouples placed at the first 7 levels near the horizontal elements of the lateral shoulder.

The new modelling didn't sort out the problem regarding the other thermocouples placed outside the hot zone; therefore, to define the heating curves for the diagonals and the uprights elements, a temperature curve evaluated as the average of the temperatures recorded in the hot zone and in the cold zone was considered at each level.

The following **Figure 3.34** shows the temperature distributions evaluated for the elements belonging to the central shoulder and to the later ones.

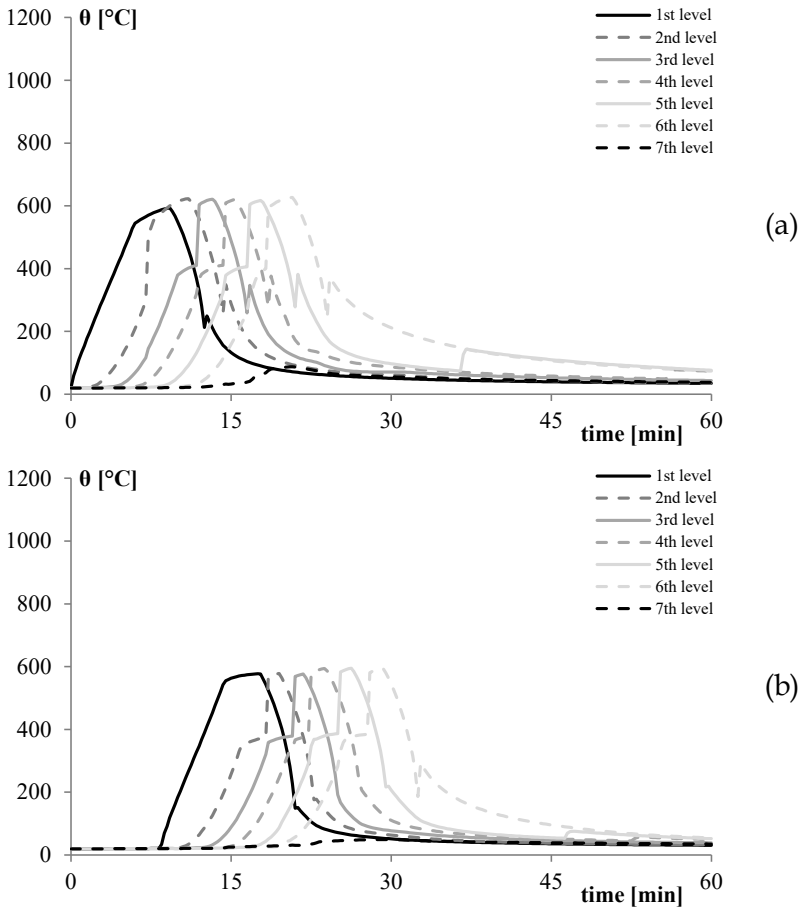

Figure 3.34. Average of the temperatures recorded in the hot zone and in the cold zone at each level, for the central shoulder (a) and the lateral ones (b).

In the following **Figure 3.35** a final schematization of the temperature distribution obtained with the proposed multi-cell zone model is shown, where it is possible to see the temperature field obtained from the model, in a simplified form.

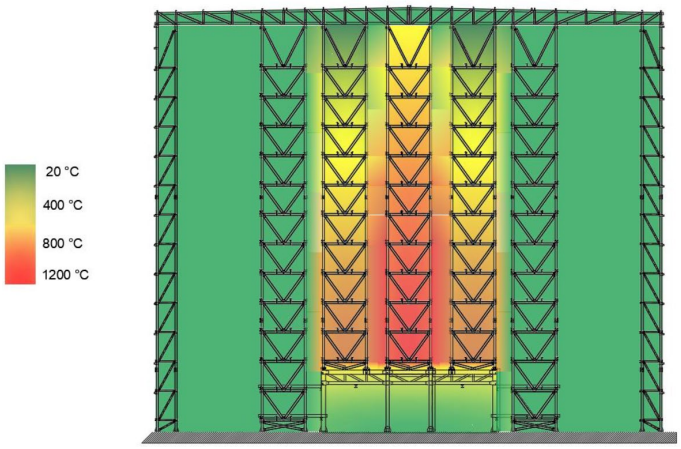

Figure 3.35. Temperature distribution within the structure for the proposed multi-cells zone model.

3.4. Proposed fire model for ARSW, FDS

The computational fluid dynamics model of the ARSW structure was created also in FDS software developed by NIST [172] to simulate the gas temperature distributions and compare them to CFAST measurement results. FDS is a computational fluid dynamics model that specifies solving Navier-Stokes equations in the limit of low-speed, thermal-driven flow on predefined rectilinear grids over time. FDS is a Fortran program that reads input parameters from a text file, computes a numerical solution to the governing equations, and writes user-specified output data to files. Smokeview developed by NIST [173] is a companion program that reads FDS output files and produces animations on the computer screen, at the same time Pyrosym provided by Thunderheadeng engineering [174] is a graphical user interface that helps to create the input file for FDS, at the same time. Smokeview and Pyrosym have a simple menu-driven interface, while FDS does not.

In Pyrosym, a large compartment that represents the whole compartment was defined as 52 m x 35m x 29.8 m in a model domain of 58.8m x 35.4m x 30m. Into FDS environment, the geometry is described in terms of rectangular obstructions

(OBS) that can heat up, burn, conduct heat, etc.; and VENTS from which air or fuel can be either injected into or drawn from the flow domain. A boundary condition needs to be assigned to each obstruction and vent, describing its thermal properties.

For this reason, firstly, in the computational domain the steel frame was modelled as shown in **Figure 3.36**, it is worth saying that the diagonal bracings belonging to the shoulder and the truss were not modelled because of the type of modelling that this type of program request, where it is only possible to model rectangular OBS.

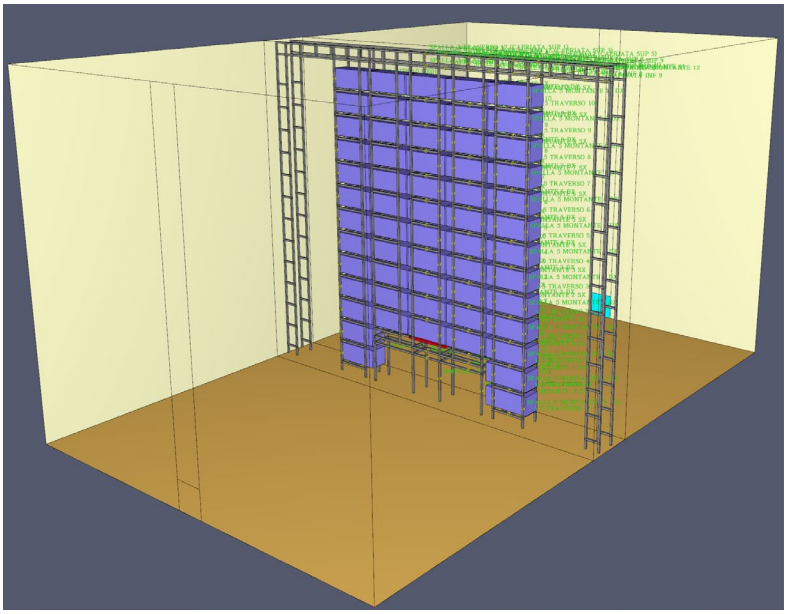

Figure 3.36. FDS model of the ARSW structure with AST devices positions.

The boundary conditions were defined as close as possible to the ones of the reality. Boundary conditions for obstructions and vents are prescribed by an attached surface (SURF) where most parameters must be defined. In FDS software, solids are assumed to consist of layers that can be made of different materials, the thermal properties of each material required are designated via the MATL name list group.

In this context, the floor and the ceiling were set as INERT which is the default

FDS boundary condition representing a smooth wall with a fixed temperature, equal to the ambient temperature, and emissivity equal to 0.9, where radiative and convective heat transfer is calculated. The walls were considered made of 0.15 m of gypsum with the properties listed in **Table 3.7**, the surface attached was set as a "layered" type, whit a layer of 0.15 m of material "gypsum".

The same type of "layered" surface was assigned to the structural steel elements, by considering the steel properties listed the **Table 3.7**, in this case, it was set that the steel elements are not allowed to participate in combustion and whose physical surface characteristics are calculated during the thermal transient with the incident flow.

Table 3.7 Material properties for test series 4.

	thermal conductivity [W/mK]	**specific heat** [kJ/kgK]	**density** [kg/m^3]	**thickness** [m]	**emissivity** [-]
steel	45.8	0.46	7850	0.004	0.7
gypsum	0.17	1.09	930	0.15	0.9

The fire load is supposed to be made of discrete wood cribs and paper rolls, but in this modelling, no detailed representation of a wood crib (i.e., 1m^3 involving alternation of sticks and air gaps) was used but a simpler approach was adopted, using solid cubes, modelled as OBS. This approach is based on the work done by Horová, 2015 [175] and Degler et al., 2015 [176].

The specified ignition of the fire was basically modelled as the ejection of gaseous fuel from a solid surface, this is essentially a burner, with a specified Heat Release Rate Per Unit Area, HRRPUA, in units of kW/m2. The solid burner was modelled with dimensions equal to 4.05m x 1.65m x 0.15 m. To obtain the same HRR represented in **Figure 3.25**b, the HRRUA for this surface was set equal to 670.2 kW/m^2, moreover, it was necessary to specify a time ramp for volumetric heat source, obtaining an HRR that lasts for 12.60 minutes.

The paper constituting the cubes is assumed to be pine wood type with the following chemical composition: C6H12O6 and a soot yield of 0.0015 g/g. No CO yield was defined. These values are the same specified for the zone model in

section 3.2.2.

The pine wood properties were considered equal to conductivity 0.14 W/m/K, specific heat 2.85 kJ/kg/K, emissivity 0.9 and density 640 kg/m^3. These values are adopted in FDS Validation Guide [177].

All the other unit loads were modelled as solid cubes with dimensions equal to 4.05m x 1.65m x 1.65 m, i.e., the real dimensions of the unit loads. To obtain the same HRR represented in **Figure 3.25**b, the HRRUA for this surface was set equal to 174.81 kW/m^2, with a specific time ramp for this volumetric heat source, obtaining the HRR that lasts for 12.60 minutes.

Since one of the aims of this simulation was to analyse the fire propagation without the predefined delay times, all the unit loads were not modelled as BURNERS but as surfaces with an ignition temperature set equal to 230 ^{o}C that is the paper auto-ignition temperature [120]. When the threshold temperature of 230°C is met on at least one face of the volume, then the six surfaces are set to start burning following the prescribed HRRPUA curve.

Two opening were placed along the length of the compartment, on both walls parallel to the DA direction of the compartment, always considered totally open.

The modelled compartments and the simplified fire load are depicted **Figure 3.36**.

To obtain the CFD simulations outputs that can interface with the following FEM analyses all the structural elements were equipped with devices which were Adiabatic Surface Temperature (AST) to summarize and transfer the thermal boundary information [178] (see **Figure 3.36**). They assume the surface to be a perfect insulator and the net heat flux is thus zero. The fictitious temperature θ_{AST} is calculated based on the incident radiative heat flux and the gas temperature near the surface [179]. Then the θ_{AST} is applied to the FEM thermal analysis as thermal constraints.

For simulations involving buoyant plumes, the FDS User's Guide [172] defines a non-dimensional parameter to assess the quality of the mesh: D*/dx, where D* is a characteristic fire diameter and dx is the nominal size of a mesh cell. Since no comparison with experimental results is possible, values were not

based on a sensitivity analysis but on existing analyses representing fire dynamics in large enclosures. Indeed, the FDS Validation Guide [177] contains a table of the values of D*/dx used in the simulation of the validation experiments which were used as guidance.

Since the steel frame was heated and most temperature devices were set at the heated frame, different mesh sizes were adopted to save computational costs without hurting modelling accuracy. The mesh size of the heated frame was 0.15 m x 0.15 m x 0.15 m, while that of another meshes were 0.6 m x 0.6 m x 0.6m, as is shown in **Figure 3.37**.

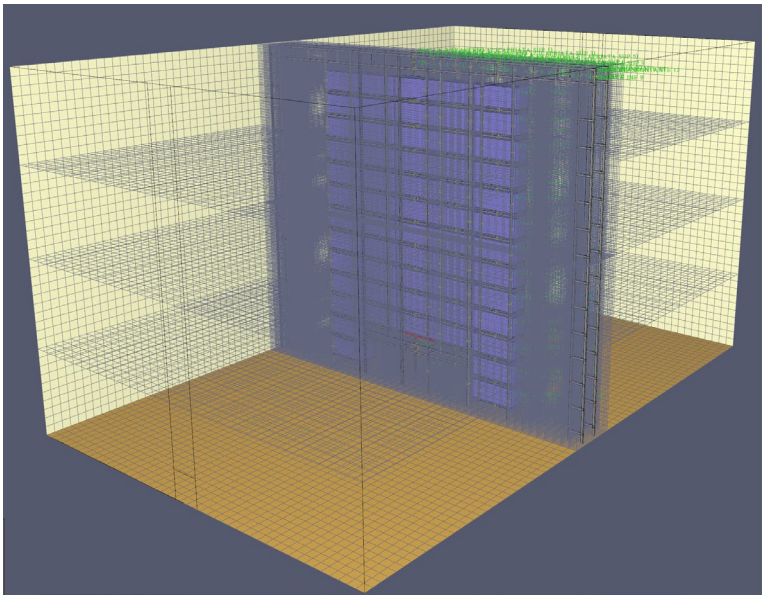

Figure 3.37. FDS model with mesh definition.

These CFD simulations were launched on a high-performance computing cluster, to do this the whole model was split into 102 meshes and ran in parallel through Open Multi-Processing (OpenMP) techniques, in this way the simulations required 48 h to complete, using 102 cores (102 MPI processes with 1 OpenMP threads per process).

3.4.1. Results discussion

The results obtained from the CFD simulations are reported below by distinguishing among the results obtained for group of ASTs, placed in each shoulder for both the horizontal and uprights elements, such as for each the truss beams.

Figure 3.38 shows the temperature distributions recorded by the AST placed at the eleven seven of the horizontal beams of the central shoulder, (third shoulder as represented in **Figure 2.15**).

The first thing that it is possible to observe is that by using the CFD model it is possible to observe vertical and horizontal propagation without the pre-defined delay times. The second aspect is that the temperature doesn't reach the same peak for all the structural elements like the CFAST temperature. In the case of the first heated element, the horizontal beam at the 2nd level is possible to observe a very similar behaviour to CFAST.

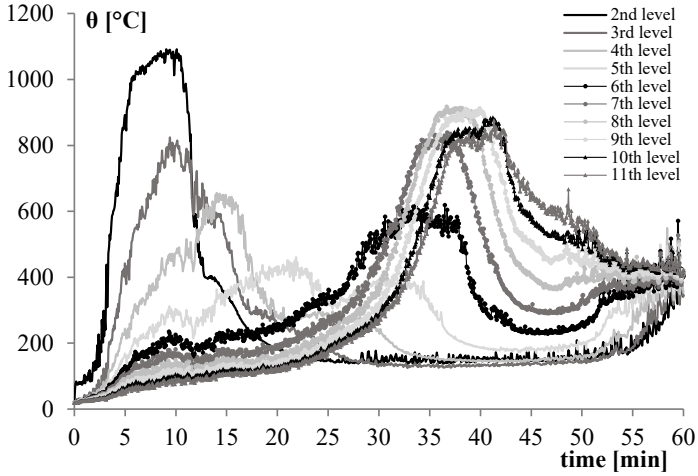

Figure 3.38. Temperature distributions computed by FDS at the horizontal beams of the central shoulder.

The **Figure 3.39** to **Figure 3.42** break down the FDS results: they are shown alongside Smokeview images for corresponding times, which helps understand the fire propagation. From **Figure 3.39** (i.e., at 5 minutes), it is possible to observe the first cube is heated and the flame is reaching the second level. **Figure 3.40** (i.e., at 12 minutes) shows that that all the first cube is consumed by the fire which

means that all the HRR of this level is used, this is the reason why the temperature distribution for the second level is very similar to the CFAST one.
Figure 3.41 (i.e., at 20 minutes) shows that going to the 3rd and 4th levels the temperature peak decreases because the fire starts to propagate within the aisle between the two shoulders, like a chimney effect. This aspect confirms the ventilation effect which may play a very important role, in changing the fire traveling trajectory. **Figure 3.42** (i.e., at 35 minutes) shows that due to this type of propagation, the fire reaches the upper levels very fast going to heat also all the truss elements, indeed all the horizontal beams from the 6th to the 11th levels are heated at the same times, with only a little delayed time among them.

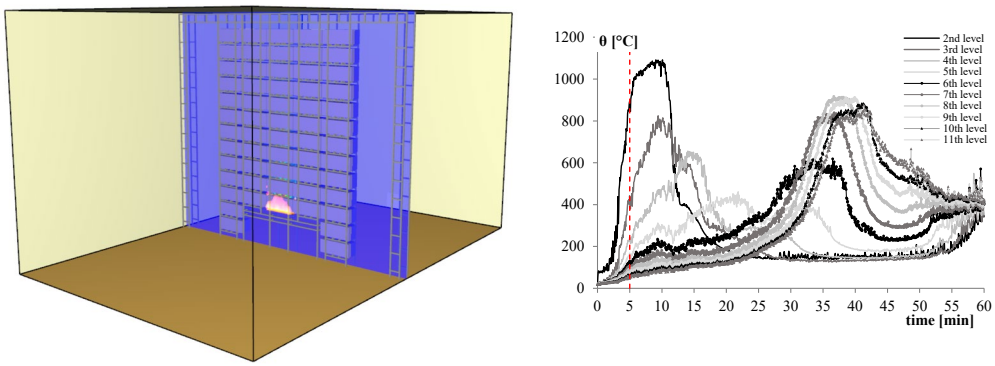

Figure 3.39. (a) Smokeview image for the simulation at 5 minutes and (b) corresponding temperatures computed by FDS.

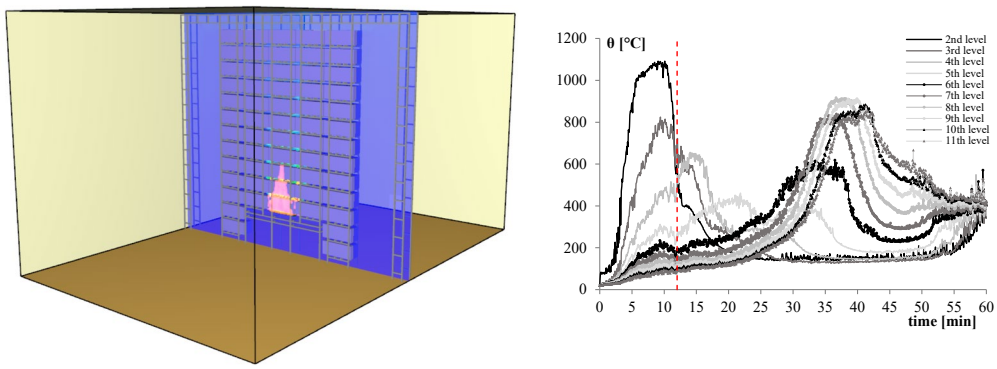

Figure 3.40. (a) Smokeview image for the simulation at 12 minutes and (b) corresponding temperatures computed by FDS.

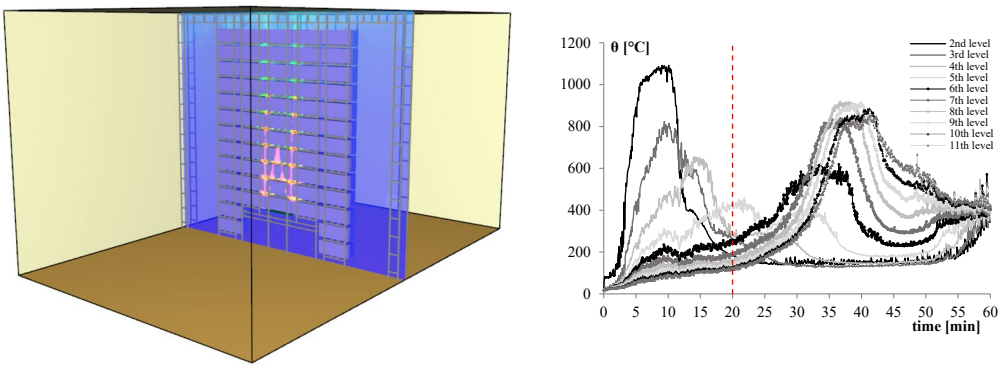

Figure 3.41. (a) Smokeview image for the simulation at 20 minutes and (b) corresponding temperatures computed by FDS.

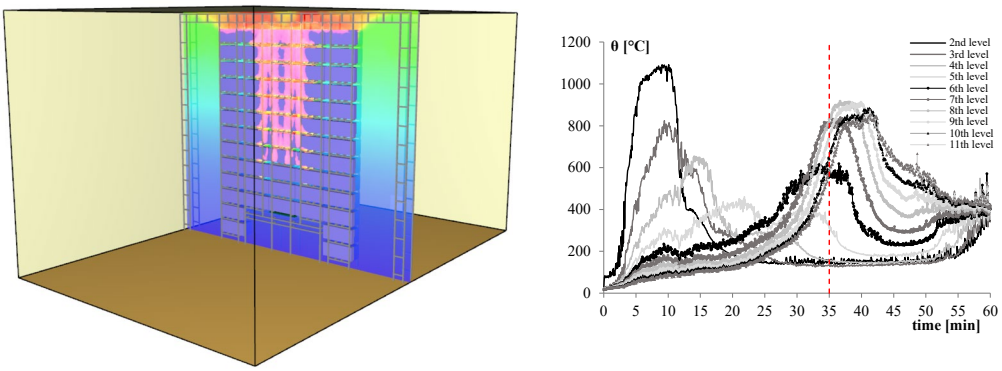

Figure 3.42. (a) Smokeview image for the simulation at 35 minutes and (b) corresponding temperatures computed by FDS.

In **Figure 3.43** the temperature distributions recorded by the AST, placed at vertical elements of the truss are illustrated, where it is possible to observe that the central ones (1,2,3, and 4), are heated with a little delay time among them. While moving towards the lateral ones (5,6,7 and 8) lower temperatures are reached and all the elements are heated together. Finally, for the elements above the aisles (9,10,11, and 12), the maximum temperatures are lower since there is no combustion material in that area.

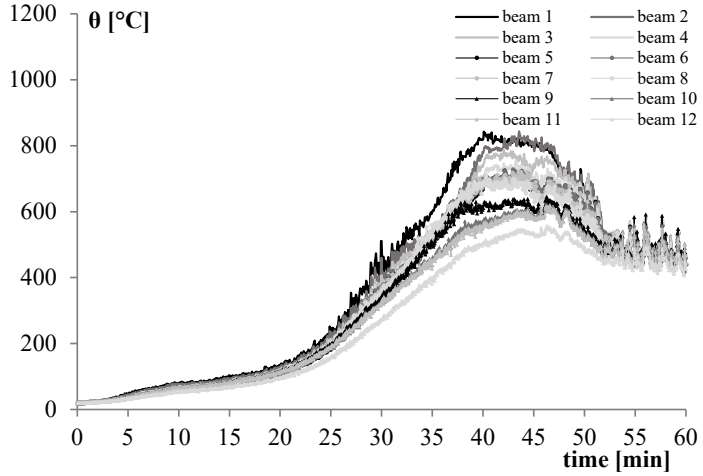

Figure 3.43. Temperature distributions computed by FDS at the vertical beams of the truss.

The same aspects can be observed also in the temperature distributions recorded by the AST, placed at the bottom chord of the truss, which are illustrated in the following **Figure 3.44**, where it is possible to see how from the elements 6 to 9 which are the ones over the aisle the temperature peak is lower than the ones reached for the elements over the five shoulders.

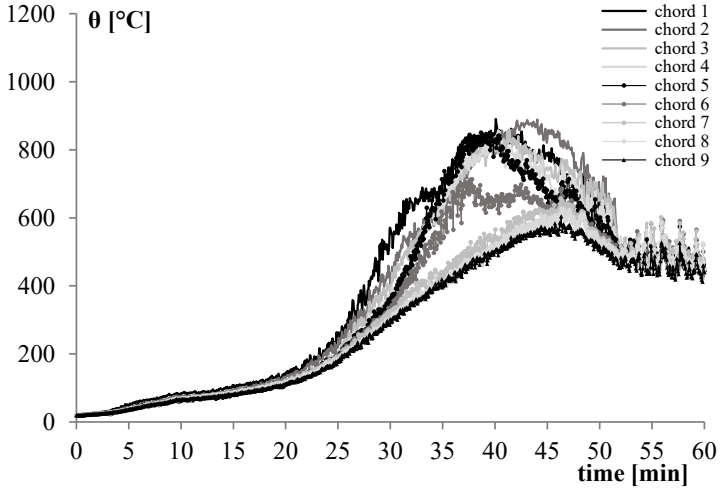

Figure 3.44. Temperature distributions computed by FDS at the bottom chords of the truss.

The same considerations can be done by analysing the results obtained for the

uprights. In particular, **Figure 3.45** shows the results obtained for the central shoulder where the fire started (III shoulder **Figure 2.15**).

It is worth saying that since the propagation occurred within the aisle, the ASTs for the adjacent shoulders, were placed for both the uprights of the single shoulder. Thus, in the **Figure 3.46** and **Figure 3.47** the temperature distributions for the adjacent shoulders, next to the ignition (II and IV shoulders) are illustrated for both the uprights on the right and on the left, where _NEAR states for near the fire, which means the upright on the left of the shoulder, while _FAR means the upright on the right of the shoulder. From the results showed in both **Figure 3.45** and **Figure 3.46**, it is possible to confirm that all the HRR of the first level is used for the combustion, confirming the results showed for the horizontal beams, indeed the uprights reached 400°C in the first 5 minutes of the fire propagations. Moreover, the results for the uprights show that after the combustion of the first level the fire started the propagation within the aisle, the AST for the 2nd and 3rd levels, on the left of the lateral shoulder (**Figure 3.46**) recorded, indeed, temperatures higher than the corresponding ones of the central shoulder (**Figure 3.45**). While, after 10 minutes, it is possible to see that the propagation occurs for all levels sequentially.

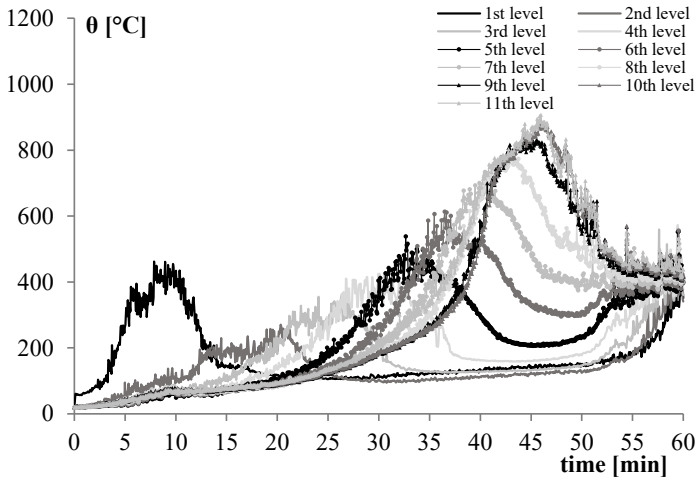

Figure 3.45. Temperature distributions computed by FDS at the uprights of the central shoulder (III shoulder).

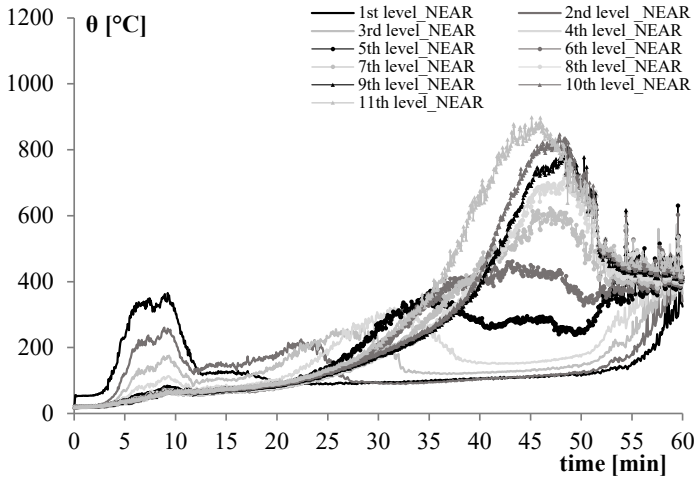

Figure 3.46. Temperature distributions computed by FDS at the upright on the left of the adjacent shoulders (II and IV shoulders).

From the results shown in **Figure 3.47** it is possible to see that in the case of the upright on the right of the lateral shoulder, which means far from the ignition, the propagation changed, in the sense that, once the fire reached the ceiling and thus the 11th level it started to propagate to the levels below.

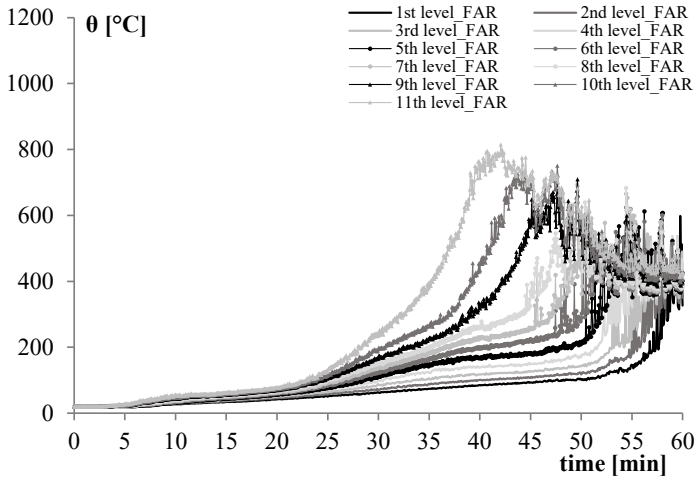

Figure 3.47. Temperature distributions computed by FDS at the upright on the right of the adjacent shoulders (II and IV shoulders).

The same considerations can be made for the external shoulders (I and V shoulders **Figure 2.15**), where the results are shown in **Figure 3.48** and **Figure 3.49**.

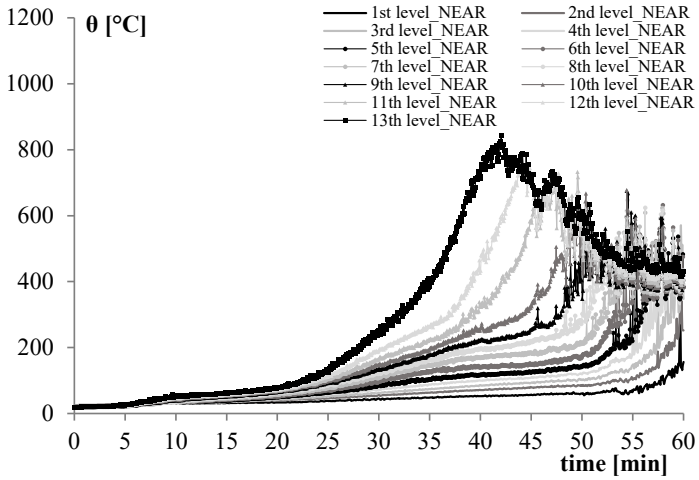

Figure 3.48. Temperature distributions computed by FDS at the upright on the left of the adjacent shoulders (I and V shoulders).

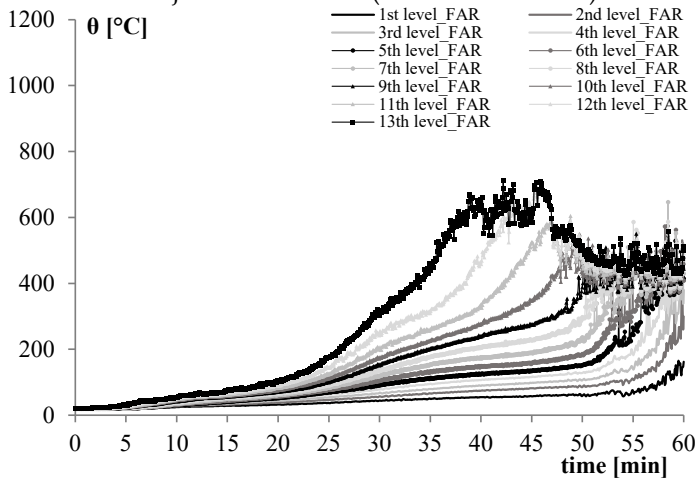

Figure 3.49. Temperature distributions computed by FDS at the upright on the right of the adjacent shoulders (I and V shoulders).

The results confirmed that, since these shoulders are both far from the ignition the propagation occurs in the same manner for the upright on the left and on the right, also in this case it is possible to see that the fire first reached the upper level and after it started to propagate to the bottom ones. It is worth saying that even though, the temperature propagation is the same for the external upright, a lower temperature peak was reached for the first tree levels (13th, 12^{th,} and 11th).

3.5. Benchmarks between fire models

The following figures compare the fire curves obtained using the previously illustrated fire models: the multi-cells zone model (CFAST), where the fire propagation was defined using the vertical and horizontal propagation times evaluated with the analytical criterion. The FDS model, in which the same fire scenario was modelled using FDS software; allowing the analysis of fire propagation without the default delay times.

In particular **Figure 3.50** shows the temperature distributions recorded by the FDS and CFAST's devices placed at the horizontal beams of the central shoulder for the first 2nd, 3rd, and 4th levels.

Thanks to these comparisons it is possible to underline some aspects already analysed previously. By comparing the temperature distributions for the 2nd level **Figure 3.50**a, it is possible to see how the proposed multi-cell zone model (CFAST) can properly predict the fire duration, in particular the temperature calculated in CFAST regarding the maximum temperature, is coherent with the one recorded by FDS. The heating phases are not too different, indeed only a time delay is observed in the FDS temperature. Moreover, the first parts of the two cooling phases are very similar, while after 13 minutes, the temperatures start to diverge.

The comparison of the temperatures for the 3rd level (see **Figure 3.50**b) allows a first validation of the fire propagation times calculated analytically and used in the zone model. Indeed, the heating phases of the two distributions start at the same time, and also the fire duration is similar, with the cooling phases similar to around 15 minutes. The comparison shows that the temperature obtained from the multi-cell zone models is characterized by the same temperature peak for all the levels, unlike the FDS model where the temperature peaks are lower due to the chimney effect that changes the fire propagation.

These aspects are more evident for the 4th level (see **Figure 3.50**c) due to this different fire propagation also the heating phase is different for the two fire models.

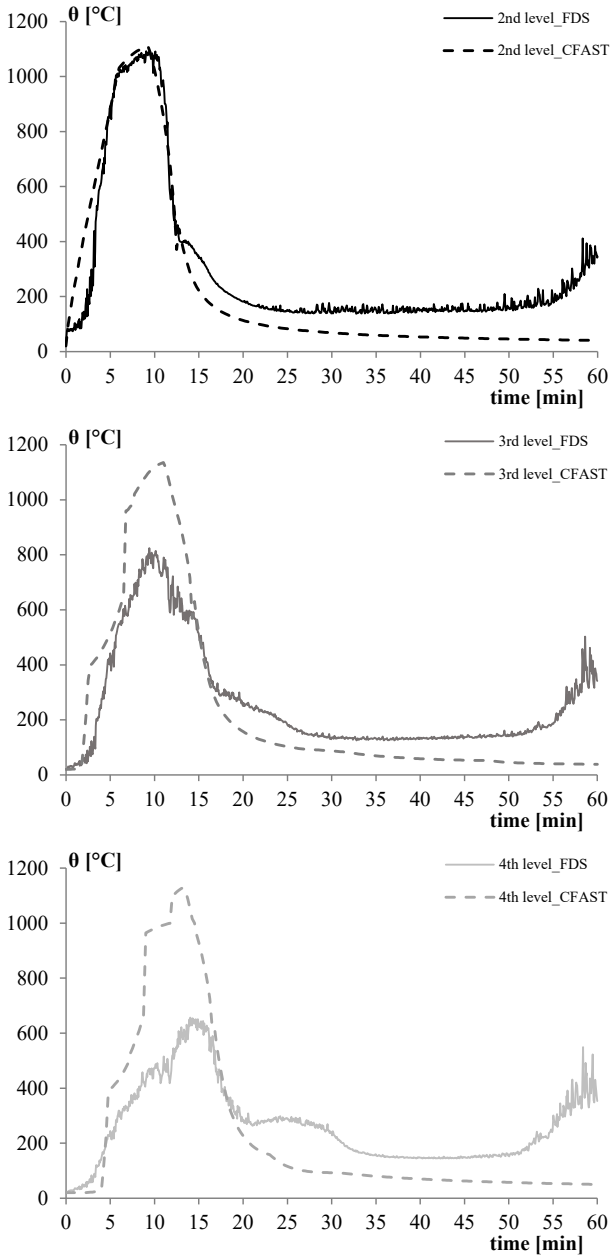

(a)

(b)

(c)

Figure 3.50. Temperature distributions computed by FDS and CFAST at the horizontal beams of the central shoulder for the first three levels.

The CFD model in this case underlines on one hand the ventilation effect, which may play a very important role in changing the fire traveling trajectory, but on the other hand, allows the validation of the fire propagation times calculated analytically and used in the multi-cells zone model.

Figure 3.51 shows the temperature distributions recorded by the FDS and CFAST devices placed at the uprights of the central shoulder for the first 2nd, 3rd, and 4th levels. In this case, since the propagation occurred within the aisle, in the comparisons the temperature distributions recorded from the ASTs of the adjacent shoulders are also provided. "FDS_left" stands for the AST placed on the left of the aisle and "FDS_right" stands for on the right of the aisle and so belongs to the adjacent shoulder.

More or less the same considerations made for the horizontal beams can be made also in the case of the uprights. By comparing the temperature distributions for the 1st level **Figure 3.51**a, it is possible to see how the proposed multi-cell zone model (CFAST) can properly predict the fire duration, whole the temperature calculated in CFAST regarding the maximum temperature, is higher than the one recorded by FDS. The heating phases are not too different, indeed only a time delay is observed in the FDS temperature, while the two cooling phases are very similar. The two FDS temperature distributions are similar with the distribution recorded from the thermocouple on the right that better fits with the CFAST ones.

The comparison of the temperatures for the 2nd level (see **Figure 3.51**b) allows another validation of the fire propagation times calculated analytically and used in the zone model. Indeed, the heating phases of the two distributions start at the same time. In this case, the two FDS distributions are different and only the one on the right can be compared with the CFAST one. These aspects are more evident for the 3rd level (see **Figure 3.51**c) due to this different fire propagation also the heating phase is different for the FDS distribution.

Finally, from these comparisons, it is possible to see how, the results are similar for the first moments of the fire, at the same time before then the chimney effect starts, the analytical time propagations are similar to the numerical ones obtained from FDS. On the other hand, due to the chimney effect in the FDS

model, the multi-cell zone model temperatures are higher and so on the safe side.

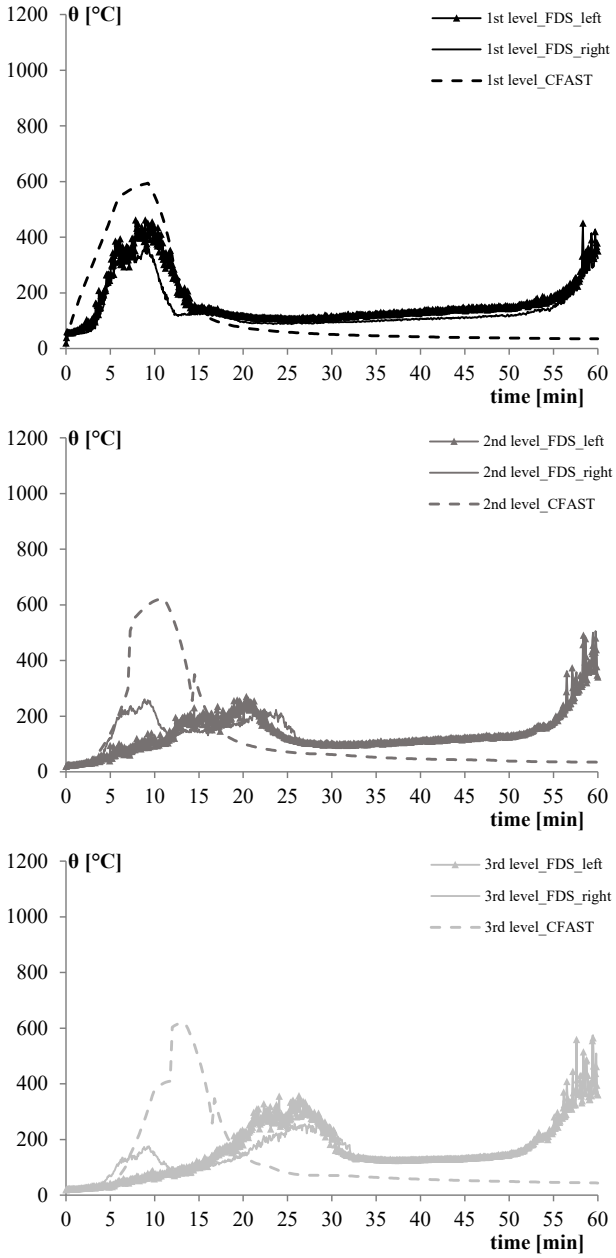

Figure 3.51. Temperature distributions computed by FDS and CFAST at uprights of the central shoulder for the first three levels.

Chapter 4

4. Thermo-mechanical modelling of ARSWs

This chapter presents the second part of this work regarding the study of a typological self-supporting automated warehouse in fire conditions, thus after defining the fire modelling, it was necessary to evaluate the mechanical response and the analysis of the collapse mechanism. For this reason, several thermo-mechanical analyses were performed using the SAFIR software. These analyses were carried out by considering different types of fire models, such as localized fire (LOCAFI and Heskestad method), the results of the zone model by using CFAST software, and the results of the computational fluid dynamics using the FDS software. All these analyses discussed in §4.3 have shown that to correctly estimate the collapse times and the shape of the global mechanism, it is necessary to go beyond the time of collapse provided by the software, by manually eliminating the elements that collapse. §4.4 shows an iterative procedure based on subsequent implicit thermo-mechanical analyses to obtain a progressive collapse by using SAFIR; this aspect has been analysed and validated by modelling the same structure with a second structural software, ABAQUS CAE that allows the implementation of implicit analyses and explicit ones, by obtaining the same results but with an automatic procedure.

4.1. Steel structures collapse analysis

Besides the choice of the fire model the types of methodologies of analysis that the designer adopts to properly interpret it, influence the results of a fire-induced progressive collapse.

Nowadays, the well-known Finite Element Analysis (FEA) is the most used tool to perform structural analysis in fire conditions by using advanced calculation models. Besides the method used to discretize the elements, the event "collapse" has a dynamic nature, as it can be highly impulsive. Trying to evaluate a building failure means making choices about the analysis type. Four approaches can be used: linear static, nonlinear static, linear dynamic, and nonlinear dynamic analyses. In the literature, there is no uniform conclusion about what type of analysis is the most suitable to use; for example, Powell [180] comparing various analysis types, concludes that the static analysis is a conservative approach to evaluating progressive collapse, while Kaewkulchai and Williamson [181] proved that the static analysis is not on the safe side.

The dynamic analysis seems the most adapted in fire conditions, moreover, when choosing a dynamic nonlinear approach, the solution scheme can be implicit or explicit. The majority of commercial FE packages work with an implicit solver only, which is the case of SAFIR developed at the University of Liège in Belgium [182]. Mei et al underline [82] how the use of the implicit approach could be seen as a limit in a fire-induced collapse analysis since the implicit solution cannot handle the numerical singularity that under-goes when the structure starts collapsing. The static analysis can be inadequate in dealing with great strains that can happen in short periods during the kine-matic. Such analyses lead to an embryonic collapse state in the best possible way. Then designers or researchers must evaluate the post-critical status by observing deformed shapes or temperatures, neglecting any dynamic interaction during the collapse. The use of the explicit solution scheme to solve singularity issues has been proposed recently by Sun et al. [29] proposed a method based on two steps: implicit static and explicit dynamic, and successfully used it to continue the analysis beyond the temporary instabilities that would cause singularities in the implicit analysis.

Moving in this context, in order to analyse all these aspects of the ARSW structure shown in §2.2.3, several thermos-mechanical analyses were performed by

using first the implicit analysis with SAFIR software and after exploring the method proposed by Mei et al [82] based on three steps static/dynamic implicit/dynamic explicit, by modelling the same structure with a second structural software, ABAQUS CAE.

4.2. Modelling structures in fires with SAFIR: theoretical background and capabilities

This section provides a general description of the SAFIR software developed at the University of Liège in Belgium [182].

SAFIR® is a software based on the finite element method (FEM), the software allows modelling the behaviour of structures in fire, considering material and geometrical non linearities, the thermal elongation, as well as the reduction of strength and stiffness of the materials at elevated temperature.

By using the Safir program, it is possible to carry out an analysis of a structure exposed to fire which consists of several steps. Indeed, the analysis of a structure in the fire situation requires the determination of the temperatures in the structure (thermal analysis), as well as evaluation of stresses, strains, and displacements (mechanical analysis). SAFIR allows performing these two types of analyses with an easy transfer of information between the two.

In particular, the strategy that the SAFIR adopts is a weak coupling from the thermal analysis to the mechanical analysis. The temperature field in the different parts of the structure is evaluated in the first step up to the end of the fire, and then the mechanical behaviour is determined in a subsequent analysis.

The temperatures influence the mechanical behaviour, but the results of the mechanical analysis do not influence the temperature distribution. This strategy is valid in most cases because temperatures strongly affect the mechanical response of structures, whereas the opposite influence is negligible except in very specific situations [182]. As a finite element program, SAFIR accommodates various elements for different idealization, calculation procedures and various material models for incorporating stress-strain behaviour. The elements include the

2-D SOLID elements, 3-D SOLID elements, BEAM elements, SHELL elements and TRUSS elements.

Before conducting the thermal analysis, the fire attack must be defined by the user and input in SAFIR as an entry. Several methods can be used to characterize the fire attack and transfer the information to the program.

For beam elements, each section is drawn by arranging a set of triangular and quadrangular elements side by side, each one made of its own material, which allows the user to draw virtually any section types. This offers more flexibility than relying on a library of predefined section types. This discretization of the section is used for the thermal analysis (calculation of the temperature at each node) as well as for the mechanical analysis (determination of forces and stiffness in the section based on the temperatures in each element used in the thermal analysis which will form a fibre in the beam element).

It is worth saying that SAFIR does not have any failure criterion embedded as such. The simulation will run until the time specified by the user is reached or until it cannot converge to a state of equilibrium for the structure, or it encounters numerical problems at the material level. It is then the responsibility of the user to judge whether the last converged step corresponds to the fire resistance time or to a premature numerical failure.

The problem to be solved is defined in input ASCII files. These can be constructed using a text editor or using the general-purpose graphic pre-processor GiD [183] for which specific interface routines with SAFIR have been developed. SAFIR is written in FORTRAN language, versions 77 and 90, and is provided as an executable file to run in a Windows© environment. The results are provided in two ASCII files: one user-readable file that can be directly examined in a text editor and one file organized in an XML format that can be visualized by the accompanying graphic post-processor DIAMOND. This latter format allows visualizing the results also by any other graphic post-processor.

To accommodate large models in reasonable computational times, the system of equations inherent to the finite element method is solved using a sparse matrix solver. The direct solver PARDISO [184] is adopted by using a symmetrical matrix of the system. **Figure 4.1** shows a schematic representation of the different

steps and files that may be involved in the case of a frame structure comprised of two types of different sections, one for the columns and one for the beam.

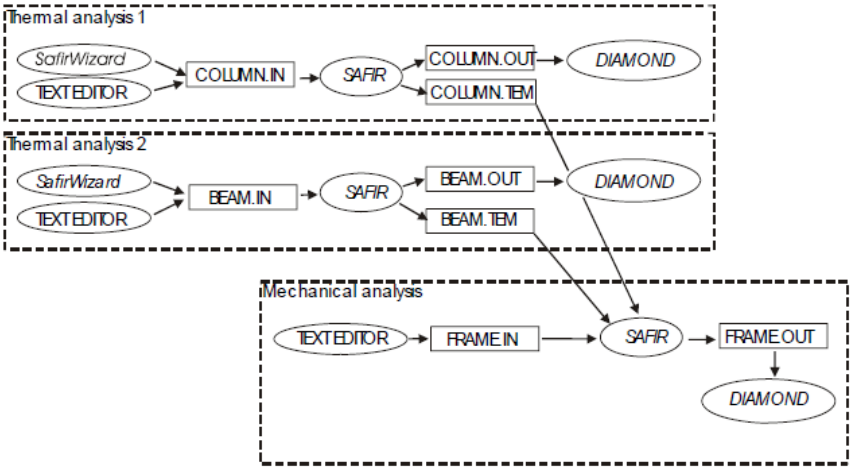

Figure 4.1. Workflow of a thermo-mechanical analysis in SAFIR [185]

The next sections give more detailed information about the thermal analysis, the mechanical analysis, and the constitutive material models available in SAFIR.

4.2.1. Thermal analysis

The first step referred to as "thermal analysis", allows the evaluation of the temperature distribution inside the structural members. In particular, the thermal analysis is made using 2-D SOLID elements, to be used later, on cross-sections of BEAM elements or on the thickness of SHELL elements. For the first case, the temperature obtained is non-uniform in the cross sections of the beam element, but there is no heat transfer along the axis of the beams. A general structure with different structural elements will require separate thermal analyses for each of these section types. From these analyses, the temperatures across the cross-section are obtained and stored for subsequent structural analysis.

Linear isoparametric finite elements with classical shape functions are used to represent the geometry, as a function of the coordinates of the nodes, and the

temperature field in the element, based on the temperature at the nodes [185]. Heat transfer by conduction according to the Fourier law is assumed in the material.

The weighted residual method is used in the finite element formulation of the problem and, summing the contributions from all the elements, **Eq. 4.1** is obtained, which describes in matrix form the equilibrium of heat fluxes in the structure at any given instant in time:

$$[K]\{T\} + [C]\{\dot{T}\} = \{g\} \tag{4.1}$$

Where:

[K] = matrix of the conductivity.

[C] = matrix of the capacity.

$\{\dot{T}\}$ = vector of the temperatures at the nodes.

$\{g\}$ = vector accounting for the heat exchanges at the boundaries.

Numerical integrations by the method of Gauss are performed on the volume of the element to evaluate the conductivity and the capacity matrix.

The fact that the thermal properties are temperature-dependent is considered, including the fact that these thermal properties vary in the element, i.e., from one point of integration to another. The **Eq. 4.1,** expressing the thermal equilibrium at a given time, must be integrated in time to yield the evolution of the temperatures during the fire. This is done by the implicit single step scheme of the generalized central point [185]. Convergence is checked considering the residue in **Eq. 4.1**, i.e., the out of balance thermal flux. If the equilibrium is not satisfied, a correction of the temperatures must be applied. This correction is evaluated by setting the linearized form of the residue (using Newton method) to zero. Iterations are then performed until the residue and/or the corrections made on the temperature reach an acceptable low level.

4.2.1.1.Boundary conditions for thermal analysis

The fire action is given as input data in SAFIR. To model the effect of the fire on the structure, it is necessary to prescribe boundary conditions for the thermal

analysis that can have various forms. In particular, the following boundary conditions can be introduced:

First option: It is possible to prescribe the evolution of the temperature as a function of time at different nodes. This capability is particularly useful for benchmark purposes, or when it is necessary to apply the temperatures recorded during a fire test in the mechanical model as closely as possible because the focus of the analysis is on the mechanical response.

Second option: It is possible to prescribe the evolution of the temperature of hot gases that surround the section, in the form of a time–temperature relationship. All the standard fire curves are already implemented in SAFIR, but it is possible to define a user-defined time–temperature relationship contained in a "my fire.fct" file.

The heat flux exchanged between a boundary and the hot gas is computed using the Eurocode 1 part 2 [1] formula with a linear convective term and a radiation term:

$$q_n = \alpha_c \cdot (\theta_g - \theta_s) + \varepsilon \cdot \sigma \cdot \left[(\theta_g + 273)^4 - (\theta_s + 273)^4 \right] \quad (4.2)$$

Where:

α_c = the coefficient of heat transfer by convection [W/m^2K^4];

θ_g = the gas temperature in the fire compartment, or near the member [°C];

θ_s = the temperature of the boundary [°C];

ε = emissivity of the material.

σ = the Stephan Boltzmann constant equal to $5{,}67 \cdot 10^{-8}$ [W/m^2K^4];

Third option: It is possible to prescribe a boundary condition as a heat flux. The heat flux from one or several localized fires can be considered, different models are available to represent localized fires and directly transfer the generated heat flux in SAFIR, these flux constraints are named either "Hasemi" or "LOCAFI".

For the Hasemi and the LOCAFI models, each fire source is described in a .txt file, by:

- the 3D position of the source in the structure (where the flame originates),

- the vertical elevation of the ceiling (used to check whether the flame touches the ceiling or not);
- the diameter of the circular fire source (as a function of time);
- the rate of heat release of the fire (as a function of time). In case of multiple fires, the input fluxes from each fire are simply added.

All results are also organized in the *.tem files in the same way as for the Hasemi model and LOCAFI model. The structure can be subjected to one or several local fire sources. In case of multiple fires, the fluxes from each fire are simply added.

Fourth option: finally, the thermal flux can be imported from a computational fluid dynamics (CFD) calculation owing to a dedicated interface [186].

The second and the third options will be further analysed in the following paragraphs.

4.2.2. Mechanical analysis

The second step referred to as "structural analysis" is carried out to evaluate the response of the structure due to static and thermal loading. For each calculation, the loads are applied to the structure, described as. BEAM, TRUSS, and SHELL elements. The temperature history of the structure, due to fire, is read from the files created during the temperature analysis. As the computation strategy is based on a step-by-step procedure, the following information can be obtained until failure occurs in the structure:

- Displacement at each node of the structure.
- Axial and shear forces and bending moments at integration points in each finite element.
- Strains, stresses, and tangent modulus in each mesh at integration points of each finite element.

The mechanical problem can be solved in a *quasi-static manner* using the following equation:

$$\{\Delta F\} = [K]\{\Delta u\} \tag{4.3}$$

Where:

[K] is the stiffness matrix of the structure,

$\{\Delta F\}$ the vector of incremental applied nodal forces;

$\{\Delta u\}$ the vector of incremental nodal displacements.

The vector of incremental displacements Δu is divided in two parts, one for which the displacements must be determined from **Eq. 4.1** and one that contains the displacements imposed by the user.

The vector of incremental forces ΔF is also divided into two parts, one where the variation as a function of time is imposed by the user and one where the reaction is calculated (at the nodes where the displacement is imposed). During a fire situation, the applied loads are normally kept constant, but SAFIR allows varying the forces as a function of time if desired.

The stiffness matrix is usually taken as the tangent matrix, recalculated at every iteration of every time step (pure Newton–Raphson procedure). The iterative procedure to integrate in time from one converged time step n (point A) to the next step n + 1 is illustrated in **Figure 4.2**. At converged time step n, the stress-related strain is noted ε_σ (T_n) and the plastic strain ε_{pl}.

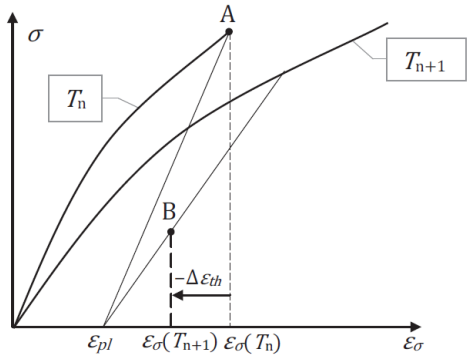

Figure 4.2. First step of the time integration procedure in SAFIR

The procedure is as follows:

1. The increment of thermal expansion at every point of integration is calculated on the base of temperature increments from n to n + 1.
2. The properties of the materials (strength, stiffness, etc) are updated corresponding to the new temperatures. As a result, the virgin stress-strain law

($\sigma - \varepsilon_\sigma$) is different at temperature T_{n+1} compared with T_n (**Figure 4.2**).

3. Plastic strains ε_{pl} at the points of integration, as well as nodal displacements, are kept constant at the beginning of the step. Because the displacements are frozen, the total strains are also constant. However, the thermal strain component in the total strain has changed by $\Delta\varepsilon_{th}$ because of the temperature variation. Therefore, a new value of the stress related strain e s ε_σ (T_{n+1}) is calculated. In case of temperature increase, the thermal strain increases so the stress related strain decreases (considering elongation as positive); compared to the converged step, the structure is in an artificial state of compression.
4. A new stress and a new tangent modulus are calculated as a function of the new stress related strain ε_σ (T_{n+1}) considering the new material properties (stress strain law at T_{n+1}).
5. These stresses are integrated on the volume of the elements to compute the internal nodal forces which are not anymore in equilibrium with the applied nodal forces. In case of temperature increase because the displacements are constrained, the structure undergoes an internal state of out of balance compression.
6. The stiffness at the integration points is integrated to compute the stiffness matrix of the structure.
7. The out-of-balance forces are applied to the structure, leading to incremental displacements, new strains (stress related component), new stresses and new nodal forces.
8. The procedure described under point 5 to 7 is repeated several times at constant temperature until the convergence criteria is satisfied.
9. Plastic strains are updated after convergence.

The convergence criteria are based on the energy norm rate (ENR) calculated as the vector product of the incremental forces and the incremental displacements at each iteration. The ENR of the current iteration is compared to the cumulated ENR from the beginning of the calculation and convergence is assumed when the ratio of both is lower than a limit defined by the user.

It must be stressed that at every iteration to reach equilibrium in the structure,

internal iterations may be required in each point of integration to find the stress that corresponds to the strain and temperature (Step 4 in the procedure above), in accordance with the material constitutive law.

The quasi-static procedure that has been described here is valuable if the structure is relatively stable. Yet this procedure fails when the structure or a part of it is not statically stable. The displacements increase, whereas the internal nodal forces decrease, and it is impossible to find a position for which the equilibrium is satisfied. This may prevent the software to provide a good insight into the failure mode because the computation stops at a time when the displacements are limited and their evolution in the post-critical phase are not accessible. More than that it may occur that simulation stops at an early stage because of the occurrence of a local instability (buckling of an individual bar in a statically indeterminate structure, for example). To circumvent this problem, a dynamic equation has been introduced:

$$F_{ext} = [K]u + [M]\ddot{u} \tag{4.4}$$

Where:

[M] is the matrix of masses of the structure (rendered diagonal in SAFIR) and $\ddot{u}$ the vector of nodal accelerations.

The damping matrix has not been introduced in Eq. (4.4) because it is usually computed as a linear combination of the mass matrix and the stiffness matrix, and this may create problems when the stiffness matrix is not anymore positively defined. Instead, numerical damping is being used (Newmark method with = 0.45 and = 0.80). More information can be found in [187].

Because the mass matrix is constant the procedure simply implies computation of the nodal velocities and accelerations and utilization of a modified matrix for the system of equations.

An automatic procedure has been established in the software that continuously monitors and controls size of the time steps based on the number of iterations required to converge and on an automatic return to the previously converged step when convergence is not possible within a limited number of itera-

tions. The time step is automatically reduced or increased depending on the difficult or easy convergence. The user must introduce the value of the initial time step, the maximum value of the time step to be accepted, the minimum value at which the simulation stops if convergence cannot be achieved and the final time when the simulation stops even if stability is still ensured.

4.3. Finite element model by using SAFIR software.

A typological frame in the cross-aisle direction of the ARSW structure shown in §2.2.3 was modelled in SAFIR by using *beam* elements. All the structural section types considered are listed in **Table 2.2**. The structure was analysed in 3D space by blocking out-of-plane displacements thanks to restraints. At the structural base, fixed restraints were considered while the braces, horizontal beams of the shoulders, and diagonal and vertical elements of the truss were modelled as pinned beams.

The cross-aisle view of the FE model in the GID environment is shown in the following **Figure 4.3**.

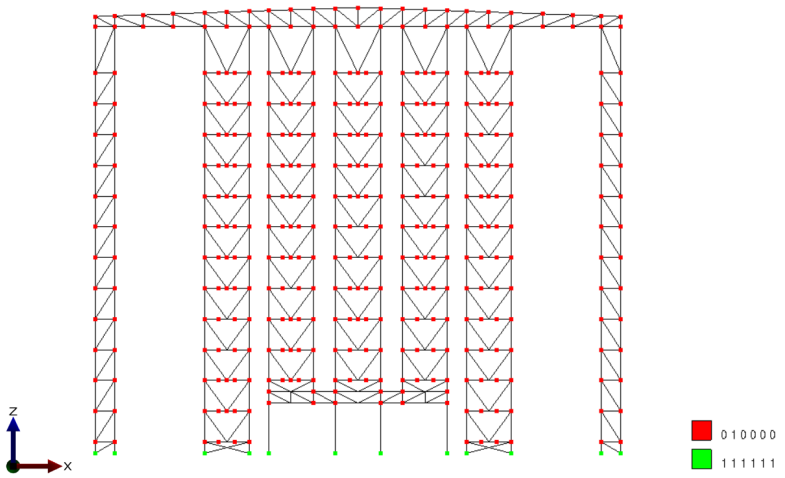

Figure 4.3 The cross-aisle view of the FE model in the GID environment.

The combination of actions for accidental situation given by NTC2018 [1] was considered:

$$G_{k1} + G_{k2} + \sum_{i=1}^{n} \psi_{2i} Q_{ki} + A_d(t) \quad (4.5)$$

Where:

$G_{k,1}$ is the structural loads;

$G_{k,2}$ is the non-structural loads;

$Q_{k,i}$ are the characteristic value of the variable loads on the structure;

A_d (t) are the indirect fire actions;

$\psi_{2,\,i}$ is the combination coefficient for the quasi-permanent value of the i th variable action, in the case of the industrial buildings, are equal to 0.8

For this reason, the unit loads equal to 25.000 N were multiplied by 0.8 and applied as concentred forces at the four intersections between uprights and beams. Since SAFIR doesn't consider the self-weight of the element, each force has been added to the weight of the structural element that converges in the node by referring to its section and its length. In this way, many different loads have been defined to be applied in each node because of the variety and the quantity of the section types. Regarding the truss and the lateral shoulder, to the self-weight was added the weight of the sandwich panels equal to 22 kg/m². All the loads in Newton (N) obtained in this way are shown in the following **Figure 4.4**.

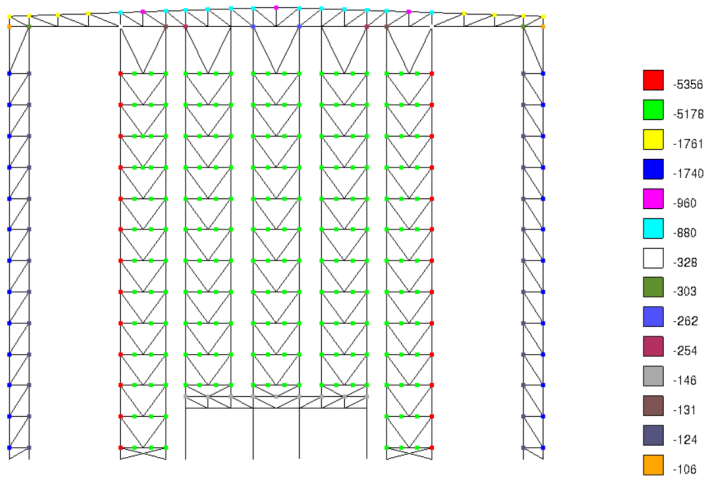

Figure 4.4 Intensity of loads (in N) applied in the FE model.

In all the considered cases, dynamic analyses were carried out by considering the nonlinear geometry and material nonlinearity. In addition, it should be noted that, for a more correct modelling of Class 4 steel elements through beam elements, all elements have been assigned a modified constitutive low to consider in beam-based numerical models, local instabilities that can occur in thin sections [188]. The stress-strain relationship in compression is modified by a reduction in the limit of proportionality (f_p), the effective yield strength ($f_{y,eff}$) and the strain corresponding to the beginning of the horizontal plateau (see **Figure 4.5**).

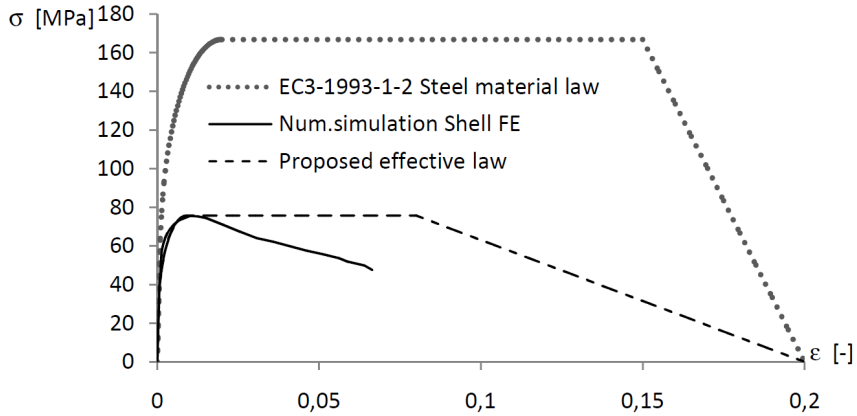

Figure 4.5. Effective law proposed by Franssen et al. [188] versus actual steel material law from the EC3 part 1-2.

The elastic stiffness during unloading after the first plasticisation in compression is also reduced according to a damage model to consider the plastic deformation of the plate. The level of reduction depends on the slenderness of each plate that belongs to the section and the conditions at the edge of the plate, this means that for every section type listed in the **Table 2.2** a new material was created and associated with the mechanical analyses.

4.3.1. Fire scenario with nominal fire curve ISO834

Other than the natural curves obtained with the different fire models described in the previous chapter, a fully developed fire using ISO 834 fire curve was considered. In this way, each cross-section has been subjected to the same

fire curve, substantially reducing the number of .TEM files to 18 as the number of the cross-sections for the cross-aisle frame. Once the thermal results were obtained the mechanical part was carried out.

The following **Figure 4.6** shows the deformed shapes of the structure at 432 seconds (i.e., 7.2 minutes), which is the last step of the structural analysis provided by SAFIR, since all the structural elements are heated with the same fire curve, the deformed shape shows an expansion of all structure.

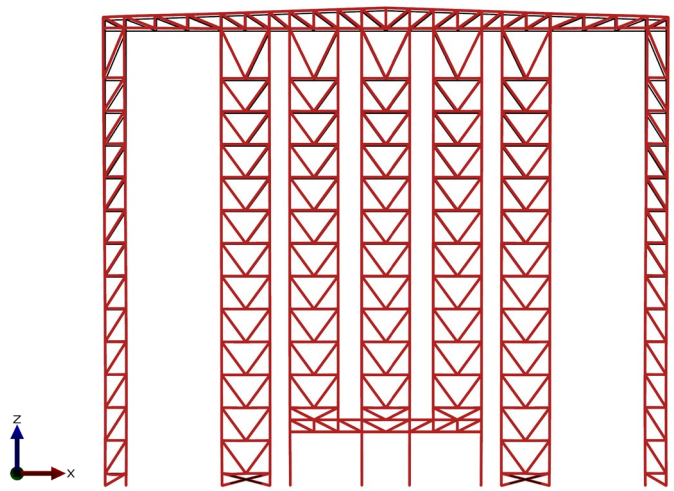

Figure 4.6. ISO834 fire curve: deformed shape at 7.2 minutes in the Diamond environment.

In order, to study the collapse, or better the reason why the analyses stopped at 432 seconds, it was necessary to study the output file provided by the software, where it was found that a critical element that could have stopped the analysis could be the transversal beam of the lateral shoulder at the first load level, which is a coupled U section 80x40mm and 2mm thickness.

Figure 4.7 shows the temperature distribution within the cross-section, obtained from the thermal analysis, where it is possible to appreciate a little temperature difference among the web and flanges.

In particular, the thermal results confirm that since this section is characterized by a high section factor A_m/V (i.e., small thickness), faster heating.

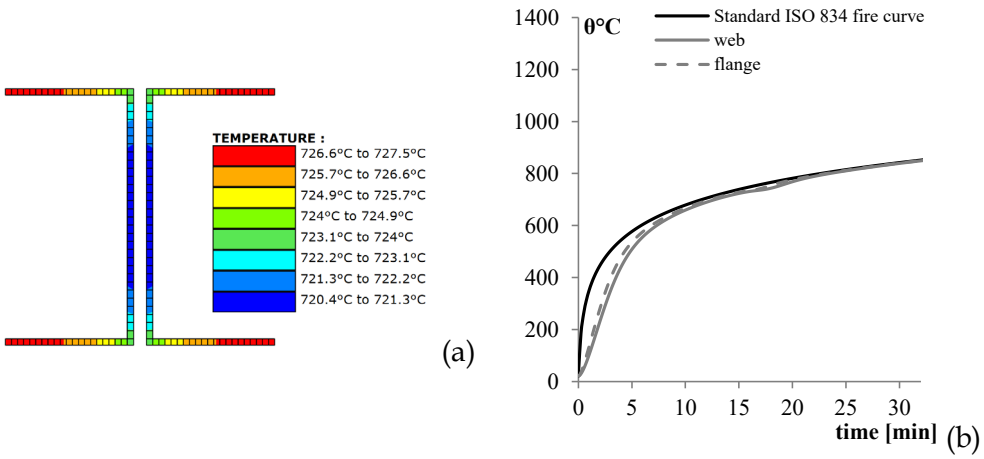

Figure 4.7. ISO834 fire curve: temperature distribution within the cross section in the Diamond environment at 7.2 minutes (a), temperature distribution over time (b).

To investigate the achievement of the capacity of the beam, the compression resistance axial force at different exposure times was calculated. To calculate the normal compressive stress strength for the Class 4 section the first step was the evaluation of the effective cross-sectional area. This one was evaluated by considering both the capacity methods explained before in §2.2.2, indicated as "Actual EC" and "New EC". In the following **Table 4.1** is shown the comparison between the area for the coupled U 80x40x2mm and the effective cross-area calculated with the effective width method, according to EC3 part 1-5 [50].

Table 4.1 ISO834 fire curve: effective cross-sectional area for the coupled U section 80x40x2mm according to the capacity methods of the actual EC3.

A	**A_{eff}**	**reduction**
[mm²]	[mm²]	
600	537	10%

Once that the A_{eff} is known it was possible to evaluate the design buckling resistance at different exposure times, by using the **Eq. 2.19,** to better evaluate these values the non-uniform temperature distribution was considered, therefore the **Eq. 2.19** becomes the following one:

$$N_{b,fi,t,Rd} = \chi_{fi} \sum_{i} A_{i,eff} \cdot k_{0.2p,\theta i} \cdot f_y \tag{4.6}$$

The following **Table 4.2** shows the results also in terms of temperature θ, the corresponding reduction factors for the 0.2% proof strength at elevated temperatures, $k_{0.2p,\theta}$.

Table 4.2 ISO834 fire curve: design buckling resistance at different exposure times for the coupled U section 80x40x2mm according to the capacity methods of the actual EC3.

time	**θ web**	**θ flange**	**$k_{p0.2,\theta,web}$**	**$k_{p0.2,\theta,flange}$**	**$N_{b,fi,t,Rd}$**
[s]	[°C]	[°C]	[-]	[-]	[kN]
0	21	21	1.00	1.00	104
3.1	353	406	0.71	0.64	69
4.0	432	479	0.61	0.55	60
4.5	467	510	0.61	0.51	56
5.0	496	536	0.54	0.45	49
5.5	521	557	0.48	0.40	44
6.0	542	575	0.43	0.36	39
6.5	561	591	0.39	0.32	35
7.0	577	605	0.35	0.29	32
7.1	579	608	0.35	0.29	31
7.2	580	610	0.35	0.28	31

Moreover, the following **Table 4.3** shows the comparison between the area for the coupled U 80x40x2mm and the effective cross-area calculated according to the capacity methods of the new EC3.

Table 4.3 ISO834 fire curve: effective cross-sectional area for the coupled U section 80x40x2mm according to the capacity methods of the new EC3.

A	**A_{eff}**	**reduction**
[mm^2]	[mm^2]	
600	324	46%

From the previous table it is possible to see how with the new expression the reduction of the effective area is higher than the one obtained with the actual EC3.

Once the A_{eff} is known, it was possible to evaluate the design buckling resistance at different exposure times, by using the **Eq. 2.27,** to better evaluated these values the non-uniform temperature distribution was considered, therefore the **Eq. 2.27** becomes the following one:

$$N_{b,fi,t,Rd} = \chi_{fi} \sum_{i} A_{i,eff} \cdot k_{y,\theta i} \cdot f_y \tag{4.7}$$

The following **Table 4.4** shows the results also in terms of temperature θ, the corresponding reduction factors of the yield strength at elevated temperature θ $k_{y,\theta}$.

Table 4.4 ISO834 fire curve: design buckling resistance at different exposure times for the coupled U section 80x40x2mm according to the capacity methods of the new EC3.

time	θ_{web}	θ_{flange}	$k_{y,\theta,web}$	$k_{y,\theta,flange}$	$N_{b,fi,t,Rd}$
[s]	[°C]	[°C]	[-]	[-]	[kN]
0	21	21	1.00	1.00	67
3.1	353	406	1.00	0.99	63
4.0	432	479	0.93	0.83	55
4.5	467	510	0.85	0.83	50
5.0	496	536	0.79	0.67	45
5.5	521	557	0.72	0.60	40
6.0	542	575	0.65	0.55	37
6.5	561	591	0.59	0.50	33
7.0	577	605	0.54	0.46	30
7.1	579	608	0.54	0.45	30
7.2	580	610	0.53	0.45	30

The previous buckling resistances calculated with both capacity methods are shown also in the following **Figure 4.8** in comparison with the axial force provided by SAFIR, where a positive axial load indicate compression in the beam

element. For the sake of clarity, the graph is followed by **Table 4.5** where the differences between the two capacity methods are shown.

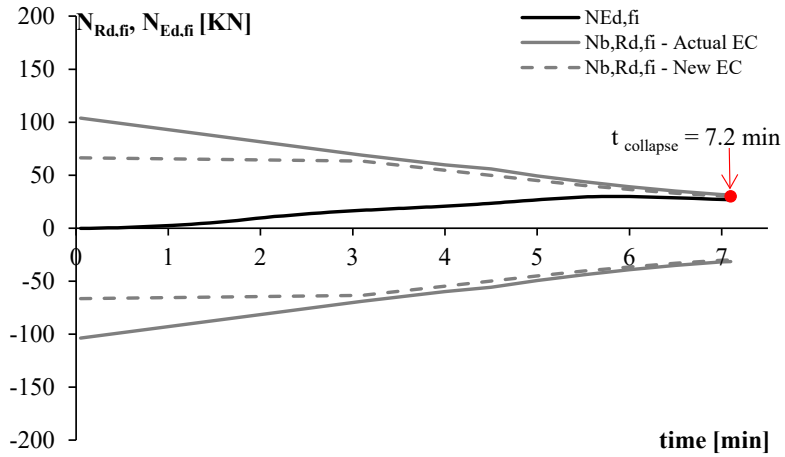

Figure 4.8. ISO834 fire curve: comparison between stress and resistance.

Table 4.5 ISO834 fire curve: difference between design buckling resistance according to the two capacity methods.

time	$\Delta N_{b,fi,t,Rd}$
[s]	[-]
0	37
3.1	6
4.0	5
4.5	6
5.0	4
5.5	3
6.0	3
6.5	2
7.0	2
7.1	1
7.2	1

This comparison confirms that the critical element is the selected transversal beam, the thermal action has induced an increment of the initial compression load, and when this one becomes equal to the reduced buckling resistance the element achieves its capacity leading the analysis to stop. Moreover, the results confirm that to consider a non-uniform temperature distribution for calculating the cross-section proprieties is essential, even though the difference between the different parts seems small.

In addition, from the comparison of the two capacity methods it is possible to see that these provide different results within the first 3 minutes, with lower values obtained with the new EC expressions, while after this time the results are very similar to each other, this because once the element reaches the 500°C the two reduction factors ($k_{y,\theta}$ and $k_{0.2p,\theta}$) become similar to each other (see **Figure 2.4**).

4.3.2. Fire scenario with zone model

The second thermo-mechanical analysis was carried out by considering the natural fire curves obtained from the proposed zone model explained in §3.3.2. In this case, each cross-section has been subjected to different natural fire curves, increasing the number of .TEM files from 18 to 82. Once the thermal results were obtained for each section, it was possible to carry out the mechanical part.

The following **Figure 4.9** shows the deformed shapes of the structure at 348 seconds (i.e., 5.8 minutes), which is the last step of the structural analysis provided by SAFIR. From the deformed shape it is possible to see that at that time the critical element could be the transversal beam of the central shoulder at the 2nd load level, which is a coupled C section 150x50x15mm and 2mm thickness, which shows a buckling shape.

Figure 4.10 shows the temperature distribution within the cross-section, obtained from the thermal analysis, where it is possible to appreciate a little temperature difference among the web, the flanges, and the lips.

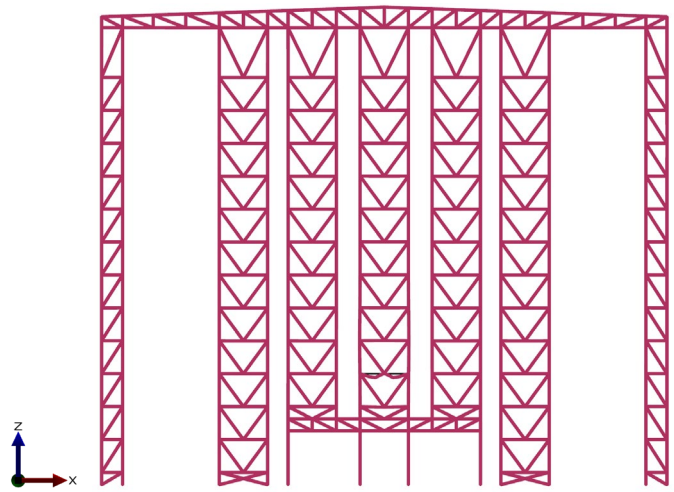

Figure 4.9. Zone model, CFAST: deformed shape at 5.8 minutes in the Diamond environment.

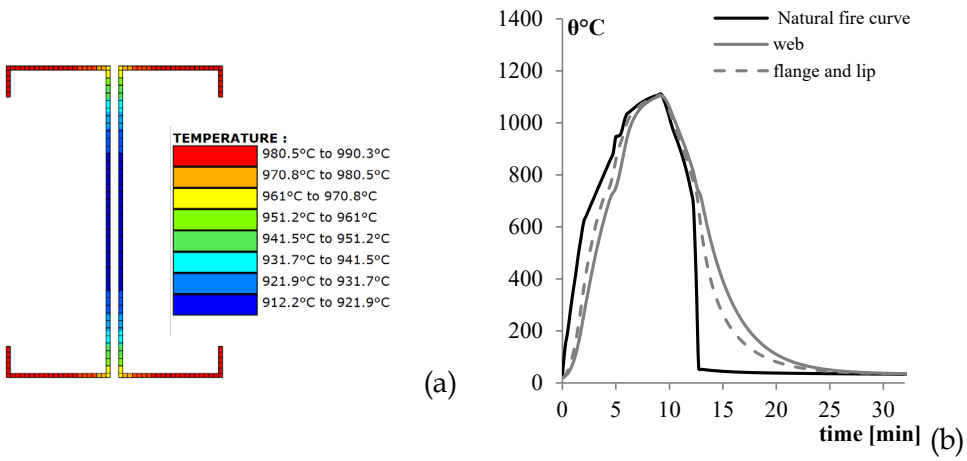

Figure 4.10. Zone model, CFAST: temperature distribution within the cross section in the Diamond environment at 5.8 minutes (a), temperature distribution over time (b).

To investigate the achievement of the capacity of the beam of the beam, the compression resistance axial force at different exposure times was calculated. To calculate the normal compressive stress strength for the Class 4 section the first step was the evaluation of the effective cross-sectional area. In the following **Table 4.6** is shown the comparison between the area for the coupled C section

150x50x15mm and 2mm thickness and the effective cross-area calculated with the effective width method, according to the actual EC3 part 1-5 [50].

Table 4.6 Zone model, CFAST: effective cross-sectional area for the coupled C section 150x50x15x2mm according to the capacity methods of the actual EC3.

A	**A_{eff}**	**reduction**
[mm²]	[mm²]	
1080	842	22%

Once the A_{eff} is known it was possible to evaluate the design buckling resistance at different exposure times, by using **Eq. 4.6.** Thus, the following **Table 4.7** shows the results also in terms of temperature θ, the corresponding reduction factors for the 0.2% proof strength at elevated temperatures, $k_{0.2p,\theta}$.

Table 4.7 Zone model, CFAST: design buckling resistance at different exposure times for the coupled C section 150x50x15x2mm according to the capacity methods of the actual EC3.

time	**θ_{web}**	**θ_{flange}**	**$k_{p0.2,\theta,web}$**	**$k_{p0.2,\theta,flange}$**	**$N_{b,fi,t,Rd}$**
[s]	[°C]	[°C]	[-]	[-]	[kN]
0.	20	21	1.00	1.00	154
1.0	76	111	1.00	0.99	153
2.0	258	362	0.83	0.70	114
3.5	546	648	0.43	0.22	43
4.0	628	714	0.25	0.12	25
4.5	699	751	0.13	0.10	17
5.0	740	835	0.11	0.06	12
5.3	770	884	0.09	0.05	10
5.5	814	916	0.07	0.05	8
5.8	862	947	0.06	0.04	7

Moreover, the following **Table 4.3** shows the comparison between the area for the coupled C section 150x50x15x2mm and the effective cross-area calculated according to the capacity methods of the new EC3. Where it is possible to see how with the new expression the reduction of the effective area is higher than the one

obtained with the actual EC3.

It is worth saying that, since in this case the section is characterized by a stiffness part (lip), it was necessary also to calculate the reduced thickness to consider the distortional buckling, with both capacity methods.

Table 4.8 Zone model, CFAST: effective cross-sectional area for the coupled C section 150x50x15x2mm according to the capacity methods of the new EC3.

A	**A_{eff}**	**reduction**
[mm²]	[mm²]	
1080	562	48%

Once the A_{eff} is known, it was possible to evaluate the design buckling resistance at different exposure times, by using **Eq. 4.7.** Thus, the following **Table 4.9** shows the results also in terms of temperature θ, the corresponding reduction factors of the yield strength at elevated temperature θ $k_{y,\theta}$.

Table 4.9 Zone model, CFAST: design buckling resistance at different exposure times for the coupled C section 150x50x15x2mm according to the capacity methods of the new EC3.

time	**θ_{web}**	**θ_{flange}**	**$k_{y,\theta,web}$**	**$k_{y,\theta,flange}$**	**$N_{b,fi,t,Rd}$**
[s]	[°C]	[°C]	[-]	[-]	[kN]
0.1	20	21	1.00	1.00	109
1.0	76	111	1.00	1.00	109
2.0	258	362	1.00	1.00	105
3.5	546	648	0.64	0.35	46
4.0	628	714	0.40	0.21	28
4.5	699	751	0.23	0.17	19
5.0	740	835	0.18	0.09	13
5.3	770	884	0.15	0.07	10
5.5	814	916	0.10	0.06	8
5.8	862	947	0.08	0.05	7

The previous buckling resistances calculated with both capacity methods are

shown also in the following **Figure 4.11** in comparison with the axial force provided by SAFIR, where a positive axial load indicate compression in the beam element.

This comparison confirms that the critical element is the selected transversal beam, the thermal action has induced an increment of the initial compression load which corresponds to an expansion of the beam, after 3 minutes the load starts to decrease, and the beam starts to deflect inward, at this point the section has reached a temperature equal to 400°C more or less and so the steel resistance starts to decrease. The load decreases until 5.8 minutes with an inward deflection for a tension load, with a little catenary effect, for the beam.

Also in this case, it is possible to see that the two capacity methods provide different results within the first 2 minutes, with lower values obtained with the new EC expressions, while after this time the results are very similar to each other.

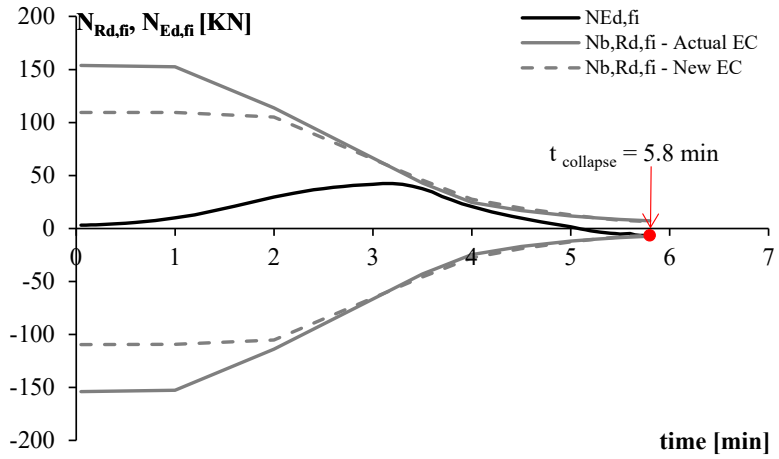

Figure 4.11. Zone model, CFAST: comparison between stress and resistance.

4.3.3. Fire scenario with localized models

Since the literature assess that the most indicated simplified fire model for a member outside the fire area is the localised model [189], the third thermo-mechanical analysis was carried out by considering these types of models, which

are implemented in SAFIR like different boundary conditions for thermal analyses as explained before in §4.2.1.1.

In SAFIR, the flux constraint "Hasemi" allows computing the flux applied to each point of integration (POI) of the steel beams based on the simple Hasemi model. While the flux constraint "LOCAFI" allows computing the flux by using the solid flame model. It is worth noting that the Heskestad model is embedded in the flux constraint named "LOCAFI". With the flux constraint "LOCAFI" applied, the heat transfer computation in SAFIR automatically shifts between the virtual solid flame model and the Heskestad model considering the relative position of the point of integration (POI) and the fire flame. For members in the axis of the flame, thus when the POI is in the flame, the Heskestad model is applied. Hence, the heat flux to the member is then evaluated considering both the convective flux, with the flame temperature, and radiative heat flux with this temperature, while a view factor of 1 is considered.

The flame temperature is calculated by the Heskestad model [1] in the centreline of the flame at the height of the POI. When the POI is located outside the flame, only the radiative heat flux is considered with the LOCAFI model.

4.3.3.1.Heskestad/LOCAFI model

In SAFIR the geometric method of the LOCAFI project developed by [108] has been implemented as a geometric method that compared to the simplified model is based on the numerical integration of some integral inside the model. The method is divided into two global steps; calculation of the incident heat flux received by a section, then calculation of the temperature of the section itself.

In the case of a localized fire, this thermal heat flux is strongly dependent on the relative position of the fire source and the vertical member.

The LOCAFI project allowed the development of a method for the vertical member that is outside the fire area with a distinction between parts located inside the smoke layer under the ceiling and those outside the layer. Indeed, in the case of a localized fire, if a vertical member is not engulfed by the flames, the

convective heat flux is negligible, and for this reason the flames produced by the localized fire affect mainly an exposed member through the radiative heat flux.

Nevertheless, this is not true in the smoke layer that spreads under the ceiling and where the convective heat flux cannot be neglected compared to the radiative heat flux. For a localized fire, the width of the hot layer is small compared to the height of the compartment. Thus, the convective heat fluxes are limited over a reduced length of the member. Because of this, the LOCAFI method provides two configurations: sections of the member outside the smoke layer and sections of the member inside the smoke layer.

Thus, the most important part of the modelling, in the LOCAFI method, concerns the radiative heat flux, this one has been modelled by using the concept of the virtual solid flame, i.e., the flame has seen a solid surface that radiates toward the member.

The main point is the definition of the flame shape and its radiative properties:

1) The characteristics of flame are affected mainly by the area of combustible that burns and by the energy released by the combustion, depending on these characteristics two situations are considered, flames impact the ceiling and flames do not impact the ceiling. Two shapes of the virtual solid flame are investigated: a cylinder and a cone (see **Figure 4.12**). The characteristics of the solid flame, such as the radiative properties (emissivity and temperature) and geometric properties (height, diameter) are calculated using the equation still available in the Eurocode [1] and shown before.

   As the HRR increases, the flame length will also increase up to the ceiling and at this point the flame may spread under the ceiling. Thus, while the lower part of the flame remains unchanged, an additional part is added under the ceiling, in the method a disk centred on the flame axis is used (see **Figure 4.12**).

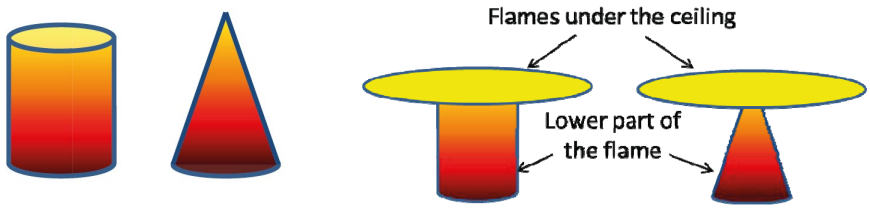

Figure 4.12. Cylindrical flame and conical shape for a flame not impacting the ceiling (a) and a flame impacting the ceiling (b) [108].

2) Once the flame shape and its properties are known, the next step is the calculation of the radiative heat flux received by a structural member. This step is divided into two other steps, in the first step, columns are modelled as vertical members with an equivalent rectangular shape, independently of their original shape, this allows for taking the shadow effect into account. In the second step, the vertical member is discretized into a several sections (see **Figure 4.13**).

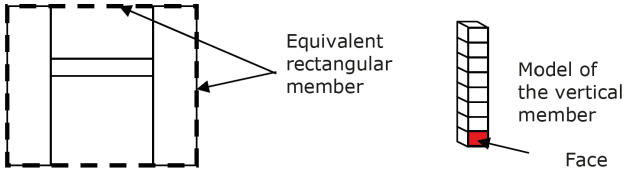

Figure 4.13. H column modelling and modelling of a vertical member [108].

For a rectangular section, the heat flux is determined for the four faces and a mean value is calculated for the whole section by averaging the heat fluxes of faces by their width. For a specific face, the radiative heat flux received is evaluated by dividing the solid flame into small parts where the radiative properties are constant. **Figure 4.14** shows the divisions (bands) of the solid flame if the flame is impacting or not the ceiling. The radiative heat flux received by a face is the sum of all these small parts, evaluated by the following equation:

$$flux_{flame \to face_i} = \sum_{b_j} \sigma \cdot \varepsilon \cdot \left(\theta_{f,j} + 273\right)^4 \cdot F_{b_j \to face_i} \tag{4.8}$$

Where:

ε is the member emissivity;

$\theta_{f,j}$ is the temperature of the band b_j in [C°];

$F_{b_j \to face_i}$ is the configuration factor between band b_j and face i; the configuration factor measures the fraction of the total radiative heat leaving a given radiating surface that arrives at a given receiving surface, its value depends on the size of the radiating surface, on the distance from the radiating surface to the receiving surface and on their relative orientation. The mathematical formulation of the configuration factor involves a surface integral, which can be computed through a direct numerical integration. This approach was implemented into SAFIR while for the analytical model few simplifications were made.

As stated previously, sections of the vertical member which are not in the smoke layer are surrounded by gases at ambient temperature thus the convective flux is negligible. This is the case over a wide length of the vertical member as this model is dedicated to localised fires where the smoke height is small compared to the ceiling height (on the contrary, two zones' models are the best solutions to handle these cases).

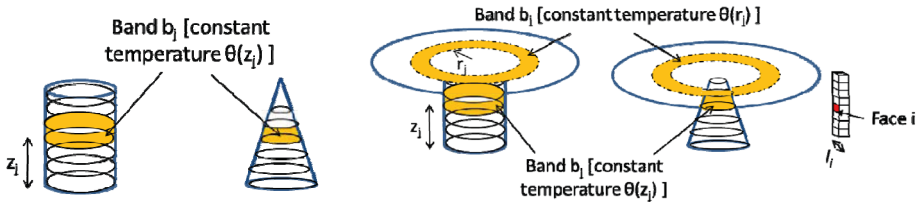

Figure 4.14. Cylindrical flame and conical shape for a flame not impacting the ceiling (a) and a flame impacting the ceiling (b) [108].

However, sections inside the smoke layer are surrounded by hot gases even if the flame is not impacting the ceiling and the convective heat flux must be considered. This is done by computing the gas temperature using the equation provided by EC1 part 1-2 [10] and showed before in the Hasemi model, and in a consistent way with the radiative calculation under the ceiling.

For a member inside the fire area, the convective heat flux is a major component of the total heat flux. In addition, the concept of solid flame where the external surface of the flame radiates toward a member is not pertinent. A distinction is made between sections of the vertical element which are inside the smoke layer under the ceiling or outside the smoke layer. When the segment is outside the smoke layer, the heat flux can be evaluated by using the Heskestad method, with a slight modification. When the segment is in the hot layer, the total heat flux received is taken as the maximum between Hasemi model and Heskestad model.

Once the heat flux has been evaluated it is possible to evaluate the temperature distribution of the section.

4.3.3.2. LOCAFI implementation in SAFIR

The Hasemi model is in accordance with the model from Annex C of EN 1991-1-2 [1] if the flame touches the ceiling. With this model, the heat flux received by the section is isotropic, which means that the direction from the fire to the section is not considered.

In the LOCAFI fire model, each fire source can be assumed as cylindrical or conical. At each time step, the length of the flame is calculated according to equation C.1 of EC1 part 1-2 [1].

The geometric model based on view factors has been implemented in SAFIR®. The main features of this implementation are:

1) The thermal model of SAFIR® calculates the temperature by a series of 2D thermal analyses performed at each longitudinal point of integration of each beam finite element of the structure chosen by the user. These elements can have any orientation in space: vertical in columns, horizontal in truss chords or inclined in truss internal members.
2) For each section, the heat flux at any time is calculated separately for each surface of the boundary. This means that the thermal attack from the local fires to the section is anisotropic: the boundaries that are facing the fire

receive the highest flux while the boundaries on the opposite side receive no flux at all. When a LOCAFI flux is calculated on a boundary, heat losses are automatically added from the boundary to the far field supposed to be at ambient temperature.

3) The length of the flame (i.e., the length of the fire source in the direction of the axis of the cylinder or of the axis) is calculated according to Eq. C.1 of EN 1991-1-2 or **Eq. 3.16.**
4) The temperature evolution along the centreline of the fire source up to the ceiling is calculated according to Eq. C.2 of EN 1991-1-2 **or Eq.2.37**. If the length of the flame exceeds the source to ceiling distance, a disk will form underneath the ceiling, and the horizontal flame length L_h of the Hasemi model is used to calculate the radius of this disk (see the blue radius in **Figure 4.15**a)
5) If this length is longer than half the diameter of the flame at that level, (see the green radius in **Figure 4.15**a) it will calculate the radius of the disk (equal to the horizontal flame length) and, as a function of the radial distance, an adiabatic temperature corresponding to the flux of Hasemi.
6) The fire source is divided into horizontal slices of equal depth (10cm) and, if there is a disk, the disk is divided into concentric rings with a radial depth of 10 cm, see **Figure 4.15**b. The temperature of each slice is uniform and taken as the temperature along the centreline at mid-level of the slice, see point 4). The temperature of each ring is uniform and calculated from the Hasemi model at mid radial distance, see point 5).

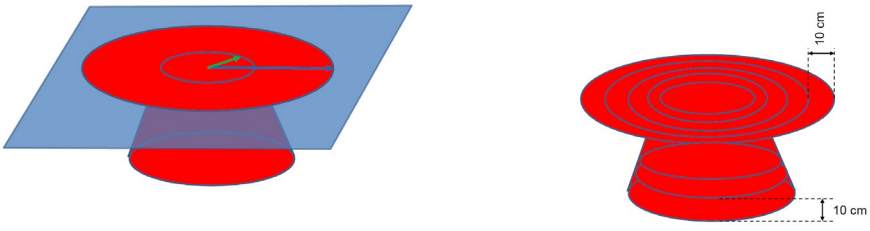

(a) (b)

Figure 4.15. LOCAFI model [108].

7) Each slice and each ring are divided into 72 sectors of 5 degrees opening each, see **Figure 4.16**a.

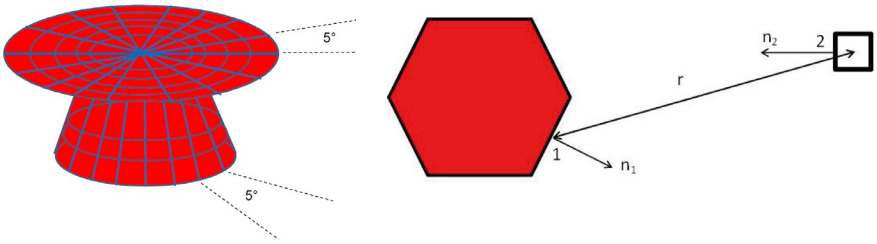

(a) (b)

Figure 4.16. (a) divisions of the flame (b) distance r between a facet of the fire and the section [108].

8) These two divisions mentioned under 6) and 7) define a series of facets that form the boundary of the flame. The radiative flux from each facet is calculated to each boundary of the section. It is based on the normal to the facet n1 and the normal to the boundary of the section n2, the position of the canter of the facet, the distance r between the canter of the facet and the position of the longitudinal point of integration of the beam finite element that is considered. The real position of the receiving surface is thus not considered, which introduces an approximation of maximum ½ of the transverse dimension of the cross section of the beam finite element. This is shown in **Figure 4.16**b where the section is a square tube, and the fire source is divided into 6 sectors of 60 degrees opening. If cosine (n1;r)<0 or cosine (n2, r)<0, the facet and the boundary don't "see" each other and there is no flux.

4.3.3.3. Results and discussion

To create the input file, needed to carry out the thermal part, the fire source was described in a .txt file, by assigning the 18 fires where for each of them, the following parameters were defined:

- the 3D position of the fire, which was set as in the CFAST model at the middle height of each load cell;
- the vertical elevation of the ceiling which corresponds to the height of each load level;
- the HRR curves as a function of time, which were assigned for each fire with the predefined delayed times, this means that the HRRs input curves are the same as the CFAST model, illustrated in **Figure 3.28** and **Figure 3.29**;
- the diameter of the fire source as a function of time, calculated by using the **Eq. 3.17**

All results of the thermal analysis are organized in the *.tem files. The following **Figure 4.17** illustrates the LOCAFI/HESKESTAD results obtained for the horizontal beam belonging to the central shoulder. Since the input boundary conditions of a localized fire is a flux, it is worth saying the results are directly in terms of temperature distribution within the cross-section.

By analysing temperature results, also in this case it is possible to appreciate, how the time delay imposed for the HRR curves was found also in the temperature curves. All the curves reach a maximum temperature equal to about 877 °C so lower temperatures than the CFAST with a peak equal to equal to 1120 °C.

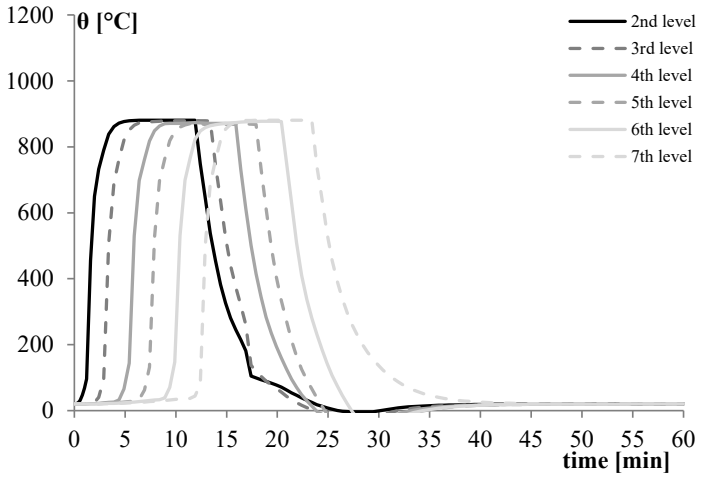

Figure 4.17. LOCAFI model: Temperature distributions of the horizontal elements at the first 6 levels

Figure 4.18 shows the temperature distribution along the first level of the upright, obtained with LOCAFI, in comparison, with the one obtained from the thermal analysis carried out with the CFAST natural fire curve. By analysing the results, it is possible to see that LOCAFI provides different temperatures along the vertical development of the column, unlike by using the zone model where it is possible to obtain only one uniform temperature, on the other hand, it is possible to see that CFAST could be seen as a mean value of the LOCAFI one.
Consideration of a localized fire thus resulted in a transient and largely non-uniform temperature distribution in the structure, which was then used by SAFIR in a subsequent structural analysis, with the elements having any orientation in space.
The structural part of SAFIR® then, in a subsequent analysis, calculated the mechanical behaviour of the structure based on this transient and non-uniform temperature distribution in the structure.

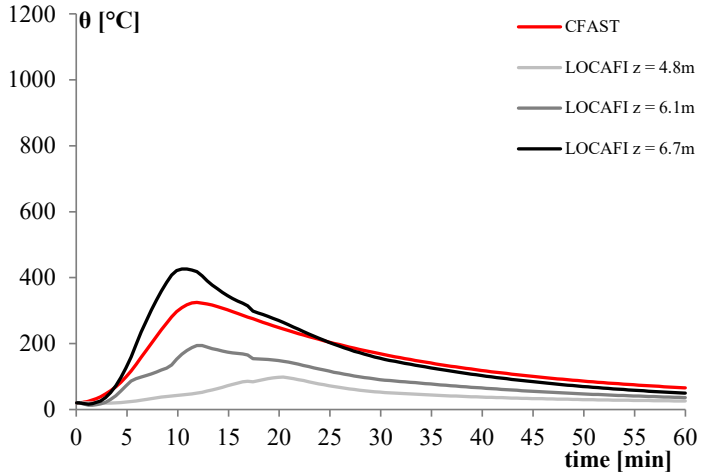

Figure 4.18. Temperature distributions along the 1st level of the upright, comparison between LOCAFI model and CFAST one.

The following **Figure 4.19** shows the deformed shapes of the structure at 234 seconds (i.e., 3.9 minutes), which is the last step of the structural analysis provided by SAFIR.

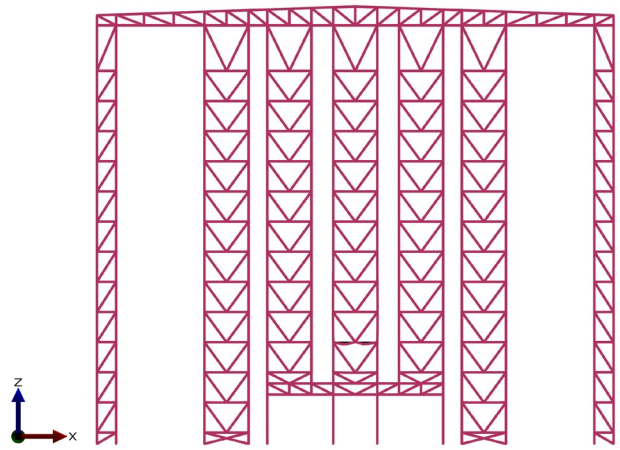

Figure 4.19. LOCAFI model: deformed shape at 3.9 minutes in the Diamond environment.

From the deformed shape it is possible to see that at that time the critical element could be the transversal beam of the central shoulder at the first load level, which is a coupled C section 150x50x15mm and 2mm thickness, which shows a buckling shape. **Figure 4.20** shows the temperature distribution within the cross-section, obtained from the thermal analysis, where it is possible to appreciate a little temperature difference among the web, the flanges, and the lips.

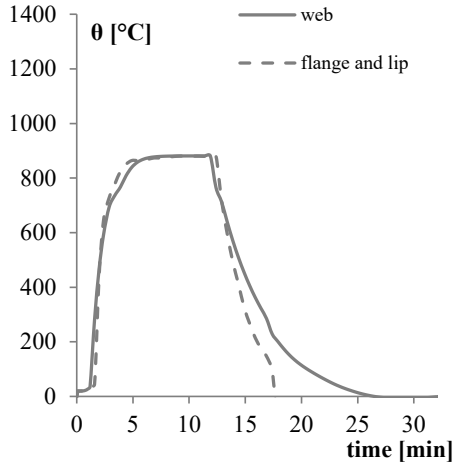

Figure 4.20. LOCAFI model: Temperature distribution over time of the horizontal beam at 2nd level.

To investigate the achievement of the capacity of the beam, the compression resistance axial force at different exposure times was calculated, like in the previous analyses. Since the element that led to the analysis to stop is the same as the zone model the effective cross-sectional area will be the same, for both the capacity methods.

For this reason, **Table 4.10** shown the result in terms of temperature θ, the corresponding reduction factors for the 0.2% proof strength at elevated temperatures, $k_{0.2p,\theta}$ and the design buckling resistance at different exposure times, according to the capacity methods of the actual EC3.

Table 4.10 LOCAFI models: design buckling resistance at different exposure times for the coupled C section 150x50x15x2mm according to the capacity methods of the actual EC3.

time	**θ_{web}**	**θ_{flange}**	**$k_{p0.2,\theta,web}$**	**$k_{p0.2,\theta,flange}$**	**$N_{b,fi,t,Rd}$**
[s]	[°C]	[°C]	[-]	[-]	[kN]
0	20	20	1.00	1.00	154
0.8	22	25	1.00	1.00	154
1.0	27	33	1.00	1.00	154
1.2	36	45	1.00	1.00	154
1.6	281	437	0.80	0.61	103
2.0	465	646	0.57	0.22	50
2.4	592	728	0.32	0.11	27
2.9	694	778	0.14	0.08	16
3.4	736	825	0.11	0.07	12
3.9	767	850	0.09	0.06	11

At the same time the following **Table 4.11** shows the results also in terms of temperature θ, the corresponding reduction factors of the yield strength at elevated temperature θ $k_{y,\theta}$ and the design buckling resistance at different exposure times, according to the capacity methods of the new EC3.

Table 4.11 LOCAFI models: design buckling resistance at different exposure times for the coupled C section 150x50x15x2mm according to the capacity methods of the new EC3.

time	θ_{web}	θ_{flange}	$k_{y,\theta,web}$	$k_{y,\theta,flange}$	$N_{b,fi,t,Rd}$
[s]	[°C]	[°C]	[-]	[-]	[kN]
0	20	20	1.00	1.00	109
0.8	22	25	1.00	1.00	109
1.0	27	33	1.00	1.00	109
1.2	36	45	1.00	1.00	109
1.6	281	437	1.00	0.92	99
2.0	465	646	0.86	0.36	54
2.4	592	728	0.49	0.20	30
2.9	694	778	0.24	0.14	18
3.4	736	825	0.19	0.10	13
3.9	767	850	0.15	0.08	11

The previous buckling resistances calculated with both capacity methods are shown also in the following **Figure 4.8** in comparison with the axial force provided by SAFIR, where a positive axial load indicate compression in the beam element.

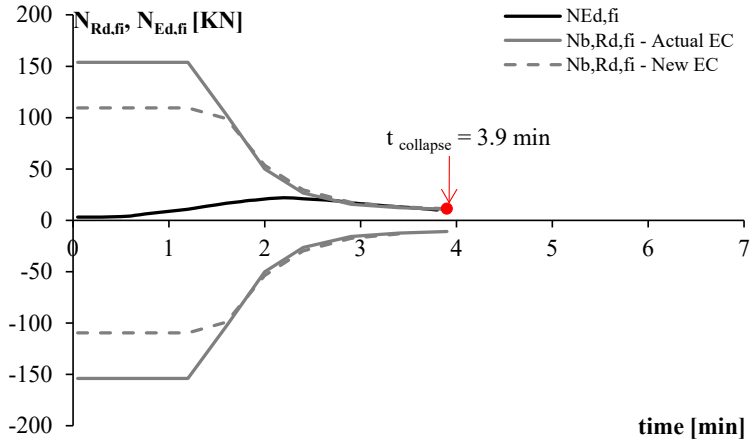

Figure 4.21. LOCAFI models: comparison between stress and resistance.

This comparison confirms that also by using the localized fire model for all the structural elements the critical element is the horizontal beam of the 2nd level, but in this case, the last step of the structural analysis provided by SAFIR is lower than the one obtained with the zone model. This is because the temperature, increases faster, by reaching a temperature equal to 400°C before 2 minutes, which leads the beam to achieve its capacity before with a lower increase of the initial compression load and without reaching the catenary effect.

4.3.4. Fire scenario with a combined fire model

Since the localized model provided more accurate results along the uprights, another thermo-mechanical analysis was carried out by considering different fire models for different structural elements. For all the uprights the LOCAFI model was used while for all the other structural elements, the zone model was used. The following **Figure 4.22** shows the deformed shapes of the structure at 336 seconds (i.e., 5.6 minutes), which is the last step of the structural analysis provided by SAFIR.

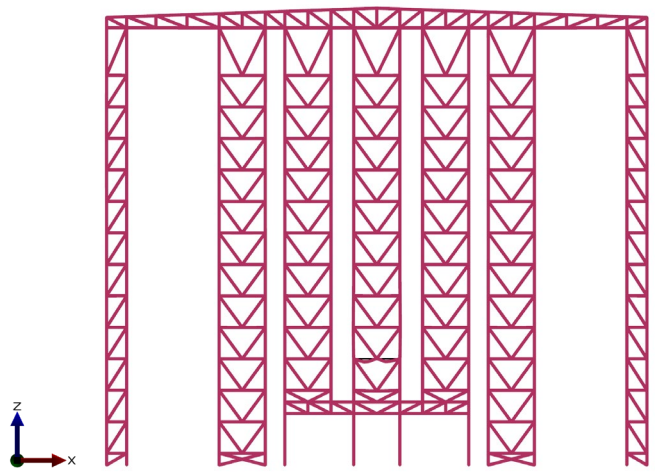

Figure 4.22. Combined model CFAST-LOCAFI: deformed shape at 5.8 minutes in the Diamond environment.

From the deformed shape it is possible to see that at that time the critical element

could be the transversal beam of the central shoulder at the 2nd load level, which is a coupled C section 150x50x15mm and 2mm thickness, which shows a buckling shape. Since this element is the same as the fire scenario with the multi-cell zone model for all the elements, the results of the thermal analysis are the same as shown in **Figure 4.10**.

To investigate the achievement of the capacity of the beam, the compression resistance axial force at different exposure times was calculated. Also in this case, the effective cross-sectional area, and the design buckling resistance at different exposure times according to both capacity methods, are the same as shown in §4.2.2. For this reason, the results are illustrated directly in the following **Figure 4.23** in terms of comparison among the buckling resistances calculated with both capacity methods and the axial force provided by SAFIR.

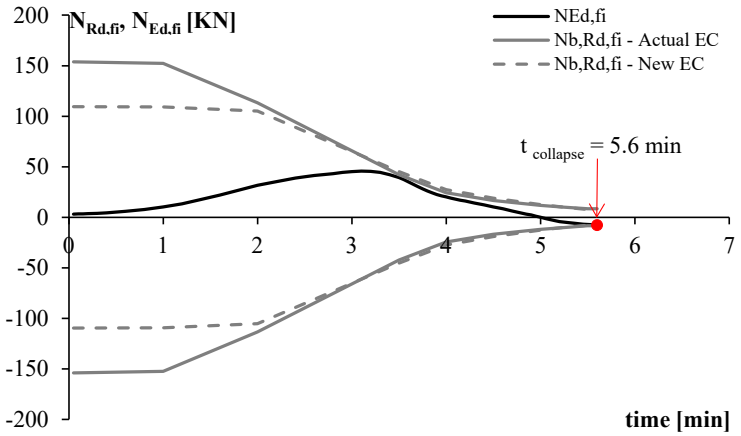

Figure 4.23. Combined model CFAST-LOCAFI: comparison between stress and resistance.

This comparison confirms that the critical element is the selected transversal beam, this one exhibits the same behaviour, indeed, the thermal action has induced an increment of the initial compression load which corresponds to an expansion of the beam, after 3 minutes the load starts to decrease, and the beam starts to deflect inward, at this point the section has reached a temperature equal to 400°C more or less and so the steel resistance starts to decrease. The load decrease until 5.6 minutes with an inward deflection for a tension load, with a little

catenary effect, for the beam.

Within the time interval of these analyses, it seems that the use of the zone model or the localized one for the columns doesn't produce significant differences in terms of structural behaviours, this is due also to the fact that the element that led the analysis to stop is the same horizontal beam which is heated by the zone fire model also in this case.

4.3.5. Fire scenario with FDS

The fifth thermo-mechanical analysis was carried out by considering the natural fire curves obtained from the computational fluid dynamic model obtained with FDS. As analysed in §3.4.1, since this fire model has produced a wider propagation, by heating also the truss and the external shoulders, this has led to an increase in the number of .TEM files from 82 to 192 in the corresponding thermo-mechanical analysis. Once the thermal results were obtained for each section, it was possible to carry out the mechanical part. The following **Figure 4.24** shows the deformed shapes of the structure at 373.5 seconds (i.e., 6.2 minutes), which is the last step of the structural analysis provided by SAFIR.

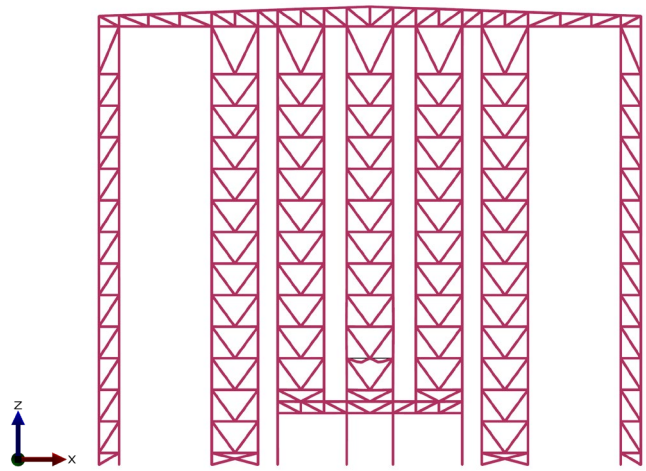

Figure 4.24. CFD model, FDS: deformed shape at 6.2 minutes in the Diamond environment.

From the deformed shape it is possible to see that at that time the critical element could be the transversal beam of the central shoulder at the 2nd load level, which is a coupled C section 150x50x15mm and 2mm thickness, which shows a buckling shape. **Figure 4.24** shows the temperature distribution within the cross-section, obtained from the thermal analysis.

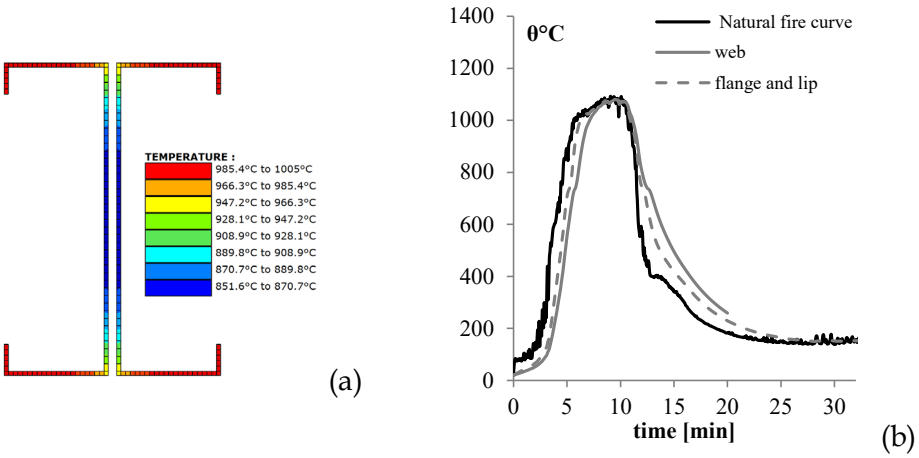

Figure 4.25. CFD model, FDS: temperature distribution within the cross section in the Diamond environment at 6.2 minutes (a), temperature distribution over time (b).

To investigate the achievement of the capacity of the beam, the compression resistance axial force at different exposure times was calculated. To calculate the normal compressive stress strength for the Class 4 section the first step was the evaluation of the effective cross-sectional area. This one is the same evaluated before and showed in **Table 4.6** according to the capacity methods of the actual EC3 and **Table 4.8** according to the capacity methods of the new EC3. Once the A_{eff} is known it was possible to evaluate the design buckling resistance at different exposure times, by using **Eq. 4.6.** Thus, the following **Table 4.12** shows the results also in terms of temperature θ, the corresponding reduction factors for the 0.2% proof strength at elevated temperatures, $k_{0.2p,\theta}$. In the same way once that the A_{eff} according to the capacity methods of the new EC3 is known, it was possible to evaluate the design buckling resistance at different exposure times, by using **Eq. 4.7.** Thus, the following **Table 4.13** shows the results also in terms

of temperature θ, the corresponding reduction factors of the yield strength at elevated temperature $k_{y,\theta}$.

Table 4.12 CFD model, FDS: design buckling resistance at different exposure times for the coupled C 150x50x15x2mm according to the capacity methods of the actual EC3.

time	**θ_{web}**	**θ_{flange}**	**$k_{p0.2,\theta,web}$**	**$k_{p0.2,\theta,flange}$**	**$N_{b,fi,t,Rd}$**
[s]	[°C]	[°C]	[-]	[-]	[kN]
0	20	20	1.00	1.00	3
1.0	34	42	1.00	1.00	5
1.7	45	57	1.00	1.00	5
2.0	51	65	1.00	1.00	6
2.5	66	86	1.00	1.00	7
3.3	120	165	0.98	0.93	15
4.2	294	418	0.79	0.63	30
4.7	435	583	0.61	0.34	42
5.8	745	934	0.10	0.04	1
6.2	847	994	0.06	0.03	7

Table 4.13 CFD model, FDS: design buckling resistance at different exposure times for the coupled C 150x50x15x2mm according to the capacity methods of the new EC3.

time	**θ_{web}**	**θ_{flange}**	**$k_{y,\theta,web}$**	**$k_{y,\theta,flange}$**	**$N_{b,fi,t,Rd}$**
[s]	[°C]	[°C]	[-]	[-]	[kN]
0	20	20	1.00	1.00	3
1.0	34	42	1.00	1.00	5
1.7	45	57	1.00	1.00	5
2.0	51	65	1.00	1.00	6
32.5	66	86	1.00	1.00	7
3.3	120	165	1.00	1.00	15
4.2	294	418	1.00	0.96	30
4.7	435	583	0.92	0.52	42
5.8	745	934	0.18	0.05	7
6.2	847	994	0.09	0.04	7

The previous buckling resistances calculated with both capacity methods are

shown also in the following **Figure 4.26** in comparison with the axial force provided by SAFIR, where a positive axial load indicate compression in the beam element.

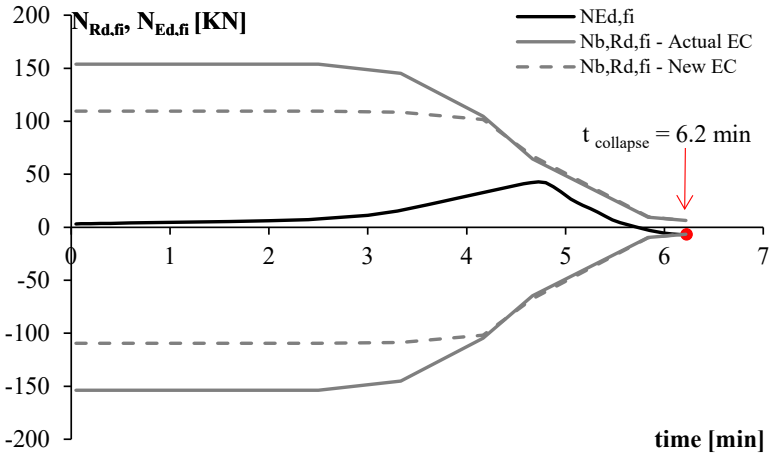

Figure 4.26. CFD model, FDS: comparison between stress and resistance.

This comparison confirms that also in this case the critical element is the selected transversal beam, the thermal action has induced an increment of the initial compression load which corresponds to an expansion of the beam, but in this case this redistribution is slower than the zone model's one, indeed after 4.7 minutes the load starts to decrease, and the beam starts to deflect inward, at this point the section has reached a temperature equal to 400°C more or less and so the steel resistance starts to decrease. The load decreases until the achievement of the capacity of the beam at 6.2 minutes with an inward deflection for a tension load, with a little catenary effect.

Also in this case, it is possible to see that the two capacity methods provide different results within the first 2 minutes, with lower values obtained with the new EC expressions, while after this time the results are very similar to each other.

4.3.6. Benchmarks between thermo-mechanical analyses with different fire models

The following figures compare the results for typological elements obtained using the previously illustrated fire models: the multi-cells zone model (CFAST), the LOCAFI model and the FDS model.

In particular, **Figure 4.27** shows the temperature distributions for the horizontal beams of the central shoulder for the first 2nd, 3rd, and 4th levels evaluated with the thermal analysis carried out by using the input fire curves obtained the three fire models: FDS, CFAST and LOCAFI. Regarding the comparison between the FDS and CFAST results, since the steel elements are characterized by a high A_m/V, these show similar heating and cooling phases to their fire curves and so the considerations are the same as obtained for the input fire curves, shown in §3.5. Indeed, by comparing the temperature distributions for the 2nd level (see **Figure 4.27**a), it is possible to see how the proposed multi-cell zone model (CFAST) can properly predict the fire duration, in particular the temperature calculated in CFAST regarding the maximum temperature, is coherent with the one recorded by FDS. The heating phases are not too different, indeed only a time delay is observed in the FDS temperature. Moreover, the first parts of the two cooling phases are very similar, while after 13 minutes, the temperatures start to diverge. On the other hand, the LOCAFI temperature is characterized by a faster hating phase with a temperature peak lower than the other ones, but also in this case the cooling phase follows the other ones after 11 minutes. The comparison of the temperatures for the 3rd level (see **Figure 4.27**b) shows that the heating phases of the three models distributions start at the same time, and also the fire duration is more or less similar, to the LOCAFI results which show faster heating and cooling phases, while the FDS and CFAST ones are similar in terms of sloping. The CFAST model provides a higher temperature peak while the LOCAFI and FDS ones are similar. These aspects are more evident for the 4th level (see **Figure 4.27**c) due to different fire propagation in the FDS model the heating phase is different compared to other two fire models, which are coincident with

each other.

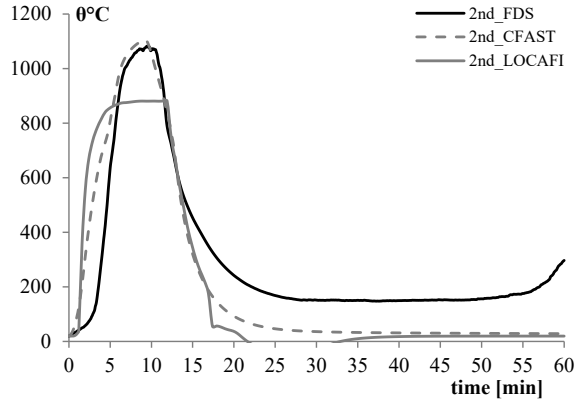

(a)

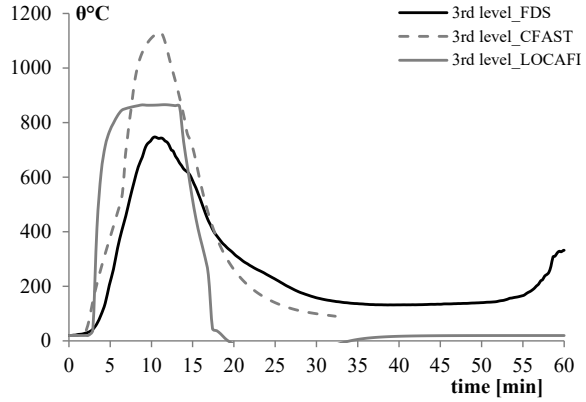

(b)

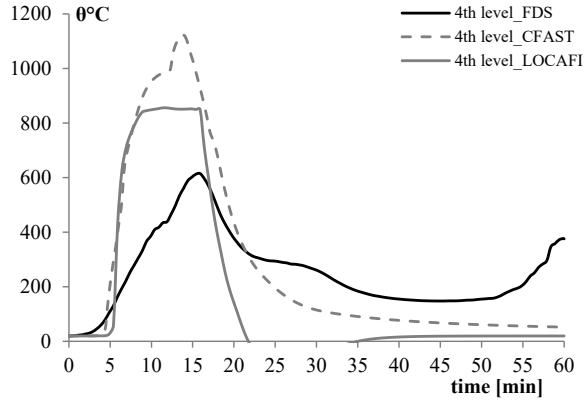

(c)

Figure 4.27. Comparison between temperature distributions for the horizontal beams of the central shoulder for the first three levels obtained with CFAST, FDS and LOCAFI fire models.

In particular, **Figure 4.28** shows the comparison among the results of the analysis, already shown and commented on in §4.3 but this time, in terms of evolutions of the axial forces in the horizontal beams belonging to the 2nd, 3rd, and 4th levels of the central shoulder, as a function of time evaluated with the thermal analysis carried out by using the input fire curves obtained the three fire models: FDS, CFAST and LOCAFI. In the same way **Figure 4.29** shows the same comparison in terms of bending moments.

By comparing distributions for the 2nd level (see **Figure 4.28**a), is possible to see that in all the cases the thermal action induces an increment of the initial compression load which corresponds to an expansion of the beam, but since the heating phases are different this increment is more or less faster. The FDS redistribution is the slowest one, indeed only after 4.7 minutes does the load start to decrease, and the beam starts to deflect inward, at this point the section has reached a temperature equal to 400°C more or less and so the steel resistance starts to decrease. In all the cases the changes in the axial load correspond to a change in the bending moment sign as is seen in **Figure 4.29**a

The loads decrease until the achievement of the capacity of the beam with an inward deflection for a tension load, with a little catenary effect for the FDS and CFAS models. While for the LOCAFI model, since the temperature, increases faster, the beam achieves its capacity before with a lower increase of the initial compression load and without reaching the catenary effect.

The beam of the 3rd level (see **Figure 4.28**b), starts with the same axial load as the 2nd one, but due to the heating of the beam of the 2nd level and its expansion, it has an opposite behaviour, indeed the load starts to increase in tension, and after 2-3 minutes when the beam itself begins to be heated, the beam starts to expand, and the axial load increases in compression. The same considerations can be made for the 4th and level **Figure 4.28**c, where it is possible to appreciate the same behaviour of the 2nd level but with lower axial loads and bending moments (see **Figure 4.29**c).

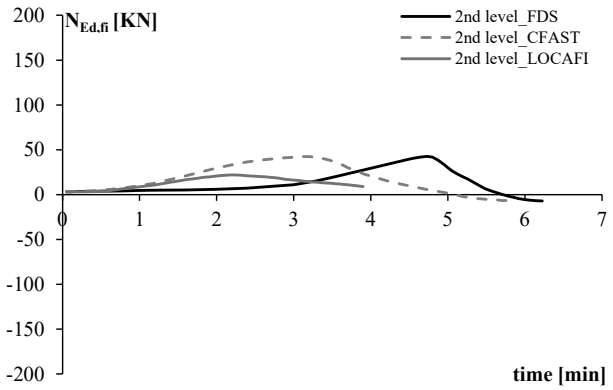

(a)

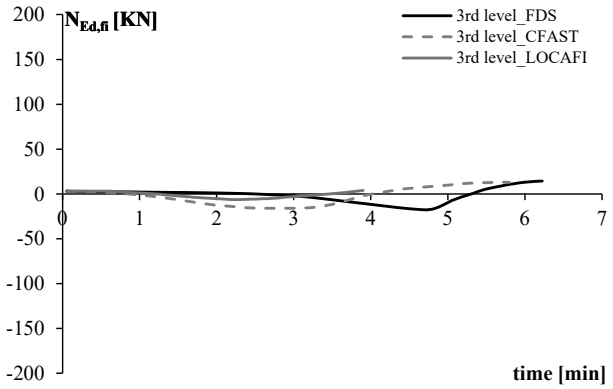

(b)

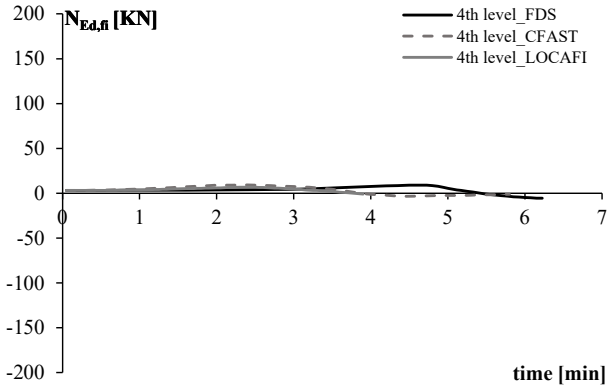

(c)

Figure 4.28. Comparison between axial forces in the horizontal beams of the central shoulder for the first 3 levels obtained with CFAST, FDS and LOCAFI fire models.

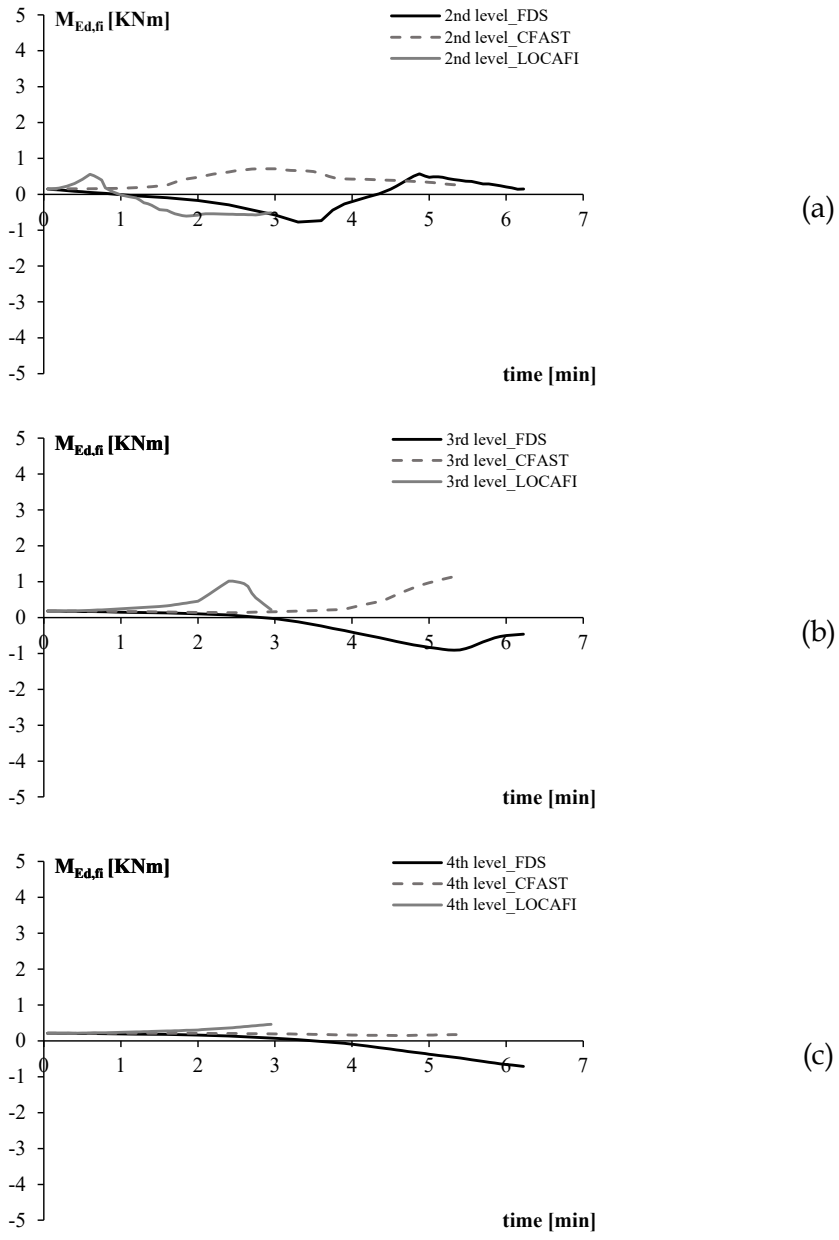

Figure 4.29. Comparison between bending moments in the horizontal beams of the central shoulder for the first 3 levels obtained with CFAST, FDS and LOCAFI fire models.

Figure 4.30 shows the temperature distributions for the upright of the central shoulder along the first level evaluated with the thermal analysis carried out by using the input fire curves obtained from the three fire models: FDS, CFAST, and LOCAFI.

By analysing the results, it is possible to see that LOCAFI provides different temperatures along the vertical development of the column, unlike by using the zone model where it is possible to obtain only one uniform temperature, on the other hand, it is possible to see that CFAST could be seen as a mean value of the LOCAFI one. The comparison underlines, that the FDS results are in good agreement with the LOCAFI one at the same height of the position for the FDS device.

Finally, this comparison confirms that the CFAST model provides higher temperature distribution compared to the other ones, and for this reason, can be considered on the safe side compared to both LOCAFI and FDS which are fire models more indicated for the upright.

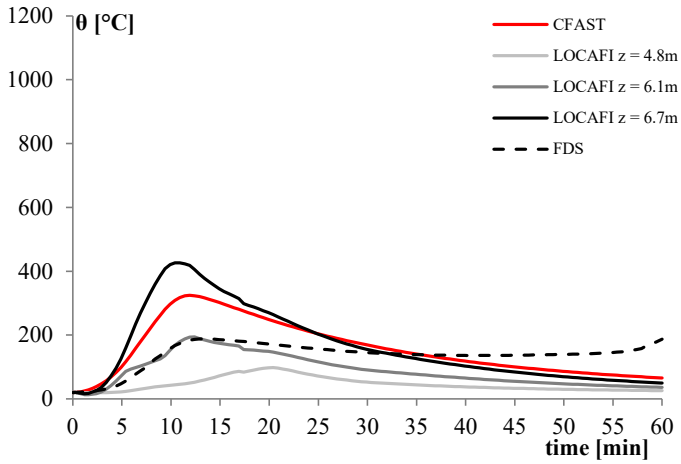

Figure 4.30. Comparison between temperature distributions for the upright of the central shoulder for the first level obtained with CFAST, FDS and LOCAFI fire models.

Figure 4.31 shows the comparison in terms of evolutions of the axial forces for the upright of the central shoulder along the first level evaluated with the thermal analysis carried out by using the input fire curves obtained from the three

fire models: FDS, CFAST, and LOCAFI. The results confirm the previous consideration, indeed the FDS and LOCAFI one is in good agreement, while since with the CFAST model, the temperature is higher the load shows a higher increment.

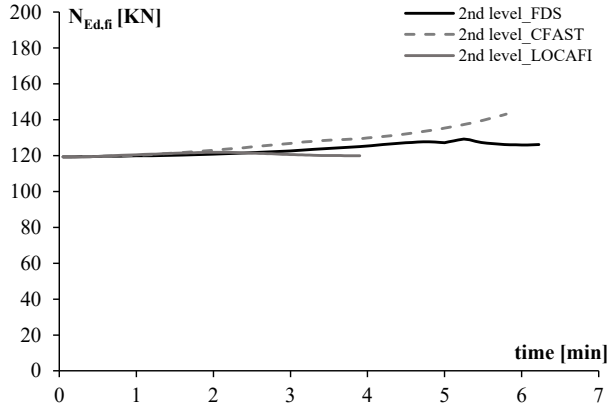

Figure 4.31. Comparison between axial forces in the upright of the central shoulder for the first level obtained with CFAST, FDS and LOCAFI fire models.

4.4. Study of a progressive collapse by using the SAFIR software

All the thermo-mechanical analyses carried out by varying the fire model, have shown that the collapse time for this type of structure is of the order of a few minutes, and to study the collapse it is essential not only to carry out advanced analyses but also to refine them as much as possible, for example to investigate the achievement of the capacity of the beam in terms of compression resistance axial force, the non-uniform temperature distribution had to be considered, combined with the assessment of the effective width to consider the local instability, and the assessment of χ coefficient to consider the global instability in compression.

Moreover, for all the analyses, with all the fire models, the analysis stopped at the achievement of the capacity of the most stressed elements. For this reason, it was not possible to analyse the global collapse and the correct collapse time.

This is due to the type of analysis that SAFIR allows to implement, which is dynamic analysis as shown in §4.2.2 but it is an implicit analysis, which stops when convergence problems are reached. Since ARSWs are characterized by elements with a reduced deformed capacity (class 4 sections), that does not allow the development of a full plastic stress distribution in the section which leads to a not complete plastic redistribution along the members in the structure, for these reasons the last step of the analysis corresponded to the achievement of the capacity of the most stressed structural elements, as the previous analyses showed.

All these aspects lead to affirm that to correctly estimate the collapse times and the shape of the global mechanism, it could be necessary to go beyond the time provided by SAFIR, manually eliminating the elements that fail.

The following **Figure 4.32** shows the comparison among the results of the analysis carried by using the multi-cell zone model, already shown and commented on in §4.3.2 but this time, in terms of evolutions of the axial forces in the horizontal beams belonging to the first 5 levels of the central shoulder, as a function of time.

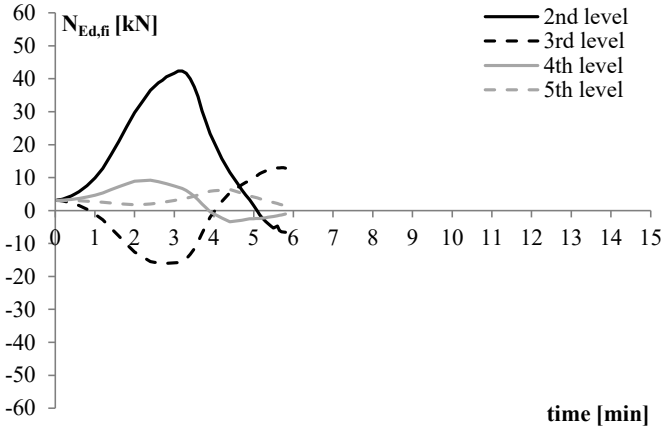

Figure 4.32. Evolutions of the axial forces in the horizontal beams belonging to the first 5 levels of the central shoulder.

Figure 4.33 shows the comparison among the evolutions of the horizontal displacements at the external point of the horizontal beams of the first 5 levels, with

a positive sign for expansion displacement.

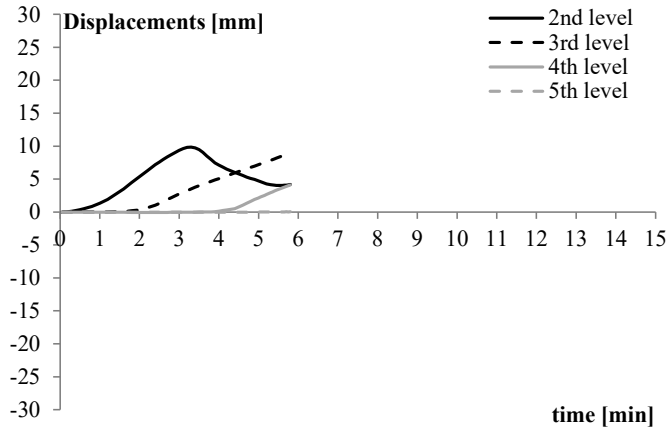

Figure 4.33. Evolutions of the horizontal displacements at the external point of the horizontal beams of the first 5 levels.

As said previously for the beam of the 2nd level, the thermal action has induced an increment of the initial compression load which corresponds to an expansion of the beam, after 3 minutes the load starts to decrease, and the beam starts to deflect inward, at this point the section has reached a temperature equal to 400°C and so the steel resistance starts to decrease. The load decreases until the achievement of the capacity of the beam at 5.8 minutes with an inward deflection for a tension load, with a little catenary effect. The beam of the 3rd level starts with the same axial load as the 2nd one, but due to the heating of the beam of the 2nd level and its expansion, it has an opposite behaviour, indeed the load starts to increase in tension, and after 2-3 minutes when the beam itself begins to be heated, the beam starts to expand, and the axial load increases in compression. The same considerations can be made for the 4th and 5th levels, where it is possible to appreciate the same behaviours but with lower axial loads. The results show that the analysis stops due to the beams belonging to the 2nd level but there is a little redistribution of the stress in the structure, and it is possible to appreciate the travelling fire among it.

Starting from the analysis carried out with the zone model, since it was

demonstrated that the element that led the analysis to stop was the horizontal beams of the 2nd level, another structural model was built by removing this element and applying the internal forces as times changes, that the previous thermos-mechanical analysis had provided. The following figures show the results of this analysis without the beam of the 2nd load level. In particular, **Figure 4.34** shows the deformed shapes of the structure at 468 seconds (i.e., 7.8 minutes), which is the last step of the structural analysis provided by SAFIR.

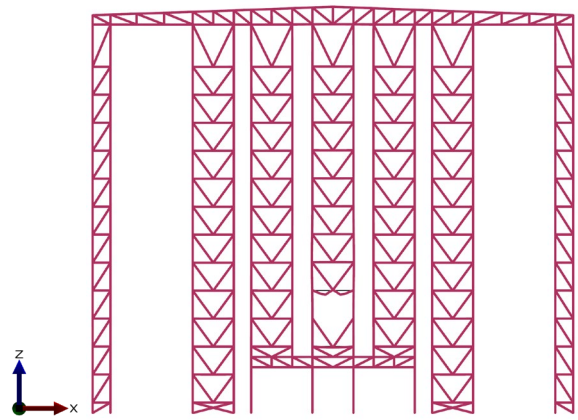

Figure 4.34. Deformed shape at 7.8 minutes in the Diamond environment of the structure without the beam at the 2nd load level.

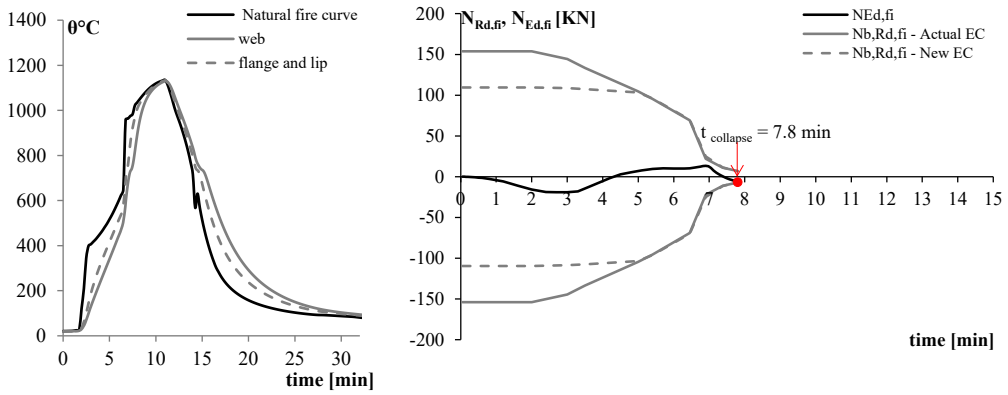

(a) (b)

Figure 4.35. Temperature distribution within the cross section over time (a), comparison between stress and resistance (b).

From the deformed shape it is possible to see that at that time the critical element was the transversal beam of the central shoulder at the 3rd load level, which is a coupled C section 150x50x15mm and 2mm thickness, which shows a buckling shape.

Figure 4.35a shows the temperature distribution within the cross-section, obtained from the thermal analysis, while **Figure 4.35**b shows the comparison among the axial force provided by SAFIR in the beam element and the buckling resistances calculated with both capacity methods.

In the same way as the previous one, however, **Figure 4.36** shows the comparison among the results in terms of evolutions of the axial forces in the horizontal beams belonging to the 3rd, 4th, and 5th levels of the central shoulder, as a function of time.

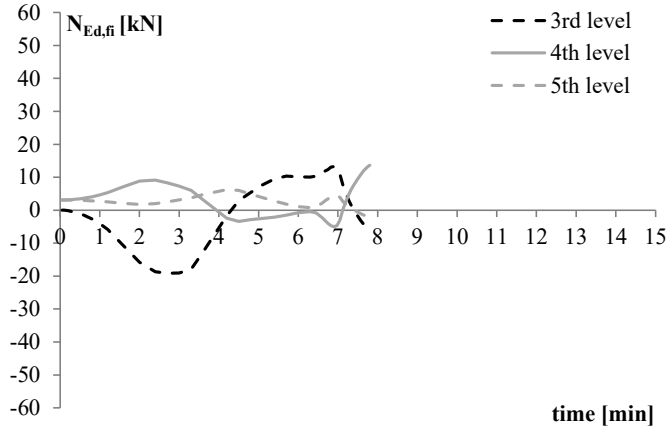

Figure 4.36. Evolutions of the axial forces in the horizontal beams belonging to the 3rd, 4th, and 5th levels of the central shoulder.

Figure 4.37 shows the comparison among the evolutions of the horizontal displacements at the external point of the horizontal beams of the same levels, with a positive sign for expansion displacement.

The first thing that it is possible to appreciate is the fact that the last step of the analysis increased from 5.8 to 7.8 minutes, in this way, the beam of the 3rd level has continued its heating corresponding to an increase of the horizontal

displacements, and the axial load in compression, until 7 minutes when the load starts to decrease, and the beam starts to deflect inward, at this point the section has reached a temperature equal to 600°C more or less and so the steel has lost about half of its strength. The load decreases until 7.8 minutes with an inward deflection for a tension load, with a little catenary effect for the beam.

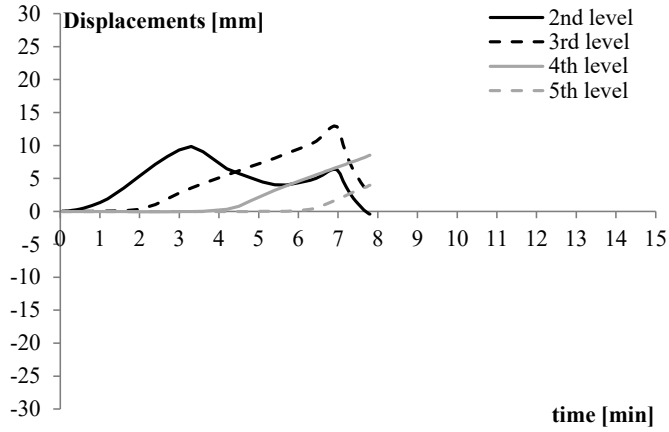

Figure 4.37. Evolutions of the horizontal displacements at the external point of the horizontal beams of the first 5th levels.

It is worth observing that, by comparing the results **Figure 4.36** and **Figure 4.37** with the previous ones in **Figure 4.32** and **Figure 4.33** it is possible to affirm that the global behaviour of the structure without one element is not changed, the load and the displacements are the same in shape and entities until the last step of the previous analysis.

For these reasons, another structural model was built by removing both the 2nd and 3rd horizontal beams of the central shoulder and applying the internal forces as times change, that the previous thermos-mechanical analysis had provided. The following figures show the results of this analysis without these elements, in particular **Figure 4.38** shows the deformed shapes of the structure at 616 seconds (i.e., 10.2 minutes), which is the last step of the structural analysis provided by SAFIR. From the deformed shape it is possible to see that at that time the critical element was the transversal beam of the central shoulder at the

4th load level, which is a coupled C section 150x50x15mm and 2mm thickness, which shows a buckling shape.

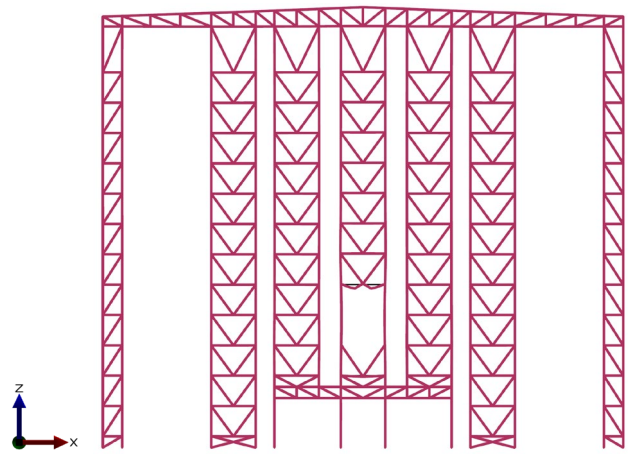

Figure 4.38. Deformed shape at 10.2 minutes in the Diamond environment of the structure without the beam at the 2nd and 3rd load level.

Figure 4.39a shows the temperature distribution within the cross-section, obtained from the thermal analysis, while **Figure 4.39**b shows the comparison among the axial force provided by SAFIR in the beam element and the buckling resistances calculated with both capacity methods.

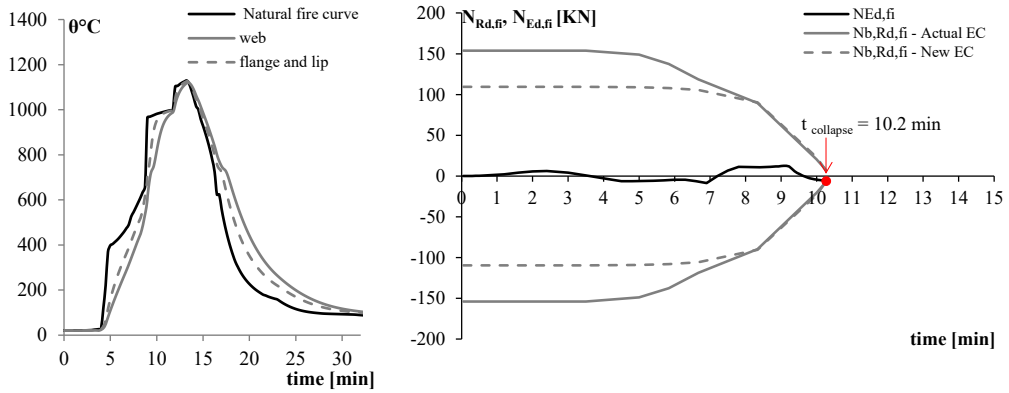

(a) (b)

Figure 4.39. Temperature distribution within the cross section over time (a), comparison between stress and resistance (b).

Figure 4.40 shows the comparison among the results in terms of evolutions of the axial forces in the horizontal beams belonging to the 4th and 5th levels of the central shoulder, as a function of time.

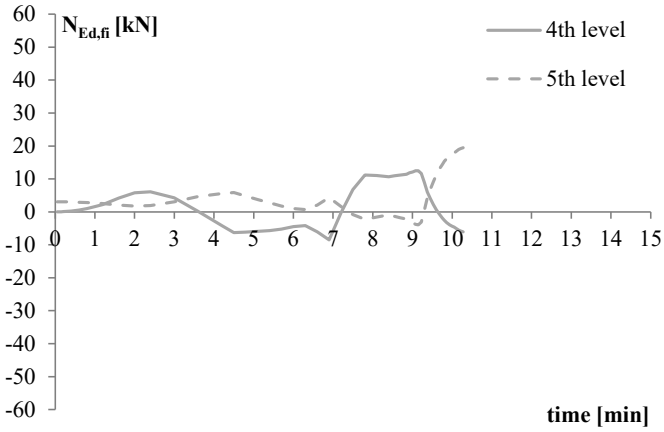

Figure 4.40. Evolutions of the axial forces in the horizontal beams belonging to the 4th and 5th levels of the central shoulder.

Figure 4.41 shows the comparison among the evolutions of the horizontal displacements at the external point of the horizontal beams of the same levels, with a positive sign for expansion displacement.

The first thing that it is possible to appreciate is the fact that the last step of the structural analysis provided by SAFIR increased from 7.8 to 10.2 minutes, in this way, the beam of the 4th level has continued its heating corresponding to an increase of the horizontal displacements, and the axial load in compression, until 9 minutes when the load starts to decrease, and the beam starts to deflect inward, at this point the section has reached a temperature equal to 600°C more or less and so the steel has lost about half of its strength. The load decreases until 10.2 minutes when the beam shows an inward deflection for a tension load, with a little catenary effect.

At this time, it is possible to see that the horizontal beam belonging to the 5th level starts its heating which corresponds to an increase in horizontal displacement and axial load in compression.

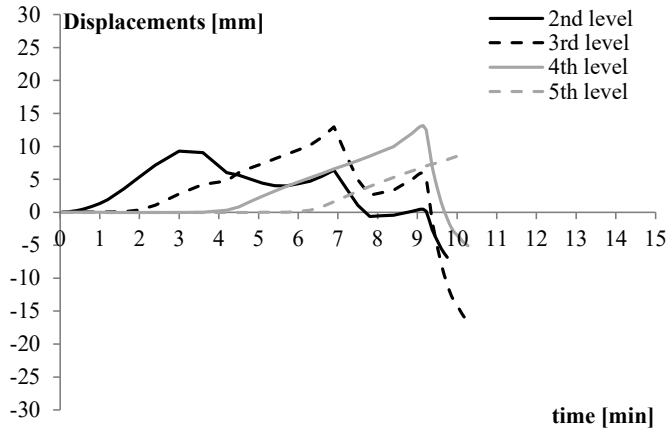

Figure 4.41. Evolutions of the horizontal displacements at the external point of the horizontal beams of the first 5 levels.

It is worth observing that, by comparing the results of the previous analysis in **Figure 4.36** and **Figure 4.37** with these the global behaviour of the structure without two elements is not changed, and the load and the displacements are the same in shape and entities until the last step of the previous analysis.

For this reason, the procedure was continued by removing the horizontal beam of the 4th level. The following figures shows the results of this analysis without these elements, in particular **Figure 4.42**a shows the deformed shapes of the structure at 617.8 seconds (i.e., 10.3 minutes), which is the last step of the structural analysis provided by SAFIR. From the deformed shape it is not possible to see the critical elements. Thus to study the reason why the analyses stopped at 617.8 seconds, it was necessary to study the output file provided by the software, where it was found that the critical element that led the analysis to stop was the diagonal element of the truss on the aisle between the central and the lateral shoulder, which is a coupled C section 150x50x15mm and 2mm thickness, like it is shown in **Figure 4.42** where it is possible to see the comparison between the axial force provided by SAFIR in the beam element and the buckling resistances calculated with both capacity methods.

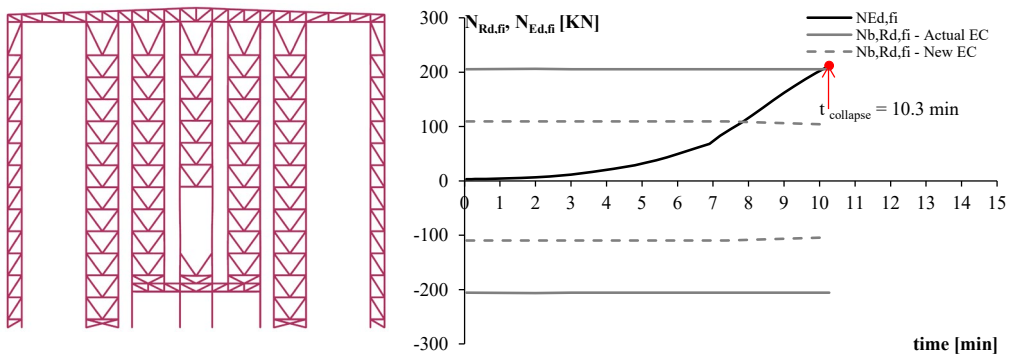

(a) (b)

Figure 4.42. Deformed shape at 10.3 minutes in the Diamond environment of the structure without the beam at the 2nd, 3rd, and 4th load levels (a), comparison between stress and resistance of the truss' diagonal (b).

Since the element is cold, there is not a reduction of the resistance but since the axial load starts to increase when this one becomes equal to the buckling resistance calculated with the capacity method of the Actual EC, the analysis stops. It is worth underlining that in this case, it is not correct to use the new EC to evaluate the capacity load since this method is calibrated at elevated temperatures and this section is not heated, indeed it could underestimate the capacity of the section.

Since the last step of the analysis was very similar to the previous one (10.2 against 10.3) another analysis was carried out by also removing the diagonal of the truss that led the analysis to stop.

The following figure shows the results of this analysis without these elements, in particular **Figure 4.43** shows the deformed shapes of the structure at 742.5 seconds (i.e., 12.4 minutes), which is the last step of the structural analysis provided by SAFIR. From the deformed shape it is possible to see that at that time the critical element was the transversal beam of the central shoulder at the 5th load level, which is a coupled C section 150x50x15mm and 2mm thickness, which shows a buckling shape.

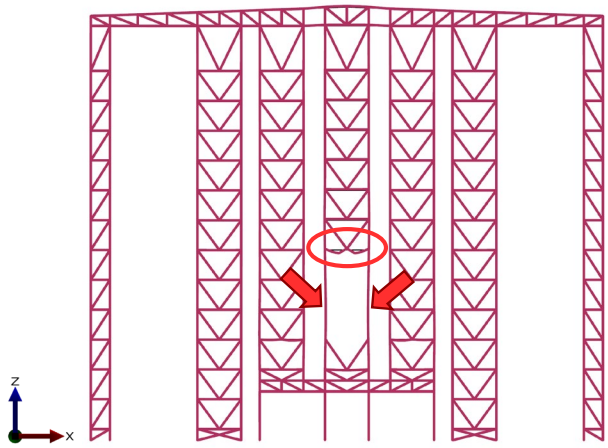

Figure 4.43. Deformed shape at 12.4 minutes in the Diamond environment of the structure without the beam at the 2nd, 3rd, and 4th load levels and the truss' diagonal

Figure 4.44a shows the temperature distribution within the cross-section, obtained from the thermal analysis, while **Figure 4.44**b shows the comparison among the axial force provided by SAFIR in the beam element and the buckling resistances calculated with both capacity methods.

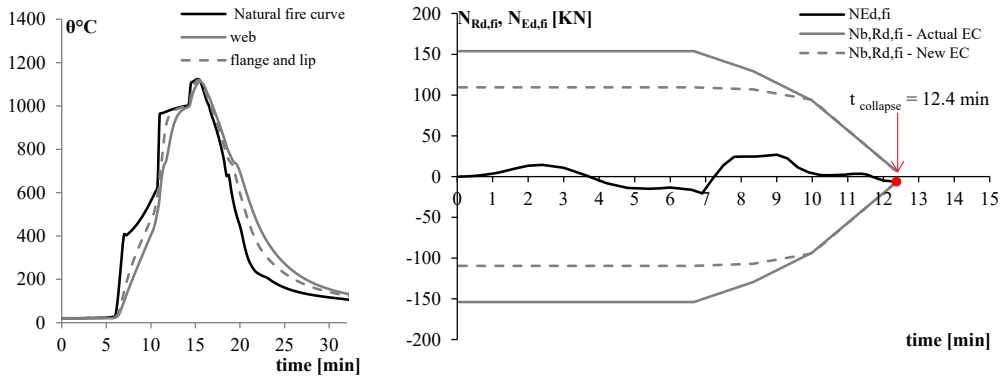

(a) (b)

Figure 4.44. Temperature distribution within the cross section over time, comparison between stress and resistance (b).

The first thing that it is possible to appreciate is the fact that the last step of

the structural analysis provided by SAFIR time increased from 10.2 to 12.4 minutes, moreover the comparison confirms the critical element is the selected transversal beam. To better understand the global behaviour **Figure 4.45** shows the comparison among the evolutions of the horizontal displacements at the external point of the horizontal beams of the same levels, with a positive sign for expansion displacement.

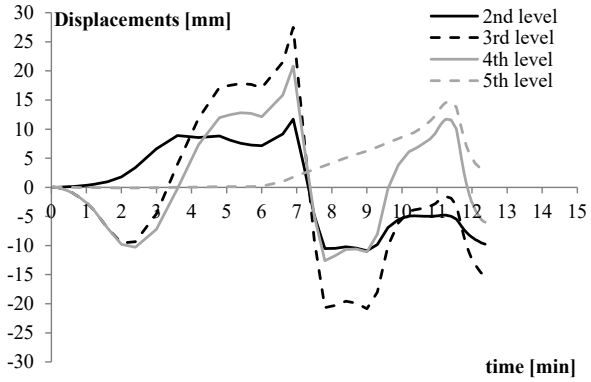

Figure 4.45. Evolutions of the horizontal displacements at the external point of the horizontal beams of the first 5 levels.

It is worth observing is that in this case since the structure has fewer structural elements, the displacements for the 2nd, 3rd, and 4th levels are not in the same in shape and entities from the beginning of the analysis, this is because the structure has less stiffness compared to the initial one. While the displacement of the 5th level has the same shape as the one shown in **Figure 4.41**, when the beam has started its heating, during this last analysis, it is possible to see how the beam of the 5th level has continued its heating corresponding to an increase of the horizontal displacements, and the axial load in compression, until 9 minutes when the load starts to decrease. The beam starts to deflect inward, at this point the section has reached a temperature equal to 600°C and so the steel has lost about half of its strength. The load decreases until 12.4 minutes with an inward deflection for a tension load, with a little catenary effect for the beam. Currently, it is possible to also see that the uprights belonging to the central shoulder without the horizontal beams that have collapsed, show a global buckling.

Finally, the shown proposed procedure has confirmed that to correctly estimate the collapse times and the shape of the global mechanism, it is necessary to go beyond the last step of the structural analysis provided by an implicit analysis, by manually eliminating the elements that collapse. Indeed, since SAFIR implements only implicit analysis, this type of analysis stops when convergence problems are reached that usually correspond to the collapse of the most stressed structural elements. This aspect has been analysed and validated by modelling the same structure with a second structural software, ABAQUS CAE that allows the implementation of implicit analyses and explicit ones.

4.5. Modelling structures in fires with ABAQUS CAE: theoretical background and capabilities

As shown before, assessing the collapse of steel structures due to fire requires an analysis capable of processing numerical singularities, such as buckling of elements, plastic hinges, and large displacements. The explicit algorithm can be a helpful tool for solving these problems. However, the time-step size could represent the downside of the explicit scheme because the analysis is conditionally stable for

$$\Delta t \leq \frac{L}{c} \tag{4.6}$$

Where:

L is a characteristic length (in this case the smallest mesh size);

c is the speed of sound in the material:

$$c = \sqrt{\frac{E}{1 - \nu^2 \rho}} \tag{4.7}$$

Where:

E is the elastic modulus;

ν is the Poisson ratio, and ρ is the density.

As deeply shown in Mei et al [82] a fire input can be more than 60 minutes long, so an entirely explicit analysis can be computationally expensive and time-

consuming. Classical strategies such as time or mass scale can be tricky to solve this problem because they can introduce unrealistic inertial effects in large models during collapse, for this reason the authors proposed a nonlinear procedure based on 3-step process: static, dynamic implicit, dynamic explicit.

In the first phase, non-structural loads (such as load unit loads) are applied to the structure using a static procedure; when the fire begins to heat frames, the analysis switches to dynamic implicit. Then, the last phase is the explicit analysis, where frames undergo large displacements and deformations until the complete collapse. Moreover, since racks have a peculiar load distribution, with point masses representing pallet loads placed at the beam-to-upright intersection, the dynamic procedure permits better capturing the dynamic effects due to concentrated masses in the collapse phase.

Abaqus/Standard uses the Hilber-Hughes-Taylor time integration. The stiffness matrix is computed and inverted, and the non-linear system of equations is solved in each time increment iteratively using Newton's method. The method is unconditionally stable, which is advantageous compared to conditionally stable explicit methods. It is also faster for typical structural analysis but computationally less efficient due to the inversion process for the stiffness matrix. On the contrary, Abaqus/Explicit uses a central-difference integration rule. As it is conditionally stable because the time step should withstand the Courant Condition of Equation (21), it is a computationally more efficient process as the integration method requires the inversion of the mass matrix only.

This means that, starting from the Dynamic equilibrium of **Eq. 4.4** that in the complete form becomes:

$$[K]x + [C]\dot{x} + [M]\ddot{x} = F_{ext} \tag{4.8}$$

Solving by using an implicit analysis means that:

$$x = [K]^{-1}\left(F_{ext} - ([C]\dot{x} + [M]\ddot{x})\right) \tag{4.9}$$

Solving by using in explicit means that:

$$\ddot{x} = [M]^{-1}\left(F_{ext} - ([C]\dot{x} + [K]x)\right) \tag{4.9}$$

4.6. Finite element model by using Abaqus CAE software

The 2D finite element model has been built in ABAQUS using B21 beam elements.

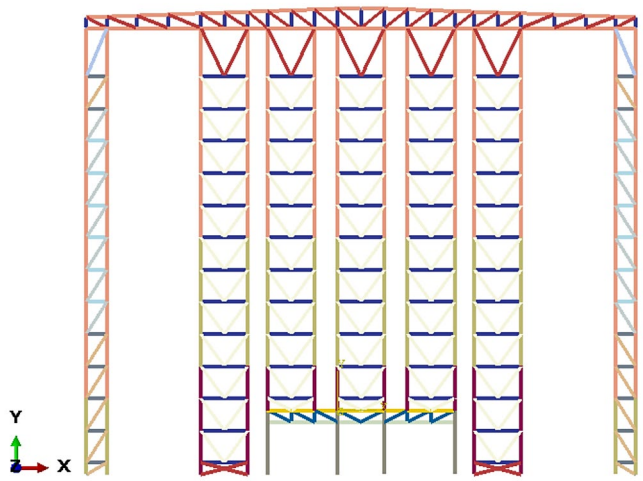

Figure 4.46 The cross-aisle view of the FE model in the ABAQUS CAE environment.

To replicate the conditions of pinned beams for braces, truss diagonals, it is impossible to use a "truss" T21 in the model since it cannot consider the buckling eventuality of the element. For this reason, an assembled connector was used, made by a Join and a Rotation connector. The Join connector constraints displacements in the two directions, X and Y, and does not activate rotational DoF, while the Rotation connector makes the rotation in the XY plane available. A schematic representation of the connector is displayed in **Figure 4.47**.

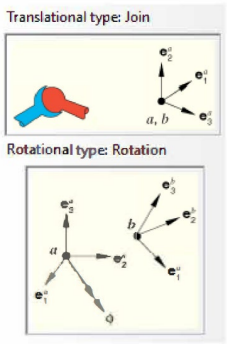

Figure 4.47 *Joint* and *Rotation* connectors [190].

Uprights were considered pinned in the cross-aisle direction and fixed in the down-aisle direction.

The analyses were carried out considering nonlinear geometry and material nonlinearity. The EC3 part l-2 formulation was adopted for the latter, and the obtained curves are reported in **Figure 4.48**. A linear interpolation was adopted between two temperature values given by the Eurocode. The nonlinear procedure before was considered to run the analyses.

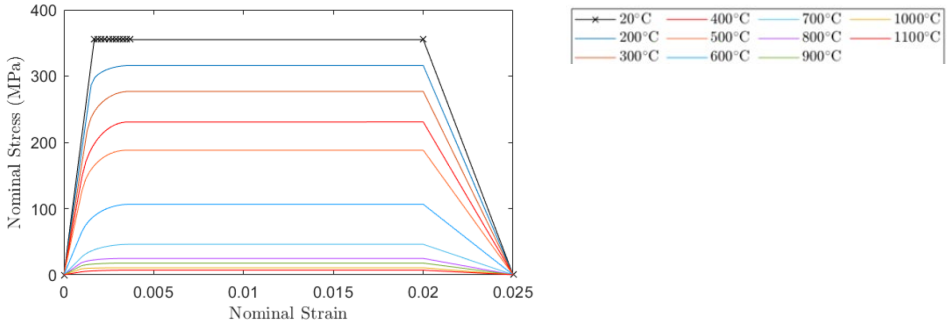

Figure 4.48 Different stress-strain curves at various temperatures according to EC3 part l-2 for steel grade S355.

In the same way of SAFIR method, the unit load loads were applied as concentred forces at the four intersections between uprights and beams.

The analysis was carried out by considering the results of the zone model proposed and shown in §3.3.2. It is worth understanding that the thermal analysis was not carried out by using ABAQUS, but the results of the thermal analyses provided by SAFIR were used, in this way for each element a uniform temperature was applied as predefined fields. Moreover, in order to compare the implicit analysis with the SAFIR results, no ABAQUS General contact was activated.

4.6.1. Results and discussion

The deformation sequence is reported in the following **Figure 4.49**. Referring to this figure, the collapse sequence is as follows:

1) 324 seconds, about 3.9 minutes: end of the implicit part. From the deformed shape, it is possible to see that at that time the critical element was

the horizontal beam of the central shoulder at the 2nd load level, which showed a collapse shape. At that time the temperature of that beam was at about 690°C, while the temperatures in the other elements were still increasing.

2) 402.2 seconds, 402.2 seconds, about 6.7 minutes, thanks to the explicit part of the analysis it is possible to see that, as with the previous horizontal beam, now the beam of the 3rd level collapsed in the same way as the previous one and at the same temperature at about 689 (the yellow one). Since the beam of 2nd level has collapsed, it is not present in the structure anymore.
3) 554.4 seconds, about 9.2 minutes, as for the previous levels, the beam of the 4th level has buckled at a temperature of 700°C. Due to reduced stiffness in the central shoulder, the stresses within the truss began to increase, particularly evident in the two diagonals above the shoulder (highlighted in red).
4) 666.9 seconds, about 11.1 minutes, the roof truss' diagonals were starting to collapse.
5) 672.9 seconds, about 11.2 minutes the horizontal beam of the 5th level collapsed at the same temperature as the previous ones, i.e., at about 700°C, the beams of the 1st level of the two shoulders adjacent to the central one, started to expand and their temperature increased.
6) 722.9 seconds, about 12 minutes the beams of the adjacent shoulders collapsed at a temperature of 700°C, it is possible to see that all the elements that were not anymore in the structures had a temperature equal to 1000 °C.
7) 812.3 seconds, about 13.5 minutes, the horizontal beam element of the 6th level of the central shoulder collapsed, while the temperatures in the upper ones were increasing.
8) 901.9 seconds, about 15 minutes, the beams of the adjacent shoulders at the 3rd level collapsed at a temperature of 700°C. Most of the elements of the structure were affected by the fire.

9) 988.3 seconds, about 16.5 minutes, also the horizontal beam of the 7th level collapsed; it is possible to see that the uprights of the central shoulder, without the horizontal beams that collapsed, showed a global buckling.
10) 1096.9 seconds, about 18.3 minutes end of the analysis.

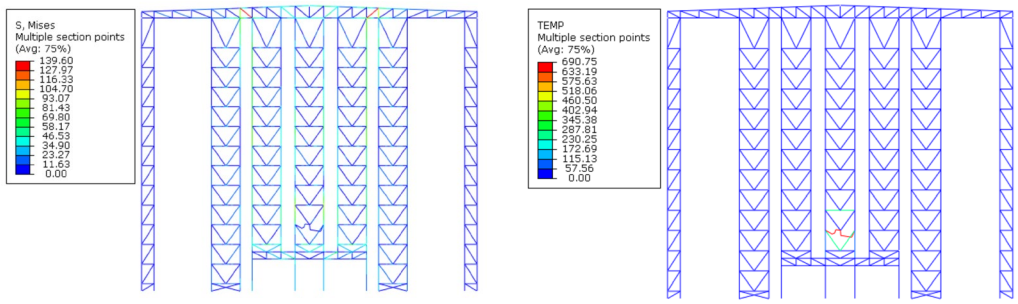

t= 324 s / 3.9 min

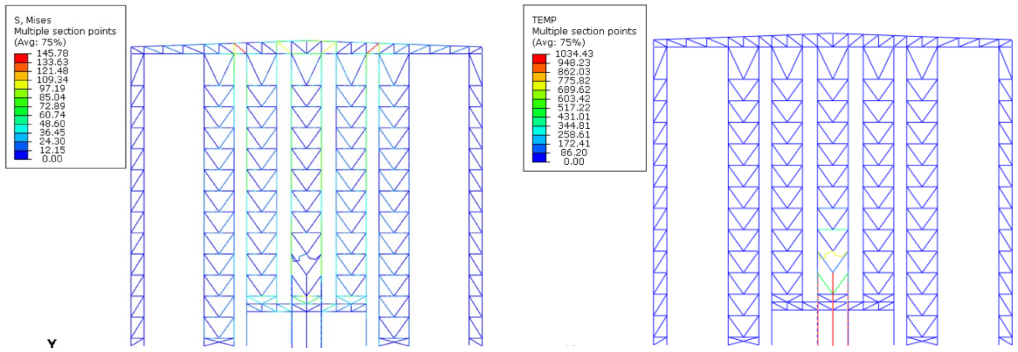

t= 402.2 s / 6.7 min

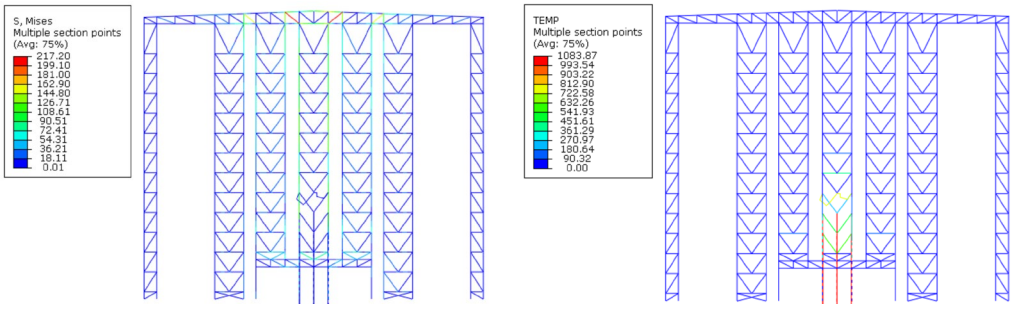

t= 554.4 s / 9.2 min

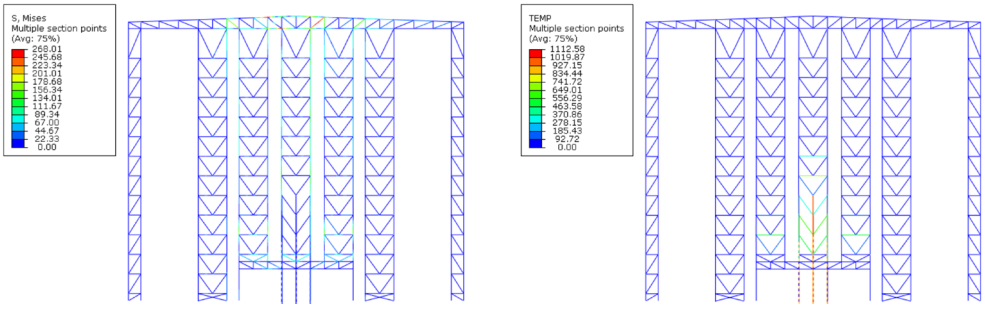

t= 666.9 s / 11.1 min

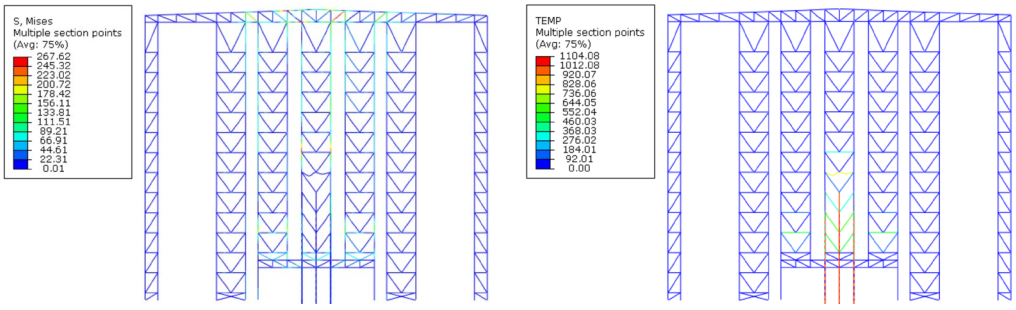

t=672.9 s / 11.2 min

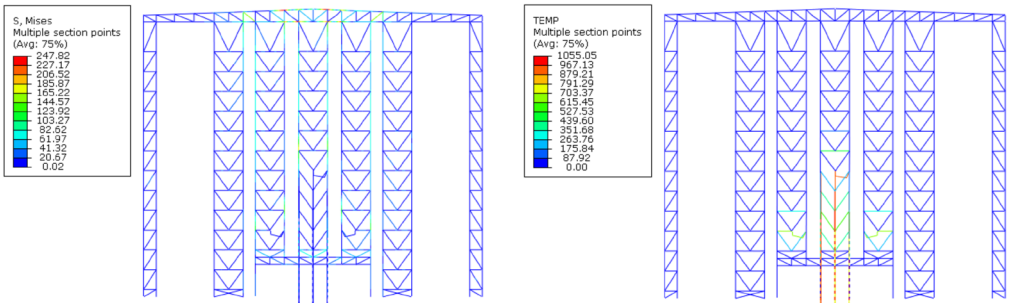

t=722.9 s / 12 min

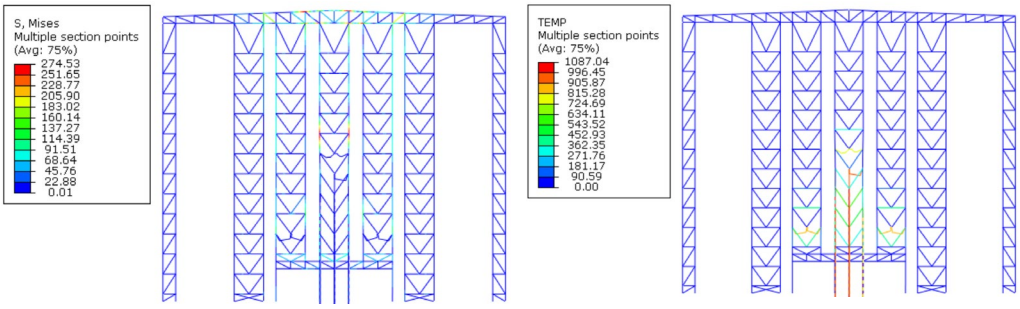

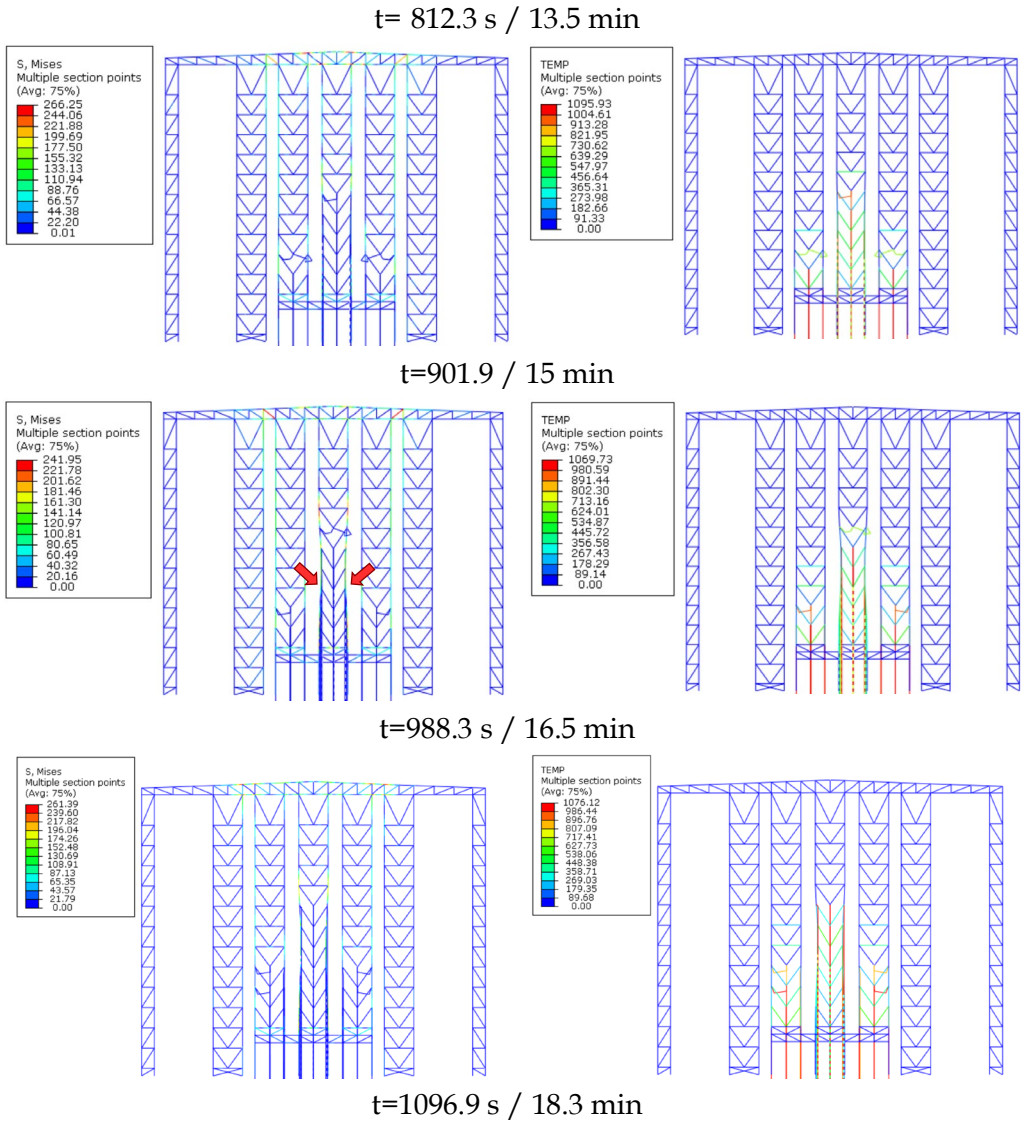

Figure 4.49 Deformation sequence. Left: Von-Mises stresses; Right: Temperatures.

From the previous considerations, it is possible to affirm that the results obtained with this implicit/explicit procedure are in line with the SAFIR ones. The sequence of the progressive collapse (the elements that collapse and their times) is the same as obtained with SAFIR, i.e., an iterative procedure only based on

subsequent implicit analyses: however, in this case the procedure is automatic while with SAFIR it was necessary for every step to remove manually the critical element by replacing it with their reactions.

In the following figures **Figure 4.50**, **Figure 4.51** and **Figure 4.52** some comparisons are shown, to validate the previous considerations and the model reliability. The following **Figure 4.50** shows the comparison between the axial force provided by ABAQUS as a result of the implicit analysis, with the buckling resistance calculated with both capacity methods for the beam belonging to the 2nd level of the central shoulder.

This comparison confirms that, in the examined case-study, the critical element is the selected transversal beam. The thermal action leads to an increment of the initial compression load due to the thermal expansion of the beam: after 3 minutes the axial load starts to decrease, and the beam starts to deflect inward; at this point the section has reached a temperature equal to 400°C more or less and so the steel resistance starts to decrease. The axial load decreases until it reaches the collapse at 3.9 minutes with an inward deflection.

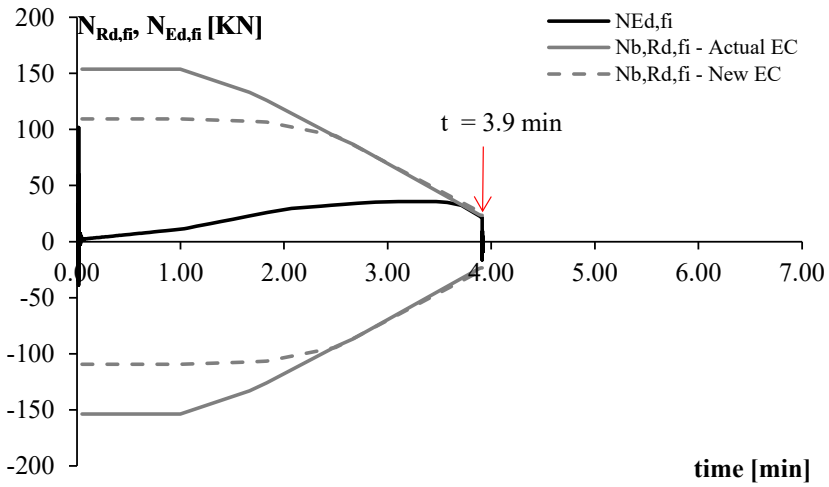

Figure 4.50 Comparison between stress and resistance at the last step of the implicit part.

The implicit part of the analysis conducted in ABAQUS gives results in line

with the SAFIR ones one showed in **Figure 4.11**, but in ABAQUS the collapse is anticipated by a few minutes, confirming that SAFIR, despite stopping at the collapse of the first most stressed elements, considers a redistribution of the internal stresses. This aspect is shown and confirmed also in terms of comparison between the displacement at the end of the beam, shown in **Figure 4.51**.

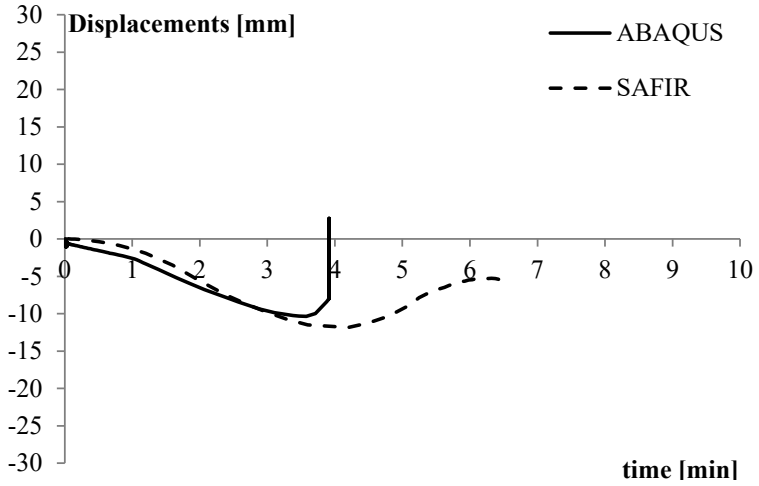

Figure 4.51 Benchmark between ABAQUS and SAFIR displacements at the end of beam of the 2nd load level.

The two displacements are similar in the first phase; in the second phase the ABAQUS one increase quickly with a beam collapse at 3.9 minutes, while the SAFIR's one still increasing with a collapse at 5.8 minutes.

Finally, **Figure 4.52** shows a direct comparison between the two deformed shapes at the collapse time obtained with ABAQUS (a) and Safir (b).

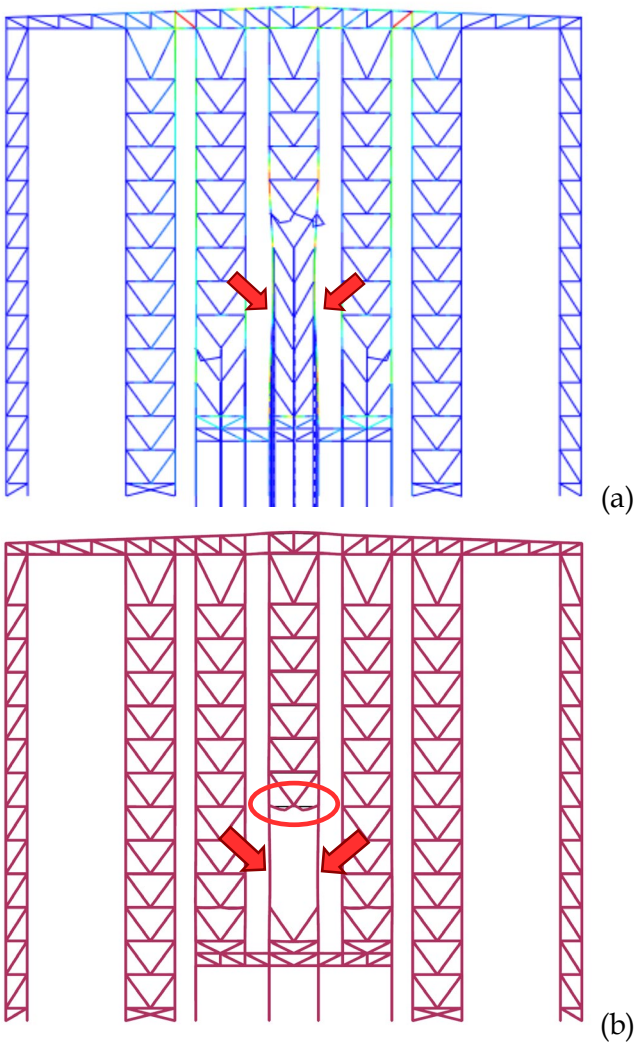

Figure 4.52 Comparison between ABAQUS (a) and SAFIR (b) collapse deformed shapes.

The two deformed shapes are in a good agreement to each other, confirming that to analyse the collapse of these structure by using an implicit analysis removing the collapsed elements, is necessary to go beyond the time provided by the first implicit analysis.

Chapter 5

5. Conclusions and future work

This research provides an assessment of a self-supporting automated multi-depth warehouse under fire conditions. The first part focused on establishing the fire modelling necessary for assessing the mechanical response and analysing the collapse mechanism in the second part of the study.

Automated Rack Supported Warehouses (ARSWs) represent a topic of great interest for both the scientific community and the manufacturers of industrial racks.

The study of the scientific literature has pointed out that numerous research has been carried out on the analysis of cold formed steel members that characterize these structures. In the last decades, the global structural behaviour of traditional racks has been investigated focusing especially from a seismic point of view. However, under fire conditions, their behaviour is still poorly known. At present, some studies exist about the fire design methods for class 4 sections which have led to new formulations to determine the effective width of steel sections at high temperatures. These formulas are proposed for the new drafts of the next generation of structural Eurocodes. The new Italian technical fire prevention regulation requires this type of structures, complying with the performance level I or II, where the absence of external consequences due to structural collapse must be demonstrated. This means that the designer must demonstrate analytically that the collapse mechanism is inward, and implosive.

In the case of multi-depth ARSW, due to their configuration and the presence

of the shuttle systems the fire could start like a localized fire within the load levels and could develop into a traveling fire both in horizontal and vertical directions. At present, fire design methods for vertically traveling fires are not developed as for horizontal ones. Indeed, in the last decade, vertically traveling fires have been analysed like multi-floor fires in high-rise buildings, which represent a different condition than the ARSWs one.

For these reasons, one of the objectives of this dissertation was to obtain a fire model that allowed the vertical and horizontal propagation of localized fires to be considered. To achieve this goal some experimental results on steel racks available in the literature were considered. In this way it was possible to obtain a multi-cells and zones fire model for ARSW structures.

The conclusions about the first part of the work are reported in the following.

Since the main assumption of the zone model is that the temperature is uniform in each compartment, to obtain different temperature distribution within the structure it was necessary to divide the whole geometry of the fire model into different cells as the load level of structure, i.e., where the combustion material (UDC) is present. In this way, a CFAST model of the ARSW structure characterized by 123 cells communicating among them through horizontal openings (ceiling/floor vent) was obtained in the examined case-study. In each cell/load level, the horizontal and vertical propagation was considered by assigning time delays to the HRR curves, along the vertical and horizontal directions. It was found that vertical time propagation is equal to the time for the flame to reach the upper level of the racks, calculated by using the flame lengths L_f proposed in EC1 part 1-2. Regarding the study of horizontal fire propagation, a time delay equal to the time required for the combustible material stored in the adjacent load cells to reach the auto-ignition temperature of the combustible material was considered.

The same fire scenario was modelled also by using FDS software, which allows the analysis of the fire propagation without the predefined delay times. The CFD model in this case underlines on one hand the ventilation effect, which may play a very important role in changing the fire traveling trajectory, but on the other hand allows the validation of the fire propagation times calculated analytically and used in the zone model.

After defining the fire modelling, the second part of this work regards the evaluation of the mechanical response and the analysis of the collapse mechanism. For this reason, several thermo-mechanical analyses were performed using the SAFIR software which allows modelling Class 4 steel elements like beam elements but considering the local instabilities that can occur in these slender sections. These analyses were carried out by considering different types of fire models, such as localized fire (LOCAFI and Heskestad method), the zone model approach by using CFAST software, and the computational fluid dynamics analysis using the FDS software. Moreover, a comparison between the two different methods, for determining the fire capacity of the ARSW Class 4 steel sections, was conducted.

All these analyses have shown that the collapse time for this type of structure is within few minutes, and to study the collapse it is essential not only to carry out advanced analyses, but also to refine them as much as possible. For example, to investigate the achievement of the capacity of the beam in terms of axial force, the non-uniform temperature distribution had to be considered, combined with the assessment of the effective width to consider the local buckling, and the assessment of χ coefficient to consider the member buckling in compression.

The comparison between the analysis carried out using the standard ISO-834 fire curve and the natural fire curve showed that, for these structures, the generalized fire is unrealistic, and it can be not on the safety side, since the natural fire can have a heating phase faster than the nominal curve one, as in the case analysed in this work.

The analyses carried out by using the simplified localized models for all the structural elements have shown that the collapse time is lower than the one obtained with the zone model. This is because the temperature increases faster, by reaching a temperature equal to 400°C before 2 minutes, which leads the beam to collapse with a lower increase of the initial compression load and without reaching the catenary effect.

For this reason, from a theoretical point of view, in the context of collapse times, the fire model that includes all aspects is the CFD fire model. However, the combination of the zone model for horizontal beam elements and the localized model

for the upright allows the vertical and horizontal propagation of localized fires to be considered, returning slightly shorter collapse times and therefore on the safety side.

Using SAFIR software, it is possible to conduct a thermo-mechanical analysis of the ARSW. Indeed, performing a dynamic analysis it is possible to consider all the geometric and mechanical nonlinearities, appreciating a reduced redistribution of stress. Moreover, all the analyses stopped at the collapse of the most stressed elements, and for this reason, it was not possible to analyse the real global collapse and the correct collapse time. This is due to the type of analyses that SAFIR allows to implement which are dynamic implicit analyses that stop when convergence problems are reached. Since ARSWs are characterized by elements with a reduced deformed capacity (class 4 sections), that does not allow the development of a full plastic stress distribution in the section and leads to an incomplete plastic redistribution along the members in the structure, the last step of the implicit analysis corresponds to the collapse of the most stressed structural members: however, this situation does not correspond to the collapse phase of the structure, also thanks to a certain structural redundancy.

Therefore, to correctly estimate the fire collapse times and the shape of the global mechanism, to go beyond the time of collapse provided by SAFIR or implicit analysis is necessary, manually eliminating the elements that collapse. The reliability of this iterative procedure, based on subsequent implicit analyses, has been examined and validated by modelling the same structure with a second structural software, ABAQUS CAE, that allows the implementation of both implicit and explicit analyses. The implicit part of the analysis conducted in ABAQUS gave results in line with the SAFIR ones, but in ABAQUS the collapse was anticipated by a few minutes, because SAFIR better considers the redistribution of the internal stresses until the collapse of the first most stressed elements. Finally, the explicit analysis conducted with ABAQUS allowed to follow a progressive collapse and a global collapse mechanism like those obtained by means of the iterative subsequent procedure implemented with SAFIR: in that case, however, the procedure is automatic and does not require removing manually the collapsed elements by users.

Even if the results of this study refer to a specific ARSW case-study with defined fire scenarios, to generalise some aspects related to the fire behaviour of these structures is possible, providing a useful guidance for designers and researchers.

First, the proposed simplified fire model can be used for the evaluation of vertical and horizontal propagation times, based on the combustible material contained in the ARSW. This simplified method can be useful for a preliminary evaluation of the collapse time of these structures, by using an implicit analysis with all the instabilities that can affect these sections/elements and progressively removing elements that collapse, to reach the global collapse mechanism. While, for estimating the real collapse of these type of structures in a more automatic way, an explicit analysis has to be conducted, with higher costs and computational time.

The project focused on many features of ARSW and fire exposures, but future research will be necessary to improve understanding as well as to extend the results to other relevant fire scenarios (e.g., other natural fire curves), not only for further validate the propagation model, but also for understanding the collapse mechanism by varying the fire scenarios.

Further studies are also needed to investigate the collapse behavior by modelling the contact between the structural elements during the explicit analyses, in order to understand if and how this aspect can influence the structural collapse.

Bibliography

[1] EN 1993-1-1, "Eurocode 3: Design of steel structures – Part 1-1: General rules and rules for buildings" 2004.

[2] S. Caprili, F. Morelli, W. Salvatore, and A. Natali, "Design and Analysis of Automated Rack Supported Warehouses", Open Civil Engineering Journal, vol. 12, no. 1, pp. 150-166, 2018.

[3] C. Couto, P.V. Real, N. Lopes, B. Zhao, "Effective width method to account for the local buckling of steel thin plates at elevated temperatures", Thin-Walled Structures, vol. 84, pp. 134–149, 2014.

[4] D.M. 3 agosto 2015 Approvazione di norme tecniche di prevenzione incendi, ai sensi dell'articolo 15 del decreto legislativo 8 marzo 2006, n. 139, GU n. 192 del 20/8/2015 – S.O. n. 51 (in Italian).

[5] J. Stern-Gottfried, "Travelling fires for Structural Design", PhD thesis, University of Edinburgh, 2011.

[6] A. Usmani, C. Roben, A. Al-Remal, A. "A Very Simple Method for Assessing Tall Building Safety in Major Fires." International Journal of Steel Structures, vol. 9(1), pp. 1-15, 2009.

[7] H. Chen and J. Y. R. Liew, "Explosion and Fire Analysis of Steel Frames" vol. 131, no.6, pp. 687-692, 2005.

[8] A. Mei, "Robustness of Automated Rack supported Warehouses in Fire", PhD thesis, Faculty of Architecture, Civil Engineering and Environmental Sciences University of Braunschweig - Institute of Technology and the School of Engineering, University of Florence, 2023.

[9] EN 1990, "Eurocode - Basis of structural design [Authority: The European Union Per Regulation", 2002.

[10] EN 1991-1-2, "Eurocode 1: Actions on structures - Part 1-2: General actions - Actions on structures exposed to fire", 2002.

[11] J.-M. Franssen, P. Vila Real "Fire Design of Steel Structures: Eurocode 1: Actions on structures Part 1-2 – General actions – Actions on structures exposed to fire Eurocode 3: Design of steel structures Part 1-2 – General rules – Structural fire design", Wilhelm Ernst & Sohn Verlag

für Architektur und technische Wissenschaften GmbH & Co. KG, Berlin, 2012 ECCS – European Convention for Constructional Steelwork.

[12] EN 1993-1-2, "Eurocode 3: Design of steel structures - Part 1-2: General rules - Structural fire design" 2005.

[13] EN 1992-1-2, "Eurocode 2: Design of concrete structures - Part 1-2: General rules - Structural fire design" 2004.

[14] EN 1992-1-2, "Eurocode 4: Design of composite and steel structures - Part 1-2: General rules - Structural fire design" 2005.

[15] J. M. Adam, F. Parisi, J. Sagaseta, X. Lu, "Research and practice on progressive collapse and robustness of building structures in the 21st century", Engineering Structures, Vol.173, pp. 122-149, 2018.

[16] EN 1991-1-7, "Eurocode 1: Actions on structures - Part 1-7: General actions - Accidental actions", 2006.

[17] ASCE, "ASCE 59-12- Blast Protection of Buildings"2011.

[18] K. Vasileios, S. George, "Calculation of Blast Loads for Application to Structural Components. Administrative Arrangement No JRC 32253-2011 with DG-HOMEActivity A5 - Blast Simulation Technology Development", 2013.

[19] B. R. Ellingwood, R. Smilowitz, D O. Dusenberry, D. Duthinh, H. S. Lew, N. J. Carino, "Best Practices for Reducing the Potential for Progressive Collapse in Buildings", NIST Interagency/Internal Report (NISTIR), National Institute of Standards and Technology, Gaithersburg, MD, 2007.

[20] F. Kiakojouri, V. D. Biagi, B. Chiaia, M. R. Sheidaii, "Progressive collapse of framed building structures: Current knowledge and future prospects", Engineering Structures, Vol. 206, p. 110061, 2020.

[21] U. Starossek, "Progressive Collapse of Structures", London, UK: Thomas Telford Ltd., 2009.

[22] F. Fu, "Structural Analysis and Design to Prevent Disproportionate Collapse", Boca Raton, FL: CRC Press, 2016.

[23] D. Isobe, "Progressive Collapse Analysis of Structures, vol. 1, no. 1", Oxford OX5 1GB, United Kingdom: Butterworth-Heinemann, 2018.

[24] H. M. Ali, P. E. Senseny, and R. L. Alpert, "Lateral displacement and collapse of single-story steel frames in uncontrolled fires", Engineering Structures, vol. 26, no. 5, pp. 593-607, 2004.

[25] J. Y. R. Liew, "Survivability of steel frame structures subject to blast and fire", Journal of Constructional Steel Research", vol. 64, no. 7-8, pp. 854-866, 2008.

[26] Y. L. Dong, E. C. Zhu, and K. Prasad, "Thermal and structural response of two-storey two-bay composite steel frames under furnace loading2 Fire Safety Journal, vol. 44, no. 4, pp. 439-450, 2009.

[27] Y. C. Wang, "An analysis of the global structural behaviour of the Cardington steel-framed building during the two BRE fire tests" Engineering Structures, vol. 22, no. 5, pp. 401-412, 2000.

[28] P. J. Moss, R. P. Dhakal, M. W. Bong, and A. H. Buchanan, "Design of steel portal frame buildings for fire safety", Journal of Constructional Steel Research, vol. 65, no. 5, pp. 1216-1224, 2009.

[29] R. Sun, Z. Huang, and I. W. Burgess, "Progressive collapse analysis of steel structures under fire conditions", Engineering Structures, vol. 34, pp. 400-413, 2012.

[30] R. Sun, Z. Huang, and I. W. Burgess, "The collapse behaviour of braced steel frames exposed to fire", Journal of Constructional Steel Research, vol. 72, pp. 130-142, 2012.

[31] C. Fang, B. A. Izzuddin, A. Y. Elghazouli, and D. A. Nethercot, "Robustness of steel-composite building structures subject to localised fire", Fire Safety Journal, vol. 46, no. 6, pp. 348-363, 2011.

[32] C. Fang, B. A. Izzuddin, A. Y. Elghazouli, and D. A. Nethercot, "Simplified energy-based robustness assessment for steel-composite car parks under vehicle fire", Engineering Structures, vol. 49, pp. 719-732, 2013.

[33] A. Agarwal and A. H. Vanna, "Fire Induced Progressive Collapse of Steel Building Structures: The Role of Interior Gravity Columns", Engineering Structures, vol. 58, pp. 129-140, 2014.

[34] B. Jiang, G. Q. Li, and A. Usmani, "Progressive collapse mechanisms

investigation of planar steel moment frames under localized fire", Journal of Constructional Steel Research, vol. 115, pp. 160-168, 2015.

[35] G. L. F. Porcari, E. Zalok, and W. Mekky, "Fire induced progressive collapse of steel building structures: A review of the mechanisms" Engineering Structures, vol. 82, pp. 261-267, 2015.

[36] C. H. Chen, Y. F. Zhu, Y. Yao, Y. Huang, and X. Long, "An evaluation method to predict progressive collapse resistance of steel frame structures" Journal of Constructional Steel Research, vol. 122, pp. 238-250, 2016.

[37] C. S. LL. PP., "Aggiornamento delle Norme Tecniche per le Costruzioni - D.M. 17 /01/2018", (in Italian) 2018.

[38] D. Tsarpalis, D. Vamvatsikos, I. Vayas, and F. Delladonna, "Simplified Modeling for the Seismic Performance Assessment of Automated Rack Supported Warehouses", Journal of Structural Engineering, vol. 147, no. 11, 2021.

[39] EN1993-1-3, "Eurocode 3, Design of Steel Structures - Part 1-3: supplementary rules for cold formed thin gauge members and sheeting ", 2005.

[40] EN 1998-1-1," Eurocode 8: Design of Structures for earthquake resistance - Part 1: General rules, seismic actions and rules for buildingds",2004.

[41] CEN European Committee for Standardization, EN 15512 "Steel static storage systems—Adjustable pallet racking systems—Principles for structural design", 2009.

[42] CEN European Committee for Standardization, "EN 16681 Steel static storage systems—Adjustable pallet racking systems—Principles for seismic design", 2016.

[43] Bernuzzi C, Draskovic N, Simoncelli M, "European and United States approaches for steel storage pallet rack design. Part 2: practical applications". Thin-walled Structures vol. 97, pp.321–341, 2015.

[44] C. S. LL. PP., "Linee guida per la progettazione, esecuzione, verifica e messa in sicurezza delle scaffalature metalliche", (in Italian), 2023.

[45] A. B. M. R. Haque and M. Shahria Alam, "Preliminary investigation on the overstrength and farce reduction factors for industrial rack clad buildings," in 11 th Canadian Conference on Earthquake Engineering, 2015.

[46] A. Kondratenko, A. Kanyilmaz, C. A. Castigliani, F. Morelli, and M. Kohrangi, "Structural performance of automated multi-depth shuttle warehouses (AMSWs) under low-to-moderate seismic actions", Bulletin of Earthquake Engineering IF 4.6, 2022.

[47] A. Natali, F. Morelli, and W. Salvatore, "On the Seismic Design and Behaviour of Automated Rack Supported Warehouses", Bulletin of Earthquake Engineering 20, pp. 1247–1295, 2022.

[48] RMI, MH 161, Specification for the Design, Testing and Utilization of Industrial Steel Storage Racks, RMI Rack Manufacturers Institute, p. 59, 2008.

[49] Australian Standards, AS 4084, Steel Storage Racking, AS Standards, Australia, 2012.

[50] EN 1993-1-5, "Eurocode 3: Design of steel structures - Part 1-5: General rules - Plated structural elements" 2006.

[51] F. Roure, M.M. Pastor, M. Casafont, M.R. Somalo, "Stub column tests for racking design: experimental testing, FE analysis and EC3"; Thin-Walled Structures, vol. 49, pp. 167-184; 2011.

[52] B.P. Gilbert, K.J.R. Rasmussen, "Experimental Test on Steel Storage Rack Components", School of Civil Engineering, Sydney, Australia, research report no. R899, 2009.

[53] D. Koen, "Structural Capacity of Light Gauge Steel Storage Rack Uprights", School of Civil Engineering, The University of Sydney, (Thesis for the degree of Master of Engineering, 2008.

[54] A. Crisan, V. Ungureanu, D. Dubina, "Behaviour of cold-formed steel perforate sections in compression. Part 1 Experimental investigations", Thin-Walled Structures, vol. 61, pp. 86-96, 2012.

[55] A. Crisan, V. Ungureanu, D. Dubina, "Behaviour of cold-formed steel perforate sections in compression. Part 2 Numerical investigations and

design considerations", Thin-Walled Structures, vol. 61, pp. 97-105, 2012.

[56] P.B.Dinis, B.Young, D.Camotim, "Local–distortional interaction in cold-formed steel rack-section columns", Thin-Walled Structures, vol. 81, pp. 185–194, 2014.

[57] Australian Standard/New Zealand Standard, "Cold-formed stainless steel structures.", AS/NZS 4600 (2nd ed.), Sydney-Wellington, 2005.

[58] J.Becque, K.J. R. Rasmussen, "Experimental Investigation of the Interaction of Local and Overall Buckling of Stainless Steel I-Columns", Journal of Structural Engineering vol.135, no.11, pp. 1349–1356; 2009.

[59] J.Becque, K.J. R. Rasmussen; "Numerical Investigation of the Interaction of Local and Overall Buckling of Stainless Steel I-Columns", Journal of Structural Engineering ,vol.135, pp. 1340–1348; 2009.

[60] F. Gusella, M. Orlando, and K. D. Peterman, "Influence of mechanical and geometric uncertainty on the seismic performance of cold-formed steel braces with additional holes", Structures, vol. 29, no. December 2020, pp. 494-506, 2021.

[61] B. W. Schafer, "Distortional Buckling of Cold-Formed Steel Columns", The American Iron and Steel Institute, final report, 2000.

[62] B.W. Schafer, "Thin-walled column design considering local, distortional and Euler Buckling" Proceedings of Structural Stability Research Council, Annual Technical Session and Meeting, Ft. Lauderdale, Florida, pp. 419–438, 2001.

[63] B.W. Schafer, "Local, distortional and Euler buckling of thin-walled columns", Journal of Structural Engineering, vol.128, pp. 289–299, 2002.

[64] AISI (American Iron and Steel Institute), North American Specification (NAS) for the Design of Cold-Formed Steel Structural Members − AISI-S100-S116, Washington DC, 2016.

[65] ABNT (Brazilian Association of Standards), Brazilian Standard on Design of Cold-Formed Steel Structures − ABNT NBR 14762:2010, Rio de

Janeiro, 2010. (Portuguese).

[66] D. Dubina, V. Ungureanu, "Elastic–plastic interactive buckling of thin-walled steel compression members", in: Proceedings of the 15th International Specialty Conference on Cold-Formed Steel Structures 2000, St. Louis, Missouri, USA, pp.223–237, 2000.

[67] D. Dubina, V. Ungureanu, "Plastic strength of Thin-Walled members" in Proceedings of the 16th International Specialty Conference on Cold-Formed Steel Structures, Orlando, Florida, USA, pp. 324-338, 2002.

[68] F.H. Smith, C.D. Moen, "Finite strip elastic buckling solutions for thin-walled metal columns with perforation patterns", Thin-Walled Structures, vol. 79, pp. 184-201, 2014.

[69] CASE, THIN-WALL A Computer Program for Cross-Section Analysis and Finite Strip Buckling Analysis and Direct Strength Design of Thin-Walled Structures, Centre for Advanced Structural Engineering, School of Civil Engineering, The University of Sydney, 2006 (Version 2.1).

[70] Z. Li, B.W. Schafer, "Buckling analysis of cold-formed steel members with general boundary conditions using CUFSM: conventional and constrained finite strip methods", in: Proceedings of the 20th International; l. Spec. Conference on Cold-Formed Steel Structures, St. Louis, MO. November 2010, 2010

[71] J.M. Davies, P. Leach, "First-order generalised beam theory", Journal of Constructional Steel Research vol.31, pp. 187 220, 1994.

[72] J.M. Davies, P. Leach, D. Heinz, "Second-order generalised beam theory", Journal of Constructional Steel Research vol.31, pp. 221-241, 1994.

[73] N. Silvestre, D. Camotim, "Nonlinear generalized beam theory for cold-formed steel members", International Journal of Structural Stability and Dynamics vol.3(4), pp. 461–490, 2003.

[74] J.Kesti, J.M.Davies, "Local and distortional buckling of thin-walled short columns", Thin-Walled Structures, vol. 34, pp. 115-134, 1999.

[75] C. Bernuzzi, F. Maxenti, European alternatives to design perforated

thin-walled cold-formed beam columns for steel storage systems, Journal of Constructional Steel Research, vol. 110, pp. 121 –136, 2015.

[76] L. Bertocci, D. Comparini, G. Lavacchini, M.Orlando, L. Salvatori , P. Spinelli "Experimental, numerical, and regulatory P-Mx-My domains for cold-formed perforated steel uprights of pallet-racks", Thin-Walled Structures vol. 119, pp. 151–165, 2017.

[77] F. Gusella, G. Lavacchini, M. Orlando, and P. Spinelli, "Axial response of cold-formed steel bracing members with holes", Journal Construction Steel Research, vol. 161, pp. 70-85, 2019.

[78] N. Baldassino, C. Bernuzzi, A. di Gioia, M. Simoncelli, "An experimental investigation on solid and perforated steel storage racks uprights", Journal of Constructional Steel Research, vol. 155, pp. 409–425, 2019.

[79] C. Bernuzzi and C. A. Castiglioni, "Experimental analysis on the cyclic behaviour of beam-to-column joints in steel storage pallet racks", Thin-Walled Structures, vol. 39, no. 10, pp. 841-859, Oct. 2001.

[80] F. Gusella, G. Lavacchini, and M. Orlando, "Monotonie and cyclic tests on beam-column joints of industrial pallet racks", Journal of Constructional Steel Research, vol. 140, pp. 92-107, 2018.

[81] K. D. Peterman, N. Nakata, and B. W. Schafer, "Hysteretic characterization of cold-formed steel stud-to-sheathing connections Journal Construction Steel Research, vol. 101, pp. 254-264, 2014.

[82] A. Mei, M. Orlando, L. Salvatori, and P. Spinelli, "Nonlinear Static and Incremental Dynamic Analyses for Seismic Down-Aisle Behaviour of Rack Structures", Ingegneria Sismica, vol. 38, no. 2, pp. 21-45, 2021.

[83] D. Jovanović, D. Zarković, V. Vukobratović, and Z. Brujić, "Hysteresis model for beam-to-column connections of steel storage racks", Thin-Walled Structures, vol. 142, pp. 189-204, 2019.

[84] C. Bernuzzi, A. di Gioia, G. Gabbianelli, M. Simoncelli, M., "Pushover Analyses of Hand-Loaded Steel Storage Shelving Racks", Journal of Earthquake Engineering, vol. 21(8), pp. 1256–1282, 2017.

[85] A. Kanyilmaz, G. Brambilla, G. P. Chiarelli, C. A. Castiglioni, "Assessment of the seismic behaviour of braced steel storage racking systems by means of full-scale push over tests", Thin-Walled Structures, vol. 107, pp. 138–155, 2016.

[86] A. Kanyilmaz, C. A. Castiglioni, G. Brambilla, G. P. Chiarelli, "Experimental assessment of the seismic behaviour of unbraced steel storage pallet racks", Thin-Walled Structures, vol. 108, pp. 391–405, 2016.

[87] N.D. Kankanamge, M. Mahendran M., "Behaviour and design of cold-formed steel beams subject to lateral–torsional buckling", Thin-Walled Structures, vol. 51, pp. 25–38, 2012.

[88] A. Ranby, "Structural fire design of thin-walled steel sections", Journal of Constructional Steel Research, vol. 46, pp. 303-304, 1998.

[89] C. Renaud, B. Zhao, "Investigation of the simple calculation method in EN 1993-1-2 for buckling of hot rolled class 4 steel members exposed to fire", Proceedings of the fourth international workshop "Structures in Fire", pp. 199–211, 2006.

[90] G. Winter, "Strength of thin steel compression flanges", Transactions of the American Society of Civil Engineers, vol. 112, 1947.

[91] C. Couto, P.V. Real, N. Lopes, B. Zhao, "Resistance of steel cross-sections with local buckling at elevated temperatures", Journal of Constructional Steel Research, vol. 109, pp. 101–114, 2015.

[92] N.D. Kankanamge, M. Mahendran, "Behaviour and design of cold-formed steel beams subject to lateral–torsional buckling", Thin-Walled Structures, vol. 51, pp. 25–38, 2012.

[93] N.D. Kankanamge, M. Mahendran, "Behaviour and design of cold-formed steel beams subject to lateral–torsional buckling at elevated temperatures", Thin-Walled Structures, vol. 61, pp. 213–228, 2012.

[94] B. Baleshan, M. Mahendran, "Fire design rules to predict the moment capacities of thin-walled floor joists subject to non-uniform temperature distributions", Thin-Walled Structures, vol. 105, pp. 29–43, 2016.

[95] L. Laíma, J.P.C. Rodrigues, "Fire design methodologies for cold-

formed steel beams made with open and closed cross-sections", Engineering Structures, vol. 171, pp. 759–778, 2018.

[96] D. de Silva, A. Bilotta, E. Nigro, "Approach for modelling thermal properties of intumescent coating applied on steel members" Fire Safety Journal, vol. 116, pp.103200, 2020.

[97] P. Nonsawat, S. Patvichaichod, "Performance analysis of automatic sprinkler systems in warehouses using fire dynamic simulation", IOP Conf. Series: Materials Science and Engineering, vol. 715, no. 1, p. 012005, 2020.

[98] X. Zhou, Y. Xin, and S. Dorofeev, "Evaluation of an oxygen reduction system (ORS) in large-scale fire tests", Fire Safety Journal, vol. 106, pp. 29-37, 2019.

[99] P. Cancelliere, D. de Silva, A. Marino, E. Nigro, L. Possidente, P. Princi, S. Pustorino, N. Tondini, "Impiego di un impianto a disponibilità superiore nel progetto delle prestazioni di resistenza al fuoco di strutture di acciaio", Fondazione Promozione Acciaio, 2021 (in Italian).

[100] R. Zaharia and J.-M. Franssen, "Fire design study of a high-rise steel storage building", in International Colloquium on Stability and Ductility of Steel Structures, pp. 745-752, 2002.

[101] J.-M. Franssen, V. Kodur, and R. Zaharia, Designing Steel Structures Far Fire Safety. London, UK: Taylor & Francis, 2009.

[102] F. Battistini, G. Galeotti, and L. Vallini, "Studio della dinamica di collasso implosivo di un deposito automatizzato in acciaio tramite FSE", 2018.

[103] M. Madeddu, S. Sassi, C.A. Castiglioni, G.P. Chiarelli, and P. Pietro Setti, "Fire Behaviour of Self Supported Automated Warehouses", Costrizioni Metalliche no.6, pp. 68-77, 2019.

[104] M. Di Felice, F. Busato, and R. Matteazzi, "Modellazione fluidodinamica dell'incendio in un magazzino automatico", 2018.

[105] G. Heskestad, "Luminous heights of turbulent diffusion flames," Fire Safety Journal, vol. 5, no. 2, pp. 103-108, 1983.

[106] G. Heskestad, "Engineering relations for fire plumes," Fire Safety Journal, vol. 7, no. 1, pp. 25-32, 1984.

[107] Y. Hasemi, Y. Yokobayashi, T. Wakamatsu, and A. Ptchelintsev, "Fire safety of building components exposed to a localized fire - scope and experiments on ceiling/ beam system exposed to a localized fire," in Proceedings of ASIAFLAM, pp. 351-361, 1995.

[108] O. Vassart, F. Hanus, M. Brasseur, R. Obiala, J.-M. Franssen, A. Scifo, , B. Zhao, C. Thauvoye, A. Nadjai, and H Sanghoon, "Temperature assessment of a vertical steel member subjected to localised fire, acronym LOCAFI", Report RFSR-CT-2012-00023, European Commission, 2016.

[109] R. Friedman, "An International Survey of Computer Models for Fire and Smoke", Journal of Fire Protection Engineering, vol. 4, no. 3, pp. 81-92, 1992.

[110] G. P. Forney and W. F. Moss. "Analysing and Exploiting Numerical Characteristics of Zone Fire Models". Fire Science and Technology, Vol.14 No.1 & No.2 (49-60), 1994.

[111] S. M. Olenick and D. J. Carpenter, "An updated international survey of computer models for fire and smoke", Journal of Fire Protection Engineering, vol. 13 no. 3 pp. 87-110, 2003.

[112] W. W. Jones, G. Forney, R. D. Peacock, and P.A. Reneke "A Technical Reference for CFAST: An Engineering Tool for Estimating Fire and Smoke Transport", Technical Note, (NIST TN), National Institute of Standards and Technology, Gaithersburg, MD, May 2, 2003.

[113] J.F. Cadorin, "Compartment Fire Models for Structural Engineering", PhD thesis (Liège University), 2003.

[114] J.F. Cadorin, J.M. Franssen. "A tool to design steel elements submitted to compartment fires - OZone V2. Part 1: pre- and post-flashover compartment fire model", Fire Safety Journal, vol. 38 (5), pp. 395-427, 2003.

[115] J.F. Cadorin, D. Pintea, J.-C. Dotreppe, J.-M. Franssen, "A tool to design steel elements submitted to compartment fires - OZone V2. Part 2: methodology and applications", Fire Safety Journal, vol. 38(5),

pp.429-451, 2003.

[116] W J. Bong, "Limitations of Zone Models and CFD Models for Natural Smoke Filling in Large Spaces", master's degree thesis, Department of Civil and Natural Resources Engineering University of Canterbury, Christchurch, New Zealand, 2012

[117] K. Suzuki, K. Harada, and T. Tanaka, "A Multi-Layer Zone Model for Predicting Fire Behaviour in a single room", Proceedings of the seventh international symposium, 2002.

[118] C. Xiaojun, Y. Lizhong, D. Zhihua, F. Weicheng "A multi-layer zone model for predicting fire behaviour in a fire room" Fire Safety Journal vol. 40, pp. 267–281, 2005.

[119] N. Johansson, "Evaluation of a zone model for fire safety engineering in large spaces" Fire Safety Journal Vol. 120, pp. 103-122, 2021.

[120] SFPE Handbook of Fire Protection Engineering, 5th edition, 2016, ISBN: 978-1-4939-2564-3.

[121] J.G.G.M. de Boer, H. Hofmeyera, J. Maljaars, R.A.P. van Herpen. "Two-way coupled CFD fire and thermomechanical FE analyses of a self-supporting sandwich panel façade system". Fire Safety Journal, pp. 154-168, vol. 105, 2019.

[122] M.J. Lewis, J.B. Moss, P.A. Rubini, "CFD Modelling of Combustion and Heat Transfer in Compartment Fires", Proceedings of the Fifth International Symposium on Fire Safety Science, International Association for Fire Safety Science, Melbourne, Australia, pp. 463–474, 1997.

[123] Hasib, R. Kumar, Shashi, S. Kumar, "Simulation of an experimental compartment fire by CFD", Building and Environment, Vol. 42, Issue 9, pp. 3149-3160, 2007.

[124] B. Merci, K. Van Maele, "Numerical simulations of full-scale enclosure fires in a small compartment with natural roof ventilation", Fire Safety Journal, Vol. 43, Issue 7, pp. 495-511, 2008.

[125] R.G. Gann, A. Hamins, K. McGrattan, H.E. Nelson, T.J. Ohlemiller, K.R. Prasad, W.M. Pitts, "Reconstruction of the fires and thermal en-

vironment in World Trade Center buildings 1, 2, and 7", Fire Technology, vol. 49, pp. 679-707, 2013.

[126] I. Fletcher, A. Borg, N. Hitchen, S. Welch, "Performance of concrete in fire: A review of the state of the art, with a case study of the Windsor Tower fire", in: Proceedings of the 4th International Workshop in Structures in Fire, pp. 779–790, 2006.

[127] M.D. Engelhardt, B. Meacham, V. Kodur, A. Kirk, H. Park, I.J. van Straalen, J. Maljaars, K. van Weeren, R. de Feijter, K. Both "Observations from the Fire and Collapse of the Faculty of Architecture Building, Delft University of Technology", Conference: Structures Congress, 2013.

[128] G. Rein, X. Zhang, P. Williams, B. Hume, A. Heise, A. Jowsey, B. Lane, J.L. Torero, "Multi-storey fire analysis for high-rise buildings", in: Proceedings of the 11th International Interflam Conference, London, UK, pp. 605–616, 2007.

[129] R. K. Janardhan, S. Hostikka "When is the fire spreading and when it travels? – Numerical simulations of compartments with wood crib fire loads", Fire Safety Journal, vol. 126, Article 103485, 2021.

[130] J. Gales, "Travelling fires and the St. Lawrence burns project", Fire Technology, vol. 50 (6), pp. 1535–1543, 2014.

[131] T. Lennon, D. Moore, "The natural fire safety concept—full-scale tests at Cardington", Fire Safety Journal, vol. 38 (7), pp. 623–643, 2003.

[132] K. Horov, T. Jàna, F. Wald, "Temperature heterogeneity during travelling fire on experimental building", Advantage Engineering Software vol. 62, 2013.

[133] D. Rush, D. Lange, J. Maclean, E. Rackauskaite, "Effects of a travelling fire on a concrete column - Tisova fire test" in: Proceedings of the International Conference on Applications of Structural Fire Engineering, ASFE 2015, CTU Publishing House, Czech Technical University in Prague, 2015.

[134] J.P. Hidalgo, A. Cowlard, C. Abecassis-Empis, C. Maluk, A.H. Majda-

lani, S. Kahrmann, R. Hilditch, M. Krajcovic, J.L. Torero, "An experimental study of full-scale open floor plan enclosure fires", Fire Safety Journal, vol. 89, pp. 22–40, 2017.

[135] J.P. Hidalgo, T. Goode, V. Gupta, A. Cowlard, C. Abecassis-Empis, J. Maclean, A. I. Bartlett, C. Maluk, J.M. Montalv´a, A.F. Osorio, J.L. Torero, "The Malveira fire test: full-scale demonstration of fire modes in open-plan compartments" Fire Safety Journal, vol. 108 102827, 2019.

[136] G. C. Clifton, "Fire models far large firecells", HERA Report R4-83, 1996.

[137] Y. Wang, I. Burgess, F. Wald, M. Gillie, "Performance-Based Fire Engineering of Structures", London, CRC Press, 2012.

[138] G. Rein, X. Zhang, P. Williams, B. Hume, A. Heise, A. Jowsey, B. Lane, and J. L. Torero, "Multi-Storey Fire Analysis for High-Rise Buildings", Proceedings of the 11th International Interflam Conference, London (UK), pp. 605-616, 2007.

[139] A. Law, J. Stern-Gottfried, M. Gillie, and G. Rein, "The influence of travelling fires on a concrete frame", Engineering Structure, vol. 33, no. 5, pp. 1635-1642, 2011.

[140] J. Stern-Gottfried, G. Rein, "Travelling fires for structural design-Part I: Literature review", Fire Safety Journal, vol. 54, pp. 74-85, 2012.

[141] J. Stern-Gottfried, G. Rein, "Travelling fires for structural design-Part II: Design methodology", Fire Safety Journal, vol. 54, pp. 96-112, 2012.

[142] E. Rackauskaite, C. Hamel, A. Law, G. Rein, "Improved formulation of travelling fires and application to concrete and steel structures", Structure, vol.3, pp. 250-260, 2015.

[143] X. Dai, S. Welcha, A. Usmani, "A critical review of "travelling fire" scenarios for performance-based structural engineering", Fire Safety Journal vol. 91, pp. 568–578, 2017.

[144] X. Dai, S. Welch, O. Vassart, K. Cábová, L. Jiang, J. Maclean, et al. "An

extended travelling fire method framework for performance-based structural design" Fire Materials, vol. 44, no. 3, pp. 437-457, 2020.

[145] M. Charlier, A. Glorieux, X. Dai, N. Alam, S. Welch, J. Anderson, O. Vassar, A. Nadjai, "Travelling fire experiments in steel-framed structure: numerical investigations with CFD and FEM", Journal of Structural Fire Engineering, 12, no. 3, pp. 309-327, 2021.

[146] D. Drysdale, "An Introduction to Fire Dynamics" (2nd Edition), Wiley, Chichester, 1998.

[147] C. Röben, M. Gillie, J.L. Torero, "Structural behaviour during a vertically travelling fire", Journal of Constructional Steel Research, vol.66, pp. 191-197, 2010.

[148] G. Flint, Fire Induced Collapse of Tall Buildings, Ph.D. Thesis, School of Engineering, The University of Edinburgh, 2005.

[149] P. Kotsovinos, Y. Jiang, A. Usmani, "Effect of vertically travelling fires on the collapse of tall buildings", International Journal of High-Rise Buildings, vol 2, pp. 49-62, 2013.

[150] A. Lönnermark, H. Ingason, "Fire Spread in Large Industrial Premises and Warehouses", in BRANDFORSK project 630-021, 2005.

[151] H.C. Kung, H.-Z. Yu and R. D. Spaulding, "Ceiling Flows of Growing Rack Storage Fires", Twenty-First Symposium (International) on Combustion, PP. 121-128, 1986.

[152] P. Field, "Effective Sprinkler Protection for High Racked Storage", Fire Surveyor, October 1985.

[153] H. Z. Yu, and H.-C. Kung, "Strong Buoyant Plumes of Growing Rack Storage Fires", The Twentieth Symposium (International) on Combustion, P. 1567, 1984.

[154] K. McGrattan, A. Hamis and D. Stroup, "International Fire Sprinkler –

Smoke & Heat Vent - Draft Curtain - Fire Test Project, Large Scale Experiments and Model Development", National Fire Protection Research Foundation, Technical Report, September 1998.

[155] J. Troup, "Protection of Warehouse Retail Occupancies with Extra Large Orifice (ELO) Sprinklers", Journal of Fire Protection Engineering, Vol. 8 (1), pp 1-12, 1996.

[156] J. Troup, "Extra Large Orifice (ELO) Sprinklers: An Overview of Full-Scale Fir test Performance", Journal of Fire Protection Engineering, Vol. 9 (3), pp 27-39, 1998

[157] H. Ingason, "Experimental and Theoretical Study of Rack Storage Fires", in BRANDFORSK project 602-971, 2006

[158] H. Ingason, "In-Rack Fire Plumes", Fire Safety Science - Proceedings of the Fifth International Symposium, 333-344, Melbourne, Australia, 3-7 March, 1997.

[159] H. Ingason, "Plume flow in high rack storages", Fire Safety Journal, Vol. 36, p. 437 - 457, 2001.

[160] H. Ingason, H., "Effects of Flue Spaces on the Initial In-Rack Plume Flow", Fire Safety Science - Proceedings of the Seventh International Symposium, 235-246, Worcester, USA, 16-21 June 2002.

[161] H. Ingason, "Heat Release Rate of Rack Storage Fires", Proceedings of 9th Interflam - Fire Science & Engineering Conference, p. 731-740, Edinburgh, 17-19th September 2001.

[162] Y. Z. Li, H. Ingason, "Scaling of wood pallet fires", SP Technical Research Institute of Sweden SP Report 2014:57. 2014

[163] ISO 5660-1, "Reaction-to-fire tests - Heat release, smoke production and mass loss rate - Part 1: Heat release rate (cone calorimeter method)", 2nd ed., 2002-12-15, ISO, 2002.

[164] ISO 5660-2, "Reaction-to-fire tests - Heat release, smoke production

and mass loss rate - Part 2: Smoke production rate (dynamic measurement)", 2nd ed., 2002-12-15, ISO, 2002.

[165] ISO9705, "Fire tests - Full-scale room test for surface products", ISO9705:1993(E), 1993.

[166] M. Dahlberg, "The SP Industry Calorimeter: For rate of heat release measurements up to 10 MW", SP Swedish National Testing and Research Institute, SP REPORT 1992:43, Borås, Sweden, 1993.

[167] M. Dahlberg, "Error Analysis for Heat Release Rate Measurement with the SP Industry Calorimeter", SP Swedish National Testing and Research Institute, SPREPORT 1994:29, Borås, 1994.

[168] Research Programme of the Research Fund for Coal and Steel, Esch/Alzette G. Heskestad. "Physical modelling of fire", J Fire Flammability, Vol.6, pp. 253-273. 1975.

[169] J.G. Quintiere, "Scaling applications in fire research", Fire Safety Journal, Vol. 15, pp. 3-29. 1989.

[170] J. Perricone, M. Wang, J. Quintiere. "Scale modelling of the transient thermal response of insulated structural frames exposed to fire". Fire Technology., Vol. 44, pp. 113-136, 2007.

[171] D.M. 3 agosto 2015 Approvazione di norme tecniche di prevenzione incendi, ai sensi dell'articolo 15 del decreto legislativo 8 marzo 2006, n. 139, GU n. 192 del 20/8/2015 – S.O. n. 51 (in Italian).

[172] K. McGrattan, S. Hostikka, R. McDermott, J. Floyd, C. Weinschenk, K. Overholt, "Fire Dynamics Simulator User's Guide (Sixth Edit)", National Institute of Standards and Technology (NIST), Special Publication 1019, 2017.

[173] G.P. Forney, "Smokeview, A Tool for Visualizing Fire Dynamics Simulation Data Volume I: User's Guide (Sixth Edit)", National Institute of Standards and Technology (NIST), Special Publication 1017-1, 2023.

[174] "PyroSim User Manual (Sixth Edit)" Thunderhead engineering, USA 2023.

[175] K. Horovà, "Modeling of Fire Spread in Structural Fire Engineering", PhD thesis, Czech Technical University in Prague, 2015.

[176] J. Degler, A. Eliasson, A. Anderson, D. Lange, D. Rush, "A-priori modelling of the Tisova Fire Test as input to the experimental work", Proceedings of the First International Conference on Structural Safety under Fire & Blast, Glasgow, Scotland, UK, pp. 429–438, 2015.

[177] K. J. Overholt, "Verification and Validation of Commonly Used Empirical Correlations for Fire Scenarios", NIST Special Publication 1169, 2014.

[178] U. Wickström, D. Duthinh, K. McGrattan, "Adiabatic surface temperature for calculating heat transfer to fire exposed structures", Proceedings of the Eleventh International Interflam Conference, London: Interscience Communications, 2007.

[179] U. Wickström, S. Hunt, B. Lattimer, J. Barnett, C. Beyler, "Technical comment—Ten fundamental principles on defining and expressing thermal exposure as boundary conditions in fire safety engineering", Fire and Materials, vol. 42(8), pp. 985-988, 2018.

[180] G. H. Powell, "Progressive Collapse: Case Studies Using Nonlinear Analysis", in Structures Congress 2005, vol. 4, no. 1, pp. 88-100, 2005.

[181] G. Kaewkulchai and E. B. Williamson, "Beam element formulation and solution procedure for dynamic progressive collapse analysis", Computers & Structures, vol. 82, no. 7-8, pp. 639-651, 2004.

[182] Franssen, J.M., Gernay, T. "Modelling structures in fire with SAFIR®: Theoretical background and capabilities", Journal of Structural Fire Engineering, 8(3):300-323,2017.

[183] Coll, A., Ribo, R., Pasenau, M., Escolano, E., Perez, J., Melendo, A., Monros, A. and Garate, J, "GiD v.13 User Manual", CIMNE (Eds), (2016).

[184] Luisier, M., Schenk, O., et al., "Fast methods for computing selected elements of the green's function in massively parallel nanoelectronics device simulations", in Wolf, F., Mohr, B. and a Ney, D. (Eds), Euro-Par 2013, LNCS 8097, Springer-Verlag Berlin, Heidelberg, pp. 533-544,

2013.

[185] Franssen, J.M., "SAFIR: a thermal-structural program for modelling structures under fire" Engineering Journal, Vol. 42 No. 3, pp. 143-158, 2005.

[186] Tondini, N., Vassart, O. and Franssen, J.M., "Development of an interface between CFD and FE software", Proceedings of the 7th International Conference on Structures in Fire, ETH Zurich, Switzerland, pp. 459-468, 2012.

[187] Franssen, J.M. and Gens, F., "Dynamic analysis used to cope with partial and temporary failures", in Franssen, J.M., Benichou, N., Kodur, V. and Sultan, M. (Eds), proceedings of SiF'04: Third International Structures in Fire Workshop, IRC, Ottawa, pp. 297-310, 2004.

[188] Franssen J.M., Cowez B, Gernay T., "Effective stress method to be used in beam finite elements to take local instabilities into account", Fire safety science-proceedings of the eleventh international symposium pp. 544-557, 2014.

[189] Y. Xia, T. Gernay2, "A comparative analysis and experimental validation of modelling strategies for structures subject to localized fires", proceedings of the 12th Asia-Oceania Symposium on Fire Science and Technology (AOSFST 2021), 2021.

[190] ABAQUS, Analysis User's Manual. Dassault Systémes Simulia Corp., 2020.